1-1-2013

Optimal Design and Control of DC-DC Resonant Converters For Wireless Power Transfer Applications

Isaac Nam
University of South Carolina - Columbia

OPTIMAL DESIGN AND CONTROL OF DC-DC RESONANT CONVERTERS FOR WIRELESS POWER TRANSFER APPLICATIONS

by

Isaac IL W. Nam

Bachelor of Science
University of South Carolina, 2009

Master of Science
University of South Carolina, 2011

Submitted in Partial Fulfillment of the Requirements

For the Degree of Doctor of Philosophy in

Electrical Engineering

College of Engineering and Computing

University of South Carolina

2013

Accepted by:

Enrico Santi, Major Professor

Roger Dougal, Committee Member

Mohammod Ali, Committee Member

Branko Popov, Committee Member

Lacy Ford, Vice Provost and Dean of Graduate Studies

DEDICATION

I dedicate this work to my father, the greatest and most loving father in the world who has sacrificed so much for me and has always been the greatest motivation for me.

ACKNOWLEDGEMENTS

I appreciate the encouragement and guidance that my advisor Dr. Enrico Santi has given me during my research. Dr. Enrico Santi has earned enormous respect through the depth of his knowledge and sincere care for his graduate students, and this fact has served as an inspiration for me to become a better electrical engineer.

Also, I wish to express my gratitude to other committee members, Dr. Roger Dougal, Dr. Mohammod Ali, and Dr. Branko Popov for encouraging me and for being an important part in my pursuit of Ph. D.

I would like to show my appreciation to my fellow graduate students in Dr. Enrico Santi's group for that we have shared useful and important knowledge through friendly interactions.

Finally, I thank the Office of Naval Research (ONR) for the partial financial support through the research grant, N00014-07-1-0025.

ABSTRACT

Wireless power transfer (WPT) technology provides galvanic isolation for improved safety and also provides reliability by eliminating the need for dedicated connectors/adapters that can get damaged due to frequent usage. For these reasons, it has become popular in medical implant charging and electric vehicle (EV) charging. Beyond these niche applications, due to aesthetic features and convenience provided by the cord-free environment, it is rapidly becoming an attractive charging solution for various portable electronics as well as household appliances.

However, currently available WPT technology demonstrates several shortcomings and various challenges due to allowed receiver position variation with respect to transmitter position. For consumers, major shortcomings and challenges include lower power transmission efficiency compared to hard-connected charging method and limited receiver positioning flexibility. For the industry, major shortcomings and challenges include increased cost of implementation and increased complexity in design and control.

In order to promote adoption of WPT technology, it is important to provide good power transmission efficiency and to improve receiver positioning flexibility while reducing complexity in design and control of resonant converters. Also, it is important to minimize the component count to reduce the cost of implementation.

In this research, novel optimal design methods have been developed for resonant converters employing two popular resonant tank topologies: series-series (SS) resonant

tank and series-parallel (SP) resonant tank. Also, a novel control method for SS resonant converter employing a symmetrical inductive coupler has been developed. These methods reduce complexity in analysis, design, and control. Using these methods, receiver positioning flexibility can be improved without a large component count while minimizing design complexity. Various simulation results and experimental results are presented to show that these methods allow achieving an optimal compromise between power transmission efficiency and power delivery robustness against variations in resonant tank parameters occurring due to magnetic coupling variation.

TABLE OF CONTENTS

LIST OF TABLES

LIST OF FIGURES

LIST OF SYMBOLS

C_1	Primary-side Capacitance or Capacitor
C_2	Secondary-side Capacitance or Capacitor
C_2'	C_2 Referred to Primary Side
$\|\|G_i(j\omega)\|\|$	Current Gain Magnitude Transfer Function of Resonant Tank
$\|\|G_i\|\|_{max}$	Peak Current Gain Magnitude of Resonant Tank
$\|\|G_V(j\omega)\|\|$	Voltage Gain Magnitude Transfer Function of Resonant Tank
$\|\|G_V\|\|_{max}$	Peak Voltage Gain Magnitude of Resonant Tank
f_O	Unity Gain Resonant Frequency
f_S	Switching Frequency
k	Magnetic Coupling Coefficient
k_L	Ratio of Magnetizing Inductance to Leakage Inductance
L_{e1}	Primary-side Leakage Inductance
L_{e2}	Secondary-side Leakage Inductance
L_{e2}'	L_{e2} Referred to Primary Side
L_m	Magnetizing Inductance
L_{S1}	Primary-side Self-inductance
L_{S2}	Secondary-side Self-inductance
L_{S2}'	L_{S2} Referred to Primary Side
η	Overall Efficiency of a Resonant Converter's Power Stage

LIST OF ABBREVIATIONS

ART ..... Asymmetrically-implemented Resonant Tank

LART ..... Loosely-coupled ART

Loosely Coupled ..... Coupling Coefficient, $k \leq 0.35$ Approximately

LSRT ..... Loosely-coupled SRT

PWM ..... Pulse Width Modulated or Pulse Width Modulation

SRT ..... Symmetrically-implemented Resonant Tank

SS ..... Series-series Resonant Tank

SP ..... Series-parallel Resonant Tank

TART ..... Tightly-coupled ART

TSRT ..... Tightly-coupled SRT

Tightly Coupled ..... Coupling Coefficient, $k \geq 0.6$ Approximately

ZCS ..... Zero Current Switching

ZVS ..... Zero Voltage Switching

CHAPTER 1
INTRODUCTION

1.1 BASIC OVERVIEW OF WIRELESS POWER TRANSFER

In magnetically-coupled wireless chargers, electric power is transmitted across a magnetic coupler via magnetic field coupling. Unlike transformers, a magnetic coupler can have a large air-gap distance and misalignment between its primary-side coil (transmitter coil, Tx) and secondary-side coil (receiver coil, Rx). An example of a magnetic coupler is shown in Figure 1.1. The figure shows a *symmetrical* implementation of Tx and Rx in which they have the same physical geometry. It should be mentioned that a magnetic coupler can also be implemented *asymmetrically* with different geometric shapes and different turns ratio for Tx and Rx.

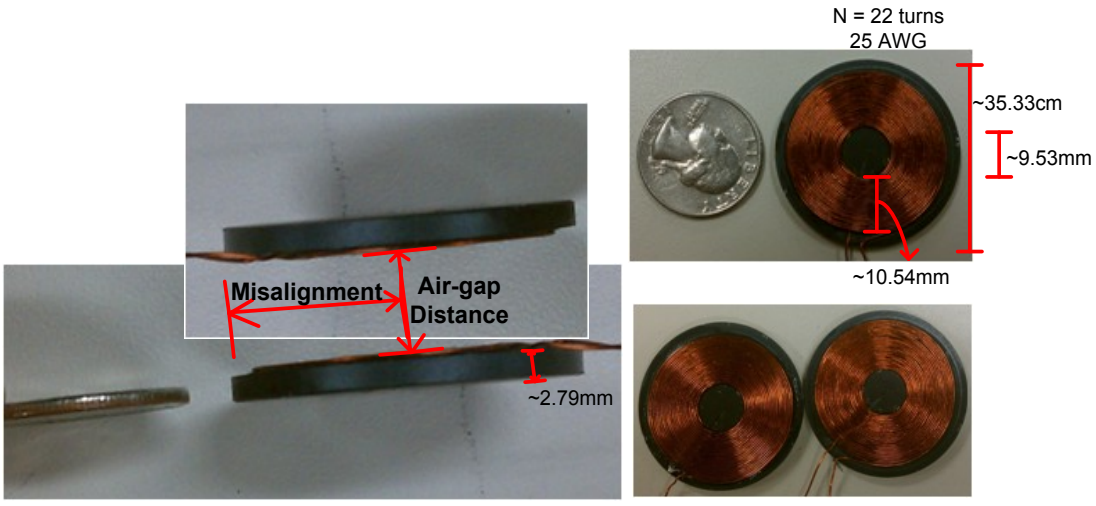

Figure 1.1: A magnetic coupler example consisting of two flat planar cores with 1:1 turns ratio.

Due to non-ideal magnetic coupling (k) caused by a large air-gap and misalignment between Tx and Rx, large leakage fluxes are generated. Effects of leakage fluxes are modeled with so called leakage inductances. Ideal (perfect) coupling refers to the condition of $k = 1$, whereas non-ideal (imperfect) coupling refers to the condition of $0 \leq k < 1$. As can be seen inside the dashed red box in Figure 1.2, a magnetic coupler for $0 \leq k < 1$ can be represented as a T-equivalent model consisting of primary-side leakage inductance (L_{e1}), magnetizing inductance (L_m), and secondary-side leakage inductance referred to the primary side ($L_{e2}' = n^2 L_{e2}$). For the T-equivalent model, magnetic coupling coefficient, k, is determined by Equation 1, where L_{S1} represents primary-side self-inductance and L_{S2}' represents secondary-side self-inductance referred to the primary side.

The T-equivalent model may or may not contain winding resistance and core equivalent resistance accounting for core loss, depending on significance of their effects in desired analysis.

A magnetic coupler is driven by a switching converter, and the magnetic coupler together with one or more resonant capacitors forms the so-called resonant tank. The purpose of constructing a resonant tank is to compensate for leakage inductances, L_{e1} and L_{e2}', so that their impedances are effectively shorted out (zero) by resonant capacitors at resonant frequency. This resonant compensation minimizes losses in a resonant tank to deliver an appropriate power at maximized efficiency. More details on resonant tank characteristics will be provided in Chapter 3. Also, theory of resonant converters is explained in more detail later in the background section. For now, it should be mentioned that a DC-DC resonant converter performs DC to AC conversion, and then AC voltage

excites a resonant tank consisting of inductance(s) and capacitance(s). Due to this AC excitation, magnetic field is induced in Tx. AC voltage and current waveforms are then induced in Rx via magnetic coupling. In a receiver, these AC waveforms are converted back to DC by the use of either passive rectification or active rectification. These rectified waveforms are then fed into a low pass filter to filter out undesirable high frequency signals. After the low pass filter stage, the transmitted power is used to charge a battery or to power up an electronic load. This process is shown in Figure 1.2, which provides a simplified overview of resonant converter operation. As Figure 1.2 shows, in wireless charging, the DC to AC conversion generates AC signals to excite a resonant tank whose inductances come from the T-equivalent model of a magnetic coupler, although additional inductor(s) are sometimes implemented.

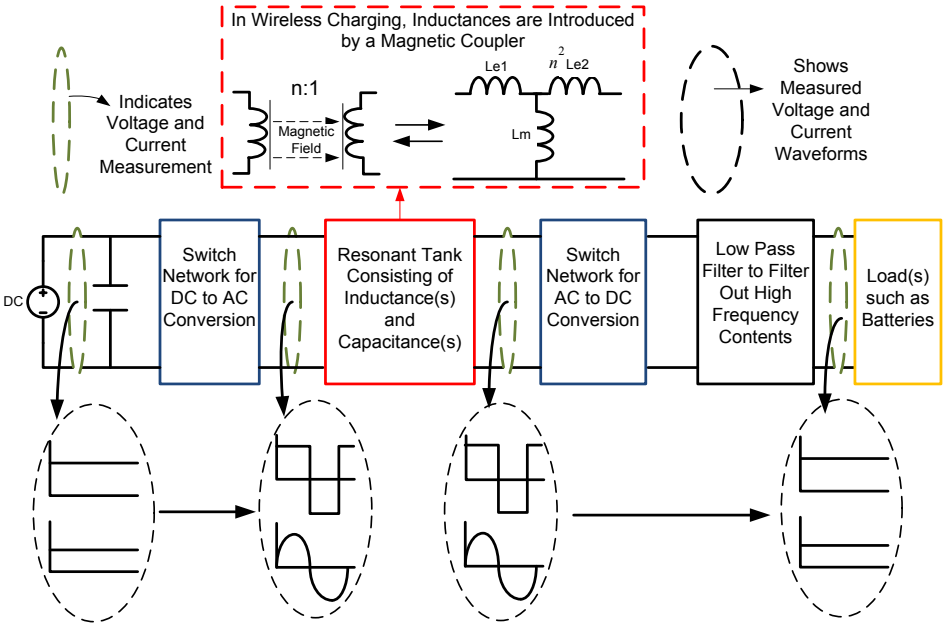

Figure 1.2: Simplified overview of resonant converter operation.

$$k = \frac{L_m}{\sqrt{L_{s1}L_{s2}'}} = \sqrt{k_1 k_2} \quad \text{..... Equation (1)}$$

where $L_{s1} = L_{e1} + L_m$; $L_{s2}' = L_{e2}' + L_m$; $k_1 = \frac{L_m}{L_{e1}+L_m}$; and $k_2 = \frac{L_m}{L_{e2}'+L_m}$

There are different possible resonant capacitor arrangements for creating various resonant tank topologies. Two popular resonant tank topologies, series-series (SS) resonant tank and series-parallel (SP) resonant tank, are shown in Figure 1.3- Note: Each topology contains the T-equivalent model of the magnetic coupler, and the secondary-side parameters are referred to the primary side. Examples of these topologies in wide range of applications can be found in [1], [6], [8]-[9], [24], [34]-[35] and [37].

In Figure 1.3, the resonant tank input is AC voltage V_i, which is created by the primary-side switch network performing DC to AC conversion. The resonant tank output is represented as an effective resistive load, R_e', referred to the primary side, which models the secondary-side rectification network and the battery load under nominal charging condition. The subscripts, $_{SS}$ and $_{SP}$, are added to distinguish between the expressions for R_e' in SS and SP resonant tank topologies: R_{eSS}' for SS resonant tank and R_{eSP}' for SP resonant tank. Primary-side resonant capacitance is denoted as C_1, and secondary-side resonant capacitance referred to the primary side is denoted as C_2'.

Resonant Topology	**Parameters Referred to the Primary Side**
Series-series (SS) Resonant Tank 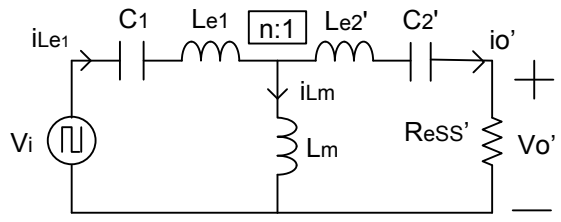	$L_{e2}' = n^2 L_{e2}$ $C_2' = \frac{C_2}{n^2}$ $R'_{eSS} = n^2 \left(\frac{8}{\pi^2}\right) R_{load}$
Series-parallel (SP) Resonant Tank 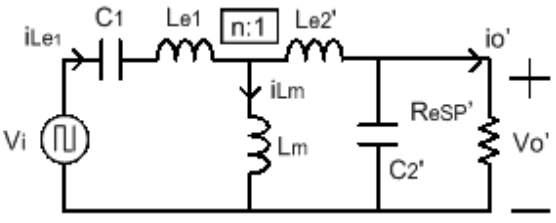	$L_{e2}' = n^2 L_{e2}$ $C_2' = \frac{C_2}{n^2}$ $R'_{eSP} = n^2 \left(\frac{\pi^2}{8}\right) R_{load}$

Figure 1.3: Series-series (SS) and series-parallel (SP) resonant tanks with secondary-side parameters referred to primary side.

In this research, detailed analysis is performed for voltage gain $\|G_V(j\omega)\|$, current gain $\|G_i(j\omega)\|$, and circulating current gain $\|G_{iLm}(j\omega)\|$ of the two resonant tank topologies. Angular frequency ω is in rad/s and defined as $2\pi f$, where frequency f is in Hz. Voltage gain $\|G_V(j\omega)\|$ is defined as the magnitude of the ratio V_O' to V_i in the frequency domain. Current gain $\|G_i(j\omega)\|$ is defined as the magnitude of the ratio of i_O' to i_{Le1} in the frequency domain. Circulating current gain $\|G_{iLm}(j\omega)\|$ is defined as the magnitude of the ratio of i_{Lm} to i_{Le1} in the frequency domain.

For the two resonant tank topologies, voltage gain evaluates power transmission characteristics. In the SS resonant tank, current gain and circulating current gain evaluate coil-to-coil power efficiency. On the other hand, in the SP resonant tank, current gain evaluates the resonant tank's power efficiency while circulating current gain evaluates coil-to-coil power efficiency. This is because current gain of the SP resonant tank is affected *also* by one *additional* circulating current path through C_2' unlike the SS resonant tank – See Figure 1.3.

As mentioned previously, the coupler can be implemented either asymmetrically or symmetrically. Due to this fact, there are two main types of resonant tank that the SS resonant tank and SP resonant tank can belong to. One is asymmetrically-implemented resonant tank (ART) type, and the other is symmetrically-implemented resonant tank (SRT) type. In ART type, the primary leakage (L_{e1}) and the secondary leakage referred to the primary side ($L_{e2}' = n^2 L_{e2}$) can be largely *different*, thus they are *not* related simply by the coupler turns ratio, n. In SRT type, L_{e1} and L_{e2}' are *equal* to each other. Thus, in SRT type, relative inductance condition is always $L_{S1} = L_{S2}'$, whereas, in ART type, it can be

$L_{S1} > L_{S2}'$, $L_{S1} = L_{S2}'$, or $L_{S1} < L_{S2}'$. Consequently, analytical complexity is higher for ART type.

These two main resonant tank types can be further divided based on the range of k. ART type can be divided into tightly-coupled ART (TART) type or loosely-coupled ART (LART) type. Also, SRT type can be either tightly-coupled SRT (TSRT) type or loosely-coupled SRT (LSRT) type. In this research, the term, 'tightly-coupled', refers to $k \geq 0.6$ approximately, whereas the term, 'loosely-coupled', corresponds to $k \leq 0.35$ approximately.

1.2 Motivation and Research Objectives

Wireless charging provides increased safety and convenience by applying galvanic isolation and by eliminating the need for frequently-used dedicated connectors/adapters. For these reasons, it has been utilized in medical implant charging [1]-[5] and electric vehicle (EV) charging [6]-[9]. Recently, wireless charging has become an attractive charging solution also for electronic household appliances and various portable electronics [10]–[13] such as cellular phones [14]-[16] and laptops [17]-[18]. This is because wireless charging can also provide aesthetically-pleasing cord-free environment that improves spatial utilization. However, current wireless charging technology demonstrates several shortcomings.

From the consumer's perspective, the shortcomings include limited receiver positioning flexibility and lower power transmission efficiency compared to wire-connected charging. From the industry's perspective, they include increased cost due to a large component count and increased complexity in design and control.

In order to promote adoption of wireless power transfer technology, it is crucial to provide good efficiency in both tightly-coupled systems and loosely-coupled systems while reducing the complexity in design optimization and control of resonant converters. Furthermore, minimization of component count to reduce the cost of implementation is highly desirable.

However, there exist various challenges due to the fact that significant variations can occur in k and R_e'. Variation in k is caused by the misalignment and air-gap changes between Tx and Rx - See Figure 1.1. This variation changes the inductances (L_{e1}, L_{e2}', and L_m) and thus causes resonant frequencies to shift. Variation in R_e' can occur passively and/or actively. Passive variation in R_e' occurs due to battery state of charge variation or due to different electronic loads. Active variation in R_e' occurs due to various rectification (AC to DC conversion) techniques. Both types of variation (k variation and R_e' variation) causes resonant peaks to change in voltage gain, current gain, and/or circulating current gain. These resonant peak changes can be described in terms of quality factor, Q. Expressions for Q depend on resonant tank topologies and author. In this research, Q describes relationship between resonant elements and effective resistive load, R_e'. Therefore, Q in this research is a load-dependent quantity. Different mathematical expressions for Q are used later in this dissertation. For now, it should be noted that Q variation can be imposed by changing R_e'. In summary, resonance characteristics of a resonant tank can vary significantly in wireless power transfer applications. Consequently, analysis, design, and control can become complex.

The parameter variations affect power transmission characteristics, efficiency, and control model complexity. More specifically, the following *general* remarks, a through d, can be made regarding various affected quantities in wireless charging applications.

a. Maximizing power transmission robustness against k variation is desirable for minimizing losses in an additional converter and/or regulator implemented in either the transmitter-side or receiver-side of a resonant converter. In some cases, high robustness in power transmission characteristics can even eliminate the need for an additional converter and/or regulator, which maximizes the overall system efficiency. It can also significantly decrease the complexity in deriving frequency-dependent models for controlling power transmission. **Note**: Power transmission robustness is maximized when voltage gain robustness is maximized.

b. Power efficiency in a resonant tank is maximized ideally when its leakage inductances are fully compensated by resonant capacitor(s) to produce effective short-circuited (zero) impedance. In a desired range of k variation, maintaining compensation of leakage inductances provides sufficient power delivery without significant losses in a magnetic coupler. Therefore, there needs to be a control method that allows tracking and achieving the compensation of leakage inductances under k variation.

c. Satisfying **a** through **b** above leads to increased receiver positioning flexibility.

d. There is a trade-off between coil-to-coil power efficiency and robustness in power delivery: high coil-to-coil efficiency of a resonant tank may be achieved at the cost of low power delivery robustness against k variation. This means that, under the condition that expected losses in an additional converter and/or linear voltage regulator are higher than expected losses in a resonant tank, it is better to increase power delivery robustness, because overall charging system efficiency can be increased by minimizing the losses in or the need for an additional converter and/or linear voltage regulator.

To achieve good overall efficiency and robustness in power transmission, to improve receiver positioning flexibility, and to reduce implementation complexity, this dissertation presents the following novel accomplishments in order.

- **NOVEL ACCOMPLISHMENT 1:**

  To obtain a novel optimal design method for SS resonant tank of SRT type by performing detailed analysis on frequency-domain characteristics of SS resonant tank of SRT type.

- **NOVEL ACCOMPLISHMENT 2:**

  To obtain a novel control method that *enables* unity gain frequency tracking (UGFT) in a SS resonant converter of SRT type under k variation *without* the need for digital communication between transmitter and receiver.

- **NOVEL ACCOMPLISHMENT 3:**

  Based on detailed analysis of *general* frequency-domain characteristics of SS and SP resonant tank topologies, derive *general* analytical equations in design-oriented form for determining various notable quantities in SS and SP resonant tank topologies. By using these equations, perform analytical comparative study on SS and SP resonant tank topologies for deciding which of the two topologies is desirable for a certain application. Also, obtain novel computer-aided optimal design methods, so that the two topologies of LART type can be designed for optimal performance for a desired nominal load under *k* variation.

1.3 RESEARCH SIGNIFICANCE

In novel accomplishment 1, frequency-domain characteristics of SS resonant tank of SRT type are analyzed in detailed to evaluate changes in the characteristics caused by *k* and Q variations. Based on the analysis, a novel design method is developed. The design method allows rapid calculation of the resonant tank parameters for achieving peak voltage gain of choice. As will be shown, unlike conventional design methods, it is a more self-contained method in which the cost of design process can be significantly reduced. By allowing rapid calculation of the resonant tank parameters, it also provides convenient evaluation of expected resonance characteristics for SS resonant tank of SRT type. Consequently, design iterations can be performed without high complexity and time-consuming efforts that conventional design methods require.

In novel accomplishment 2, a novel UGFT control method is developed for SS resonant tank of SRT type. This method does not require communication between a transmitter and a receiver in tracking and achieving the resonant frequency of highest

power efficiency (unity voltage gain frequency, f_O). Therefore, this control method can improve both power efficiency and receiver positioning flexibility in SS resonant converter of SRT type. By minimizing the need for various components in currently available wireless charging systems for portable electronics, this control method also reduces system complexity and cost of implementation.

In novel accomplishment 3, detailed analysis on *general* frequency-domain characteristics of SS and SP resonant tank topologies is performed. By deriving various *general* analytical equations, SS and SP resonant tank topologies of both SRT and ART types can be analyzed. Assuming loosely-coupled condition, equations for approximating desirable resonant frequencies under k variation are derived. Using these frequency approximations, various design equations are derived. All of the analytical equations and design equations are derived in design-oriented forms consisting only of physically-meaningful quantities that allow convenient analysis and optimal designs of the two popular resonant tank topologies. Also, these equations allow determining and evaluating various important frequency-domain quantities such as peak voltage gain, load-independent voltage gain, load-independent current gain, multiple resonant frequencies exhibiting notable features, desirable boundary for operating frequency (ω_s) range, voltage gain at ω_s, current gain at ω_s, circulating current at ω_s, and how these quantities change depending on magnetic coupling coefficient (k) and load (R_e'). Therefore, easier understanding of design and efficiency tradeoffs can be accomplished by using these equations. By using the design equations, novel computer-aided optimal design methods for loosely-coupled SS resonant tank and loosely-coupled SP resonant tank are developed to avoid time-consuming development process and to minimize costs caused by extensive

experimental evaluation and iterative practical redesigns. These design methods allow rapid and convenient evaluation of effects of variations in k and load-dependent quality factor. Optimal load-dependent quality factor values can then be determined without high complexity for a desired nominal load. By achieving optimal load-dependent quality factors, power transmission robustness against k variation can be maximized without significantly reduced coil-to-coil power efficiency. Also, an analytical comparative study is performed to show which of the two topologies is desirable for a certain application.

Overall, these novel accomplishments contribute to improving both overall power efficiency and receiver positioning flexibility, while reducing system complexity and cost of design process in inductive wireless charging systems.

1.4 Background on Resonant Converters

Unlike pulse width modulated (PWM) converters, resonant converters contain a resonant L-C network (resonant tank) that produces sinusoidal or quasi-sinusoidal voltage and current waveforms during a switching period.

To increase the power density, switched-mode power converters can be operated at high switching frequencies so as to reduce the sizes of magnetic components. However for a PWM converter performing hard switching transitions, high switching frequency operation can increase the switching loss significantly leading to poor power efficiency.

A major advantage of resonant converters is the reduced switching loss through the use of soft switching techniques known as zero voltage switching (ZVS) and zero current switching (ZCS). In ZVS and ZCS, the turn-on transitions and/or turn-off transitions of semiconductor switches can occur approximately at zero crossings of the waveforms produced by a resonant converter. Therefore, reduced switching loss can be achieved in a

resonant converter, so that it can operate at switching frequencies higher than in comparable PWM converters. Another advantage of resonant converters is that ZVS can reduce the electromagnetic interference (EMI) by significantly reducing high frequency noise at switching transitions.

However, there exists a major disadvantage of resonant converters: it is difficult to optimize the resonant elements in terms of efficiency for wide input and output ranges. Also, optimization becomes even more difficult when there are variations in k such as in wireless power transfer applications.

In this section, the fundamental theory on resonant converters is explained: the fundamental theory includes sinusoidal analysis, ZVS mechanism, and ZCS mechanisms. A simple DC-DC series LC resonant converter in Figure 1.4 is used as an example to explain the theory. Furthermore, various types (switching frequency (f_S) modulation, phase-shift method, and PWM method) for controlling the voltage gain and load current are described.

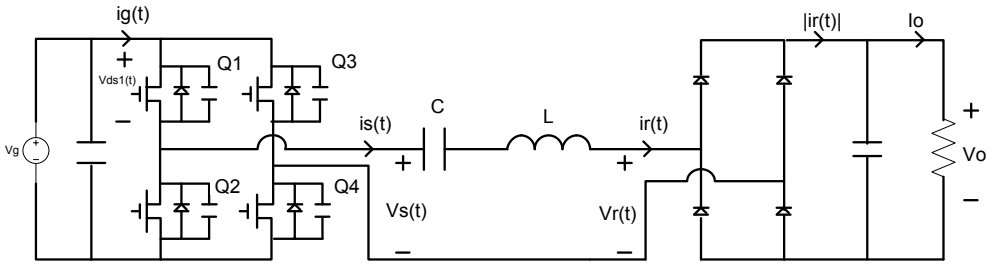

Figure 1.4: DC-DC series LC resonant converter.

1.4.1 Sinusoidal Analysis of Resonant Converters

In Figure 1.4, actively controlled switches, Q1-Q4, convert a DC source voltage, Vg, to a square wave voltage, $v_S(t)$, oscillating at the switching frequency, f_S. In most cases, the frequency of $v_S(t)$ is close to the resonant frequency, f_O, generating the quasi-

sinusoidal waveforms in the resonant tank. If the resonant tank has response at other harmonics of $v_S(t)$ that are negligible compared to response at the fundamental frequency ($f_S \approx f_O$), then the voltage and current waveforms of the resonant tank can be approximated by their fundamental frequency components. Thus, the resonant tank acts as a fundamental frequency pass filter. Applying the fundamental frequency approximation in the analysis, $v_S(t)$ can be realized as shown in Figure 1.5. This figure shows the square wave voltage, $v_S(t)$, which is what the input voltage of the resonant tank actually is. Due to the filtering effect, the sinusoidal wave voltage, $v_{S1}(t)$, is what the impedance of the resonant tank responds to. Using Fourier series, the square wave voltage, $v_S(t)$, is represented by Equation 2. Since the resonant frequency, *fo*, is close to the fundamental frequency, $f_S = \frac{\omega_S}{2\pi}$, the fundamental component of $v_S(t)$ applied to the input of the resonant tank can be expressed as Equation 3. The quasi-sinusoidal resonant tank input current, is(t), is then expressed as Equation 4 - Note: The phase shift, φ_s, is present in is(t) when f_S and f_O are not exactly equal to each other.

Figure 1.6 shows the source current, ig(t), and resonant tank input current, is(t), waveforms: ig(t) and is(t) are equal for one half of the switching cycle, but they are opposite in polarity for the other half. This can be easily understood by visualizing ig(t) as a phase-shifted full-wave rectified version of is(t) hence ig(t) having some negative polarity portion for φ_s duration. The average value of ig(t) is then determined by Equation 5.

As can be seen from Figure 1.5 and Figure 1.6, is(t) is shown to lag $v_S(t)$ by the phase shift of φ_s. This lagging occurs because the analysis performed here is based on above-resonant frequency operation: f_S is *above* but *near* f_O. With the series LC configuration,

the resonant tank introduces an *inductive* impedance to $v_{s(t)}$ for $f_S > f_O$ (above-resonance operation). On the other hand, if f_S is *below* f_O, then is(t) is leads $v_S(t)$ by a certain phase: with the series L-C configuration, the resonant tank introduces a *capacitive* impedance to $v_S(t)$ for $f_S < f_O$ (below-resonance operation). The magnitude of phase shift increases as f_S is moved farther away from f_O. It should be noted that is(t) waveform is then quasi-sinusoidal: is(t) is sinusoidal *only* if f_S is exactly equal to f_O so that the resonant tank introduces a *resistive* impedance to $v_S(t)$ causing no phase shift between is(t) and $v_S(t)$. The portion consisting of the diode bridge rectifier, output low pass filter, and load resistor is shown Figure 1.7. The series LC resonant tank's output voltage ($v_r(t)$), its fundamental component ($v_{r1}(t)$), and output current (ir(t)) waveforms are shown in Figure 1.8.

Because of the synchronous rectification performed by the diode bridge rectifier, the effective *resistive* load, Re, is applied to the output of the resonant tank as indicated in Figure 1.7. In order to determine Re, $v_{r(t)}$ is first represented as Equation 6, and its fundamental component, $v_{r1(t)}$, is then represented as Equation 7. The output current of the resonant tank, ir(t), is expressed as Equation 8. Then, the output current through the load resistor, Io, which is filtered by the low pass capacitive filter, C_f, is equal to the average value of the full-wave rectified current of ir(t), |ir(t)|, which is shown by Equation 9. Finally, effective resistive load R_e is derived as Equation 10.

Based on Equations 2 through 10, the steady-state equivalent model of the series LC resonant converter is shown as Figure 1.9. The ratio of load voltage (V_O) to source voltage (Vg), *M*, is determined by Equation 11. Substituting Equation 10 into Equation 11 yields the relationship, $M = \|Gv(j\omega_s)\|$. In reality, the voltage gain relationship is

$M \approx \|Gv(j\omega_s)\|$, because there are some losses. This relationship shows that the output voltage of resonant converters depends on the voltage gain transfer function of the resonant tank and can be controlled by modulating the switching frequency, f_S.

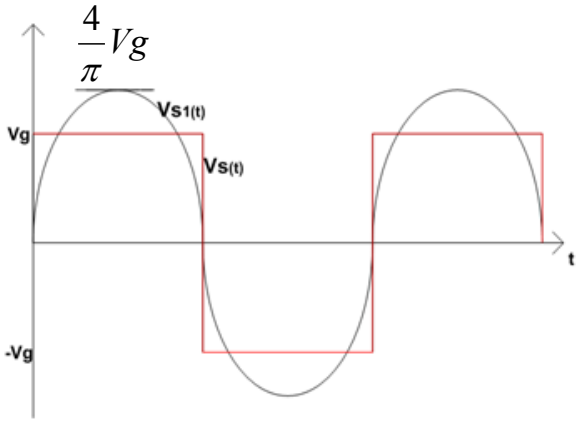

Figure 1.5: Square wave resonant tank input voltage, $v_S(t)$, and its fundamental frequency component, $v_S(t)$.

$$Vs(t) = \frac{4Vg}{\pi} \sum_{n=1,3,5,7,\ldots} \frac{1}{n} \sin(n\omega_s t) \quad \text{..... Equation (2)}$$

$$V_{s1}(t) = \frac{4Vg}{\pi} \sin(\omega_s t) = V_{s1} \sin(\omega_s t) \quad \text{..... Equation (3)}$$

$$is(t) = I_{s1} \sin(\omega_s t - \varphi_s) \quad \text{..... Equation (4)}$$

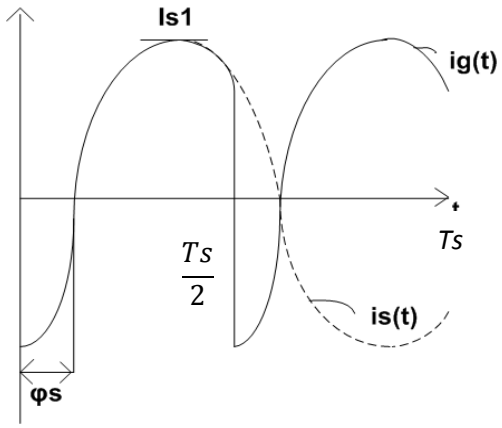

Figure 1.6: Source current, ig(t), and resonant tank input current, is(t).

$$\langle ig(t)\rangle_{Ts} = \frac{2}{Ts}\int_0^{\frac{Ts}{2}} ig(t)dt = \frac{2}{Ts}\int_0^{\frac{Ts}{2}} I_{s1}\sin(\omega_s t - \varphi_s)dt = \frac{2}{\pi} I_{s1}\cos(\varphi_s) \quad \text{..... Equation (5)}$$

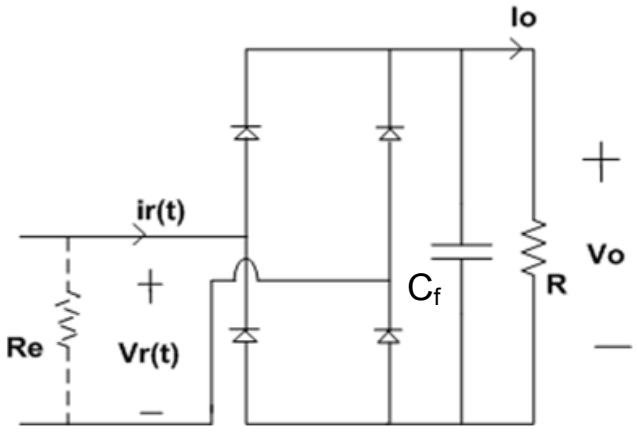

Figure 1.7: Diode bridge rectifier with low pass filter and load resistor.

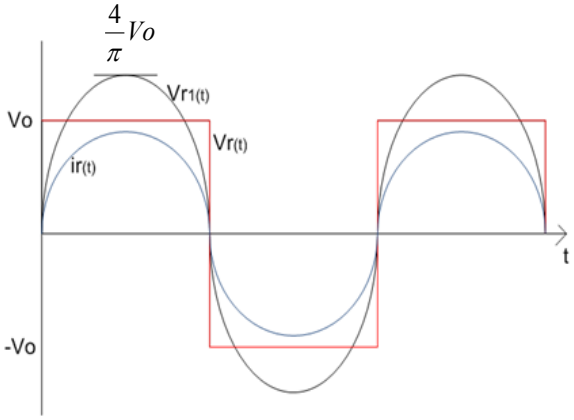

Figure 1.8: Waveforms of the series LC resonant tank's output voltage $v_r(t)$, its fundamental component $v_{r1}(t)$, and resonant tank output current ir(t).

$$Vr(t) = \frac{4Vo}{\pi}\sum_{n=1,3,5,7,\ldots}\frac{1}{n}\sin(n\omega_s t - \varphi_r) \quad \text{..... Equation (6)}$$

$$V_{r1}(t) = \frac{4V_O}{\pi}\sin(\omega_s t - \varphi_r) = V_{r1}\sin(\omega_s t - \varphi_r) \text{..... Equation (7)}$$

$$ir(t) = I_{r1}\sin(\omega_s t - \varphi_r) \quad \text{..... Equation (8)}$$

$$Io = \frac{2}{Ts}\int_{0}^{\frac{Ts}{2}} I_{r1}\,|\sin(\omega_s t - \varphi_r)|\,dt = \frac{2}{\pi} I_{r1} \quad \text{..... Equation (9)}$$

$$\mathrm{Re} = \frac{V_{r1}(t)}{i_{r1}(t)} = \frac{8}{\pi^2}\frac{Vo}{Io} = \frac{8}{\pi^2} R \quad \text{..... Equation (10)}$$

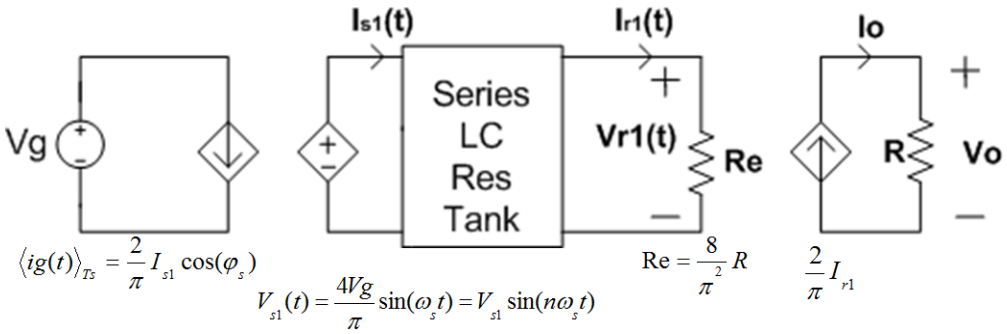

Figure 1.9: Steady-state equivalent model of series LC resonant converter.

$$M = \frac{Vo}{Vg} = \left(\frac{Vo}{Io}\right)\left(\frac{Io}{I_{r1}}\right)\left(\frac{I_{r1}}{V_{r1}}\right)\left(\frac{V_{r1}}{V_{s1}}\right)\left(\frac{V_{s1}}{Vg}\right) = (R)\left(\frac{2}{\pi}\right)\left(\frac{1}{R_e}\right)\left(\|Gv(j\omega_s)\|\right)\left(\frac{4}{\pi}\right) \quad \text{..... Equation (11)}$$

1.4.2 Zero Voltage Switching (ZVS)

ZVS is a type of soft switching mechanism that reduces the switching loss by having switching transitions of semiconductor devices at zero crossings of applied voltage waveforms. For example, in converters containing MOSFETs with built-in anti-parallel body diodes or external diodes, ZVS reduces the switching loss caused by diode reverse recovery and inherent output capacitance of a MOSFET.

ZVS can occur where the voltage across a MOSFET becomes zero before the resonant tank current becomes zero, and before the transistor turns on. Therefore in above-resonance operation of the series LC resonant converter in Figure 1.4 , the MOSFETs in Q1-Q4 can turn on softly with ZVS, leading to the reduced turn-on switching losses. Figure 1.10 shows the series LC resonant tank's input voltage ($v_s(t)$) and input current

($i_S(t)$) under ZVS. As can be seen from this figure, the soft turn-on transition occurs when $i_S(t)$ crosses zero at t1, at which point, $v_S(t)$ is in its positive half while $i_S(t)$ is making the polarity transition from negative to positive. In Figure 1.10, initially, $i_S(t)$ is negative while $v_S(t)$ is positive, and the body-diodes of MOSFETs, Q1 and Q4, are conducting. When $i_S(t)$ is at its zero crossing, t1, the MOSFETs, Q1 and Q4, turn on softly with ZVS, because during the transition, the voltages across Q1 and Q4 are zero while the current going through Q1 and Q4 are sinusoidally changing. This ZVS operation is more evident in Figure 1.11 which shows the voltage, vds1(t), across Q1 and the current, $i_{ds}(t)$, through it.

The transistor turn-off in Figure 1.11 is a hard switching transition similar to what transistors of PWM converters exhibit. ZVS can be achieved also for turn-off transitions by introducing an appropriate dead time (DT), during which all of Q1-Q4 are turned off. During this DT after the square wave resonant tank input voltage crosses zero, the remaining charge indicated by the area under the sinusoidal current curve are exchanged by the parallel capacitors of the transistors. After the capacitors are fully charged at the supply voltage, the anti-parallel diodes clamp at this voltage as seen in Figure 1.11 and these diodes allow conduction of free-wheeling diode current to circulate into the parallel capacitors, thus introducing commutation intervals. During the commutation intervals, the transistor voltages change softly due to charging and discharging of their parallel capacitors. When this happens, both the rising and falling edges of the transistor voltage are smooth as in Figure 1.12 rather than rapid vertical edges.

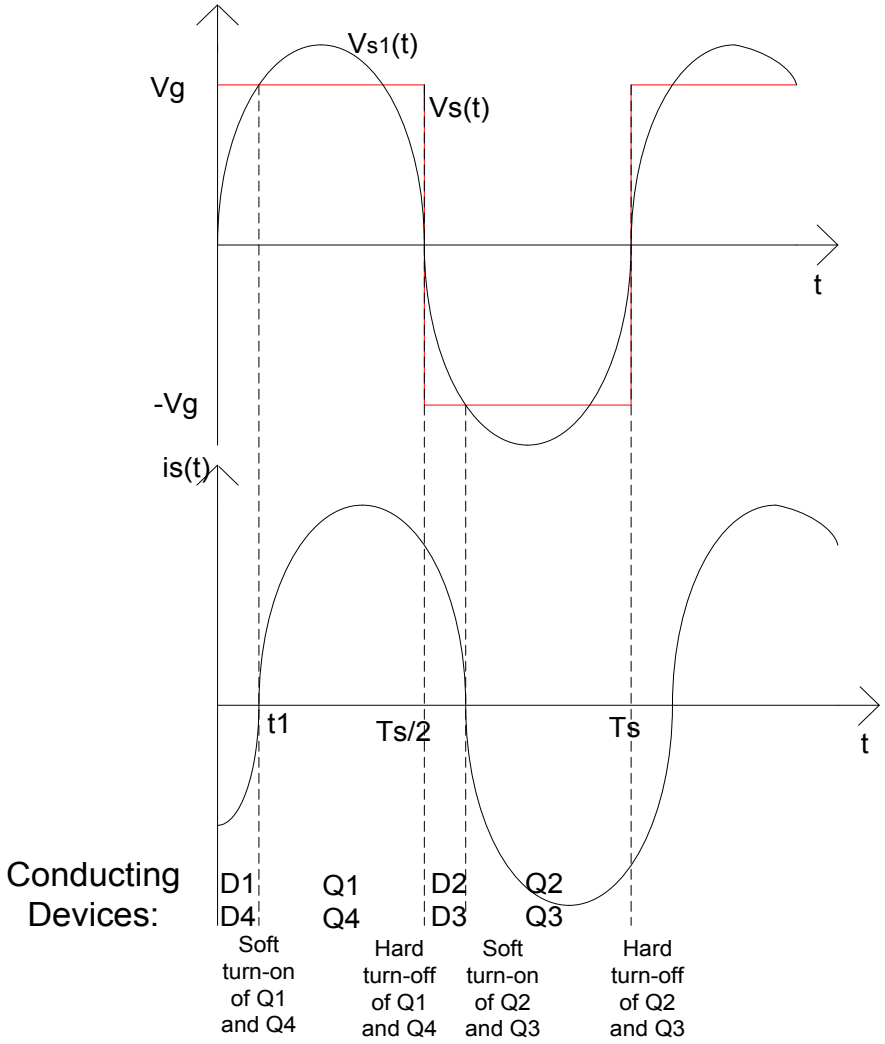

Figure 1.10: ZVS during turn-on transitions of MOSFETs in series LC resonant converter of Figure 1.4 in above-resonance operation.

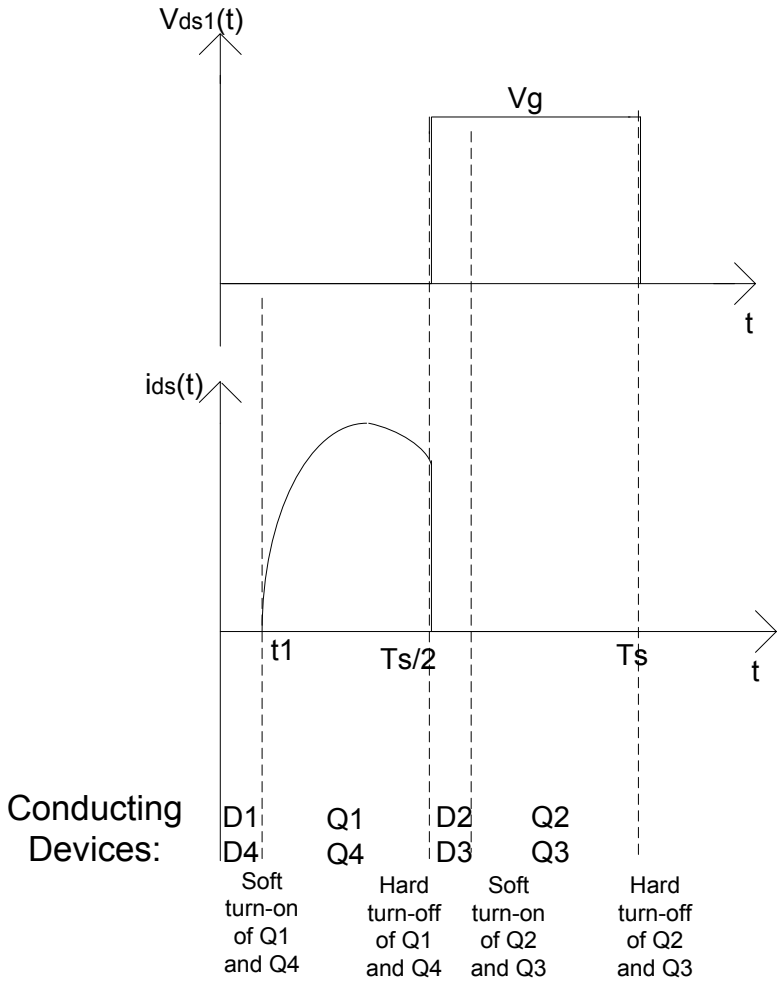

Figure 1.11: MOSFET Q1 voltage and current of series LC resonant converter in above-resonance operation for ZVS.

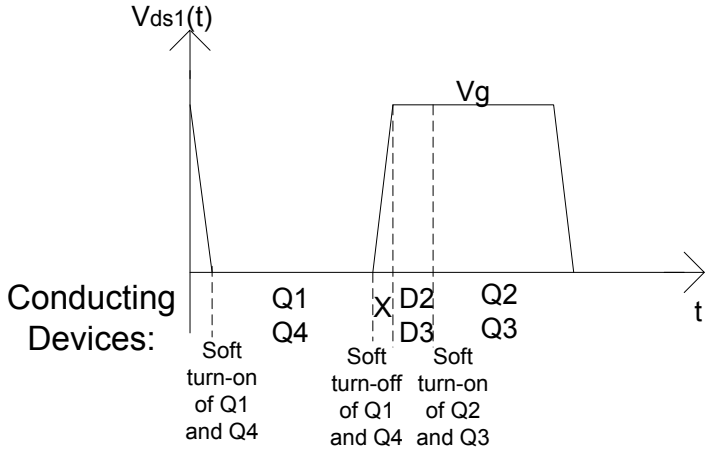

Figure 1.12: Introduction of commutation interval, X, where charging and discharging of parallel capacitors of transistors occur for soft transistor voltage transitions.

1.4.3 ZERO CURRENT SWITCHING (ZCS)

As mentioned previously, when the series LC resonant converter in Figure 1.4 is operated at $f_S < f_O$ (below-resonance operation), the series LC resonant tank has a capacitive input impedance. In this case, is(t) leads $v_S(t)$ as shown in Figure 1.13. Then, the transistor current crosses zero before the transistor voltage becomes zero, thus achieving ZCS. Figure 1.14 shows this phenomenon using the $v_{ds1}(t)$ and $i_{ds}(t)$ of Q1.

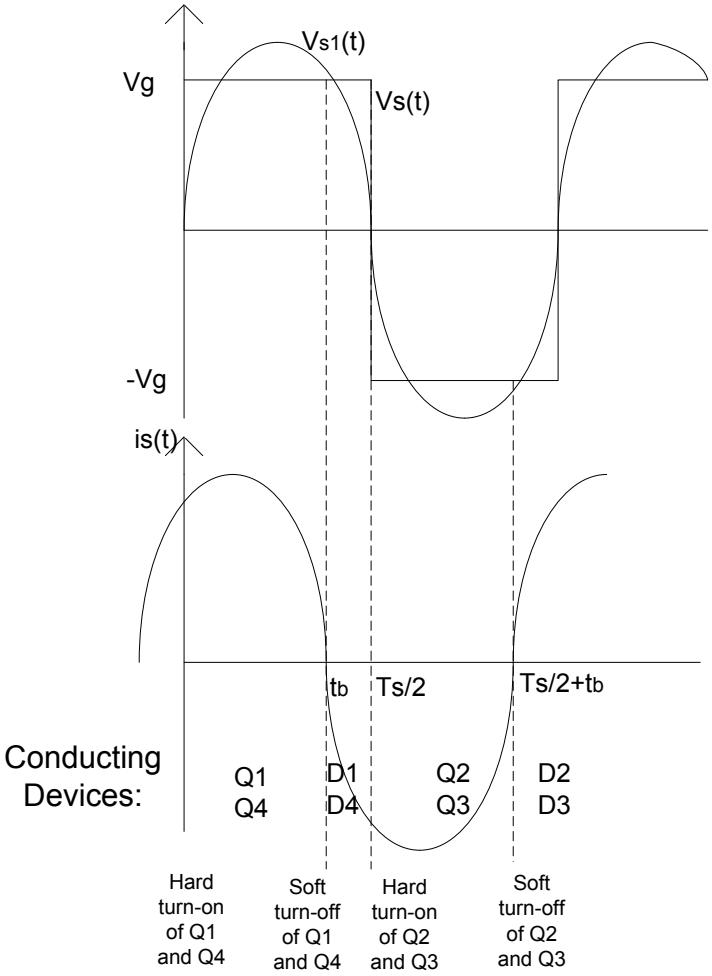

Figure 1.13: ZCS during turn-on transitions of MOSFETs in series LC resonant converter of Figure 1.4 in above-resonance operation.

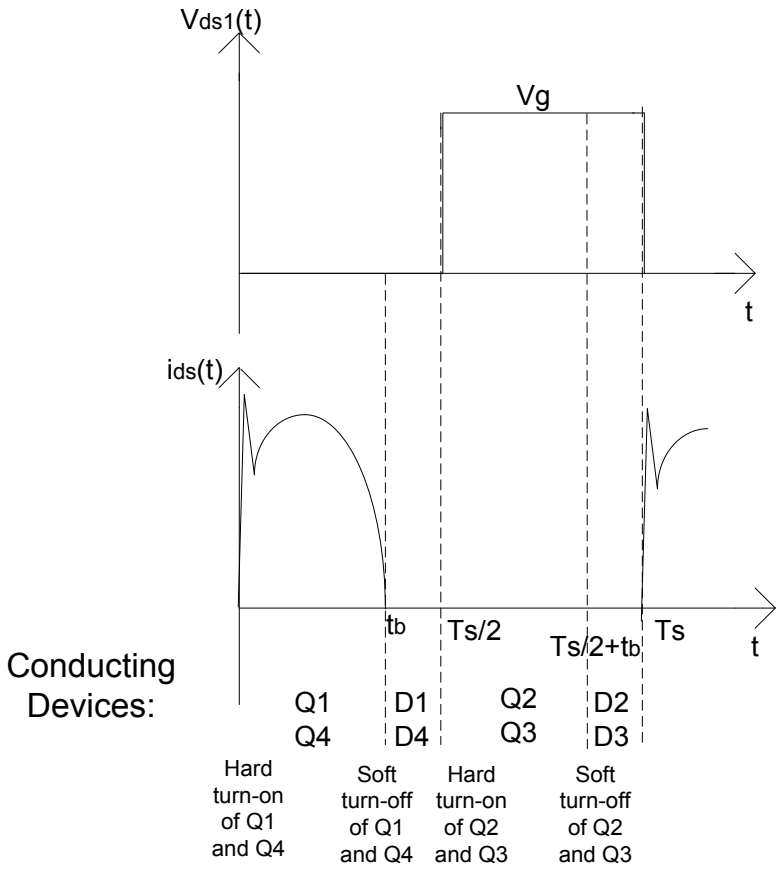

Figure 1.14: MOSFET Q1 voltage and current of series LC resonant converter in below-resonance operation for ZCS.

1.4.4 Control of Output Power Delivery via Switching Frequency Modulation

As briefly described previously, the voltage gain of a resonant converter depends on switching frequency. The series LC resonant tank in Figure 1.4 exhibit the voltage gain transfer function of Equation 12. This equation shows that the highest voltage gain possible for the series LC resonant tank is unity at the resonant frequency, $f_O = \frac{\omega_o}{2\pi}$. As the switching frequency, f_S, moves away from f_O, the voltage gain decreases. This is expected because the impedances of L and C cancel each other when $f_S = f_O$, causing the resonant tank input voltage to be applied directly across R_e. So, the limitation of the

series LC resonant tank is that it can operate only for a voltage step-down conversion (buck mode).

However when the inductor is replaced with a magnetic coupler, the highest voltage gain available, $||G_V||_{max}$, can exceed unity for boost mode operation even when the turns ratio of unity is applied for primary coil and secondary coil. This is possible due to the parallel path introduced by a magnetizing inductance, L_m. Detailed analysis is performed in later chapters clearly showing this property among other important frequency-domain characteristics. For now, it should be noted that the output voltage of a resonant tank can be controlled by varying the transistor switching frequency, f_S.

$$Gv(j\omega) = \frac{\left(\frac{j\omega}{Q_e\omega_o}\right)}{1+\left(\frac{j\omega}{Q_e\omega_o}\right)+\left(\frac{j\omega}{\omega_o}\right)^2}, \text{ where } \omega_o = \frac{1}{\sqrt{LC}} \text{ and } Q_e = \frac{\sqrt{\frac{L}{C}}}{\text{Re}} \quad \text{..... Equation (12)}$$

1.4.5 Control of Output Power Delivery via Pulse Width Modulation

In DC-DC resonant converters, using fully-controllable switches for active rectification rather than using a diode-bridge rectifier allows flexible control of the load current. It also reduces the diode conduction loss. In low power applications, the forward diode voltage drop and diode current can cause a significant efficiency loss; therefore fully-controllable switches should be used as synchronous rectifiers rather than diodes.

Implementation of fully-controllable switches on both sides of a magnetic coupler produces a bidirectional DC-DC resonant converter in which power delivery can be controlled by methods other than the switching frequency modulation technique. One of the methods is pulse width modulation (PWM) technique that varies the duration in which switches are turned on. An example of PWM technique is explained using the quantities indicated in the fully-controllable full-bridge rectifier of Figure 1.15.

In the PWM technique, the duty cycle of a resonant tank's output voltage, Vr(t), can be controlled as shown in Figure 1.16. The load current, Io, is then represented as Equation 13, which shows that Io can be changed by varying the duty cycle - Note: the change in the parameter, n, represents the duty cycle variation (on-off time variations of the secondary-side switches).

It should be noted that the PWM technique can be performed also on the primary side, varying the on-off time of the primary-side switches. The maximum power delivery occurs when the duty cycle is 50 % as can be seen from Equation 13: the parameter, n, has to be a very high number (mathematically, infinity), causing both the negative portion and positive portion of $i_r(t)$ to be half of switching period, Ts. Therefore, any deviation from 50% in duty cycle condition (on-off time variation) results in *decreasing* the output power (load current, Io) only, providing a limited control capability.

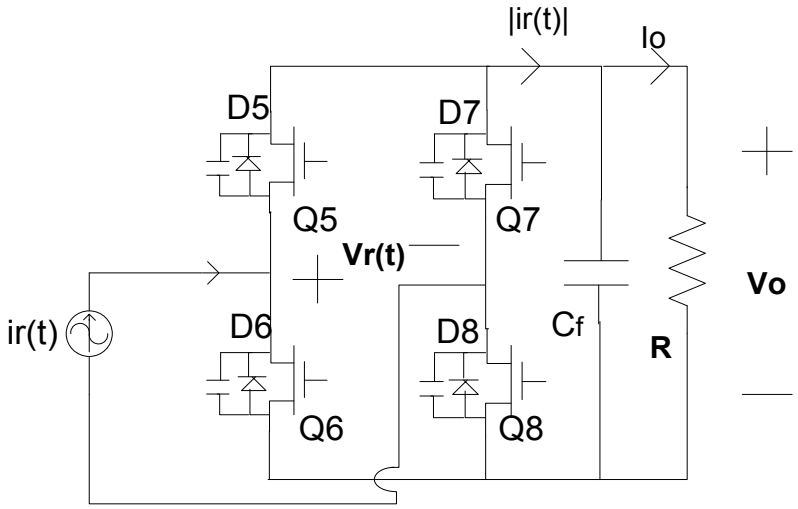

Figure 1.15: Fully-controllable full-bridge rectifier.

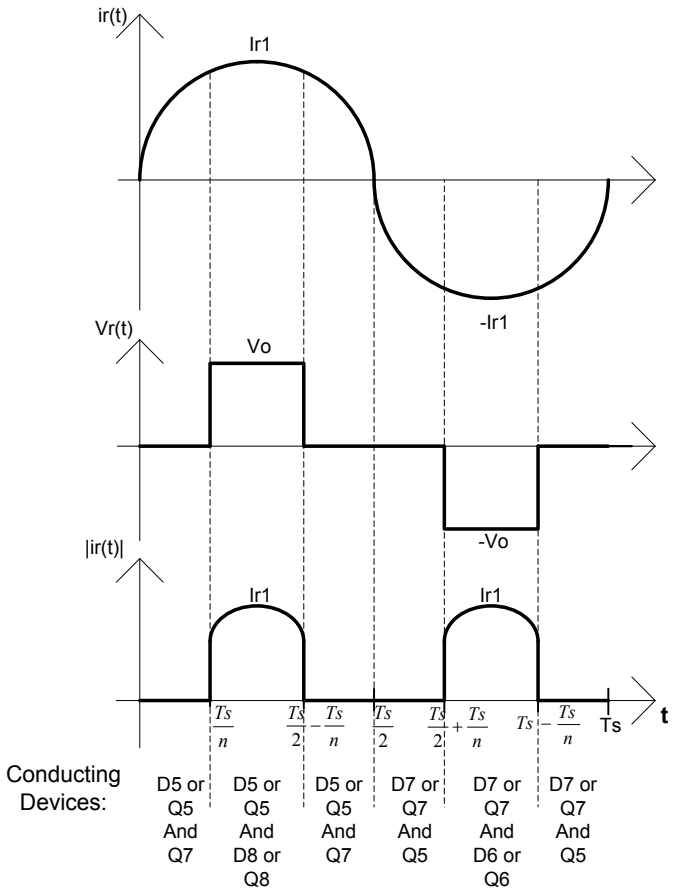

Figure 1.16: PWM technique for controlling resonant tank output power via active on-time variation of the switches in the secondary-side full-bridge rectifier.

$$\text{Io} = \langle |ir(t)| \rangle = \frac{1}{Ts}\left[\int_{\frac{Ts}{n}}^{\frac{Ts}{2}-\frac{Ts}{n}} ir(t)dt + \int_{\frac{Ts}{2}+\frac{Ts}{n}}^{Ts-\frac{Ts}{n}} -ir(t)dt\right] = \frac{2I_{r1}}{\pi}\cos\left(\frac{2\pi}{n}\right),$$

where $ir(t) = I_{r1}\sin(\omega_s t)$..... Equation (13)

1.4.6 Control of Output Power Delivery via Phase Shift Method

Another method of controlling the power delivery can be achieved with the requirement of using fully-controllable switches *both* on the primary side and secondary side. The method is called phase shift method and applies either an inductive phase shift or a capacitive phase shift to *decrease* the load current.

When an inductive phase shift is applied actively, Vr(t) waveform leads ir(t) waveform as in Figure 1.17. The load current is then expressed as Equation 14, which

shows that the load current can be controlled by varying the phase shift, t_φ-Note: the maximum power delivery occurs when $t_\varphi = 0$.

When a capacitive phase shift is applied actively, Vr(t) waveform lags ir(t) waveform as in Figure 1.18. The load current is then controlled again by controlling the phase shift, t_φ.

In summary, besides the switching frequency (f_S) modulation technique, the PWM technique and/or the phase shift technique can be used to control the power delivery (load current, Io). It is shown in Figure 1.16 through Figure 1.18 that these two methods introduce actively controlled effective load condition to a resonant tank. It will be shown later in Chapter 4 that both the PWM technique and the phase shift technique are *undesirable* in terms of control complexity and efficiency. On the other hand, f_S modulation technique is *desirable*.

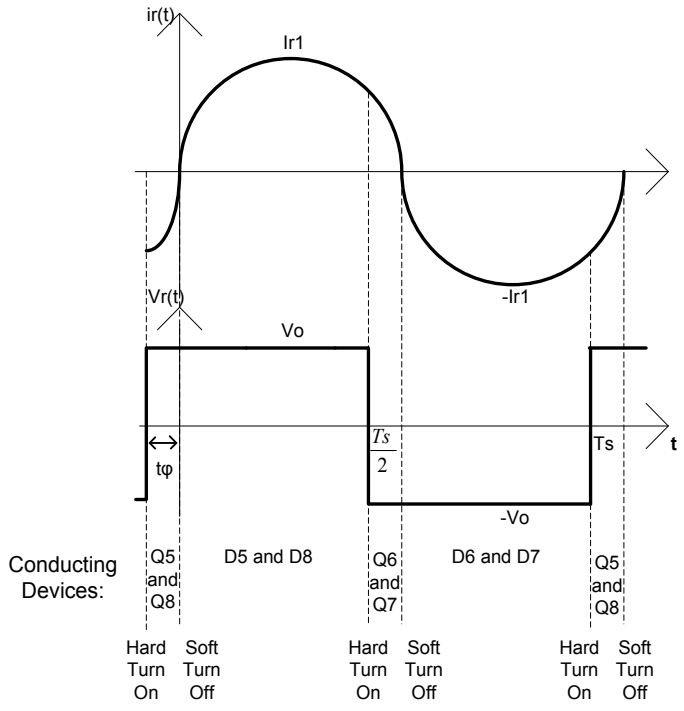

Figure 1.17: Phase-shift control to apply inductive effective load.

$\mathrm{I_O} = \langle |i_r(t)| \rangle = \frac{2I_{r1}}{\pi}\cos(\mathrm{t_\varphi})$, where $i_r(t) = I_{r1}\sin(\omega_s t)$..... Equation (14)

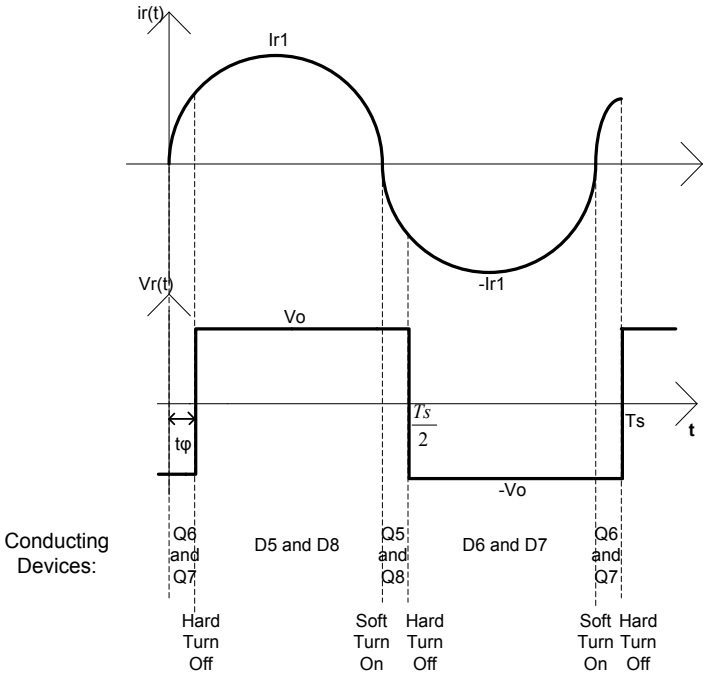

Figure 1.18: Phase-shift control to apply capacitive effective load.

1.5 THEORY OF OPERATION OF SS RESONANT CONVERTER OF SRT TYPE

The purpose of this section is to describe the ideal operation of a SS resonant converter of SRT type in wireless charging applications. Figure 1.19 shows a DC-DC full-bridge-to-full-bridge SS resonant converter of SRT type. For the sake of simple discussion, 1:1 turns ratio is also applied for coupler winding condition. This means that $L_{e1} = L_{e2} = L_{e2}'$, and consequently leakage inductance compensation is achieved by Cr: $C_1 = C_2 = C_2'$. The winding resistances and core loss resistance model are not included in the T-equivalent model.

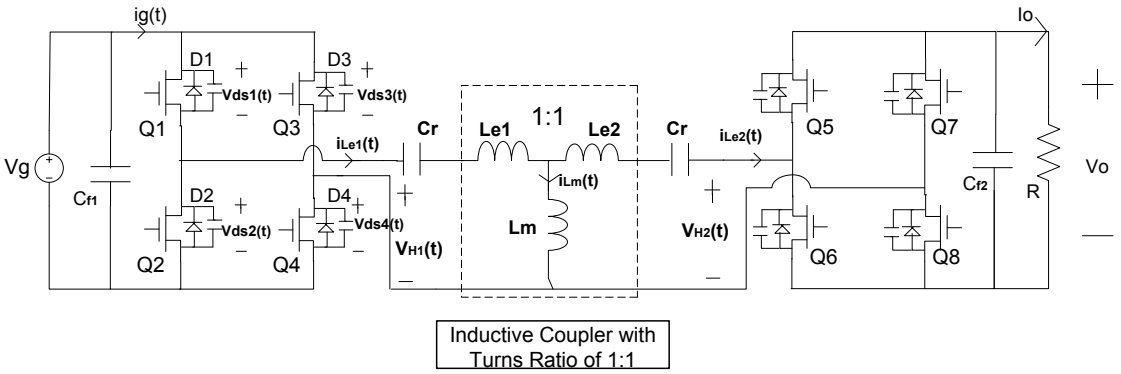

Figure 1.19: DC-DC bidirectional full-bridge SS resonant converter of SRT type.

1.5.1 THEORETICAL WAVEFORMS UNDER IDEAL SWITCHING TRANSITIONS ON PRIMARY SIDE

In Figure 1.20, various waveforms of the SS resonant converter in Figure 1.19 are shown to describe the nominal, ideal converter operation for each switching interval. Constant input and resistive load conditions are assumed with a DC input voltage source and load resistor. The nominal, ideal operation is when the switching frequency (f_S) is equal to the unity gain resonant frequency, f_O (Equation 15).

At $f_S = f_O$, the impedances of Cr-L_{e1} and Cr-L_{e2} branches are effectively shorted as mentioned before. The SS resonant tank can then be represented by the simplified equivalent model in Figure 1.21. Therefore, the resonant tank driving-square wave voltage, $V_{H1}(t)$, is directly applied across L_m, causing the circulating current, $i_{Lm}(t)$ to be triangular rather than sinusoidal. Consequently, the voltage gain of the SS resonant tank is unity regardless of the effective resistive load (R_e') while the circulating current is reduced leading to higher coupler efficiency.

It should be noted that in Figure 1.20, $i_{Le1}(t)$ is shown to lag V_{H1} by t_φ, meaning that the SS resonant tank is behaving as an inductive impedance applied to the primary-side full-bridge, and therefore the converter is assumed to be operating under the above-

resonance (ZVS) condition. Figure 1.22 shows the equivalent circuit in each of the six different stages, t_a through t_g indicated Figure 1.20, of the SS resonant converter.

For each of the six different stages depicted in Figure 1.22, the following can be observed:

1. Short amount of time before the beginning of $t = t_a^-$, at the point near when iLm(t) is at the lowest value, the capacitors across the MOSFETs, Q1 and Q4, start being discharged, whereas at this point, the capacitors across the MOSFETs, Q2 and Q3, start being charged. Eventually at $t = t_a^-$, CQ1 and CQ4 become fully discharged (Vds1(t) ≈ Vds4(t) ≈ 0), whereas CQ2 and CQ3 become fully charged (Vds2(t) ≈ Vds3(t) ≈ Vg). Then, the MOSFETs, Q1 and Q4, are turned on at this point with ZVS. Until $t = t_b$, CQ1 and CQ4 remain fully discharged while CQ2 and CQ3 remain fully charged.
2. During $t_b \leq t < t_c$, which is the commutation interval, all of the MOSFETs are turned off, and the discharging of CQ2 and CQ3 occur while CQ1 and CQ4 are being charged.
3. At $t = t_c$, CQ2 and CQ3 are fully discharged, whereas CQ1 and CQ4 are fully charged. All MOSFETs remain turned off during $t_c \leq t < t_d$, and conduction of the body-diodes, D2 and D3, of the MOSFETs, Q2 and Q3, occurs while the circulating current, $i_{Lm}(t)$, is flowing through them.
4. At $t = t_e$, which is when $i_{Lm}(t)$ is at its lowest value, the capacitors across the MOSFETs, Q1 and Q4, start being discharged, whereas at this point, the capacitors across the MOSFETs, Q2 and Q3, start being charged.

Eventually at $t = t_f = t_g^-$, CQ1 and CQ4 become fully discharged ($v_{ds1}(t) \approx v_{ds4}(t) \approx 0$), whereas CQ2 and CQ3 become fully charged ($v_{ds2}(t) \approx v_{ds3}(t) \approx Vg$). Then at $t = t_g$, the MOSFETs, Q1 and Q4, are turned on at this point with ZVS transitions.

5. And, the cycle repeats.

For the secondary-side full-bridge being either passively uncontrolled or actively controlled for synchronous rectification, the bridge operations in the switching stage intervals are the mirror image of the primary-side operations.

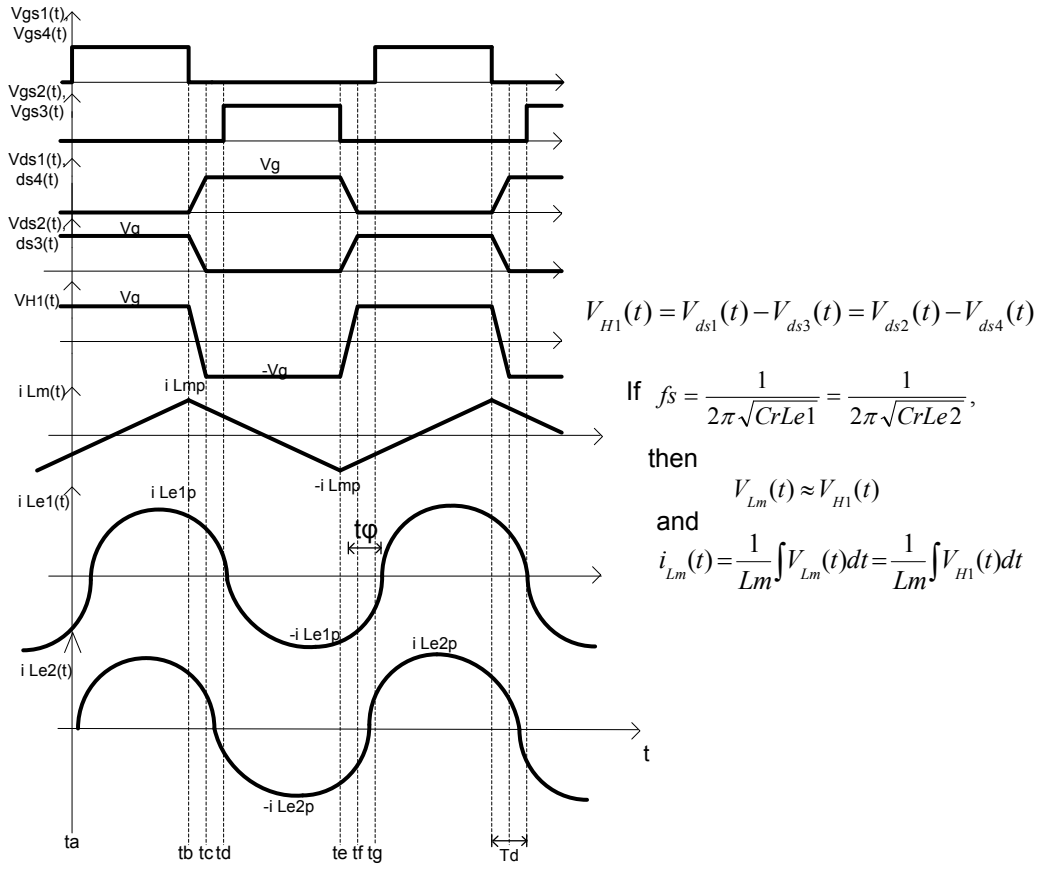

Figure 1.20: The full-bridge SS resonant converter's waveforms at unity voltage gain frequency.

$f_o = f_{o1} = \frac{1}{2\pi\sqrt{C_r L_{e1}}} = f_{o2} = \frac{1}{2\pi\sqrt{C_r L_{e2}}}$ ..... Equation (15)

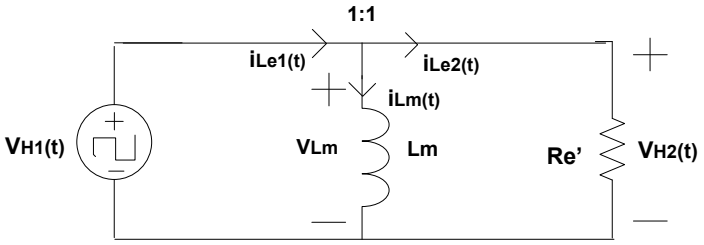

Figure 1.21: Simplified equivalent model of the SS resonant converter in Figure 1.19 at $f_S = f_O$.

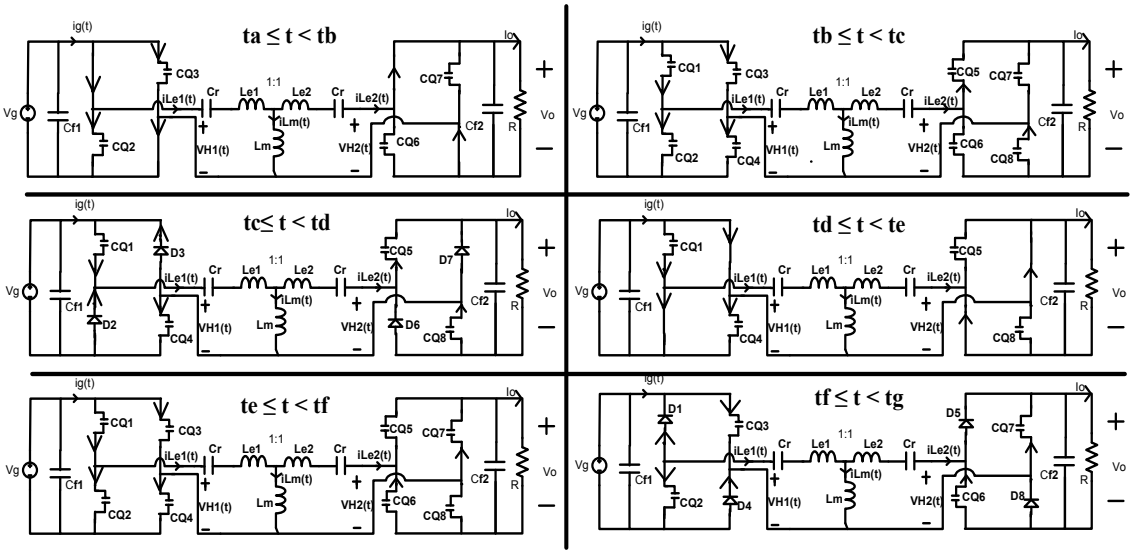

Figure 1.22: Equivalent circuits of the SS resonant converter for six different intervals (t_a through t_g indicated in Figure 1.20) in one switching cycle.

1.6 OUTLINE

Chapter 1 provides the basic overview of wireless charging operation, motivation and research objective, research significance, and background theory on resonant converters.

Chapter 2 describes an experimental setup for implementing different types of resonant tank. Also, this chapter briefly summarizes the works in [19]: It shows a resonant converter test-bed implemented for performance evaluation, and provides a summary of experimental results of the test-bed employing SS resonant tank of SRT type. The experimental results were collected under varied switching frequency (f_S) or varied load, R_e' (equivalently, varied load-dependent quality factor).

In Chapter 3, a literature review on resonant tank design methods is provided to describe conventional design methods and their shortcomings. A novel optimal design method for SS resonant tank of SRT type is presented to overcome these shortcomings. The magnitude of voltage gain transfer function, $\|G_V(j\omega)\|$, of SS resonant tank of SRT type is analyzed to extract various resonant frequencies. Through detailed study of voltage gain characteristics, various notable features of the resonant tank are described. A novel optimal design method is developed. The performance of the design method in terms of accuracy and precision is evaluated in simulation by comparing it with mathematically accurate solutions from a conventional parametric simulation-based method. The simulation results confirm the validity of the proposed design method. The design method is further validated using experimental results.

In Chapter 4, literature reviews on resonant converter control methods and on state of the art regarding wireless charging of portable electronics are provided to describe various shortcomings and undesirable features that the currently available wireless chargers exhibit. In order to avoid these shortcomings and undesirable features, this chapter presents a novel unity gain frequency tracking (UGFT) control method for SS resonant converter of SRT type. Without communication between transmitter and receiver, this control method allows tracking and achieving the resonant frequency of unity voltage gain, so that compensation of leakage inductances can be obtained under k variation. Therefore, the UGFT control method improves receiver positioning flexibility and reduces component count by maintaining good power transmission efficiency under k variation without communication ICs. The control method requires various desirable characteristics of SS resonant tank of SRT type to be achieved through an appropriate

design process following a set of design criteria. Therefore, various desirable characteristics are explained, and design criteria for achieving these characteristics are provided. A SS resonant converter of SRT type employing the control method is constructed following the criteria and validated in both simulation and experiment.

In Chapter 5, detailed *general* analysis on frequency-domain characteristics of SS and SP resonant tank topologies is performed to derive *general* analytical equations that allow determining and evaluating various notable characteristics. These *general* equations are in design-oriented form consisting only of physically-meaningful quantities. Using these equations, optimal design methods for SS and SP resonant tanks of LART type are developed to enable maximization of power delivery robustness against k variation without the cost of significantly reduced coil-to-coil efficiency. An analytical comparative study on the two resonant tank topologies is performed in this chapter as well.

Chapter 6 provides conclusion, list of publications, and future work.

CHAPTER 2
SUMMARY DESCRIPTION OF EXPERIMENTAL EVALUATION BOARD

2.1 DESCRIPTION OF EVALUATION BOARD

The purpose of Section 2.1 is to provide a brief description of the evaluation board shown in Figure 2.1, which has been used in various experiments in this research. In this section, each of the power stages on the evaluation board is described. The board was designed for the target switching frequency (f_S) range of approximately 100 kHz $\leq f_S \leq$ 600 kHz. The power stage components consider the power level $\leq$ 20 W with the current level $\leq$ 3A and voltage level $\leq$ 15V.

Functional diagrams for the power stage components of SS and SP resonant converters are shown in Figure 2.2. The components in this figure can be implemented flexibly on the evaluation board. Furthermore, each of the primary-side and secondary-side switch networks can be changed between the half-bridge configuration and the full-bridge configuration. As an example, Figure 2.1 shows the implementation of a SS resonant tank of SRT type with the full-bridge configuration for both primary-side and secondary-side switch networks.

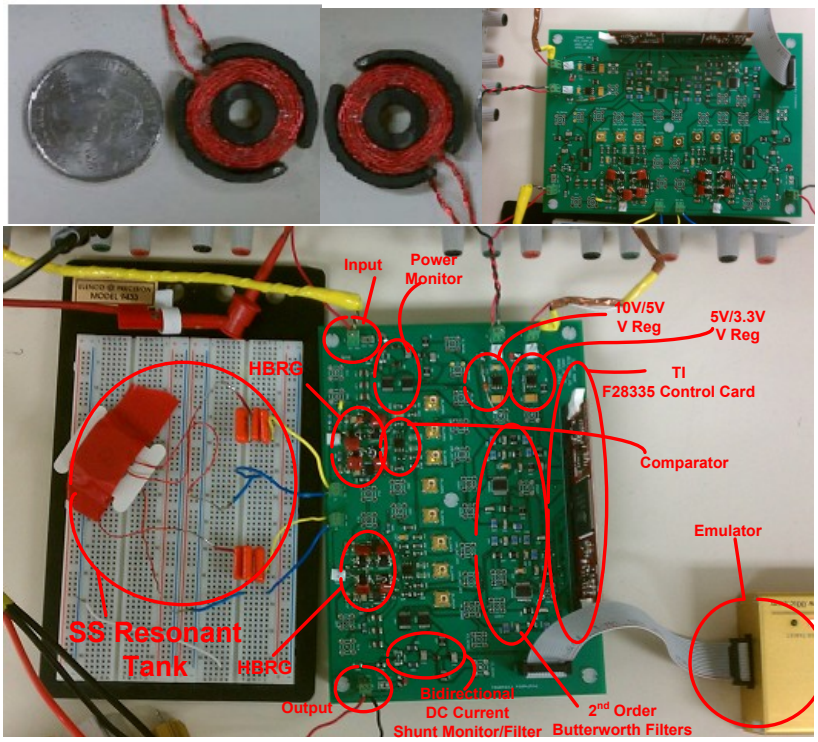

Figure 2.1: Evaluation board implementing a SS resonant tank of SRT type containing the symmetrical pot core coupler as an example.

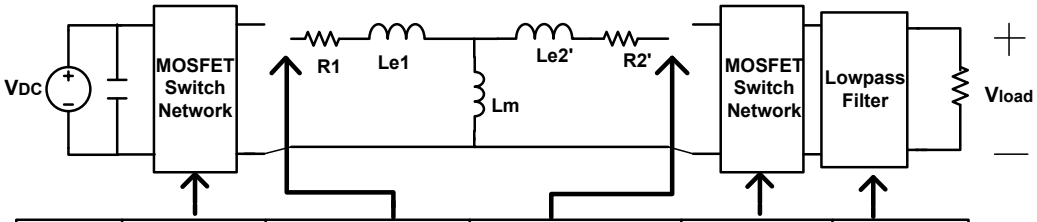

	Primary-side (Transmitter-side) Switch Network Configuration	Primary-side Resonant Capacitor Arrangement	Secondary-side Resonant Capacitor Arrangement	Secondary-side (Receiver-side) Switch Network Configuration	Low Pass Filter
SS Resonant Converter	Full-bridge Or Half-bridge	Series	Series	Full-bridge Or Half-bridge	
SP Resonant Converter	Full-bridge Or Half-bridge	Series	Parallel	Full-bridge Or Half-bridge	

Figure 2.2: Power stage component diagrams DC-DC SS and SP resonant converters.

2.1.1 HALF-BRIDGE CONFIGURATION VS. FULL-BRIDGE (HBRG) CONFIGURATION

This section briefly demonstrates the difference between operation with the half-bridge configuration and operation with the full-bridge configuration. Figure 2.3 and Figure 2.4 show the half-bridge configuration and full-bridge configuration respectively. Various theoretical waveforms in the primary side (transmitter side) are shown in the figures to show the difference in operation.

With the half-bridge configuration, the input voltage of the resonant tank, VH1(t), is a square wave oscillating between 0 and supply voltage, Vg. The DC component of Vh1(t), Vh1_DC(t) = $\frac{V_g}{2}$, is filtered out by the series resonant capacitor, Cr, on the primary side. The AC component, Vh1_AC(t), applied to the resonant tank is the square wave oscillating between $-\frac{V_g}{2}$ and $\frac{V_g}{2}$.

With the full-bridge configuration, the input voltage of the resonant tank, VH1(t), is the square wave oscillating between -Vg and Vg without the presence of any DC component.

Therefore if the same bridge output power is desired, the half-bridge input voltage needs to be twice as high as the full-bridge input voltage, provided that f_S, duty cycle, and resonant tank parameters are identical for both half-bridge and full-bridge configurations.

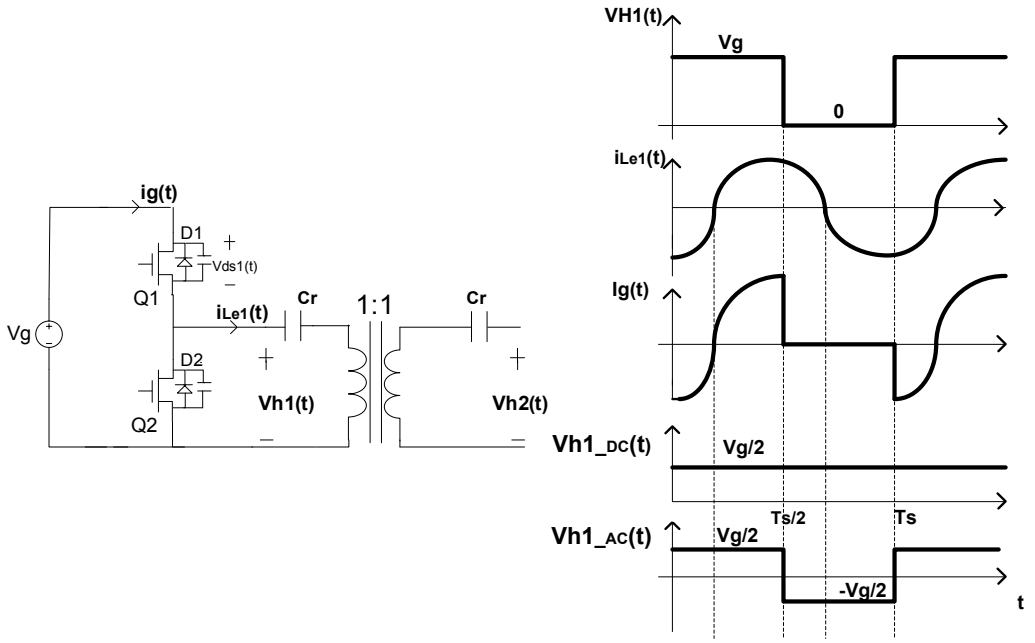

Figure 2.3: Half-bridge LCLC resonant converter's primary-side waveforms.

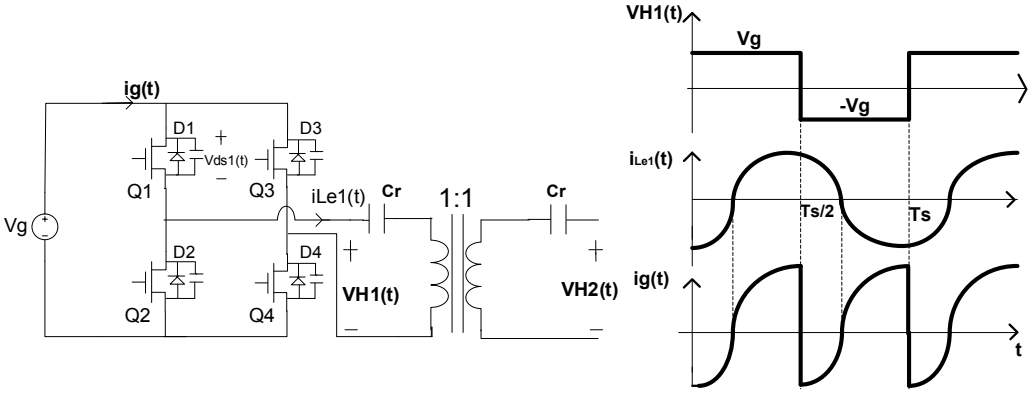

Figure 2.4: Full-bridge LCLC resonant converter's primary-side waveforms.

2.1.2 MOSFETs IN THE SWITCH NETWORKS

Each of half-bridge MOSFET drivers on the evaluation board generates gate-source voltage (Vgs) of 10V. Based on this condition and room temperature (25℃) condition, Table 2.1 lists some of the maximum or typical ratings of the MOSFETs.

These MOSFETs were chosen to make a good compromise between on-resistance (R_{ds_on}) and expected switching speed (thus to make a good compromise between conduction losses and switching losses). Under ZVS and ZCS conditions, expected

switching losses are very small compared to the conduction losses, therefore the trench gate MOSFETs were selected for low R_{ds_on} of 4 mΩ typical. The MOSFETs can tolerate the desired f_S range of 100 kHz-600 kHz for portable electronics charging applications.

TABLE 2.1 MAXIMUM OR TYPICAL RATINGS OF TRENCH GATE SILICONE MOSFET FROM VISHAY

Manufacturer/Part Name	**Vishay/Si4160DY**
Drain-Source Voltage, Vds	$30V_{max}$
Gate-Source Voltage, Vgs	$\pm 20V_{max}$
Drain-Source On-Resistance, R_{ds_on}	4mΩ typical at Vgs = 10V and Id = 15A
Total Gate Charge, Qg	36nC typical at Vds = 15V and Id = 10A
Continuous Drain Current, Id	$25.4A_{max}$ at Vgs = 10V
Turn-on Delay Time	10ns typical
Rise Time	9ns typical
Turn-off Delay Time	25ns typical
Fall Time	9ns typical
Body Diode Specifications	
Continuous Drain-Source Current, Is	$5.1A_{max}$
Pulse Diode Forward Current, Ism	$70A_{max}$ for Pulse Width ≤ 300 and Duty Cycle ≤ 2%
Diode Forward Voltage Drop, Vsd	0.73V typical for Is = 3A
Reverse Recovery Time, trr	19ns typical
Reverse Recovery Fall Time, ta	10ns typical
Reverse Recovery Rise Time, tb	9ns typical

2.1.3 HIGH SPEED, HALF-BRIDGE MOSFET DRIVER

There are four high speed, half-bridge drivers implemented on the evaluation board, supplied by a 10 V supply voltage, V_{dd}. The drivers are MAX15019 from Maxim. They are independently controlled and appropriate for high switching frequency operations. There are two types for MAX15019, CMOS and TTL. Although the CMOS type desirably offers less turn-on and turn-off propagation delays (typically about 3 - 6 ns less) compared to the TTL type, the input logic-high and logic-low voltage levels are not appropriate for the condition of 3.3 V as the peak of PWM signals from TI F28335 control card in Figure 2.1: for the CMOS type, the input logic-low is 3.3 V while the

input logic-high is 6.7 V for V_{dd} = 10 V. This means that the control card generating 3.3 V peak for PWM signals cannot turn on and off the MOSFETs using the CMOS type drivers. Therefore, the TTL type is used on the evaluation board. Table 2.2 shows a brief list of ratings for MAX15019 (TTL) driver. As can be seen from this table, the propagation delay matching is very good. The TTL type still offers the very low and well-matched propagation delays, and low rise and fall times.

TABLE 2.2 RATINGS OF HALF-BRIDGE DRIVER, MAX15019A (TTL), FROM MAXIM

Manufacturer/Part Name	**Maxim/MAX15019A (TTL)**
Operating Supply Voltage, Vdd	$12.6V_{max}$
Input Logic-High, Vih	$2V_{min}$
Input Logic-Low, Vil	$0.8V_{max}$
Rise Time, tr	5ns typical
Fall Time, tf	5ns typical
Turn-On Propagation Delay, td_on	36ns typical
Turn-Off Propagation Delay, td_off	36ns typical
Delay Matching between High-side on/off and Low-side off/on	1ns typical
Built-in Internal Bootstrap Diode Specifications	
Forward Voltage Drop, Vf	0.9V typical
Turn-On and Turn-Off Time	40ns typical

2.1.4 TEXAS INSTRUMENTS' TMS320F28335 CONTROL CARD

The converter control is performed with a F28335 control card from Texas Instruments. Table 2.3 lists some of the specifications of interest for the control card. The control card has more than enough PWM modules for driving the eight MOSFETs on the evaluation board. Also, it should be noted that it provides the floating point unit for easier math operation and also has the capture modules called, "Ecap". Later in Chapter 4, it is shown that an Ecap module is used in experimental validation of the novel UGFT control

method. Both CPU bandwidth of 150MHz and ADC conversion time of 80ns are appropriate for the desired f_S range.

TABLE 2.3 BRIEF SPECIFICATIONS OF F28335 CONTROL CARD FROM TEXAS INSTRUMENTS

TMS320F28332	
Floating Point Unit?	Yes
CPU Bandwidth Frequency (MHz)	150
RAM (kB)	68
Flash (kB)	512
EMIF	32/16-Bit
DMA (Channels)	6-Ch DMA
PWM (Channels)	18
Number of Capture Module (Ecap)	6
ADC (Channels and Bit Size)	16-Ch 12-Bit
ADC Conversion Time (ns)	80
Timers	3 32-Bit CPU,1 WD
Number of GPIOs	88

In summary, Section 2.1 serves as a brief reference for providing information on the main stage of the experimental set-up. The next section provides a brief summary of experimental performance evaluation.

2.2 EVALUATION OF EXPERIMENTAL SET-UP

The SS resonant converter of SRT type in Figure 1.19 was implemented in Pspice simulation and also in experiment. In experiment, the converter contains the symmetrical pot core coupler in Figure 2.1. The SS resonant tank exhibits $f_O \approx 500$ kHz. Experimental testing under various operating conditions was already performed in [19], which contains detailed data from both simulations and experiments. In this section, a summary of simulation data and experimental data is provided to demonstrate good performance of the experimental set-up and to show various experimental waveforms matching the

theoretical waveforms discussed in Section 1.5. In particular, the waveforms of the voltages and currents indicated in Figure 2.5 were measured.

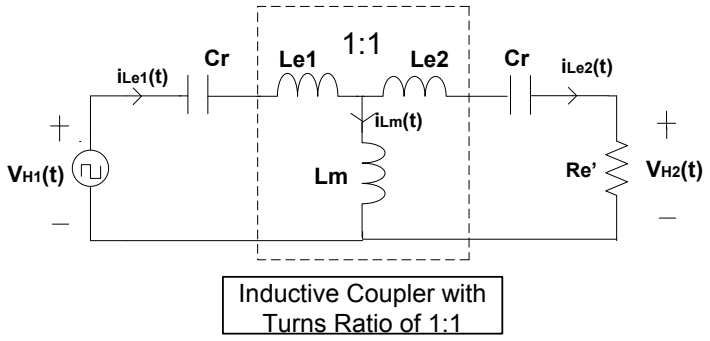

Figure 2.5: Equivalent mode of Figure 1.19 with the measured voltages and currents indicated.

2.2.1 Simulation Waveforms and Experimental Waveforms

While the secondary-side switch network was performing passive diode rectification, the quantities indicated in Figure 2.5 are measured both in Pspice simulation and experiment.

In Figure 2.6 and Figure 2.7, the quantities were measured while the converter was operating at f_S = 250 kHz < f_O ≈ 500 kHz. The resonant converter was designed to perform ZVS around 500 kHz, and therefore hard switching transitions are observed in Figure 2.6 and Figure 2.7. High distortion and switching noises are exhibited.

In Figure 2.8 and Figure 2.9, the quantities were measured while the converter was operating at f_S = 500 kHz ≈ f_O. ZVS transitions are observed, and therefore very clean waveforms were obtained. The circulating current, $i_{Lm}(t)$, through the magnetizing inductance (L_m) is triangular as expected from the previous theoretical discussion on Figure 1.20.

As can be seen from Figure 2.6 through Figure 2.9, the simulation waveforms and the experimental waveforms match very well, indicating that the experimental set-up performs as desired.

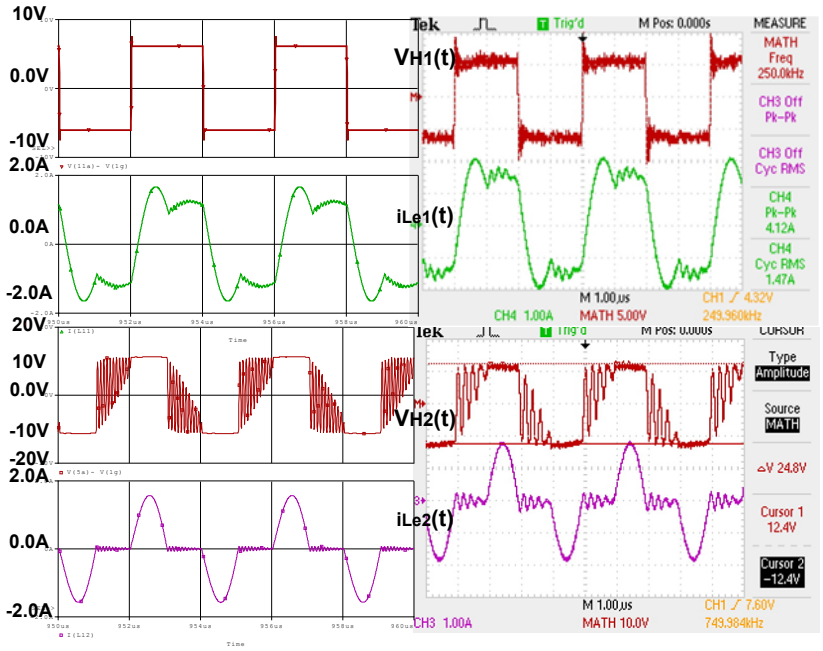

Figure 2.6: Simulation (left) and experimental (right) results for resonant tank input voltage [VH1(t)], primary (tank input) current [iLe1(t)], output voltage [VH2(t)], and secondary current [iLe2(t)] for $f_S \approx 250kHz$.

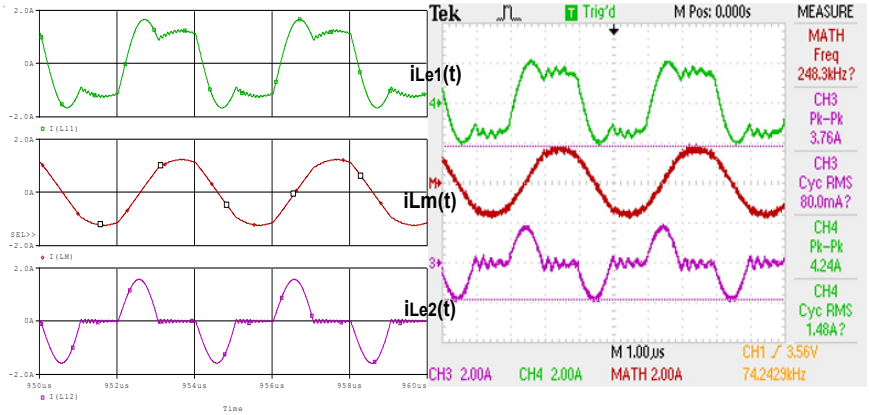

Figure 2.7: Simulation (left) and experimental (right) waveforms of primary current (top), magnetizing inductance current (middle), and secondary current (bottom) for $f_S \approx 250kHz$.

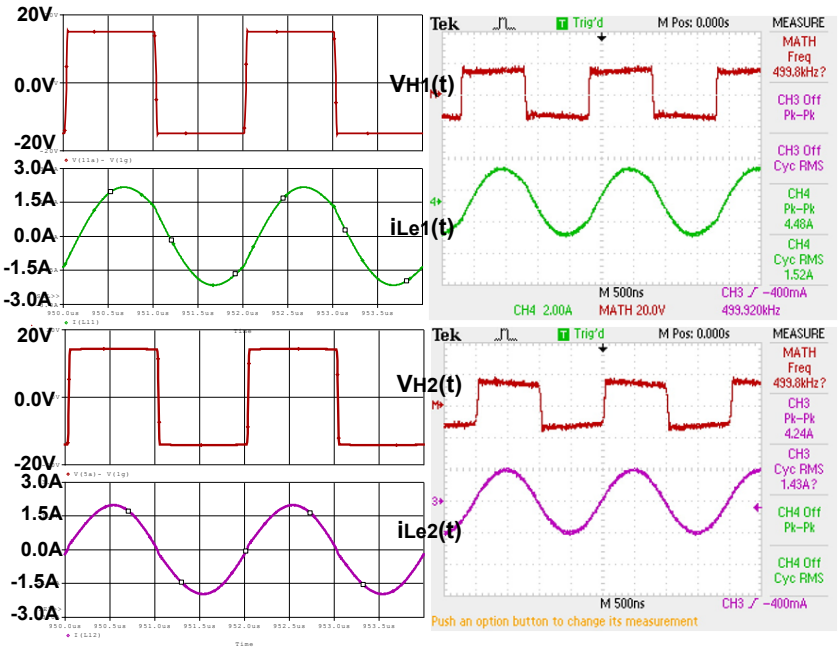

Figure 2.8: Simulation (left) and experimental (right) results for resonant tank input voltage [VH1(t)], primary (tank input) current [iLe1(t)], output voltage [VH2(t)], and secondary current [iLe2(t)] for $R_e' \approx 8.1\ \Omega$.

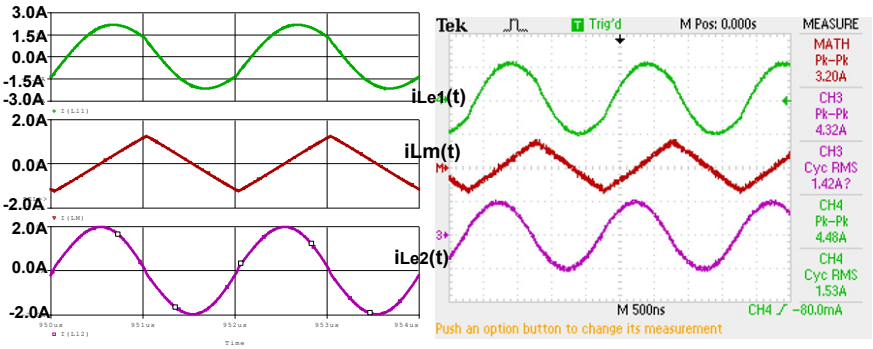

Figure 2.9: Simulation (left) and experimental (right) waveforms of primary (tank input) current [iLe1(t)], circulating current through L_m [iLm(t)], and secondary current [iLe2(t)] for $R_e' \approx 8.1\ \Omega$.

2.2.2 Efficiency Performance

This section discusses how power transmission efficiency of the SS resonant converter depends on switching frequency and load (Q). Later in this dissertation, mathematical expressions for load-dependent quality factor (Q) will be defined separately for SS and

SP resonant tank topologies. For now, it should be mentioned that the mathematical expressions for load-dependent quality factor are *directly* proportional to effective resistive load, R_e', and therefore changes in this quality factor can be imposed by varying R_e'. Figure 2.10 shows the power efficiency (η) data obtained experimentally at varied f_S while the secondary-side full-bridge is performing the passive diode rectification. As expected from the theoretical discussion, operating at the unity gain frequency, f_O = 500kHz, maximizes η due to ZVS and compensation of leakage inductances. In Figure 2.11, the experimental η of the converter is shown for varied R_e'. The secondary-side full-bridge was performing active synchronous rectification with ZCS. The maximum η of 87.2% was obtained at Pout ≈12.5W. This indicates that efficiency characteristics depend on load-dependent quality factor.

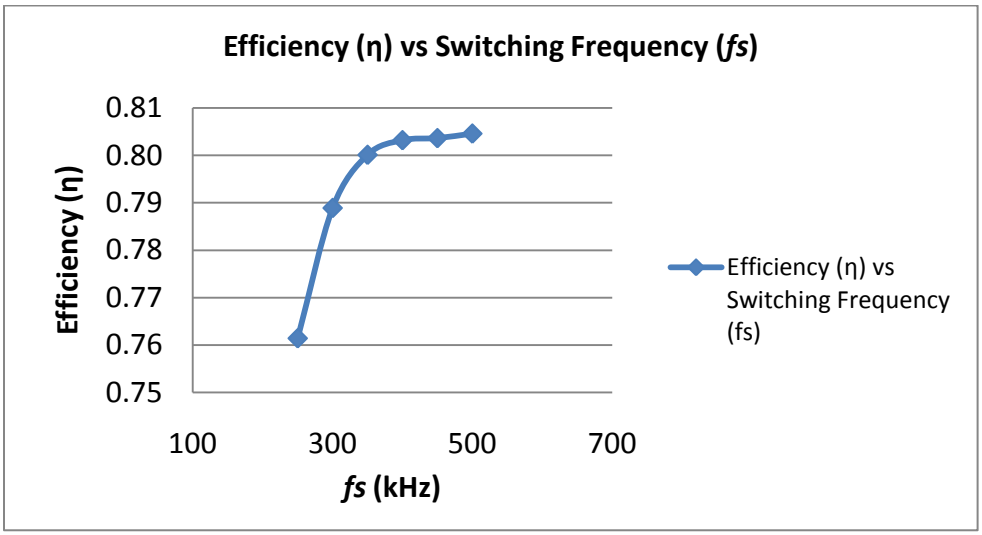

Figure 2.10: Experimental efficiency data for varied switching frequency.

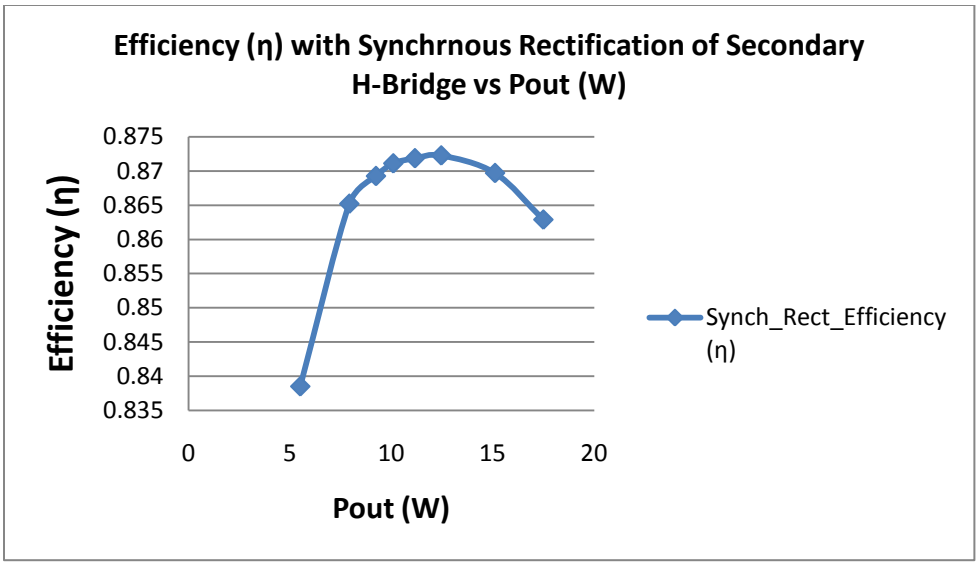

Figure 2.11: Experimental efficiency data plot for the SS resonant converter with active synchronous rectification (ZCS) under varied load condition.

CHAPTER 3

OPTIMAL DESIGN METHOD FOR SS RESONANT TANK OF SRT TYPE TO ALLOW RAPID AND CONVENIENT CALCULATION OF PARAMETERS

3.1 INTRODUCTION

In the previous chapter, it is shown that the power transmission efficiency is a Q-dependent quantity. Designing a resonant tank to exhibit an optimal Q is important for a resonant tank to exhibit several desirable features, which are explained later in this chapter.

An optimal Q condition depends on the intended applications. For example, an optimal value for Q can be the value that maximizes a resonant tank's robustness in voltage and current gains against frequency tracking error and against variations in k and R_e'. As explained more in detail later in this chapter, such robustness maximization may be available at the cost of reduced coil-to-coil efficiency. Under the condition of very small or no variations in resonant tank parameters, an optimal Q should be selected to maximize the coil-to-coil efficiency. *However* in wireless charging applications, significant variations in resonant tank parameters can occur, and *therefore* maximization of robustness can provide several advantages.

One of these advantages is that the overall efficiency of an entire wireless charging system can be optimized. This is because, although coil-to-coil efficiency of a coupler is decreased, high robustness can significantly reduce losses in or eliminate the need for an additional converter and/or linear voltage regulator. Therefore, higher power density,

improved overall power efficiency, and lower cost of implementation can be achieved. Other advantages include increase in receiver positioning flexibility and significantly reduced control complexity, which can further increase power density and further reduce cost of implementation.

There are conventional design methods used for LLC resonant tank of SRT type that applies only a single series capacitance to the primary side of a transformer or a magnetic coupler. These methods allow determining LLC resonant tank parameters needed for achieving a desirable Q for a specified nominal R_e'. Similar methods can be developed for designing the SS resonant tank topology of SRT type to obtain a desirable Q. However, as discussed in the next section, these conventional methods have several shortcomings and undesirable requirements. To overcome various shortcomings of conventional resonant tank design methods, detailed frequency-domain analysis is performed, and then a novel optimal design method for the SS resonant tank of SRT type is developed in this chapter.

3.2 Literature Review on Conventional Design Methods

Conventional design methods have been based on either 1) parametric simulations in the frequency domain with various combinations of resonant tank parameters or 2) mathematical analysis of waveforms of a resonant tank in the time domain when the switching frequency is at the frequency of peak voltage gain, $\|G_V\|_{max}$. Various shortcomings of these conventional design methods are discussed in Section 3.2.1 and Section 3.2.2.

3.2.1 Parametric Simulation-Based Resonant Tank Design Methods

Deriving physically-meaningful design equations is difficult and becomes more complex when multiple resonant frequencies are involved, because mathematical expressions for design equations can become very heavy in number of terms. Therefore, parametric simulations are commonly used to derive combinations of resonant tank parameters that are necessary for achieving a desired peak voltage gain, $||G_V||_{max}$, condition. Conventional parametric simulation-based methods are described in [20] and [21].

These design methods commonly begin by plotting $||G_V(j\omega)||$ of a resonant tank with various combinations of k and Q. As previously mentioned, mathematical expressions for Q depend on authors and resonant tank topologies. These design methods involve performing three-dimensional analysis on two dimensional graphical representation containing Q, k (or $k_L = \frac{L_m}{L_e}$), and $||G_V||_{max}$ as the axes. Figure 3.1 shows the examples from [20] and [21] used in LLC resonant tank design procedures. The numbers indicated for each curve (1.3, 1.6, 2, 2.5, and 3) in Figure 3.1 (b) represent $||G_V||_{max}$ values, and L_n is used to represent $k_L = \frac{L_m}{L_e}$. For example, choosing $L_n = \frac{L_m}{L_e} \approx 5$ and $Q \approx 0.15$ achieves $||G_V||_{max} \approx 3$ in the LLC resonant tank.

Although these conventional parametric simulation-based design methods can determine *exact* resonant parameters required for achieving a desired $||G_V||_{max}$ (Q) condition, such parametric simulations can become a trial-and-error process that requires many sets of simulations to be performed, and can consequently become very tedious. Also, there exist inevitable sources of error in experimental implementation of a resonant

tank. The sources of error include component tolerances, coupler winding resistances, capacitor ESRs, and error in constructing a coupler to exhibit desired inductances. Since they may noticeably affect the resonance characteristics, it may be of questionable value to perform such time-consuming efforts to determine *exact* solutions.

Furthermore, although parametric simulation-based design methods can greatly enhance design processes for resonant tanks that exhibit complex analytical equations with a large number of variables, it is highly desirable if convenient analytical equations in physically-meaningful form can be derived and used for approximation of design parameters.

In summary, a major shortcoming of conventional parametric simulation-based design methods is that they lack in terms of providing analytical closed-form equations in design-oriented form that provide good approximation for intuitive understanding of various tradeoffs and effects of variation in each design parameter value.

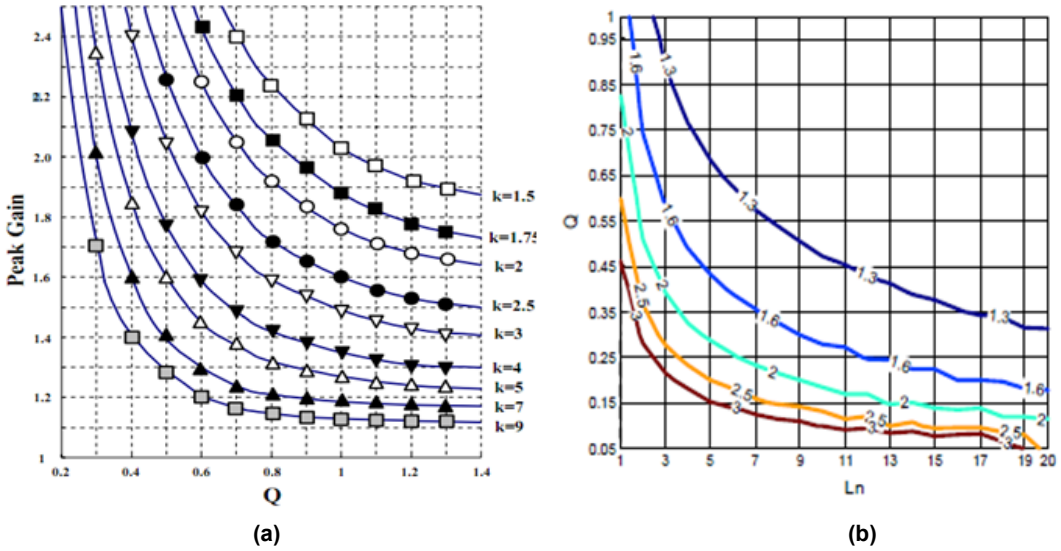

Figure 3.1: Portions of peak voltage gain curves, used (a) in reference [20] and (b) in reference [21], showing relationship among $\boldsymbol{k_L = \frac{L_m}{L_e}}$ (or coupling coefficient, *k*), Q, and peak voltage gain values in ZVS range (above peak resonance range).

3.2.2 Design Approach Based On Analytical Solutions Derived Using Time-domain Analysis

In [22], analytical solutions for determining the peak voltage gain of LLC resonant tank are derived to propose a design method based on a peak voltage gain equation. Based on waveforms for input current, magnetizing inductance current, and resonant capacitor voltage in LLC resonant tank when f_S is at the resonant frequency of $||G_V||_{max}$, reference [22] derives analytical equations for calculating $||G_V||_{max}$ and resonant frequency at which $||G_V||_{max}$ occurs.

The waveforms are analyzed in two different time intervals denoted as t_1 and t_2. During t_1, the magnetizing inductance current increases from zero to its highest value, and intersects the resonant tank input current waveform at the highest value. During t_2, the magnetizing inductance current starts to decrease from its highest value to zero. Expressions for t_1 and t_2 are derived as Equation 16 and Equation 17 respectively. Also, expressions for $||G_V||_{max}$ and resonant frequency of $||G_V||_{max}$ are derived as Equation 18 and Equation 19 respectively. As can be seen, the design equations are very computationally heavy, and no closed-form solutions are determined. Since these equations are not in physically-meaningful forms, this method still requires a number of parametric simulations to plot multiple sets of $||G_V(j\omega)||$ for various values for resonant capacitance (C_r), resonant inductance (L_r), magnetizing inductance (L_m), and load (R_L).

In summary, this method also has the major disadvantage of failing to provide analytical equations in physically-meaningful forms that can be used directly in a design process and can give quick and clear insights into effects of design parameter changes on resonance characteristics.

In the next section, a novel optimal design method for SS resonant tank topology of SRT type is presented. This method provides design equations having simple, physically-meaningful expressions, and therefore allows rapid calculation of resonant tank parameters needed for achieving a desired peak voltage gain condition.

$$n^2 R_L \left\{ C_r (1-\cos(\omega_o t_1)) \left(\frac{1}{L_m} \sqrt{\frac{L_r}{C_r}} \frac{t_1}{\sin(\omega_o t_1)} \right) - \frac{t_1^2}{2L_m} \right\} - t_1 = \frac{1}{\sqrt{L_{eq} C_r}} \left[\tan^{-1} \left\{ \frac{-\frac{1}{L_m \sqrt{C_r}} t_1}{\frac{1}{\sqrt{L_{eq}}} \left(\frac{1}{L_m} \sqrt{\frac{L_r}{C_r}} \frac{t_1}{\sin(\omega_o t_1)} \cos(\omega_o t_1) + 1 \right)} \right\} \right]. \quad \text{..... Equation (16)}$$

$$t_2 = \frac{1}{\sqrt{L_{eq} C_r}} \left[\tan^{-1} \left\{ \frac{-\frac{1}{L_m \sqrt{C_r}} t_1}{\frac{1}{\sqrt{L_{eq}}} \left(\frac{1}{L_m} \sqrt{\frac{L_r}{C_r}} \frac{t_1}{\sin(\omega_o t_1)} \cos(\omega_o t_1) + 1 \right)} \right\} \right] \quad \text{..... Equation (17)}$$

$$G_{peak} = \frac{V_o}{V_{in}} = \frac{1 - V_{cro}/V_{in}}{n \left\{ \frac{1}{L_m} \sqrt{\frac{L_r}{C_r}} \frac{t_1}{\sin(\omega_o t_1)} + 1 \right\}} \quad \text{..... Equation (18)}$$

where,

$$V_{cro} = \left(\cos(\omega_o t_1) \cos(\omega_1 t_2) - \sqrt{\frac{L_{eq}}{L_r}} \sin(\omega_o t_1) \cos(\omega_1 t_2) \right) \times \left(1 - \left(\frac{1}{L_m} \sqrt{\frac{L_r}{C_r}} \frac{t_1}{\sin(\omega_o t_1)} \right)^{-1} \right) + \frac{L_m \sin(\omega_o t_1) \cos(\omega_1 t_2)}{\sqrt{\frac{L_r}{C_r}} t_1 + L_m \sin(\omega_o t_1)}$$

$$f_{peakgain} = \frac{1}{2(t_1 + t_2)} \quad \text{..... Equation (19)}$$

3.3 Frequency-domain Characteristics of SS Resonant Tank of SRT Type

In order to clearly understand the purpose of the conventional design methods and proposed novel design method, it is important to understand the frequency-domain characteristics of the SS resonant tank of SRT type whose simplified equivalent model is shown in Figure 3.2.

This section explains various notable features that the design methods are used to achieve. Let us consider the parametric simulation plot in Figure 3.3 for voltage gain

magnitude, $||G_V(j\omega)||$, versus frequency of the SS resonant tank of SRT type. As mentioned previously, R_e' variation corresponds to Q variation, which changes the peak voltage gain available, $||G_V||_{max}$, in a resonant tank. It can be seen from Figure 3.3 that there are three distinguishable resonant frequencies: f1, f2, and f3. As R_e' increases (as $||G_V||_{max}$ and Q get higher), the resonant peaks at f1 and f3 become no longer visible, and a single peak at f2 appears.

In this section, both a general expression and a simplified expression of voltage gain transfer function, $||G_V(j\omega)||$, are used to determine the resonant frequencies along with another resonant frequency that is not visible in Figure 3.3. Also, this section explains meanings of the resonant frequencies and provides self-explanatory circuit-based names for them.

For the general expression, *no* assumptions regarding the symmetry and turns ratio of coupler are made. Whereas in the simplified expression, symmetrical core geometry and 1:1 turns ratio are assumed so that $L_e = L_{e1} = L_{e2}'$ and $C = C_1 = C_2'$. ESRs of resonant capacitors and winding resistances of coupler are assumed to be negligible.

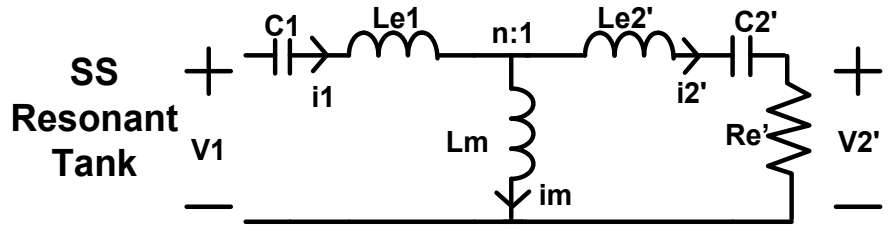

Figure 3.2: Equivalent model for SS resonant tank of SRT type.

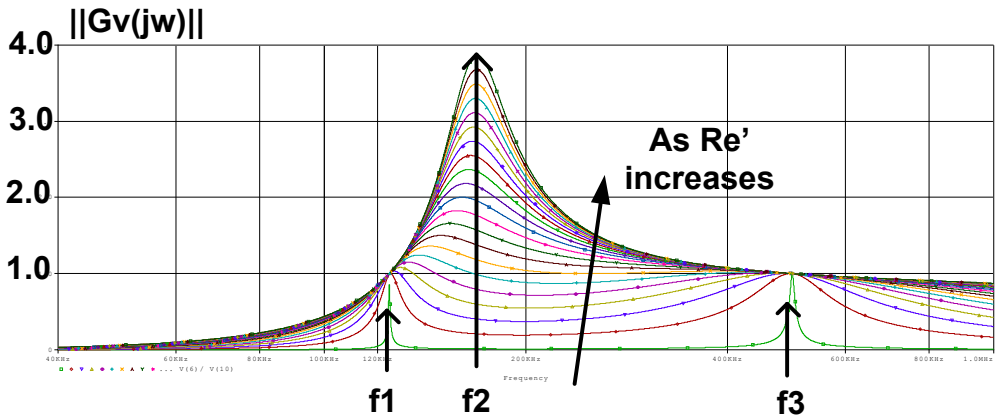

Figure 3.3: $||G_V(j\omega)||$ of SS resonant tank of SRT type for varied $R_e'(Q)$.

3.3.1 Derivation of Resonant Frequencies from General Expression of Voltage Gain Transfer Function

A general expression of the voltage gain magnitude, $||G_V(j\omega)||$, of the SS resonant tank is shown as Equation 20. The denominator can be represented in two different forms as Equation 21 and Equation 22. From these equations, it is clear that four resonant frequencies can be derived as Equation 23 through Equation 26.

$$||Gv(j\omega)||=\left|\frac{-j\omega^3 C_1 C_2' Lm\,\mathrm{Re}'}{\left[\omega^4 C_1 C_2'(Le_1(Le_2'+Lm)+Le_2' Lm)-\omega^2(C_1(Le_1+Lm)+C_2'(Le_2'+Lm))+1\right]-j\left[\omega C_2'\,\mathrm{Re}'(\omega^2 C_1(Le_1+Lm)-1)\right]}\right|$$

..... Equation (20)

$$\omega^2 C_1(Le_1+Lm)\left[\omega^2 C_2'\left(Le_2'+\frac{Le_1 Lm}{Le_1+Lm}\right)-1\right]-\omega^2 C_2'(Le_2'+Lm)+1-j\omega C_2'\,\mathrm{Re}'(\omega^2 C_1(Le_1+Lm)-1)$$

..... Equation (21)

$$\omega^2 C_2'(Le_2'+Lm)\left[\omega^2 C_1\left(Le_1+\frac{Le_2' Lm}{Le_2'+Lm}\right)-1\right]-\omega^2 C_1(Le_1+Lm)+1-j\omega C_2'\,\mathrm{Re}'(\omega^2 C_1(Le_1+Lm)-1)$$

..... Equation (22)

$$frp=\frac{1}{2\pi\sqrt{C_1(Le_1+Le_2'\|Lm)}}=\frac{1}{2\pi\sqrt{C_1\left(Le_1+\frac{Le_2' Lm}{Le_2'+Lm}\right)}}$$ .....Equation (23)

$$frs = \frac{1}{2\pi\sqrt{C_2'(Le_2' + Le_1 \parallel Lm)}} = \frac{1}{2\pi\sqrt{C_2'\left(Le_2' + \frac{Le_1 Lm}{Le_1 + Lm}\right)}}$$ .....Equation (24)

$$f_{LP} = \frac{1}{2\pi\sqrt{C_1(Le_1 + Lm)}}$$ .....Equation (25)

$$f_{LS} = \frac{1}{2\pi\sqrt{C_2'(Le_2' + Lm)}}$$ .....Equation (26)

3.3.2 Derivation of Resonant Frequencies from Simplified Expression of Voltage Gain Transfer Function

A similar derivation process is performed for the special case of $L_e = L_{e1} = L_{e2}'$ and $C = C_1 = C_2'$. A simplified expression for the magnitude of the voltage gain transfer function, $||G_V'(j\omega)||$, is given as Equation 27. From the denominator, three resonant frequencies can be derived as Equation 28 through Equation 30. For $L_e = L_{e1} = L_{e2}$ and $C = C_1 = C_2'$, all of the resonant frequencies including the ones from the previous section can be categorized in four different resonant frequency sets as in Table 3.1. Normalizing the resonant frequency sets with respect to frequency f_n results in the relationship shown in Figure 3.4. In this figure, k is the coupling coefficient defined as Equation 31- **Note**: Equation 1 is a general expression for k and is identical to Equation 31 for a symmetrical coupler with 1:1 turns ratio, because $k_1 = \frac{L_m}{L_e + L_m} = k_2$ and $L_{s1} = L_e + L_m = L_{s2}$. From this point on, L_S refers to $L_{S1} = L_{S2}$.

The resonant frequency sets have important roles in describing voltage gain patterns under load (R_e') and coupling coefficient (k) variations. In the next section, the resonant frequency sets are evaluated to explain their roles.

$$||G_V'(j\omega)|| = \left|\frac{\omega^3 C^2 L_m Re'}{\omega C Re'(\omega^2 C(L_e + L_m) - 1) + j[(\omega^2 C(L_e + 2L_m) - 1)(\omega^2 C L_e - 1)]}\right|$$ ..... Equation (27)

$$f_L = \frac{1}{2\pi\sqrt{C(Le+Lm)}} = \frac{1}{2\pi\sqrt{CL_S}} \quad \text{..... Equation (28)}$$

$$f_O = \frac{1}{2\pi\sqrt{CLe}} = \frac{1}{2\pi\sqrt{CL_S(1-k)}} \quad \text{..... Equation (29)}$$

$$f_n = \frac{1}{2\pi\sqrt{C(Le+2Lm)}} \quad \text{..... Equation (30)}$$

$$k = \frac{Lm}{Le+Lm} \quad \text{..... Equation (31)}$$

TABLE 3.1 EQUATIONS FOR FREQUENCIES OF INTEREST

Frequency Set	Corresponding Frequency in Figure 3.3	Resonant Frequency for L_e: $L_{e1} \approx L_{e2}'$ and C: $C_1 \approx C_2'$
f_n	*f1*	$\frac{1}{2\pi\sqrt{C(Le+2Lm)}}$
f_L	*f2*	$\frac{1}{2\pi\sqrt{C(Le+Lm)}}$
f_O	*f3*	$\frac{1}{2\pi\sqrt{CLe}}$
f_r	*Not Visible*	$\frac{1}{2\pi\sqrt{C\left(Le+\frac{LeLm}{Le+Lm}\right)}}$

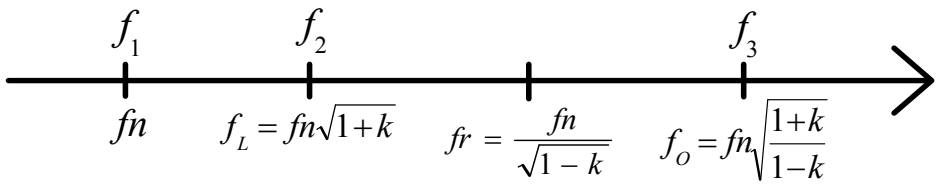

Figure 3.4: Normalization of resonant frequency sets.

Note: The figure is just to show the location of frequency sets with the respect to each other and also is not in scale, because the scale varies depending on resonant parameters.

3.3.3 Evaluation of Resonant Frequencies

A. Evaluation of f_O

As mentioned previously, resonant frequency f_O is the load-independent unity gain frequency at which the leakage inductances are compensated to maximize the resonant tank efficiency. It can be easily verified that substituting the f_O equation (Equation 29) into Equation 27 results in load-independent unity voltage gain, that is $\|G_V'(j2\pi f_O)\| = 1$ regardless of load (R_e') variation. A self-explanatory name for f_O can be then *unity gain frequency* (or *short-circuited leakage resonant frequency* to be general). In Figure 3.3, there exist two load-independent unity gain frequencies, f1 and f3. In order to determine which of these corresponds to f_O, the circulating current gain, $\|G_{iLm}(j\omega)\| = \left|\frac{i_{Lm}(j\omega)}{i_{Le1}(j\omega)}\right|$, of the SS resonant tank of SRT type is plotted for varied R_e' along with the voltage gain magnitude, $||G_V'(j\omega)||$ (Equation 27), in Figure 3.5. As can be seen from this figure, the circulating current through the magnetizing inductance (iLm) at f1 decreases as R_e' increases, whereas iLm at f3 increases as R_e' increases. It should noted that based on the equivalent model of the SS resonant tank in Figure 1.21, the circulating current through the magnetizing inductance (iLm) at $f_S = f_O$ increases as R_e' increases. Therefore, f3 corresponds to f_O.

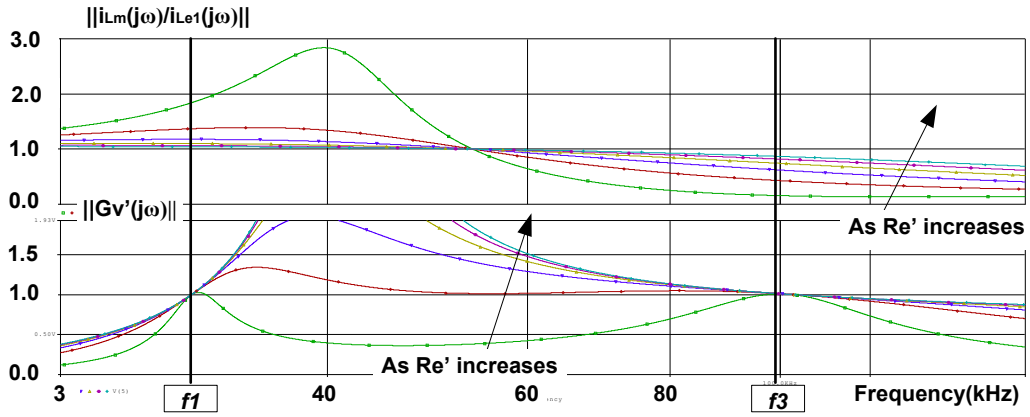

Figure 3.5: Circulating current gain magnitude $||G_{iLm}(j\omega)||$ (top) and voltage gain magnitude $||G_V'(j\omega)||$ (bottom) of the SS resonant tank of SRT type.

B. Evaluation of *fn*

By substituting Equation 30 into Equation 27, it can be easily shown that voltage gain is unity also at f_n regardless of R_e' variation, that is $||G_V'(j2\pi f_n)|| = 1$. Thus, f1 corresponds to f_n. Derivation of Equation 30 is shown graphically through the Norton-Thevenin equivalent circuit transformations shown in Figure 3.6. Thus, a self-explanatory name for f_n is *short-circuited load resonant frequency*.

When f_n is designed to be much lower than f_O, as in the bottom plot of Figure 3.7, the voltage gain as a function of frequency varies in an approximately linear fashion around frequency f_O. The accuracy of linear approximation and frequency range in which the linear approximation model is applicable increase as f_n is farther away from f_O. It is clear from the f_n and f_O equations that, as coupling coefficient, k, decreases, frequencies f_n and f_O get closer to each other. Therefore, in order for a linear model to work appropriately for a wide range of k variations, a value for the unity gain frequency, f_O, needs to be selected as large as possible in the design process for the SS resonant tank. By using a linear approximation around f_O, it will be shown in Chapter 4 that a control model can be

derived for tracking and achieving the unity gain frequency without communication between the transmitter and receiver under an allowed range of k variation. Furthermore, it will be explained later in Chapter 5 that selecting as high as possible a value for f_O is desirable for optimal design of SS resonant tank topology in *general* for achieving other desirable features as well.

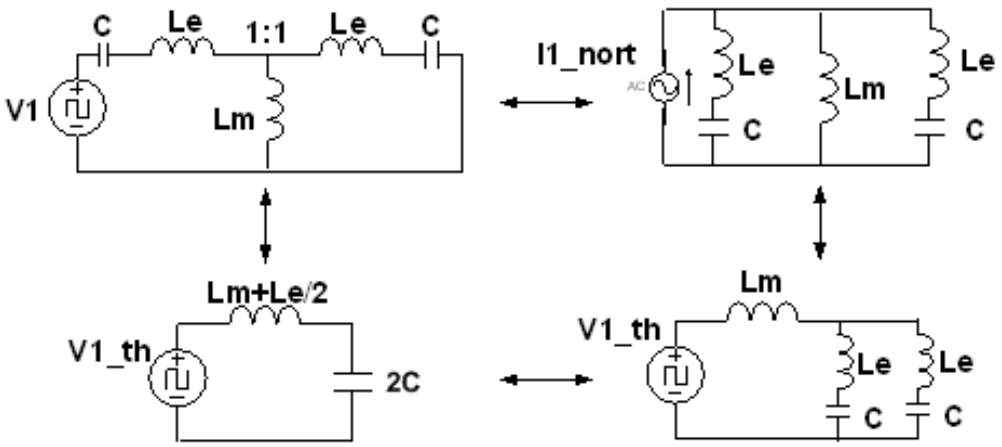

Figure 3.6: Equivalent circuit transformation for graphical derivation of equation for f_n.

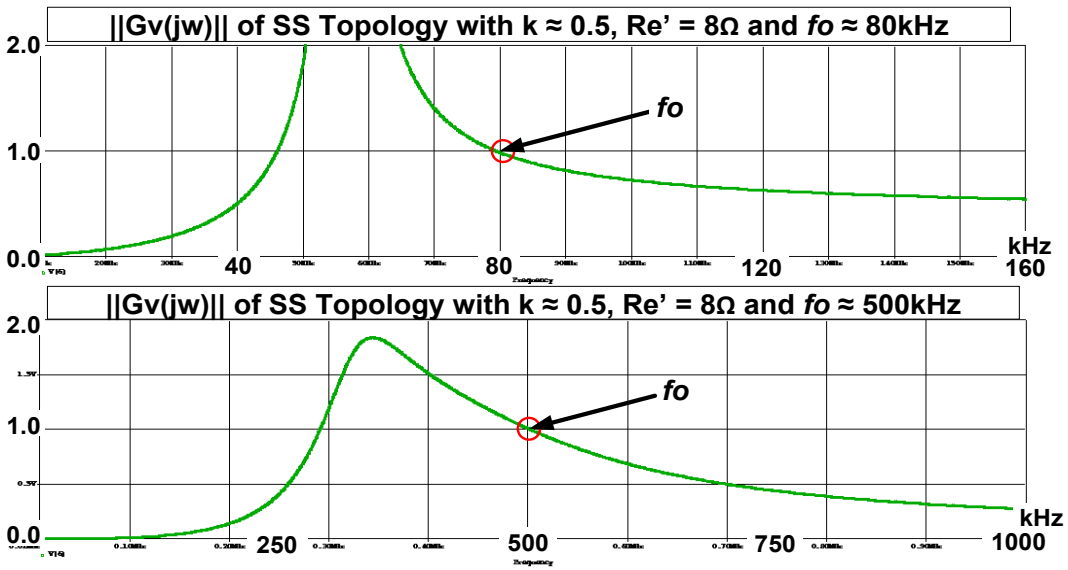

Figure 3.7: Effects of selecting a larger value for f_O in a design process.

Note: x-axis (frequency-axis) is in linear scale.

C. Evaluation of f_L

In Figure 3.8, let us consider $||G_V'(j\omega)||$ curves having $||G_V||_{max} \geq 1.5$. Under this condition, a well-defined single resonant peak appears. As this well-defined single peak increases (as $||G_V||_{max}$ increases above 1.5), the frequency of $||G_V||_{max}$ *very rapidly (exponentially)* approaches frequency f2. Also, the voltage gain is monotonically decreasing for frequencies above f2. The single peak behavior becomes more clear as Re' increases further (as Q increases further). When R_e' is increased to a very high value, the secondary side of the resonant tank is effectively open-circuited, and the equivalent circuit model can be approximated by Figure 3.9. It is clear that the resonant frequency of the equivalent model in Figure 3.9 is determined by f_L. Therefore, frequency f2 corresponds to f_L, which is the *open-circuited load resonant frequency*. It is explained later in Section 3.4 that this frequency along with f_O are very important for developing the novel optimal design method.

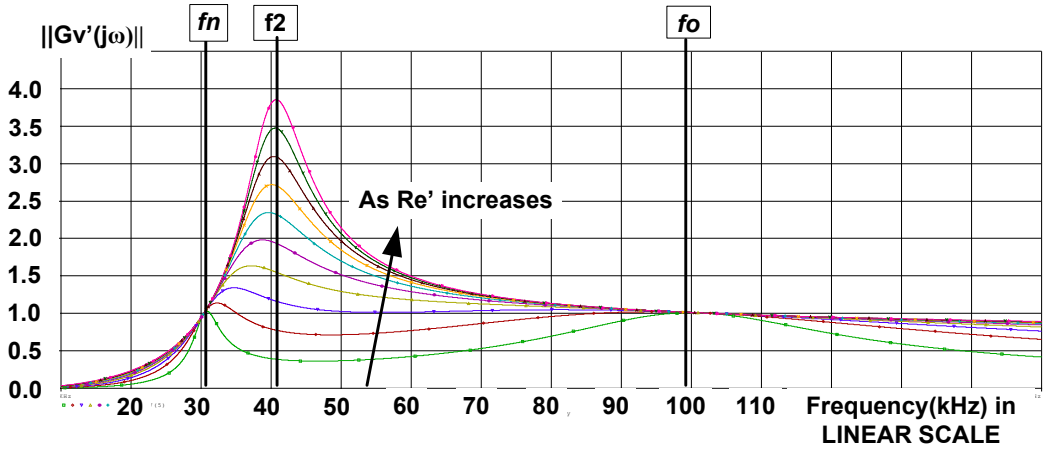

Figure 3.8:Parametric simulation results for $||G_V'(j\omega)||$ for varied R_e'.

Note: x-axis (frequency-axis) is in linear scale.

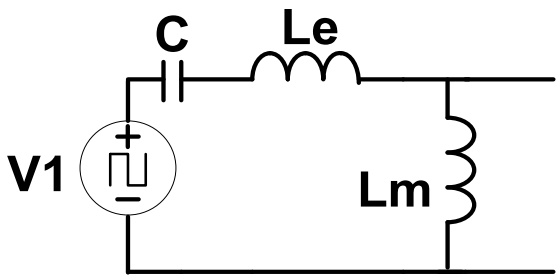

Figure 3.9: Approximated equivalent model of SS topology when R_e' (thus, Q) is high enough for $||G_V||_{max}$ to be well above unity.

D. Evaluation of f_r

Frequency f_r is of limited importance for the SS resonant tank, but it is important for SP resonant tank topology. As will be explained more in detail in Chapter 5, the f_r equation in Table 3.1 determines the *short-circuited load resonant frequency* of SP resonant tank. At this frequency, load-independent voltage gain occurs for the SP resonant tank, as shown by Figure 3.10.

It should be mentioned that as the ratio of C_2' to C_1 gets higher (as the ratio, $\frac{f_{rp}}{f_{rs}}$, gets higher), the equivalent model of the SS resonant tank becomes more like the LLC resonant tank topology (containing only a single series capacitor on the primary side). This is because a very large value of C_2' has a very *low* impedance *compared* to C_1. In this case, the frequency of load-independent voltage gain does not necessarily correspond to the voltage gain of one. This frequency, which is again the highest efficiency point, is shown as f_x in Figure 3.11. Therefore, f_r is where the *load-independent voltage gain* occurs also for the LLC resonant tank topology.

As a summary, Table 3.2 lists the resonant frequency sets with their self-explanatory names.

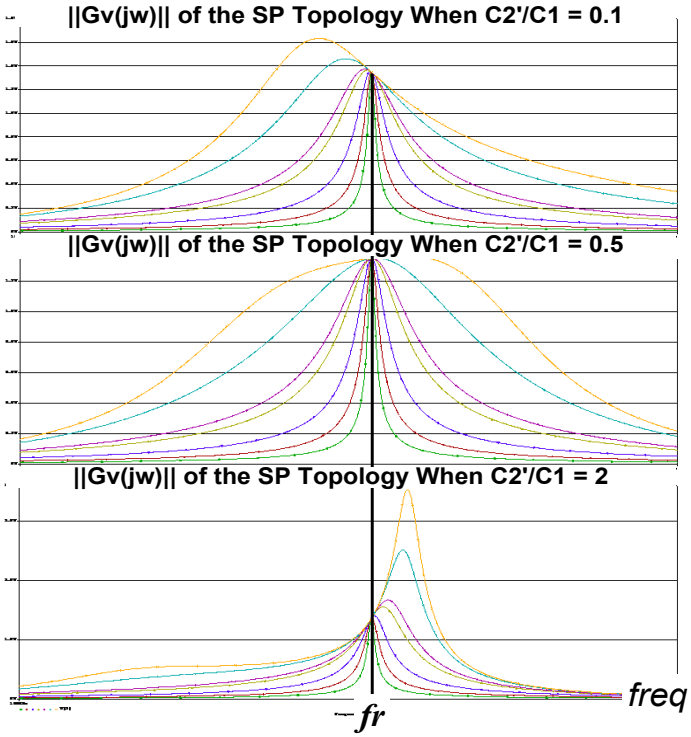

Figure 3.10: $\|G_V(j\omega)\|$ of the SP topology for varied ratio of C_2' to C_1.

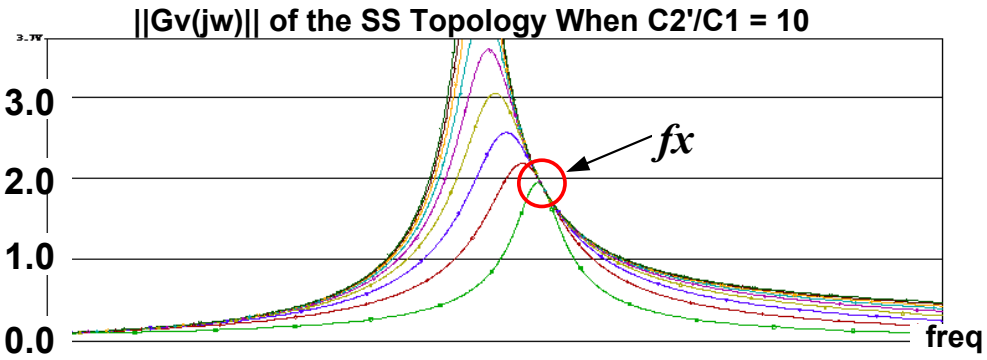

Figure 3.11: $\|G_V'(j\omega)\|$ of the SS topology when $C_2' = 10*C_1$.

TABLE 3.2 SUMMARY OF RESONANT FREQUENCIES

Frequency Set	Corresponding Frequency in Figure 3.3	Self-explanatory Name based on Equivalent Circuit Model
f_n	*f1*	Short-circuited load resonant frequency
f_L	*f2*	Open-circuited load resonant frequency
f_O	*f3*	Short-circuited leakage resonant frequency
f_r	*Not Visible*	Short-circuited load resonant frequency of LLC and SP resonant tank topologies

3.3.4 NOTABLE FREQUENCY-DOMAIN CHARACTERISTICS

Various notable frequency-domain characteristics of the SS resonant tank of SRT type are described in this section. Figure 3.12 shows again the voltage gain characteristics of SS resonant tank of SRT type for varied effective load, R_e' (thus varied Q). This figure also shows the frequency-dependent trends of power delivery and resonant tank efficiency.

In Figure 3.13, voltage gain curves are plotted for varied *k*. Figure 3.13 (a) shows the voltage gain characteristics when the single peak behavior is maintained for all of the *k* variation, whereas Figure 3.13 (b) shows the voltage gain characteristics when multiple resonant peaks are exhibited as *k* varies. Resonant frequency f_{O_n} in Figure 3.13 represents the unity gain frequency of SS resonant tank under a certain *k* condition. It should be noted that achieving $||G_V||_{max} > 1.5$ for the highest *k* in a desired range of *k* guarantees the single resonant peak behavior for the entire *k* range, because $||G_V||_{max}$ decreases as *k* increases.

From Figure 3.12 and Figure 3.13, it can be concluded that a well-defined single voltage gain peak (achieved by obtaining $||G_V||_{max} > 1.5$) places the frequency of highest efficiency (unity voltage gain frequency, f_O) above resonance. The frequency range above a resonant peak in voltage gain provides inductive impedance to the input terminal of SS resonant tank. As explained in Chapter 2, inductive input impedance is required for ZVS operation. Therefore, this frequency range is called ZVS range.

As can be seen from Figure 3.12, the peak output current level is located near f_L while the peak efficiency is at f_O when $||G_V||_{max} > 1.5$. On the other hand, when it is $||G_V||_{max} \leq 1.0$, both the output current level and efficiency are maximum at f_O. Due to this fact, a

longer range of frequency in ZVS range is obtained and can be used for controlling the voltage gain (power delivery) via switching frequency (f_S) modulation. The condition of a well-defined single voltage gain peak can reduce voltage gain sensitivity to switching frequency error (thus, unity gain frequency tracking error). Furthermore under this condition, as can be seen from Figure 3.13, the danger of f_{On} falling into the below-resonance region *under k variation* can be avoided.

Also, under the single voltage gain peak condition, Figure 3.12 and Figure 3.13 show that voltage gain characteristics can become robust against k and load (Q) variations, indicating that power delivery can become robust as well. Complexity in deriving a linear model for load voltage control around f_O is *significantly* reduced. This is shown by Figure 3.7 as well as the control range indicated in Figure 3.12: the voltage gain as a function of frequency varies in an approximately linear fashion around frequency f_O.

However, it must be noted that achieving high Q is *not* desirable for maximizing the power efficiency in a SS resonant tank. The effects of high Q on power efficiency can be understood by considering that a high value of Q is obtained due to a high value of R_e' – Note: Q and R_e' are directly proportional to each other. With a high value of R_e', the circulating current i_{Lm} is high even if unity voltage gain operation is performed – See Figure 1.21. Therefore, achieving high Q comes at the cost of reduced coil-to-coil power efficiency of a magnetic coupler. Achieving an appropriate value of Q is required for an optimal tradeoff between robust voltage gain and high coil-to-coil efficiency.

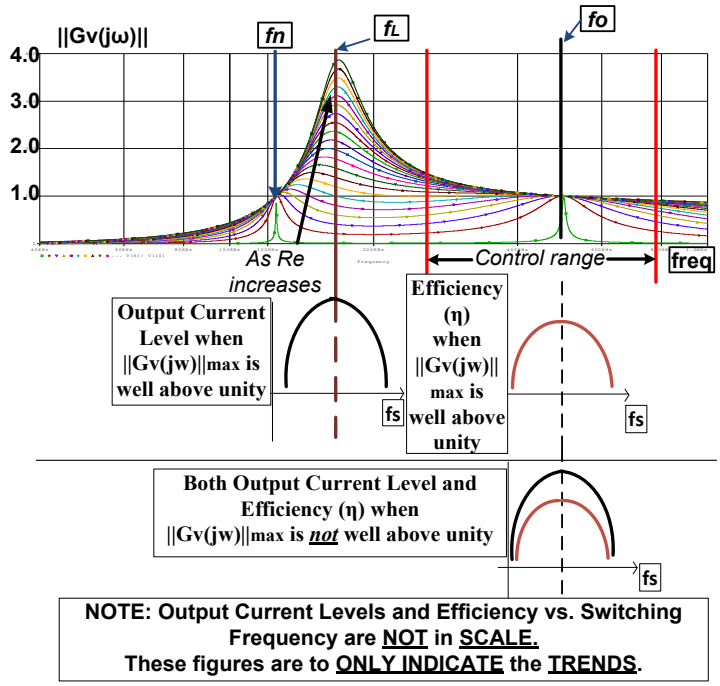

Figure 3.12*: Voltage gain* $||G_V(j\omega)||$ curves for varied R_e' showing also the frequency-dependent trends of output current level (power delivery) and efficiency.

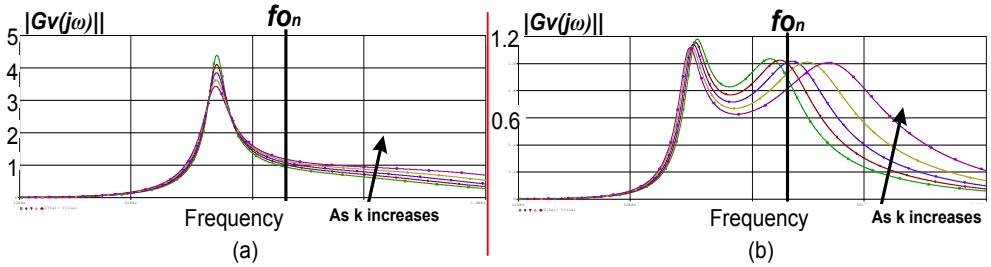

Figure 3.13: Voltage gain of SS resonant tank at various *k*, when the single resonant peak behavior is achieved (a) and is not achieved (b).

3.4 Novel Optimal Design Method For the SS Resonant Tank of SRT Type

3.4.1 Derivation of Design-oriented Equation For Peak Voltage Gain Approximation

Previously, Figure 3.8 and Figure 3.12 show that voltage gain at f_L is a Q-dependent quantity. Therefore, it is a *designable* quantity, meaning that by achieving a value of Q for a specified nominal R_e', it is possible to obtain desired voltage gain characteristics. By substituting Equation 28 into Equation 27, voltage gain at f_L, $||G_V'(j2\pi f_L)||$, is derived in design-oriented form as shown by Equation 32.

This equation can then be used as a starting point in a design process to determine the parameters of SS resonant tank of SRT type required for achieving either double voltage gain peak condition or single voltage gain peak condition. It can *also* be used for a parametric simulation-based design method similar to the conventional methods described previously.

For example, if a designer intends to achieve dual voltage gain peaks, the condition is $||G_V'(j2\pi f_L)|| < 1.5$. Otherwise, achieving a single voltage gain peak requires that $||G_V'(j2\pi f_L)|| \geq 1.5$ – See Figure 3.8. It should be noted that when $||G_V'(j2\pi f_L)|| = 1.5$, $||G_V||_{max} > 1.5$. Also, it should be noted that $||G_V||_{max}$ increases as k decreases, as can be seen from Equation 32. Therefore, if Equation 32 is used to achieve $||G_V'(j2\pi f_L)|| \geq 1.5$ at the highest expected value of k in a k variation range, the condition of single voltage gain peak is obtained for the entire range of k.

As can be seen from Figure 3.3 and Figure 3.8, when the single peak behavior is achieved, the frequency of $||G_V||_{max}$ is very close to f_L, and approaches closer to f_L exponentially as $||G_V||_{max}$ increases. Thus, the f_L equation in Table 3.1 is a good approximation for the resonant frequency of $||G_V||_{max}$ when a well-defined single peak is obtained in voltage gain. Thus, Equation 32 also provides good approximation for $||G_V||_{max}$.

$$\|G_V'(j2\pi f_L)\| = Q\sqrt{1+\frac{1}{k_L}} = \frac{Q}{\sqrt{k}}, \quad \text{..... Equation (32)}$$

where $Q = R_e'\sqrt{\frac{C}{L_S k}}$ and $k_L = \frac{L_m}{L_e} = \frac{k}{1-k}$

3.4.2 Proposed Design Equation for Resonant Capacitance

The resonance capacitance can be determined by substituting $\frac{f_o}{f_L} = \sqrt{k_L + 1}$ into Equation 32. It can be concluded from Table 3.1 that $2\pi f_O L_m = \frac{1}{2\pi f_O C}$. Using the equations, $Q = R_e' \sqrt{\frac{C}{L_S k}}$, $k_L = \frac{L_m}{L_e} = \frac{k}{1-k}$, and $f_o = \frac{1}{2\pi\sqrt{L_e C}}$, Equation 33 is derived as the design equation for the resonant capacitors. This equation is in terms of the design parameters from Equation 32 and frequency f_O, thus it accounts for both the unity voltage gain at f_O and $||G_V||_{max}$ near f_L, under a desired nominal value for R_e' and expected value for k.

$$C = \frac{Q\sqrt{k_L}}{2\pi f_O \, Re'} \quad \text{..... Equation (33)}$$

3.4.3 Summary Of Criteria On Q ($||G_V||_{MAX}$) Selection

In wireless charging applications, design specifications call for desired *ranges* of R_e' and k_L rather than *fixed* values. Then, if ensuring the single peak behavior is desired for the *entire ranges* of R_e' and k_L, $||G_V(j2\pi f_L)|| \geq 1.5$ can be achieved using the *lowest* value R_e' and *highest* value of k_L. This is because $||G_V||_{max}$ and Q *increase* as R_e' *increases* but *decreases* as k_L *increases* (see Equation 32). It should be noted that increasing Q causes the circulating current gain $||G_{iLm}(j2\pi f_O)||$ to increase. This results in increased core loss and conduction losses on the primary side. Also, as Q increases, the phase shift between voltage V1 and current i_{Le1} gets closer to 90 degrees at f_O, thus lowering the conduction loss in the primary-side switches *but* undesirably increasing the reactive energy. Therefore, selecting a large value for $||G_V||_{max}$ should be avoided. However, as explained previously, increasing Q has several benefits such as ZVS range extension, lower

efficiency sensitivity to frequency variation, and increased power delivery robustness against k and R_e' variations.

Due to these tradeoffs, selecting a desirable Q (thus, appropriate $||G_V||_{max}$) for optimization needs to take into account the following parameters:

- R_{ds_on} of all switches being used
- Resonant capacitors' ESRs
- Winding resistances of coupler
- Expected ranges of k and R_e' variations
- Desired f_O
- Effects on efficiency due to $||G_V(j\omega)||$'s sensitivity to f_S variation around fo

Later in Chapter 5, design procedures for determining optimal boundaries of load-dependent quality factor will be discussed.

3.4.4 Example Design Procedure

This section describes an example design procedure to demonstrate how to use the proposed design equations. This example design will show that by using the design equations, a designer can decide which of the two coupler geometries is desirable for optimization of a wireless charging system by achieving the single voltage gain resonant peak condition for a desired nominal load, R_e'.

Typically, a design process for resonant tank begins with performing finite element simulations (FES) to optimize coupler geometry. Performing FES provides a coupler's T-equivalent model parameters (thus, k) with good accuracy. For example, Figure 3.14 shows FES inductance value extraction of an inductor made of flat spiral coil on a ferrite disk core. For a faster simulation time, mesh analysis and tolerance are set up so that maximum error of 5 % is tolerated for the inductance extraction. The experimental

construction of the same inductor and network analyzer's impedance measurement are shown in this figure as well. As can be seen, FES shows that the inductance value is 20.14 μH, while the experimental parameter extraction shows the inductance value of approximately 20.77 μH. Therefore, the percent error in inductance calculation is only about 3 %.

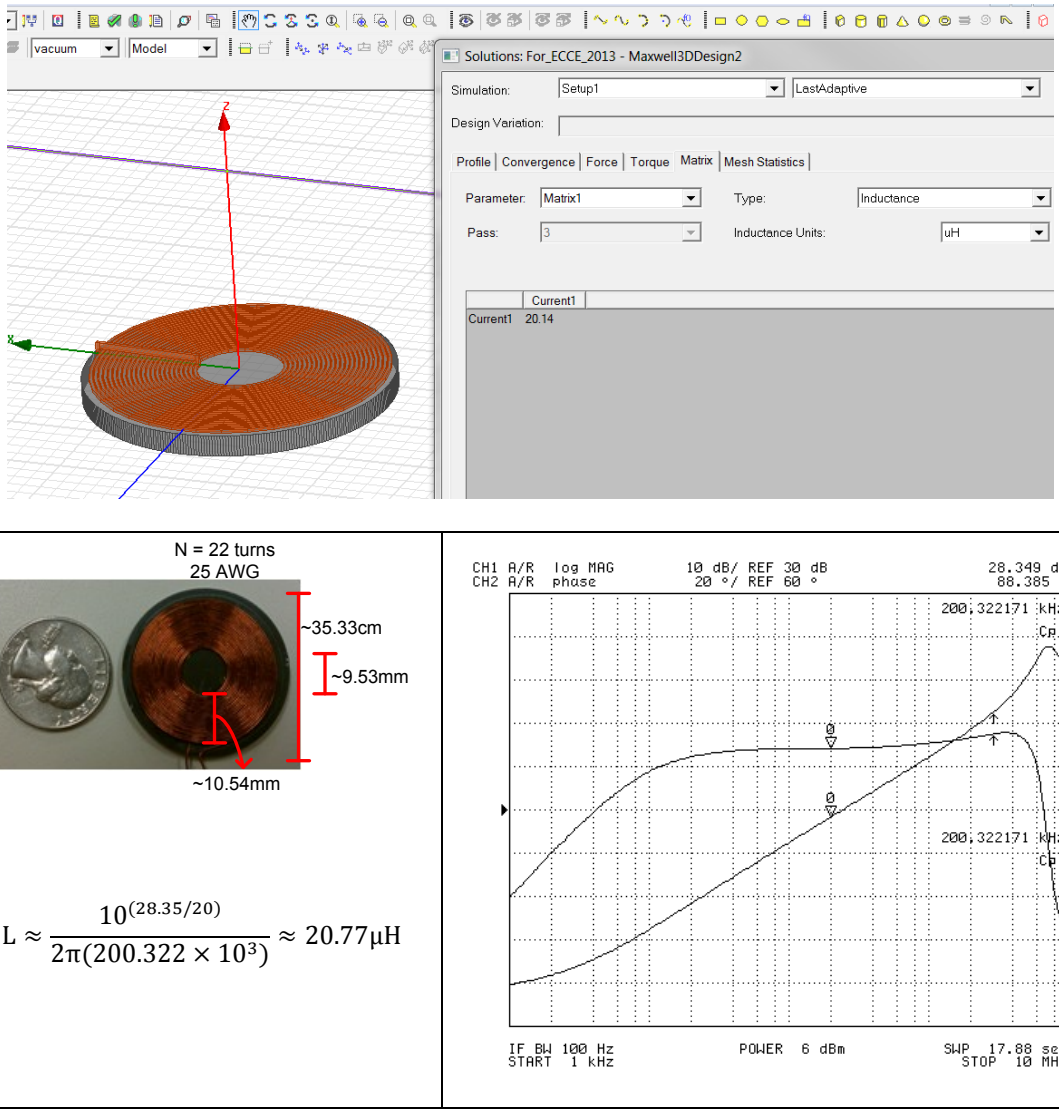

Figure 3.14: FES simulation and experimental characterization of a flat spiral inductor on a ferrite disk core.

Considering a case in which a designer has several coupler geometries under evaluation, their T-equivalent model parameters can be extracted along with k in FES. For example, let us consider two possible geometries in Figure 3.15. Both of the geometries shown have 6 winding turns. A symmetrical coupler with both sides containing either of these two geometries can be constructed. Two possible symmetrical coupler geometries, Geo A and Geo B, are shown in Figure 3.16.

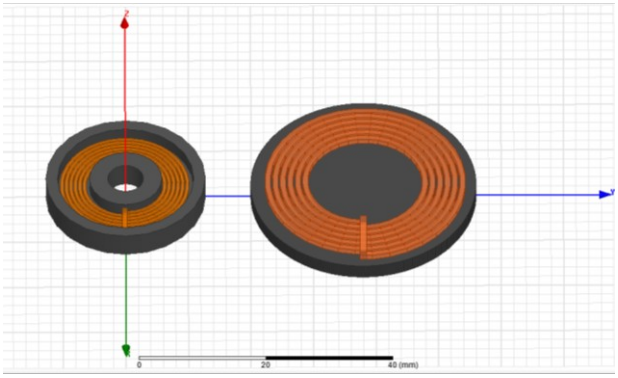

Figure 3.15: Two selected geometries for a coupler: ferrite pot core (left) and disk core (right).

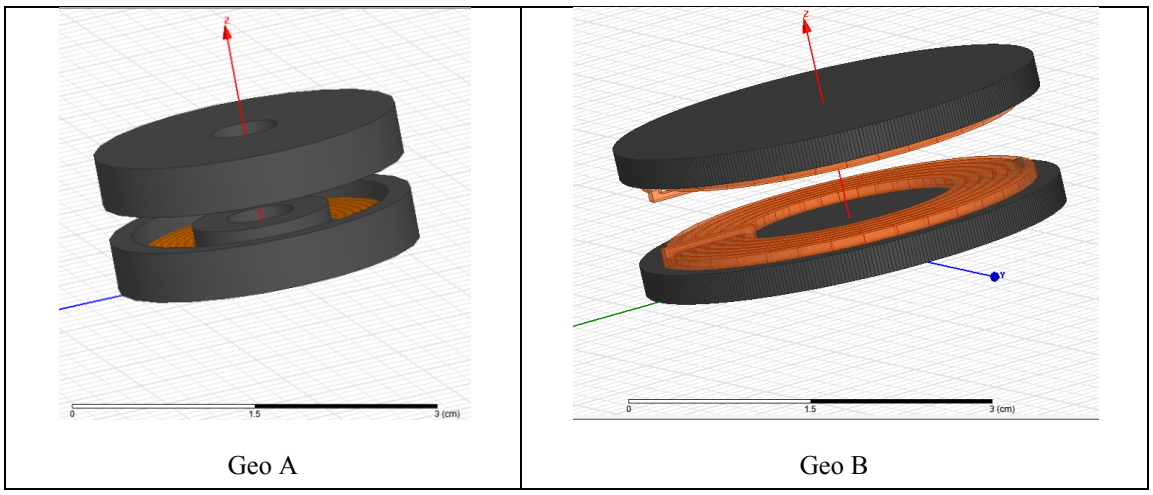

Geo A | Geo B

Figure 3.16: Two possible symmetrical coupler geometries, Geo A and Geo B.

Under the same condition of zero misalignment and 5 mm air gap between each coupler side, performing FES determines expected values of k for these two magnetic couplers. With maximum error tolerance set to 1 %, Geo A is simulated to extract the T-

equivalent model parameters (L_{S1}, L_{S2}', and L_m of Equation 1) in Figure 3.17 (a). In Figure 3.17 (b), coupling coefficient, $k = L_m/L_{S1} = L_m/L_{S2}$' for the symmetrical coupler, is extracted. According to Figure 3.17 (a), $L_{S1} \approx 2.7345$ µH and $L_{S2}' \approx 2.7248$ µH, generating $L_{S1} \approx L_{S2}'$ with *less* than 0.4 % error. The magnetizing inductance, L_m, is approximately 1.3628 µH. Thus, coupling coefficient $k = \frac{L_m}{\sqrt{L_{S1}L_{S2}'}}$ is approximately 0.499. This agrees with the *k* extraction in Figure 3.17 (b) as shown.

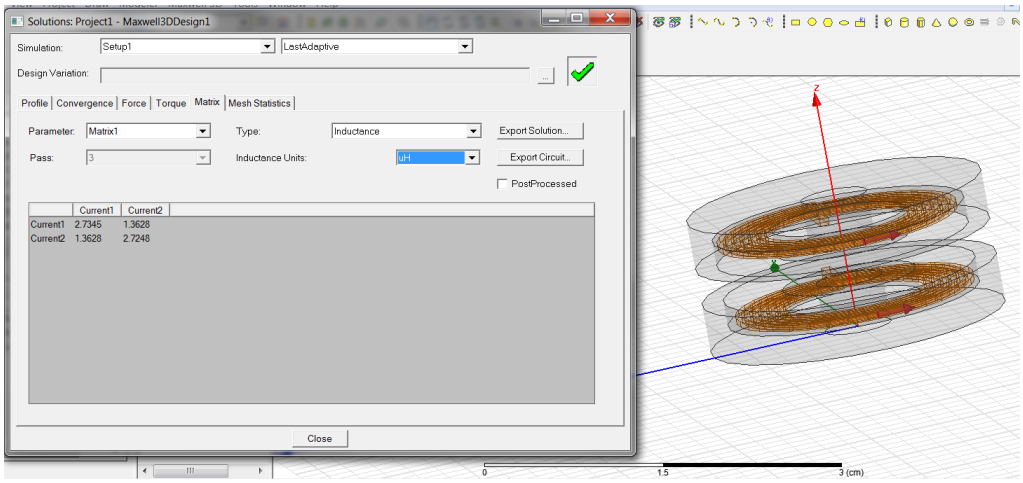

(a)

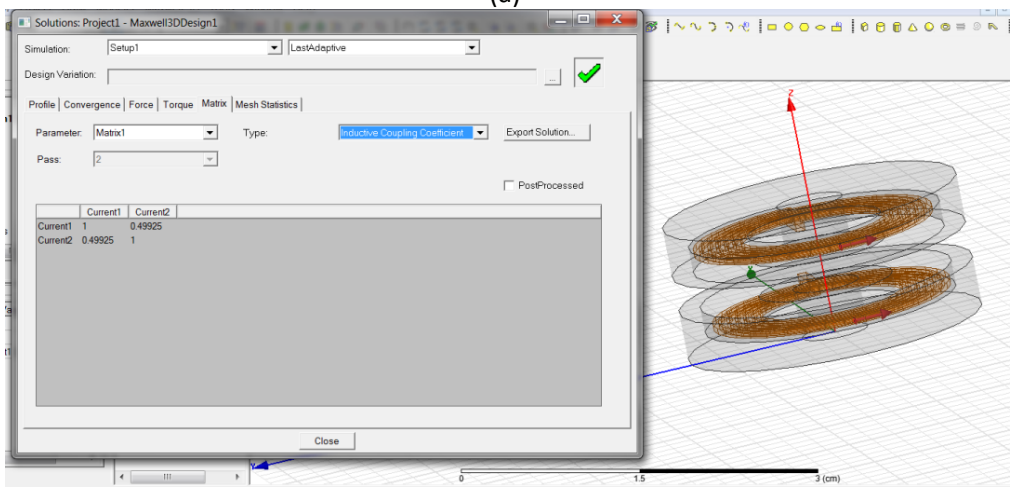

(b)

Figure 3.17: FES simulation of Geo A to extract its T-equivalent model parameters and *k*.

In Figure 3.18, FES simulations are performed for Geo B to extract the T-equivalent model parameters and *k*. Figure 3.18 (a) shows that $L_{S1} \approx 2.3604$ µH and $L_{S2}' \approx 2.3614$ µH, generating $L_{S1} \approx L_{S2}'$ with *less* than 0.05 % error. The magnetizing inductance L_m is approximately 1.2861 µH. Figure 3.18 (a) and Figure 3.18 (b) agree that the coupling coefficient, *k*, is approximately 0.545.

So in summary, Geo A has L_S: $L_{S1} \approx L_{S2}' \approx 2.73$ µH and $L_m \approx 1.36$ µH with $k \approx 0.50$. Geo B has L_S: $L_{S1} \approx L_{S2}' \approx 2.36$ µH and $L_m \approx 1.29$ µH with $k \approx 0.55$.

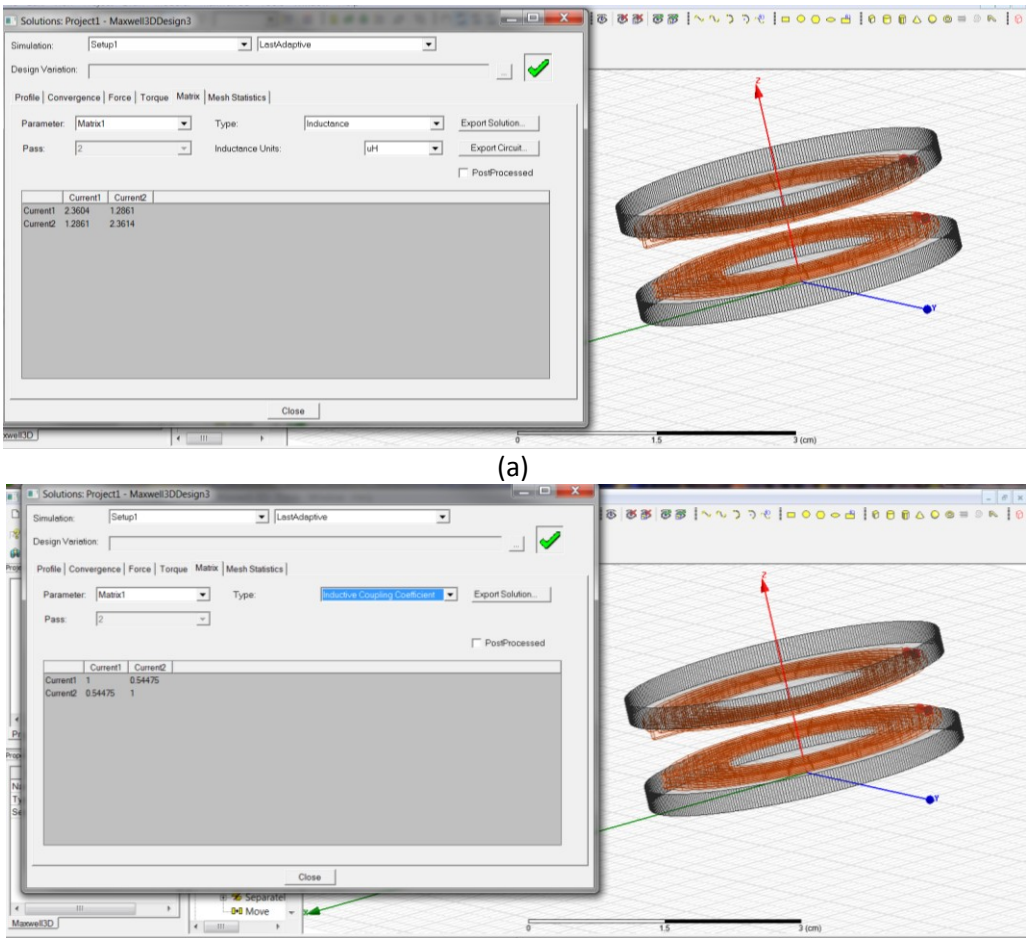

Figure 3.18: FES simulation of Geo B to extract its T-equivalent model parameters and *k*.

Based on evaluation of magnetic coupling (*k*) *alone*, Geo B would be selected since it demonstrates the better coupling. However, an optimal design calls for good robustness

in various quantities (e.g. $\|G_V(j\omega)\|$) and minimization of control complexity as well. It was shown that achieving the single voltage gain peak condition is desirable for maximization of robustness and minimization of control complexity, which can be better for maximizing efficiency and power density of an overall system.

Assuming that the wireless charging system's nominal output of 5V and 2A are desired, R_{load} = 2.5 Ω: the effective resistive load, R_e', is approximately $R_e' = R_{load}\frac{8}{\pi^2} \approx 2.026\ \Omega$. In order to achieve the single voltage gain peak condition, $\|G_V(j2\pi f_L)\|$ (Equation 32) has to be greater than or equal to 1.5. As mentioned previously, too high values of $\|G_V\|_{max}$ (Q) should be avoided so that coil-to-coil efficiency is not significantly decreased. Therefore, by choosing $\|G_V(j2\pi f_L)\| = 1.5$ as the design target and substituting it into Equation 32 along with each of the corresponding coupling coefficients, one finds that Geo A requires Q ≈ 1.061 while Geo B requires Q ≈ 1.112. Assuming that the desired operating frequency is 200 kHz, and substituting it into Equation 33, one finds that C ≈ 462.2 nF is needed for desirable leakage compensation in Geo A while C ≈ 591.8 nF is needed in Geo B.

For Geo A, substituting the resonant capacitance value, L_S, k and R_e' into the Q expression in Equation 32, one finds that the achievable Q, that can satisfy the desired R_e' condition and desired operating frequency condition, is Q ≈ 1.179. This is 11.12 % higher than Q ≈ 1.061.

For Geo B, performing the same procedures, one finds that Q ≈ 1.368, which is 23.02 % higher than the desired, Q ≈ 1.112.

At this point, a resonant tank designer has three choices to decrease the Q values as close as possible to be the desired values. One is to change the coupler geometries slightly (thus slightly increasing L_S values). Another is to decrease the resonant capacitance values slightly (thus slightly increasing the operating frequency above 200 kHz). The remaining choice is to do both these.

Without design modification and *also without* operating frequency adjustment, a SS resonant tank of SRT type employing Geo A is simulated in Pspice for its voltage gain, $||G_V(j\omega)||$, and circulating current gain, $||G_{iLm}(j\omega)||$. Also, a SS resonant tank of SRT type employing Geo B is simulated in Pspice for its $||G_V(j\omega)||$ and $||G_{iLm}(j\omega)||$. In Figure 3.19, the top two plots are obtained for the SS resonant tank of SRT type employing Geo A while the bottom two plots are obtained for that employing Geo B.

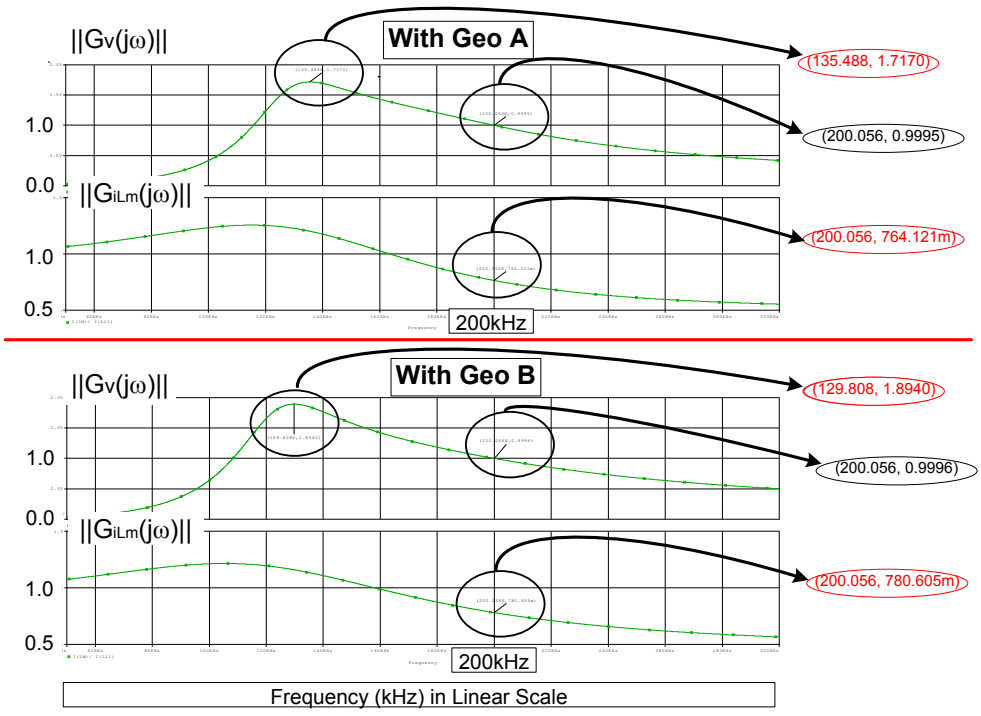

Figure 3.19: Voltage gain, $||G_V(j\omega)||$, and circulating current gain, $||G_{iLm}(j\omega)||$, for SS resonant tank of SRT type employing Geo A (top two plots) and Geo B (bottom two plots).

As can be seen from Figure 3.19, the desirable single voltage gain peak condition is achieved. The unity voltage gain is also obtained at f_O = 200 kHz as desired. The figures of merit (achieved values of $||G_V||_{max}$ and $||G_{iLm}(j2\pi f_O)||$) are highlighted in red.

For Geo A, $||G_V||_{max} \approx 1.717$, and $||G_{iLm}(j2\pi f_O)|| \approx 0.7641$. For Geo B, $||G_V||_{max} \approx 1.894$, and $||G_{iLm}(j2\pi f_O)|| \approx 0.7806$.

In conclusion, although Geo B provides the better magnetic coupling, Geo A is more desirable to obtain the single voltage gain peak condition with the smaller circulating current loss (smaller reactive energy). This is because *depending* on a desired value for R_e' and unity gain frequency, a coupler exhibiting higher L_S with lower k may be more desirable. It should be noted that design optimization may require evaluation on how much change in Q is needed to achieve the single voltage gain peak for a given R_e'. Based on this evaluation, a more desirable coupler can be constructed for specified values for R_e' and operating frequency. With the proposed design equations, this evaluation process is significantly shorter compared to the conventional design methods.

In order to show further usefulness of the presented design equations, Section 3.4.5 describes a step-by-step design process, and Section 3.5 provides simulation and experimental results for evaluating the performance of proposed design equations in calculating desired parameters of SS resonant tank of SRT type.

3.4.5 Step-by-Step Design Using The Design Equations

The step-by-step design procedure demonstrated in this section assumes that the following quantities are known or selected prior to design process.

- Output power and output voltage or current (thus, R_e' value is specified)
- Desired peak voltage gain, $||G_V||_{max}$, above 1.5 for a single voltage gain peak

- Desired unity gain frequency, f_O
- Expected coupling coefficient, k (or k_L) - Note: With a desired coupler geometry for desired ranges of distance and misalignment, a finite element simulation (FES) tool can be used to determine expected range of k.

1. Using Equation 32, determine Q that provides $\|G_V\|_{max}$ for a desired load, R_e', at an expected k.
2. With the Q value so calculated, determine the value of resonant capacitances using Equation 33.
3. Using f_O equation in Table 3.2, calculate the leakage inductances for achieving the desired unity gain frequency.
4. Using the expected value of coupling coefficient (either k or k_L), expected magnetizing inductance, L_m, is then determined.

The next section shows simulation validation of this step-by-step design process and simulation accuracy evaluation of the design equations. It also shows experimental results for validating the design equations.

3.5 Evaluation And Validation Of The Presented Design Equations

3.5.1 Simulation Evaluation

In this example for validation of design equation applicability, desired SS resonant tank specifications are listed in Table 3.3. The coupling coefficient, k, of 0.85 is chosen as a desired parameter.

TABLE 3.3 DESIRED LCLC RESONANT TANK CHARACTERISTICS

f_O (kHz)	R_e' (Ω)	Desired $\|G_V\|_{max}$ at R_e'	$k_L = L_m/L_e$	$k = L_m/(L_m+L_e)$
≈ 500	≈ 15	≈ 2.3	≈ 5.5	≈ 0.85

Following the proposed step-by-step design procedure,

1. Using Equation 32, determine Q necessary to meet the desired specifications:

Highest Resonant Voltage Gain Peak Desired at $R_e' = 15\Omega$:

$$\|G_V(j2\pi f_L)\| = Q\sqrt{1+\frac{1}{k_L}} = Q\sqrt{1+\frac{1}{5.5}} = 2.3$$

Therefore, $Q \approx 2.116$

2. Using Equation 33, determine capacitance for each of two capacitors in the SS resonant tank of SRT type:

$$C = \frac{Q\sqrt{k_L}}{2\pi f_O * R_e'} \approx \frac{2.116\sqrt{5.5}}{2\pi(500\times10^3)(15)} \approx 105.3\text{nF}$$

3. Determine leakage inductance for each side of coupler required for achieving unity voltage gain at f_S = 500 kHz:

$$L_e = \frac{1}{(2\pi f_O)^2 C} \approx \frac{1}{\left(2\pi(500\times10^3)\right)^2(105.3\times10^{-9})} \approx 0.9623\mu\text{H}$$

4. Determine magnetizing inductance based on desired $k \approx 0.85$ which corresponds to $k_L \approx 5.5$:

$$L_m = k_L L_e \approx 5.5(0.9623\mu\text{H}) \approx 5.2926\mu\text{H}$$

The calculated SS resonant tank parameters are simulated in PSpice to obtain the voltage gain plot in Figure 3.20. In order to represent the parameters calculated from the design equations as reasonably accurately as possible, the maximum of four decimal digits are used for the calculated resonant tank parameters. Figure 3.20 shows that $\|G_V\|_{max}$ achieved is approximately 2.35 which is *slightly* higher (*only* by about 2%) than the desired $\|G_V\|_{max}$ of 2.3. Also, the unity voltage gain is obtained at 500 kHz as expected.

This slight overachievement of $\|G_V\|_{max}$ is expected for the following reasons. Peak voltage gain $\|G_V\|_{max}$ is approximated by $\|G_V(j2\pi f_L)\|$, which is greater than or equal to1.5

under the condition of single voltage gain peak. This peak voltage gain estimation by $||G_V(j2\pi f_L)||$ is always less than actual $||G_V||_{max}$. The estimation error becomes however very small with increasing $||G_V(j2\pi f_L)||$ above 1.5. This is because $||G_V(j2\pi f_L)||$ approaches $||G_V||_{max}$ very rapidly (in an exponential-like manner) with increasing Q. In summary, if $||G_V(j2\pi f_L)||$ is used as $||G_V||_{max}$ approximation to determine required Q for a given R_e', the calculated value of Q is a slight overestimation of an actually-required value of Q required for achieving a desired value of $||G_V||_{max}$. As will be explained in detail later in this section, this slight overachievement of $||G_V||_{max}$ is very desirable in experimental implementation due to the fact that parasitic resistances reduce $||G_V||_{max}$.

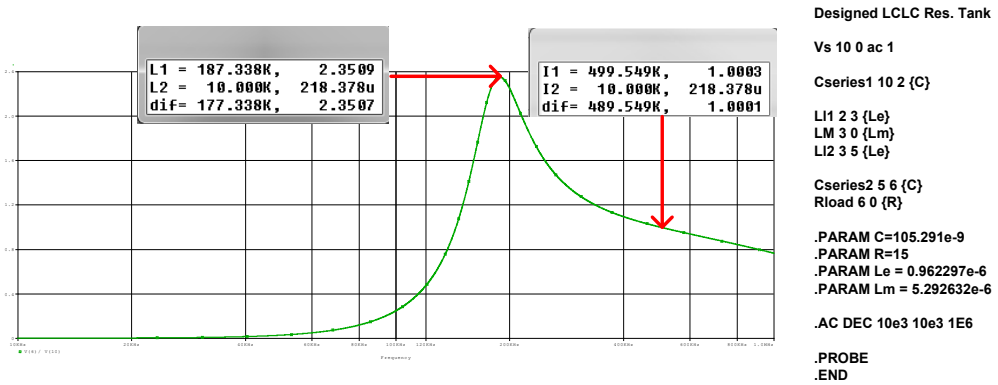

Figure 3.20: Simulated voltage gain plot of the SS resonant tank of SRT type whose parameters are calculated by the proposed step-by-step design procedure.

In Table 3.4, the proposed peak voltage gain equation, Equation 32, is compared with the peak voltage gain results from the parametric simulations. For obtaining the data listed in Table 3.4, the resonant tank parameters, C = 100nF, L_m = 40µH, and L_e = 10µH (therefore k = 0.8 and k_L = 4), are used under Q variation (imposed by changing R_e'). The reason for using $k = 0.8$ is that an experimentally constructed pot-core coupler in Figure 3.21 demonstrates $k \approx 0.8$ when the coil-to-coil is approximately 1.5 mm, 2x - 3x the thickness of a typical smart phone battery cover.

The results from the parametric simulations represent the accurate values that the proposed peak voltage equation aims to obtain. Plotting the data in Table 3.4 results in Figure 3.22. It can be seen from both Table 3.4 and Figure 3.22 that Equation 32 provides good approximation of $||G_V||_{max}$ for values above 1.5 as expected: Less than 5% error is exhibited for $||G_V||_{max} \approx 1.68$, and as expected, the percent error rapidly decreases as $||G_V||_{max}$ increases.

For a more thorough evaluation, the proposed step-by-step design method in section 3.4.3 is used to determine the SS resonant tank parameters for various sets of *k* from 0.1 to 0.95 and desired $||G_V||_{max}$ from 1.5 to 6. It is *arbitrarily* assumed for the resonant tank that the desired *fo* and output power are 300kHz and 1kW respectively while the desired output voltage is 100V, resulting in Re' of 10Ω. Simulations are used to validate the design procedure. The simulation data are listed in Table 3.5, and the percentage errors from this table are plotted in Figure 3.23.

Table 3.5 shows that the desired f_O = 300 kHz is obtained for all values of *k* and $||G_V||_{max}$. It can be seen from both Table 3.5 and Figure 3.23 that the % error between desired $||G_V||_{max}$ and achieved $||G_V||_{max}$ is still less than 9% for *all k* even in the case of $||G_V||_{max} = 1.5$, which is the lower limit value for the desired design space of single-peak condition: $||G_V||_{max} \geq 1.5$. The % error rapidly decreases with decreasing *k* or increasing $||G_V||_{max}$ (Q). Therefore, the proposed peak voltage gain equation performs *well* for the *entire* range of *k* when the desirable *well-defined* single voltage gain peak is obtained.

The small underestimation of $||G_V||_{max}$ by Equation 32 is desirable for experimental implementation. This is clear from the data in Table 3.5. For example, at $k = 0.95$, the peak gain, $||G_V||_{max}$, of 1.63 is obtained when a desired $||G_V||_{max}$ is 1.5. Therefore, when

Equation 33 is used in a design procedure, its small underestimation property results in achieving $||G_V||_{max}$ *slightly higher* than a desired value. Because of this, a safety margin is provided to compensate for the voltage gain decreasing effect caused by parasitic resistances.

TABLE 3.4 EVALUATION OF THE PROPOSED PEAK VOLTAGE GAIN EQUATION

Q	$\|\|G_V\|\|_{max}$ calculated using Equation 32	$\|\|G_V\|\|_{max}$ determined using parametric simulations	% error
1.5	1.677	1.758	4.6
2	2.236	2.285	2.1
2.5	2.795	2.829	1.2
3	3.354	3.381	0.80
3.5	3.913	3.93	0.43
4	4.472	4.489	0.38
5	5.590	5.605	0.27

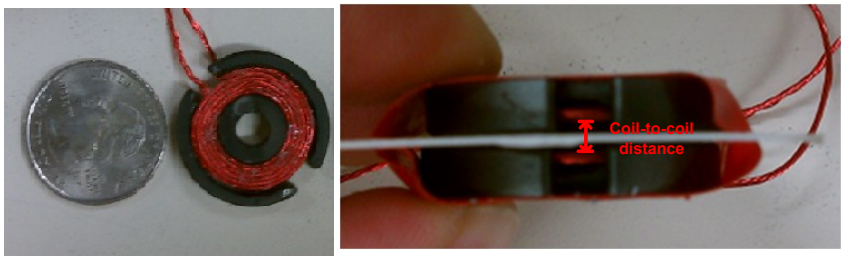

Figure 3.21: Coil-to-coil distance of pot core coupler.

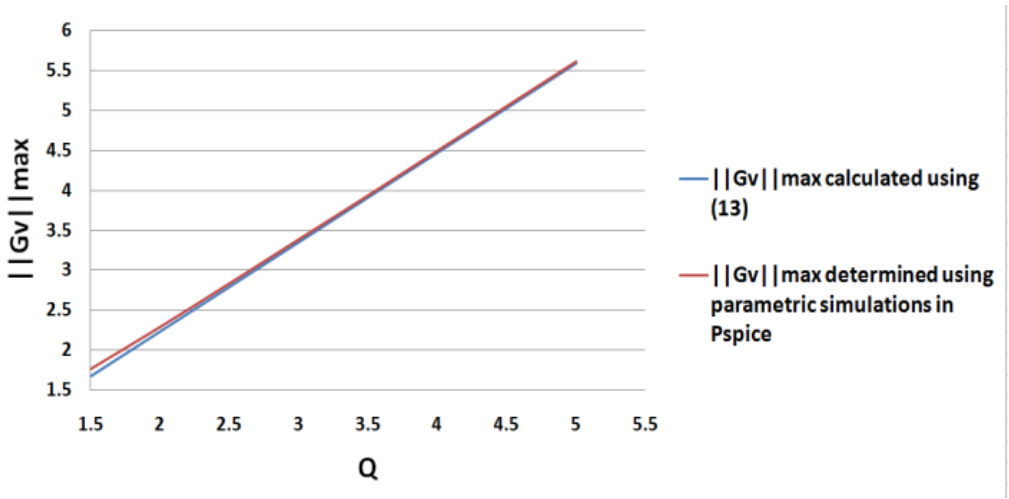

Figure 3.22: Comparison between $||G_V||_{max}$ calculated using Equation 32 and $||G_V||_{max}$ determined using parametric simulations.

TABLE 3.5 THE SS TOPOLOGY PARAMETERS CALCULATED FOR VARIOUS *K*'S TO ACHIEVE DESIRED $||G_V||_{MAX}$ USING THE PROPOSED DESIGN METHOD

k	kL	Desired ‖Gv‖max	fo	Re'	Q	C1 = C2'	Le1 = Le2'	Lm	Achieved ‖Gv‖max	Error (%)
0.95	19	1.5	300000	10	1.462	3.381E-07	8.325E-07	1.582E-05	1.63	8.67
0.8	4	1.5	300000	10	1.3416	1.424E-07	1.977E-06	7.908E-06	1.6081	7.21
0.7	2.33	1.5	300000	10	1.255	1.017E-07	2.767E-06	6.457E-06	1.5931	6.21
0.5	1	1.5	300000	10	1.0607	5.627E-08	5.002E-06	5.002E-06	1.5628	4.19
0.3	0.43	1.5	300000	10	0.8216	2.853E-08	9.864E-06	4.227E-06	1.5325	2.17
0.1	0.11	1.5	300000	10	0.4743	8.388E-09	3.355E-05	3.728E-06	1.506	0.40

k	kL	Desired ‖Gv‖max	fo	Re'	Q	C1 = C2'	Le1 = Le2'	Lm	Achieved ‖Gv‖max	Error (%)
0.95	19	2	300000	10	1.9494	4.508E-07	6.244E-07	1.186E-05	2.078	3.90
0.8	4	2	300000	10	1.7889	1.898E-07	1.483E-06	5.931E-06	2.0598	2.99
0.7	2.33	2	300000	10	1.6733	1.356E-07	2.076E-06	4.843E-06	2.0482	2.41
0.5	1	2	300000	10	1.4142	7.503E-08	3.751E-06	3.751E-06	2.0272	1.36
0.3	0.43	2	300000	10	1.0954	3.805E-08	7.398E-06	3.17E-06	2.0106	0.53
0.1	0.11	2	300000	10	0.6325	1.118E-08	2.516E-05	2.796E-06	2.0012	0.06

k	kL	Desired ‖Gv‖max	fo	Re'	Q	C1 = C2'	Le1 = Le2'	Lm	Achieved ‖Gv‖max	Error (%)
0.95	19	3	300000	10	2.924	6.762E-07	4.162E-07	7.908E-06	3.0434	1.45
0.8	4	3	300000	10	2.6833	2.847E-07	9.886E-07	3.954E-06	3.0317	1.06
0.7	2.33	3	300000	10	2.51	2.034E-07	1.384E-06	3.229E-06	3.0247	0.82
0.5	1	3	300000	10	2.1213	1.125E-07	2.501E-06	2.501E-06	3.013	0.43
0.3	0.43	3	300000	10	1.6432	5.707E-08	4.932E-06	2.114E-06	3.0048	0.16
0.1	0.11	3	300000	10	0.9487	1.678E-08	1.678E-05	1.864E-06	3.0005	0.02

k	kL	Desired ‖Gv‖max	fo	Re'	Q	C1 = C2'	Le1 = Le2'	Lm	Achieved ‖Gv‖max	Error (%)
0.95	19	4	300000	10	3.8987	9.016E-07	3.122E-07	5.931E-06	4.0306	0.76
0.8	4	4	300000	10	3.5777	3.796E-07	7.414E-07	2.966E-06	4.022	0.55
0.7	2.33	4	300000	10	3.3466	2.712E-07	1.038E-06	2.421E-06	4.017	0.43
0.5	1	4	300000	10	2.8284	1.501E-07	1.876E-06	1.876E-06	4.0088	0.22
0.3	0.43	4	300000	10	2.1909	7.609E-08	3.699E-06	1.585E-06	4.0032	0.08
0.1	0.11	4	300000	10	1.2649	2.237E-08	1.258E-05	1.398E-06	4.0003	0.01

k	kL	Desired ‖Gv‖max	fo	Re'	Q	C1 = C2'	Le1 = Le2'	Lm	Achieved ‖Gv‖max	Error (%)
0.95	19	5	300000	10	4.8734	1.127E-06	2.497E-07	4.745E-06	5.0238	0.48
0.8	4	5	300000	10	4.4721	4.745E-07	5.931E-07	2.373E-06	5.017	0.34
0.7	2.33	5	300000	10	4.1833	3.39E-07	8.302E-07	1.937E-06	5.0131	0.26
0.5	1	5	300000	10	3.5355	1.876E-07	1.501E-06	1.501E-06	5.0067	0.13
0.3	0.43	5	300000	10	2.7386	9.511E-08	2.959E-06	1.268E-06	5.0024	0.05
0.1	0.11	5	300000	10	1.5811	2.796E-08	1.007E-05	1.118E-06	5.0003	0.01

k	kL	Desired ‖Gv‖max	fo	Re'	Q	C1 = C2'	Le1 = Le2'	Lm	Achieved ‖Gv‖max	Error (%)
0.95	19	6	300000	10	5.8481	1.352E-06	2.081E-07	3.954E-06	6.0195	0.32
0.8	4	6	300000	10	5.3666	5.694E-07	4.943E-07	1.977E-06	6.0139	0.23
0.7	2.33	6	300000	10	5.02	4.068E-07	6.918E-07	1.614E-06	6.0107	0.18
0.5	1	6	300000	10	4.2426	2.251E-07	1.25E-06	1.25E-06	6.0055	0.09
0.3	0.43	6	300000	10	3.2863	1.141E-07	2.466E-06	1.057E-06	6.002	0.03
0.1	0.11	6	300000	10	1.8974	3.355E-08	8.388E-06	9.32E-07	6.0002	0.00

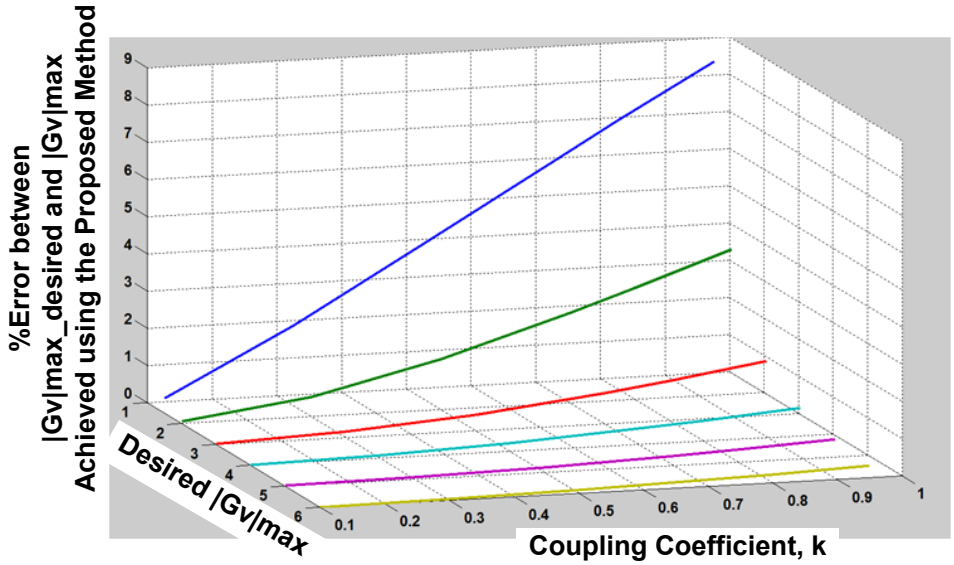

Figure 3.23: % error between desired $||G_V||_{max}$ and $|||G_V||_{max}$ achieved using the proposed design method for various combinations of k and desired $||G_V||_{max}$ (Q).

3.5.2 Experimental Evaluation

Using the evaluation board in Figure 2.1 and the symmetrical pot core coupler in Figure 3.21, experimental validation is performed in this section. The SS resonant tank parameters are extracted using Agilent 4395A Network Analyzer. From the parameter extraction, primary and secondary leakage inductances (L_e), magnetizing inductances (L_m), resonant capacitance (C), effective load resistance (R_e'), unity gain resonant frequency (f_O), and $||G_V||_{max}$ of the experimental setup are determined.

The proposed design method is then used to determine the SS resonant tank parameters that would provide the same $||G_V||_{max}$ and unity gain resonant frequency as the experimental setup under the same load condition - Note: The goal is to see if the proposed design method can produce the SS resonant tank parameters that match well the experimental parameters given that $||G_V||_{max}$ and unity gain resonant frequency (f_O) of the experimental setup are the design target condition.

The experimental SS topology set-up with $R_e' \approx 15\Omega$ exhibits the $\|G_V(j\omega)\|$ characteristics shown in Figure 3.24. The experimental SS topology setup exhibits $\|G_V\|_{max} \approx 2.25$ (7.03dB) at frequency $f_L \approx 200$ kHz, and unity gain frequency $f_O \approx 480$ kHz. The experimentally extracted parameters are listed in Table 3.6. Using the proposed design method, the resonant tank parameters are determined to achieve the same characteristics as the experimental setup: $\|G_V\|_{max} \approx 2.2$ and $f_O \approx 480$ kHz at $R_e' \approx 15\Omega$ and are *also* listed in Table 3.6. The results show that the proposed design method determines with good accuracy what the resonant tank parameters have to be in order to achieve the same characteristics as the experimental setup.

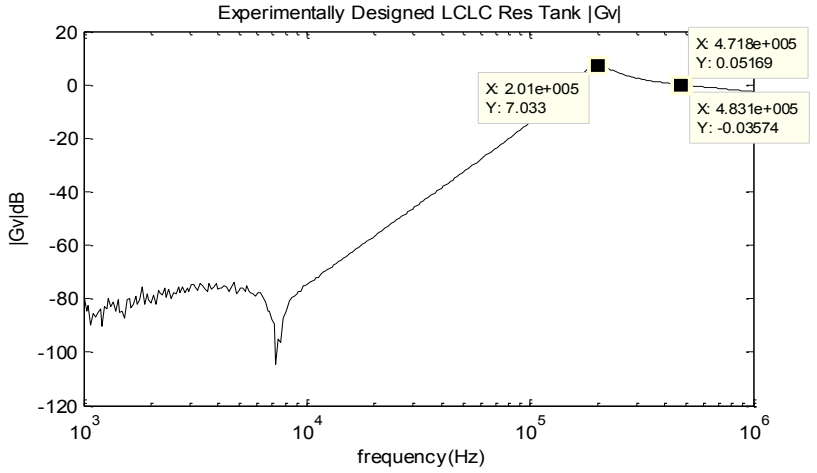

Figure 3.24: $\|G_V(j\omega)\|$ in dB of SS resonant tank of SRT type using Agilent 4395A Network Analyzer.

TABLE 3.6 EXPERIMENTAL PARAMETERS VS. PARAMETERS CALCULATED USING THE PROPOSED DESIGN METHOD

	k	**L_m (µH)**	**L_{e1} (µH)**	**L_{e2}' (µH)**	**C_1 (nF)**	**C_2' (nF)**
Experimentally Extracted SS Topology Parameters	0.844	5.745	0.993	1.137	101.6	100.7
SS Topology Parameters Calculated Using Proposed Method	0.844	5.724	1.058	1.058	103.9	103.9

3.6 CHAPTER SUMMARY

In this chapter, various resonant frequencies of interest are derived from the general voltage gain equation, $||G_V(j\omega)||$, and from the simplified voltage gain expression, $||G_V'(j\omega)||$, of the SS resonant tank topology. The important roles of these frequencies of interest are explained in detail.

Based on the evaluation results of the frequencies of interest, a peak voltage gain equation is proposed. The accuracy of this peak voltage gain equation is validated analytically by comparing with the results obtained from conventional parametric simulations. The comparison results show that the proposed peak voltage gain equation provides the advantage of more convenient design while exhibiting good approximation.

An example of design optimization process is explained. After using FES to determine expected values for *k* and T-equivalent model parameters, it is shown that the presented design equations allow comparative evaluations of various coupler geometries so that desirable resonant tank characteristics can be achieved with an appropriate coupler geometry for a desired value of R_e'. This process demonstrates that magnetic coupling (*k*) alone is not the figure of merit. In fact, it is important to evaluate different coupler geometries for their inductance values with specified values of operating frequency and load. It is shown that depending on operating frequency and load conditions, a coupler geometry with higher inductance values and slightly lower *k* can be more desirable in achieving the single voltage gain peak condition at the cost of lower *k*.

In conclusion, a convenient step-by-step design method for the SS resonant tank of SRT type is developed to allow rapid calculation of the resonant tank parameters with good accuracy and precision while avoiding the complexity and time-consuming tasks

that the conventional design methods require. The proposed design method is validated through simulation results and experimental results. Both simulation results and experimental results show that the proposed design method eliminates the disadvantages of existing design methods, which include the need for complex mathematical analysis in deriving analytical design solutions and/or the need for time-consuming simulations for understanding exact effects of k and Q on peak voltage gain. Evaluation of trade-offs in robustness and coil-to-coil efficiency further increases the usefulness of the presented novel design method. This is because the novel design method allows rapid and convenient calculation of the resonant tank parameters to be used in various time-domain simulations for quickly evaluating efficiency characteristics, feasible/achievable performance, and waveform characteristics.

CHAPTER 4

NOVEL UNITY GAIN FREQUENCY TRACKING (UGFT) CONTROL OF SERIES-SERIES (SS) RESONANT CONVERTER OF SRT TYPE TO IMPROVE EFFICIENCY AND RECEIVER POSITIONING FLEXIBILITY IN WIRELESS CHARGING OF PORTABLE ELECTRONICS

4.1 INTRODUCTION AND LITERATURE REVIEW

Conventional wireless charging systems contain various components, whose elimination would significantly reduce both complexity and cost of implementation. These components include additional converters and/or linear voltage regulators, and ASICs for digital communication between transmitter and receiver through the magnetic coupler using various components for high frequency modulation as in [23]. For example, according to the Qi standard [12], unidirectional back scatter digital communication from a receiver to a transmitter is performed via high frequency modulation of either resonant tank resistive load or resonant capacitance. Then, digital signal processing techniques are applied in the transmitter to demodulate the communication signal from the receiver. Furthermore, following [11]-[12] and [18], current commercial wireless chargers either employ arrays of transmitter coils to improve receiver positioning flexibility, and/or they employ visual/auditory feedback to guide the receiver positioning. In some cases, even physical limitations such as device holders are used to constrain the receiver positioning.

Minimizing the component count (including the number of coils) while improving the receiver positioning flexibility is highly desirable for reducing both analytical complexity

and cost of implementation. Also, it is important to maintain good power conversion efficiency as magnetic coupling varies due to receiver positioning variation.

In order to accomplish these goals, this chapter presents a novel unity gain frequency tracking (UGFT) control method that allows compensation of leakage inductances without communication between the transmitter and receiver as coupling variation occurs. The UGFT control method uses a resonant converter employing a series-series (SS) resonant tank with a symmetrical implementation of coupler. An example of such resonant converters is shown in Figure 4.1, which is the topology selected for the discussion and validation of the UGFT control method. For the sake of simpler discussion, magnetic coupler turns ratio of unity is used. This results in approximately identical values of primary and secondary leakage inductances (L_e: $L_{e1} \approx L_{e2}$'), and consequently results in approximately identical compensating series capacitors (C: $C_1 \approx C_2$').

It will be shown that the SS resonant converter needs to be designed properly to meet various criteria that guarantee several desirable features, so that the novel UGFT control method can be successfully implemented. As mentioned in Chapter 3, although the SS resonant tank topology is analyzed in the literature, e.g. [11] and [24], detailed discussion of frequency-domain characteristics of the topology is lacking. Therefore this chapter explains frequency-domain characteristics that are pertinent to the UGFT control method. This provides a good foundation for design optimization and for realizing the UGFT control method. Various design criteria for the control method are described. Throughout the analysis and discussion, illustrative simulation results are provided.

Finally, SS resonant converters of SRT type are designed following the criteria in both simulation and experiment. In this chapter, simulation and experimental results are reported to validate UGFT control method.

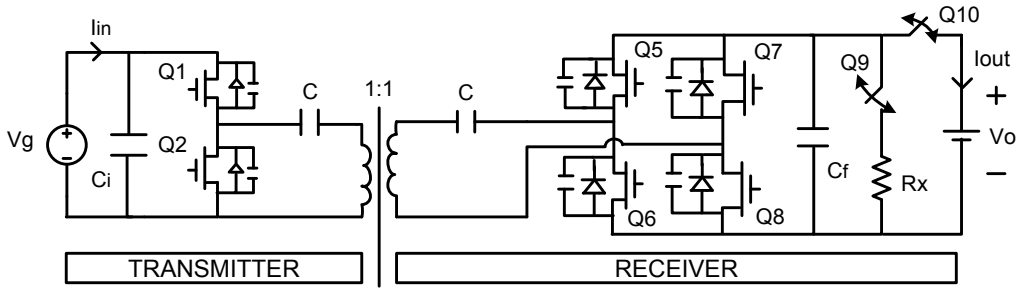

Figure 4.1: Series-series (SS) resonant converter topology for UGFT control method.

4.2 Characteristics of Series-Series (SS) Resonant Converter

As previously demonstrated, the main challenge in the design and control of the resonant converter is to ensure robust and efficient operation under effective load (R_e') variation and coupling coefficient (k) variation. The variation in R_e' is caused by changes in the battery state of charge (SoC) and the desired charging current. The k variation is caused by receiver coil (Rx) position changes with respect to transmitter coil (Tx) position.

The effects of these changes can be studied using the simplified model of Figure 4.2, so that the resonant tank can be appropriately designed to ensure robust and efficient operation. Figure 4.2 (a) shows a simplified model of the resonant converter in Figure 4.1, which is the SS resonant tank equivalent model shown previously but with the indication of several quantities to be discussed in this chapter. Resistance Rs in Figure 4.2 (b) represents the total parasitic resistance terms, and Zs represents a very small impedance introduced by a slight error in unity gain frequency tracking.

In this section, detailed frequency-domain analysis of this model is performed to provide various design criteria for achieving several notable characteristics, which play a crucial role in making the proposed control method simple and effective.

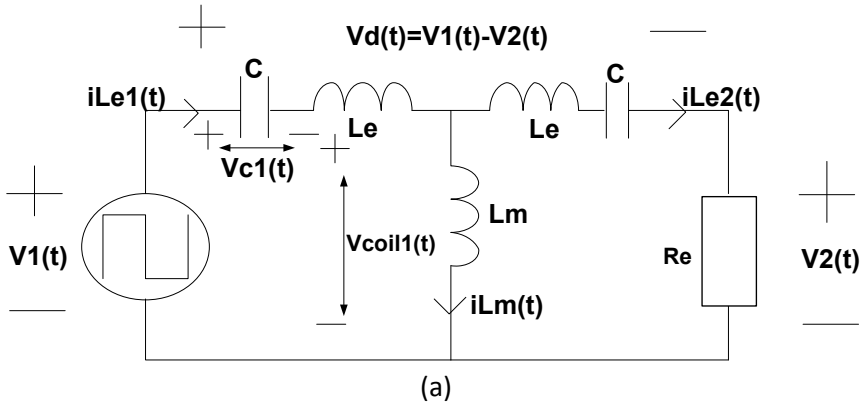

(a)

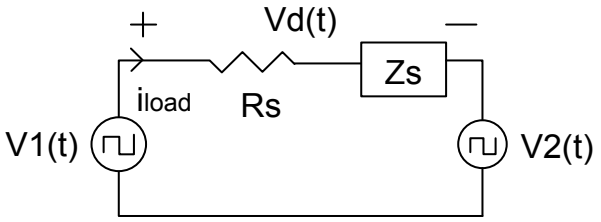

$$V1(t) \approx V_g \operatorname{sgn}(\sin(2\pi f_O))$$
$$V2(t) \approx V_o \operatorname{sgn}(\sin(2\pi f_O))$$

(b)

Figure 4.2: Simplified model of the symmetrical SS resonant converter (a) and its equivalent model when $f_S \approx f_O$ (b).

4.2.1 Frequency-domain Characteristics of SS Resonant Tank with Effective Resistive Load

From Figure 3.12 and Figure 3.13, it was concluded that a well-defined single peak behavior can be obtained for $\|G_V(j2\pi f_L)\| \geq 1.5$ (implying $\|G_V\|_{max} > 1.5$). It was shown that this condition provides the following *desirable* features:

1. The frequency of highest efficiency (f_O) is placed above resonance in the zero voltage switching (ZVS) region.
2. As can be seen from Figure 3.12, the peak output current level is located near f_L while the peak efficiency is at f_O, when $\|G_V\|_{max} > 1.5$, whereas both

the output current level and efficiency are maximum at f_O when $|G_V|_{max}$ = 1.0.

3. Because of 2, a large range of frequencies in ZVS region is obtained when $||G_V||_{max} > 1.5$ and can be used for controlling the charging current via switching frequency (f_S) modulation.

4. Voltage gain sensitivity to small switching frequency tracking error is minimized.

5. Under k variation, the danger of falling into the below-resonance region is avoided so that operation in ZVS region can be maintained for all k.

6. Voltage gain characteristics become very robust against both k and load (Q) variations.

7. Deriving an accurate linear model around f_O for load voltage control becomes *simplified*. As shown previously, the voltage gain as a function of frequency varies in an approximately *linear* fashion around f_O as a function of R_e' (Figure 3.12) and as a function of k (Figure 3.13(a)).

To describe several *general* criteria for deriving a linear output voltage control model, Figure 4.3 shows the voltage gain curve of the SS resonant tank for two different cases: Figure 4.3 (a) is plotted for k = 0.2, whereas Figure 4.3 (b) is plotted for k = 0.5. To increase both the accuracy of linear control model and range of controllable frequency range *near* f_O, selecting too high a value for $||Gv(j\omega)||_{max}$ should be avoided while selecting f_O to be as high as practical, so that both Δfx and Δfy, which are proportional to frequency f_O, consequently increase. Selecting high f_O is desirable also for minimizing the reactive loss caused by circulating current through L_m, because the impedance of L_m increases with increasing f_O, thus decreasing the current through it. As k *decreases,* $||G_V(j\omega)||_{max}$ *increases* whereas Δfx *decreases*. Therefore, it is *unlikely* that a *single* linear load voltage control model be applicable to a very *wide* range of k. To tolerate a wide

range of k variation, multiple linear load voltage control models are needed with each model applicable to a bounded range of k.

There are a few Li-ion battery charging characteristics that need to be taken into account in developing the UGFT control method. Thus, a brief summary of Li-ion battery characteristics is provided in the next section.

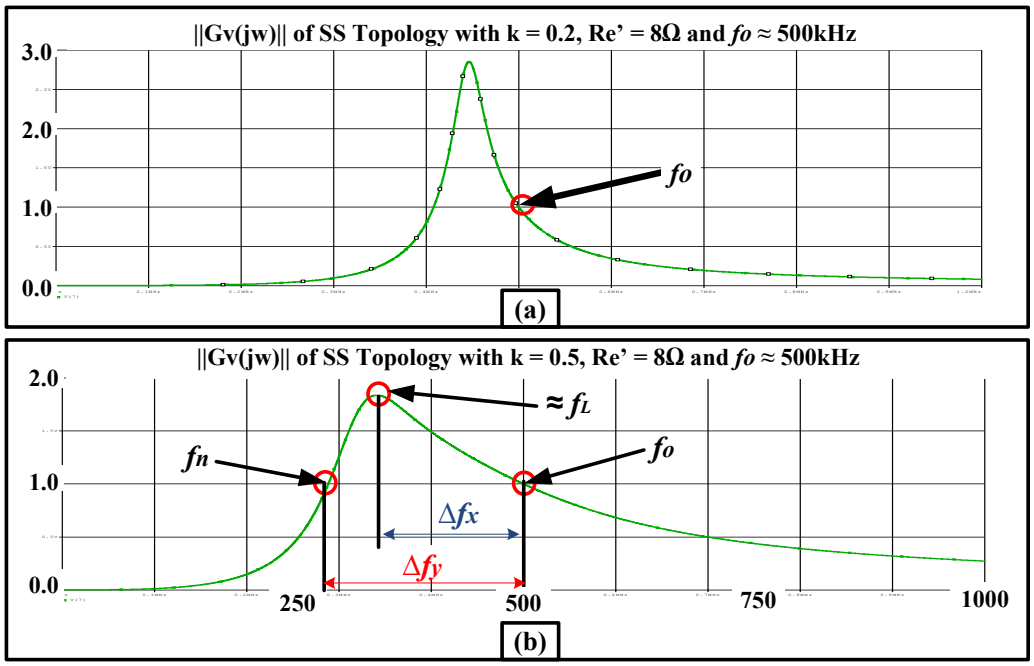

(a) and (b) in the Same Frequency (kHz) in *Linear* Scale:

Figure 4.3: Effects of Q selection on voltage gain control model derivation.

4.2.2 Brief Summary of Li-ion Battery Characteristics

Figure 4.4 (a) shows the simulation results of the discharge characteristic of a 7.2 V 2 Ah Li-ion battery for the nominal discharge current (top) and for various discharge currents (bottom). Figure 4.4 (b) shows experimental data for 0.3A constant current discharge of a 7.4 V 1.6 Ah Li-ion battery. The voltage versus SoC characteristic of Li-ion batteries exhibits very *small* variations, $\left|\frac{\partial(V)}{\partial(SoC)}\right| \approx 0.5\,V$, approximately for 15 % ≤ SoC ≤ 90 %. Therefore, if the voltage gain characteristic of a SS resonant tank are robust

against f_S error and against variations in k and Q, a device-specific coupler can be implemented to match the coupler output voltage to the battery voltage by using the coupler turns ratio rather than continuously using an additional converter and/or voltage regulator.

Although high current charging can quickly charge a battery to about 70% SoC, increasing the charge current does not significantly speed up the charging process beyond that point [25]. Therefore, fast charging at higher charging currents should be avoided when SoC > 70 %. In the consumer market, maximum battery run-time is generally preferred although this comes at the cost of short battery life.

Accounting for these Li-ion battery characteristics, the proposed control method provides the nominal charging current level between 0.5 C to 1 C with optional higher current charging via switching frequency modulation in the range of 15 % ≤ SoC ≤ 90 % - Note: Li-ion battery voltage is almost constant in this SoC range. Furthermore, the proposed control method considers a charging level above 90 % SoC for a Li-ion battery load that has a standard built-in over-charge and over-discharge protection circuitry.

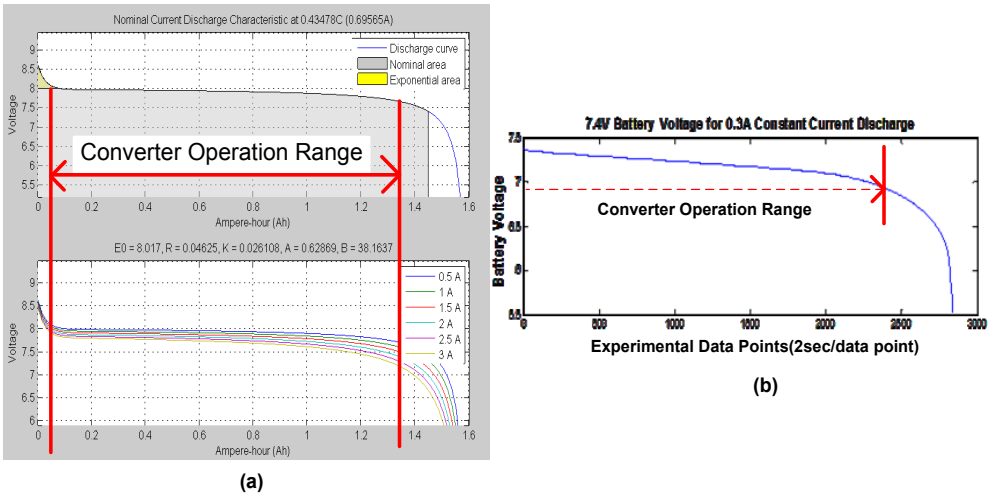

Figure 4.4: Simulation results (a) and experimental results (b) of Li-ion battery characteristics.

4.2.3 SS Resonant Converter with Li-ion Battery Load

Chapter 3 and Section 4.2.1 described the desirable features provided by a voltage gain curve exhibiting a single resonant peak with a load resistor. This section explains how to achieve these desirable features when using a Li-ion battery load. Various important characteristics of a SS resonant converter having a battery load are also explained in this section.

As supported by Figure 4.4, Li-ion batteries are less complex to model compared to other batteries [27] due to their small voltage variations in the nominal operating range. A nominal value of R_e' can be determined for nominal voltage rating and nominal charging current rating of a Li-ion battery. This is because, during most of SoC curve, battery load voltage and load current are fairly constant (under conventional CC-CV charging) as can be seen in [25]–[26]. However still, when a Li-ion battery load is used rather than a load resistor, the frequency-domain modeling of the SS resonant tank becomes more complex: the resonant characteristics depend strongly on how the input voltage V1 is matched with the load battery voltage V2 and also depend on parasitic elements such as coupler winding resistance and ESRs - See Figure 4.2.

The SS resonant converter with a Li-ion battery load is simulated in Simulink under three different input-to-output voltage matching conditions: Case A for supply voltage (V1) > load battery's fully-charged voltage rating ($V2_{FULL}$); Case B for V1 = $V2_{FULL}$; Case C for V1 < $V2_{FULL}$. The battery load is a 7V 2Ah Li-ion battery with a 50% SoC having the parameters listed in Table 4.1. Table 4.2 lists the SS resonant tank parameters used in the Simulink simulations. It will be shown that Case C is preferable.

Efficiency, load current, and voltage gain data are collected from Simulink simulations at various switching frequencies f_S. In order to evaluate the sensitivity of these quantities against parasitic resistance terms, the total parasitic resistance of 80 mΩ (40 mΩ on each side of coupler) is first added and then omitted in the SS resonant tank.

For Case A, Figure 4.5 (a) shows the efficiency and voltage gain while Figure 4.5 (b) shows the battery charging current. For Case B, Figure 4.5 (c) shows the efficiency and voltage gain while Figure 4.5 (d) shows the battery charging current.

In Case A and Case B, the highest voltage gain of the resonant tank cannot be above unity, and consequently the maximum load current occurs at $f_S \approx f_O$. Ideally, the maximum efficiency should also occur at f_O. However in reality, due to a high current caused by a voltage difference ($V_d(t)$ indicated in Figure 4.2) across the small parasitic resistance, the loading effects cause the frequency of maximum efficiency to become very sensitive to parasitic resistances and to be different from f_O. Therefore, cases A and B are *not* desirable and will *not* be considered further. This also indicates that phase shift control in [28]–[30] and duty cycle modulation technique in [30] are *not* desirable, because they cause a large voltage drop across small parasitic resistance terms when $f_S = f_O$. Instead, charging current control via switching frequency (f_S) modulation is desirable.

In order to achieve the advantageous characteristics demonstrated in Figure 3.12 and Figure 3.13 for the voltage gain curves with only a single resonant peak, $V1 < V2_{FULL}$ (Case C) needs to be obtained. However choosing V1 to be too small requires f_S to be decreased significantly in order to provide a large enough voltage gain for reasonably fast charging. A significant decrease in f_S is undesirable, because the converter operation is forced to move far away from the peak efficiency operating point at frequency f_O.

Therefore, for a reasonable choice of V1 under the coupler turns ratio of unity and symmetrical implementation of coupler, V1 is selected by using Equation 34. This results in voltage matching that takes into account the overall voltage drop across the total parasitic resistance (R_{lumped}) when the charging current of 0.5C is flowing.

The total parasitic resistance (R_{lumped}) from the SS resonant converter's input terminal to the output terminal in the simulation is approximately 120 mΩ, thus V1 ≈ 7.7V is calculated using Equation 34 and applied in simulation. By matching the voltages using Equation 34, the *desirable* features of the voltage gain curve having a single resonant peak can be achieved *also* with a battery load. This is demonstrated by the frequency-dependent efficiency and voltage gain curves in Figure 4.6 (a), and load current curves in Figure 4.6 (b).

The characteristics shown in Figure 4.6 exhibit a number of desirable features: the voltage gain characteristic is monotonically decreasing around frequency f_O, maximum efficiency is obtained at the unity gain frequency and is less sensitive to the parasitic resistance terms, and charging current can be varied over a wide range with a small variation of switching frequency, f_S, without a significant loss of efficiency. Furthermore, a large decrease in f_S is *not* required to increase the charging current to a desirable level for a faster charging option.

Since, in the SS resonant converter, *both* the input of the resonant tank and the load are voltage driven around the resonant frequency, *both* the input current and output current decrease *naturally* as a battery load is being charged (as the battery load's voltage increases). To demonstrate this, various waveforms of the SS resonant converter are shown in Figure 4.7 at the SoC of 20% (a), 50% (b), 80% (c), and 97% (d). The SS

resonant converter is operating at $f_S \approx f_O$ = 200 kHz. Both the supply current (Iin(t)) and charging current (Iout(t)) levels stay in the appropriate range of 0.5C to 1C level throughout the charging process and decrease naturally to become appropriately small when SoC ≈ 97% as in Figure 4.7 (d). For the case of the load battery with SoC ≈ 97%, the equivalent model for the SS resonant tank is also shown in Figure 4.7 (d). Therefore, at $f_S \approx f_O$, the primary-side current, $i_{Le1}(t)$, is approximately equal to the triangular waveform of magnetizing current, $i_{Lm}(t)$. This is because the square wave input voltage, V1(t), is applied across the magnetizing inductance, L_m. It should be noted that $i_{Le1}(t)$ lags V1(t) by π/2 at $f_S \approx f_O$ when the load battery is fully charged, as shown by Figure 4.7 (d). This information along with the low input current can be used as a threshold point to terminate the charging process.

TABLE 4.1 LI-ION BATTERY MODEL PARAMETERS USED IN SIMULATION

Nominal Voltage (V)	7
Rated Capacity (Ah)	2
Maximum Capacity (Ah)	2
Fully-charged Voltage (V)	8.15
Nominal Discharge Current (A)	0.87
Internal Resistance (Ω)	0.035
Capacity at Nominal Voltage (Ah)	1.8

TABLE 4.2 SS RESONANT TANK PARAMETERS USED IN SIMULATION

Unity Gain Frequency, f_{nom}, when *k* is the Highest in an Allowed Variation Range (kHz)	200
Highest Coupling Coefficient, k	0.85
Resonant Capacitors [μF]	2.146
Leakage Inductances, ($L_{e1} = L_{e2}$) [nH]	295.1
Magnetizing Inductance, L_m [μH]	1.623
Winding Resistance Each Side of Coupler [mΩ]	40
Effective Load (R_e') in Simulation [Ω]	5

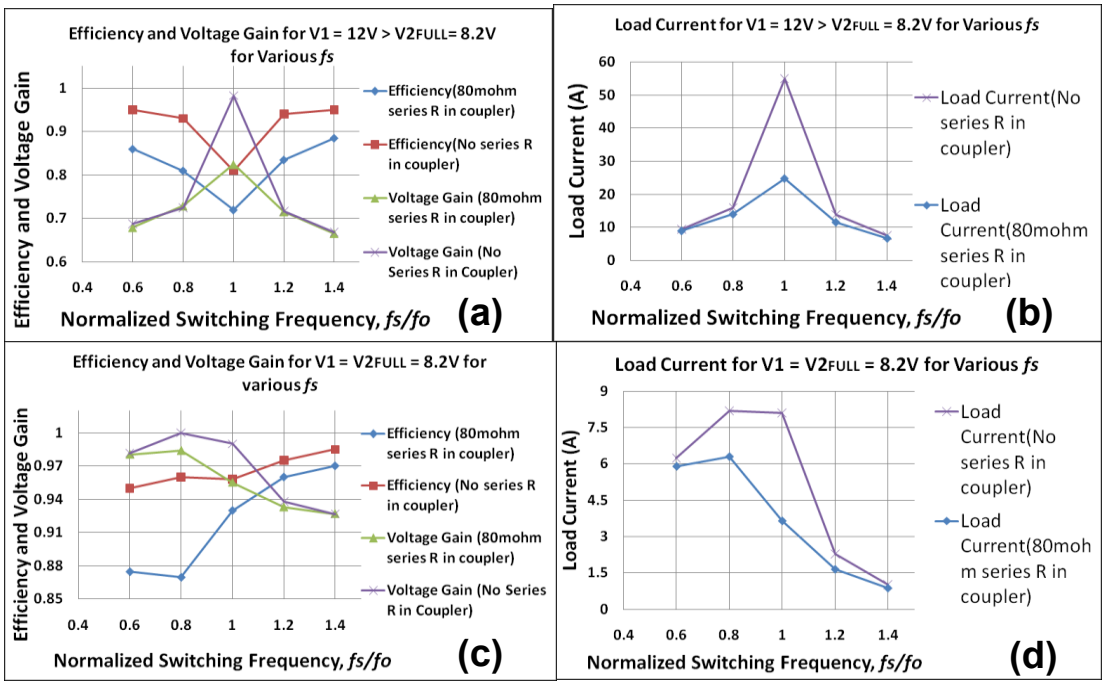

Figure 4.5: Efficiency, load current, and voltage gain (V2/V1) data collected at various Switching frequencies (f_S) with SoC = 50% for Case A (a and b) and Case B (c and d).

$$V1 = I(0.5C) * R_{lumped} + \frac{(V2(full) + V2(nom))}{2} \quad \text{..... Equation (34)}$$

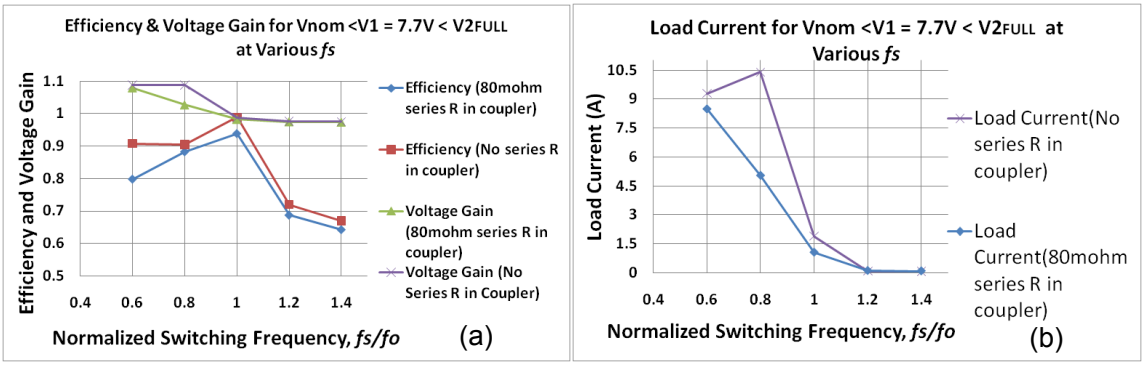

Figure 4.6: Simulink simulation data for efficiency and voltage gain (a), and load current (b) collected at various switching frequency (f_S) with SoC = 50% for Case C.

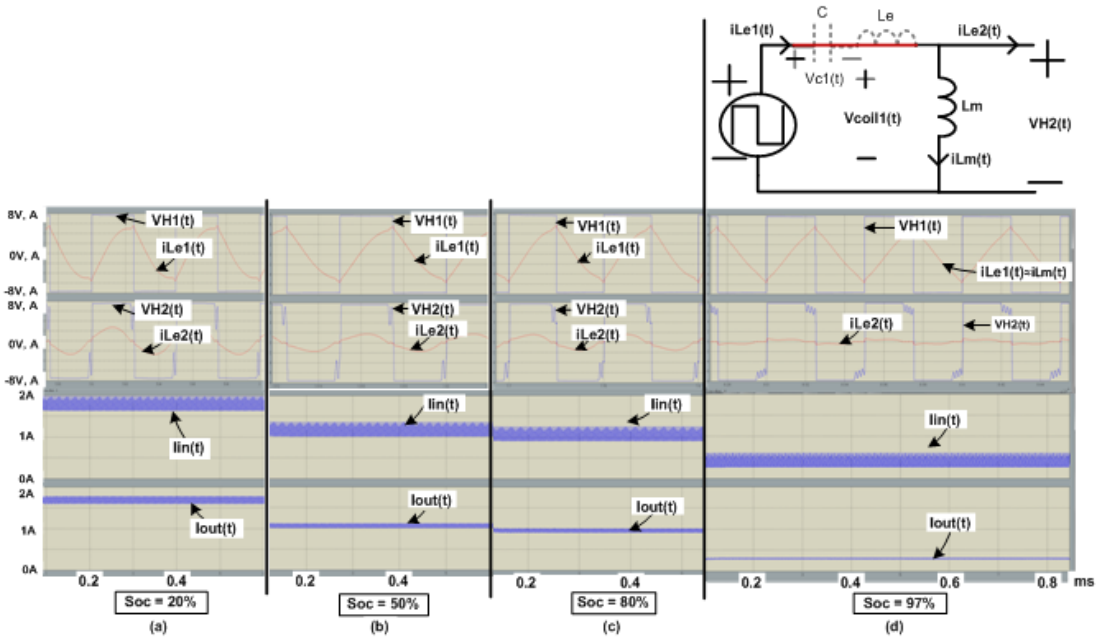

Figure 4.7: Various resonant tank waveforms and input and output currents at different SoC. (Note: Red line in the model represents the impedance compensation occurring at $fs \approx fo$).

In summary, the voltage matching by using Equation 35 provides the desirable features obtained when the single resonant voltage gain peak behavior is obtained. With the proper voltage matching ratio, *most* of the charging process can occur at the frequency of highest efficiency (f_O) *without* actively moving away from this frequency. This is further supported by the fact that the need for a control method to decrease the charging current is minimized due to the *natural* decrease in the charging current level as the load battery is being charged. Therefore, *continuous* use of an additional voltage regulator and/or converter throughout the entire charging process can be avoided. In conclusion, a control scheme is required that can track and ensure unity gain frequency (f_O) operation with good accuracy and precision. This is discussed in the next section.

4.3 Novel Unity Gain Frequency Tracking (UGFT) Control Method

By using the desirable features explained in the previous sections, it is possible to track and achieve the unity gain frequency (f_O) operation under allowed k variation *without* any communication between the transmitter and receiver. In this section, the development of UGFT control method is described, the control process is explained, and simulation and experimental results are reported to validate the UGFT control.

4.3.1 Description of the Proposed Operation Process

Prior to explaining the derivation of linear UGFT control equation, this section explains the operation of the proposed receiver topology in Figure 4.8. The proposed operation of the receiver and its interaction with the transmitter are described as follows:

1. The receiver is placed in proximity of the transmitter with Q5-Q8 and with Q10 turned-off while Q9 is turned-on thus introducing a known fixed resistive load, R_X, into the SS resonant tank.
2. The transmitter, which periodically sends a very short pulse ("ping"), recognizes the receiver placement by the supply current change and performs the tracking procedure described below to track the unity gain frequency (f_O). This tracking procedure is based on a linearized UGFT model for the resonant tank under the well-defined loading condition due to the dummy load, R_X - Note: The unity gain frequency f_O is load independent.
3. When f_O is tracked, the receiver understands this by measuring $V_x(t) \approx \frac{V_g}{2}$ for a half-bridge switch network in the transmitter or $V_x(t) \approx V_g$ for a full-bridge switch network in the transmitter.
4. The receiver then turns off Q9 and turns on Q10 to charge the load Li-ion battery at $f_S \approx f_O$. This unity gain frequency operation continues until a significant change in the charging occurs, for example if the charging

current either changes suddenly or becomes very low. A sudden large change in the charging current may indicate a sudden movement of the receiver with respect to the transmitter. A very low current indicates the fully-charged load state or complete decoupling.

5. If a significant change is detected, the charging stops, Q9 is turned on, Q10 is turned off and the tracking procedure is performed again. If the transmitter cannot track the unity gain frequency f_O within a known frequency range, it means that the receiver has moved too far away from the transmitter.

In summary, Q9 and Q10 are *never* turned on *simultaneously* and do *not* perform switching transitions *frequently* throughout the charging process. In fact, they are intended to make switching transitions *only* under the following conditions: the charging current changes rapidly by a large amount; the charging current is very low due to the fully-charged battery state or complete decoupling. Therefore, the losses due to Q9 and Q10 would be significantly lower than the losses caused by using a linear voltage regulator *continuously* or using a converter *frequently* to adjust the voltage matching under a non-unity gain operation. Since switching occurs infrequently, switching losses are small. The overall operation process including the UGFT control process can be summarized by the block diagram in Figure 4.9.

Therefore, the main purpose of Q9 and Q10 is to introduce a known fixed load (R_X) into the SS resonant tank during UGFT process. Introducing R_X achieves various advantages. One of two main advantages is that UGFT can be performed with a good precision and accuracy, consequently simplifying the control model. The other is that it improves the robustness of overall control process against the resonant tank parameter variations.

As explained in Chapter 3, the desirable single voltage gain peak condition can be achieved with a fairly large value of R_X. This means that losses in the Q9-R_X branch during unity gain tracking operation can be fairly low. The criteria on selecting R_X for the proposed UGFT control method are explained in the next section - Note: Since the unity gain frequency is load independent, it is not affected by the battery load being different from the fixed load Rx used to track the unity gain condition.

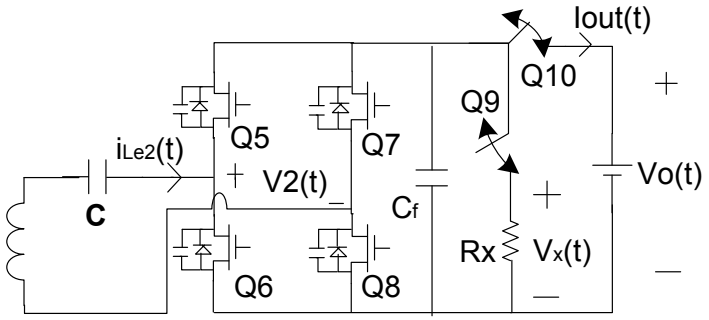

Figure 4.8: Proposed receiver topology.

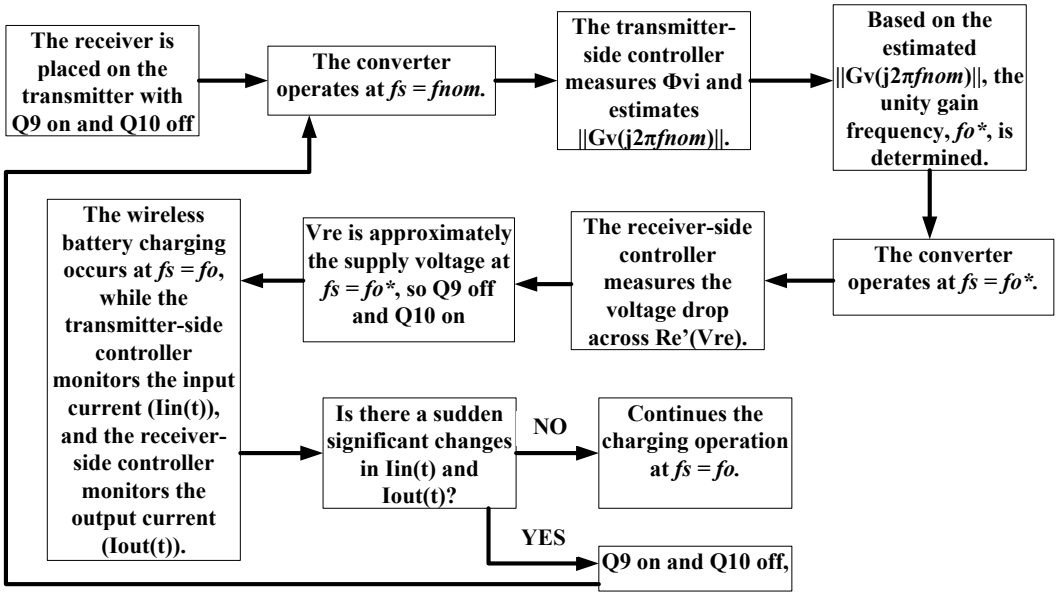

Figure 4.9: Proposed operation process employing UGFT.

4.3.2 Criteria for Selection of R_X

In Chapter 3, the approximation for a peak voltage gain of a SS resonant tank having a symmetrical coupler implementation is expressed as Equation 32. When using this equation to obtain $||G_V||_{max}$ that is appropriate for deriving a UGFT control model, the following points need to be considered:

1. Obtaining too high a value of $||G_V||_{max}$ leads to the requirement of deriving a linear output voltage control model at frequencies very far above f_O due to *non-linear* behavior around *fo.* Therefore, it should be avoided.
2. Deriving a linear voltage gain control model in the *vicinity* of f_O is required for obtaining the UGFT control model. It can be found that a good linearity can be obtained for a peak voltage gain in the range of $1.5 < ||G_V||_{max} < 2.5$.
3. Equation 32 can be used to determine the required R_X value that guarantees a single resonant peak in the voltage gain curve. Since $||G_V||_{max}$ decreases as k (and consequently k_L) increases, Equation 32 should be evaluated for a value of $||G_V||_{max}$ above 1.5 and using the upper limit of k_L in an allowed k variation range. This determines R_X that guarantees the single peak behavior for the entire expected range of k variation.

It should be noted that following criteria 1-3 above and using design Equation 32 gives an accurate result under the condition that the total parasitic resistance in the SS resonant tank is small. If a large value of total parasitic resistance is expected, the obtained R_X value needs to be checked using parametric simulations.

4.3.3 Development of Novel UGFT Control without Communication

When SS resonant tank of SRT type is designed to have the voltage gain curve with a single resonant peak, voltage gain can be estimated from transmitter-side measurements *only*, and the unity gain frequency reference can be determined under k variation.

Figure 4.10 shows plots of $||Gv(j\omega)||$ and $\Phi_{vid}(j\omega)$ for $0.35 \leq k \leq 0.85$ when the desirable case of $||G_V||_{max} > 1.5$ is achieved. The plots are obtained using the equivalent model of Figure 4.2, but including the parasitic resistances of 40 mΩ on each side of the coupler. As a result, loading effects cause $||G_V||_{max}$ to *not always* increase with decreasing *k*. Phase difference Φ_{vid} is the phase of the input impedance of the equivalent circuit of Figure 4.2 and therefore represents the phase shift between the input voltage, V1(t), and input current (primary-side current), $i_{Le1}(t)$, as a function of frequency – Note: Φ_{vid} is measurable from the transmitter side.

In Figure 4.10, frequency f_α is *approximately* the unity gain frequency for the highest value of *k* expected (k_{max}) in a range of interest. It should be noted that for any given frequency in frequency range xx (between frequencies f_α and $2f_\alpha$), $||G_V(j\omega)||$ and $\Phi_{vid}(j\omega)$ vary monotonically and are approximately equally spaced as a function of *k*, so that linearization is possible.

Choosing a single frequency in the range of $f_\alpha \leq f \leq 2f_\alpha$ in Figure 4.10 (in this case, f_α is chosen), one can construct point by point a plot of $||G_V(j2\pi f_\alpha)||$ as a function of $\Phi_{vid}(j2\pi f_\alpha)$ for different values of *k*. For example, in the case of Figure 4.10, since five parametric plots are given, five points can be found. A linear approximation of this plot is given by Equation 35. Parametric simulations can be used to check for its accuracy when current sensing resistance, winding resistance and capacitor ESR terms are included. In particular, parameter *n* can be adjusted to improve accuracy and compensate for the gain decrease caused by the parasitic resistance terms.

Furthermore, the linear curve-fitting Equation 36 can be determined and used to find estimated unity gain frequency reference f_O* as a function of $||G_V(j2\pi f_\alpha)||$. Within an

allowed k variation range, the equation is valid and provides the unity-gain frequency reference.

The derivative (slope) terms in Equation (35) and Equation (36) are obtained from the parametric simulations. During UGFT tracking, $\Phi_{vid}(j2\pi f_\alpha)$ is measured. Equation (35) is then used to estimate $\|G_V(j2\pi f_\alpha)\|$ and this value is sued in Equation (36) to find the estimated unity gain frequency f_O*.

The accuracy of this approximation may not be high enough for a large k variation, therefore there needs to be a boundary for k that limits unity gain tracking operation. In simulations and experiments, $0.65 \leq k \leq 0.9$ is used as the unity gain operation range for validating the UGFT control. If a wide range of k variation is desired, more sets of equations 35 and 36 can be used with each set being applicable to a bounded k range.

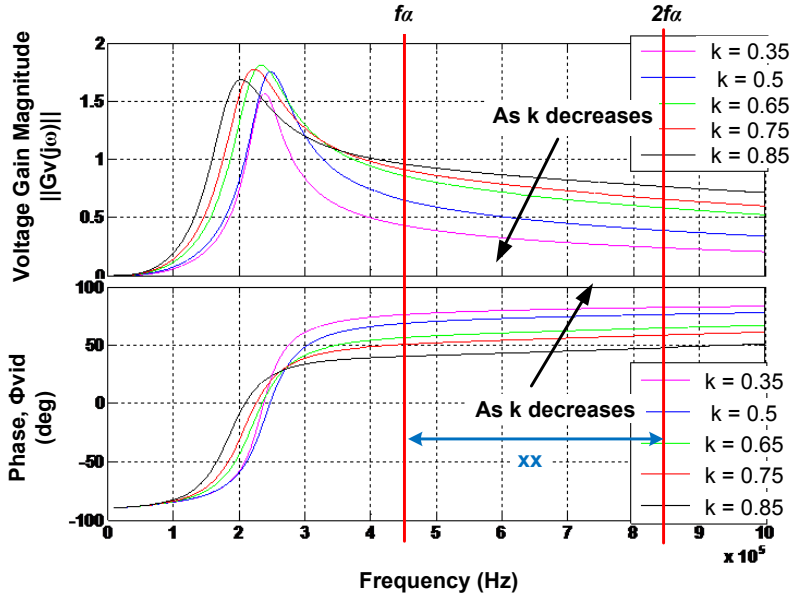

Figure 4.10: Voltage gain magnitude,$\|G_V(j\omega)\|$, and phase shift, $\Phi_{vid}(j\omega)$, between input voltage and input current of the SS resonant tank of SRT type for $0.35 \leq k \leq 0.85$.

$$\|G_V(j2\pi f_\alpha)\| \approx \frac{d[\|G_V(j2\pi f_\alpha)\|]}{d[\varphi_{vid}(j2\pi f_\alpha)]}\varphi_{vid}(j2\pi f_\alpha) + n \quad \text{..... Equation (35)}$$

$$f_o{}^* \approx \frac{df}{d[\|Gv(j2\pi f_\alpha)\|]}(1 - \|Gv(j2\pi f_\alpha)\|) + f_\alpha$$ ..... Equation (36)

4.4 VALIDATION

4.4.1 SIMULATION

Figure 4.11 shows the Matlab Simulink model of a full-bridge to full-bridge SS resonant converter of SRT type implementing the proposed UGFT control model. In order to demonstrate the unity voltage gain frequency tracking control, the Simulink model has dummy resistor load, R_X = 6.2 Ω, to mimic the case in which Q9 is on and Q10 is off. The Simulink model also contains switches in the resonant tank to introduce different *k* conditions via coupler inductance variations.

The blue block in Figure 4.11 contains the proposed UGFT control. Figure 4.12 shows what is inside this blue block. The two inputs to this block are input voltage, V1(t), of the resonant tank and primary-side resonant capacitor voltage, Vc(t). These two inputs are fed into the green blocks (Fourier transformation blocks) to determine the phase difference, $\Phi_{vid}(j2\pi f_\alpha)$. Frequency f_α is 200 kHz in this simulation. The inside of one of the Fourier transformation blocks is shown in Figure 4.13.

Inside the red-dotted line in Figure 4.12, $\Phi_{vid}(j2\pi f_\alpha)$ is fed into a set of algebraic blocks representing Equation 35 to determine $\|G_V(j2\pi f_\alpha)\|$, which is then fed into another set of algebraic blocks representing Equation 36 to calculate f_O*. By using the phase locked loop (PLL) shown inside the blue-dotted line in Figure 4.12, PWM signals are generated at f_O* and fed into the gates of the MOSFETs, Q1-Q4, to produce square wave input V1(t) for the resonant tank.

In order to demonstrate the unity voltage gain tracking, the simulation is performed with a fixed resistor load (R_X) of 6.2 Ω to mimic the case in which Q9 is always on and Q10 is always off. In this simulation, to just demonstrate the performance of unity-gain tracking operation, the controller is set to periodically go back to $f_S = f_\alpha$ = 200 kHz to extract $\Phi_{vid}(j2\pi f_\alpha)$, and then apply $f_S = f_O^*$ after a short time. At the end of this process a new f_O^* is determined and applied if there have been any coupler parameter variations.

Figure 4.14 shows the simulation results of waveforms of various resonant tank quantities in order to demonstrate the UGFT control performance. In this figure, V1(t) is the input voltage of the resonant tank, and V2(t) is the output voltage of the resonant tank. Quantities, $i_{Le1}(t)$, $i_{Le2}(t)$, and $i_{Lm}(t)$, are primary-side current, secondary-side current, and magnetizing current respectively. The control process corresponding to the operation in Figure 4.14 is as follows,

1. At t = 0, the converter operation starts with k = 0.75 at f_α = 200 kHz, and then the steady-state currents start flowing at t ≈ 0.06ms. The unity-gain tracking controller is set to start at t = 0.78.
2. During 0.78ms ≤ t < 0.98ms, $\Phi_{vid}(j2\pi f_\alpha)$ is measured, and f_O^* is tracked. The controller calculates this value and applies it at t = 0.98ms.
3. During 0.98ms ≤ t < 1.38ms, the converter operates at $f_S \approx f_O$. The converter is then set to go back to the operation at f_α at t = 1.38ms.
4. During 1.38ms ≤ t < 1.78ms, again, $\Phi_{vid}(j2\pi f_\alpha)$ is measured, and f_O^* is tracked. The controller calculates this value and applies it at t = 1.78ms.
5. During 1.78ms ≤ t < 2ms, since no changes are applied to the coupler parameters, the converter operation is the same as during interval 0.98ms ≤ t < 1.38ms.
6. At t = 2ms, k is changed from 0.75 to 0.85. So during 2ms ≤ t < 2.18ms, the converter does not operate under unity gain, and at t = 2.18ms, the converter starts operating at $f_S = f_\alpha$ to perform unity gain tracking.
7. During 2.18ms ≤ t < 2.58ms, $\Phi_{vid}(j2\pi f_\alpha)$ is measured. The controller calculates f_O^* and applies it at t = 2.58ms.

8. During 2.58ms ≤ t < 2.98ms, the converter operates $f_S \approx f_O$, and at t = 2.98ms, the operation at $f_S = f_\alpha$ begins again to measure $\Phi_{vid}(j2\pi f_\alpha)$ and to determine f_O*.

Figure 4.15 shows the results for V1(t) and V2(t) in a close-up scale. When the peak value of V1(t) (denoted as $V1_{pk}$) is equal to peak value of V2(t), the unity gain operation is achieved. As can be seen from this figure, the proposed UGFT method performs well. The maximum difference between the peaks of V1(t) and V2(t) is approximately 0.48 V (approximately 6.5 % error) during the unity gain operation.

As mentioned previously, a phase locked loop (PLL) is used in the simulation for adjusting f_S to be equal to the calculated f_O*. When a new f_O* is determined by the controller, this f_O* is applied as the reference input to the PLL. The gate signal oscillating at f_α is then locked on to the reference, f_O*. Figure 4.16 shows the PLL operation in the simulation. As can be seen clearly in this figure, the reference input to the PLL is changed between f_α and f_O* whenever the controller calculates and applies f_O*. For example, the output of the PLL is set to be applied to the gates at t = 0.98 ms as shown by the commutative gate signals in Figure 4.16.

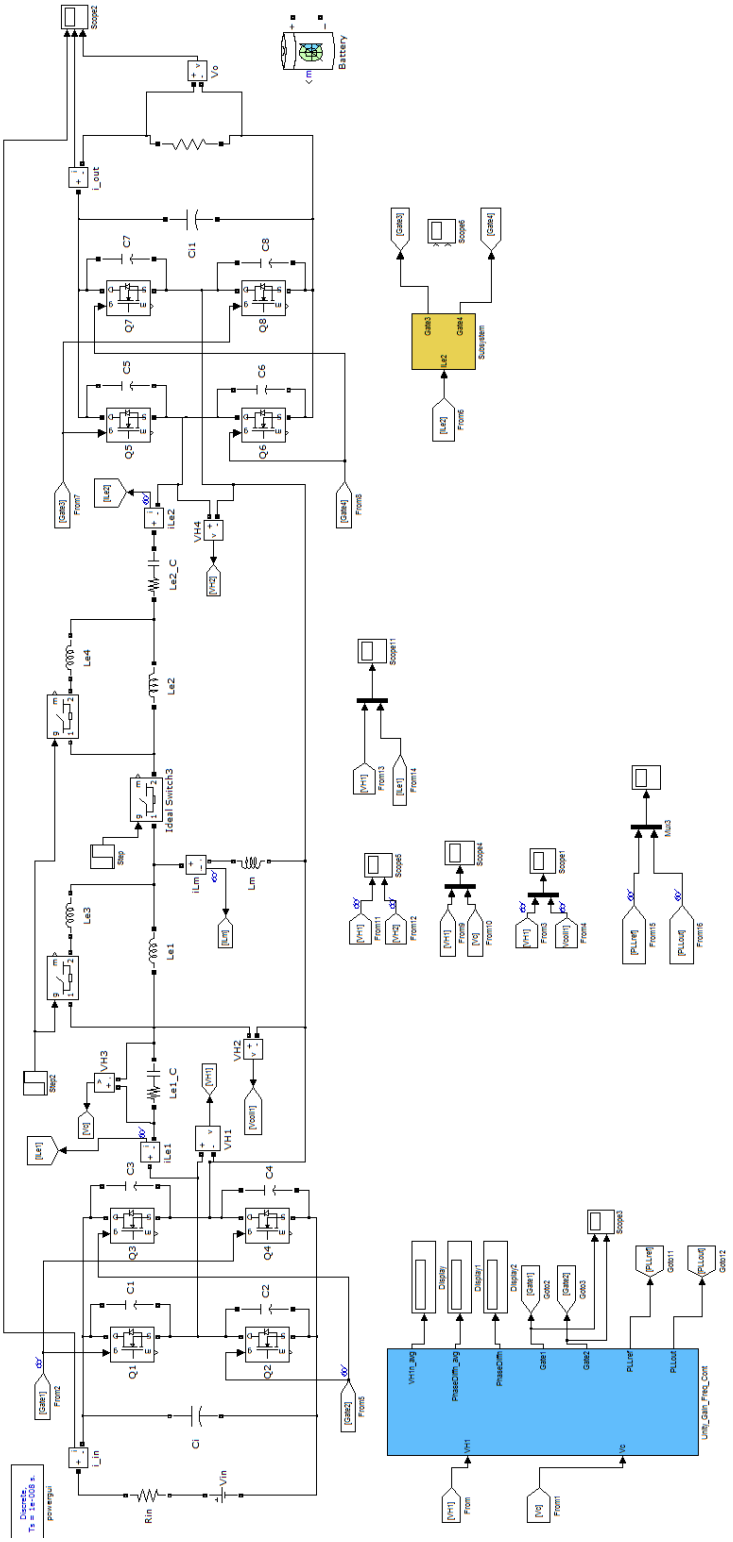

Figure 4.11: Simulink model of SS resonant converter of SRT type implementing proposed UGFT control method.

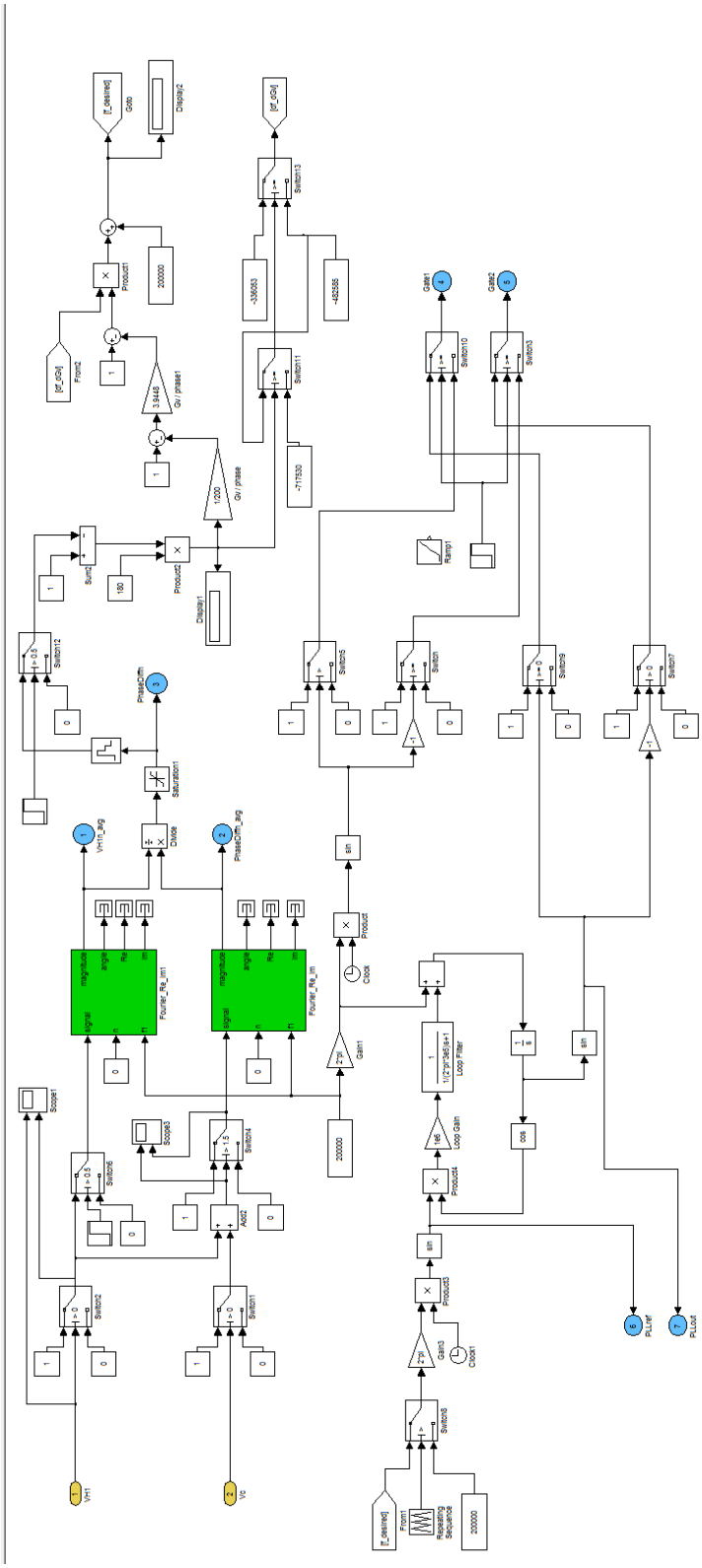

Figure 4.12: Inside of the UGFT Control block.

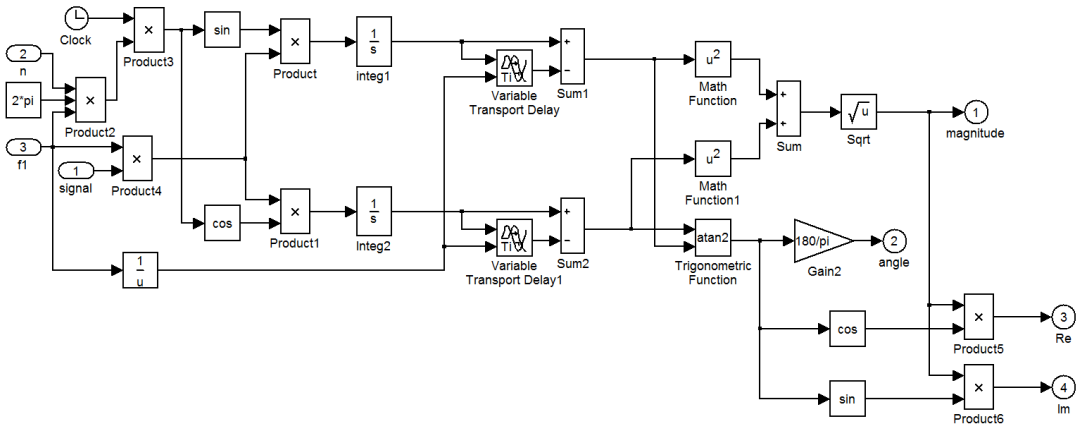

Figure 4.13: Inside of Fourier transformation block.

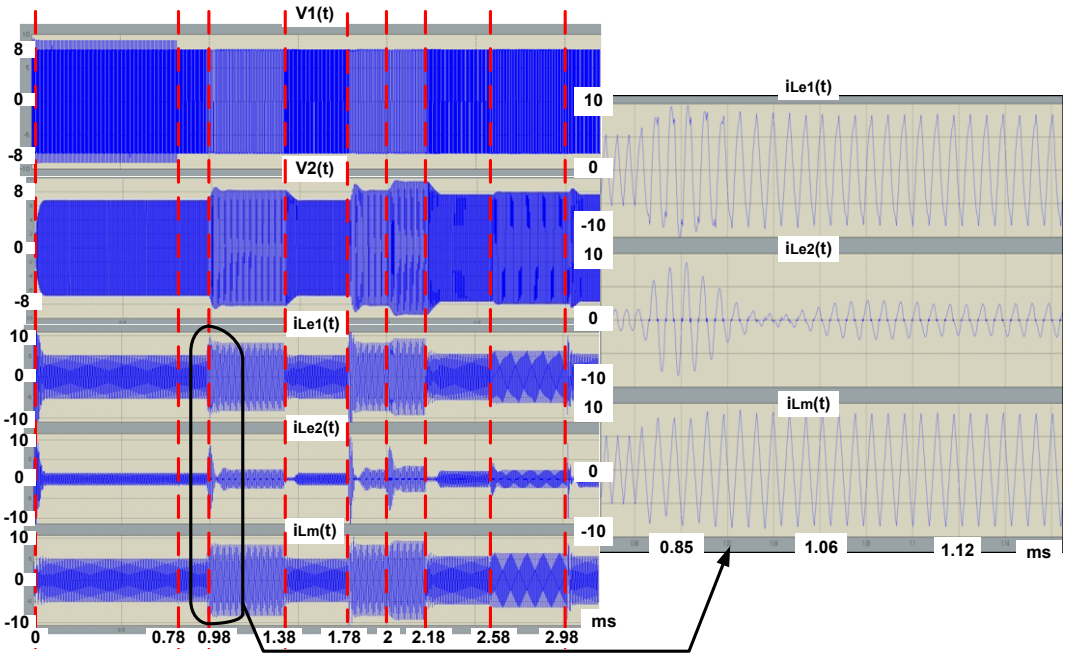

Figure 4.14: Unity-gain frequency tracking operation.

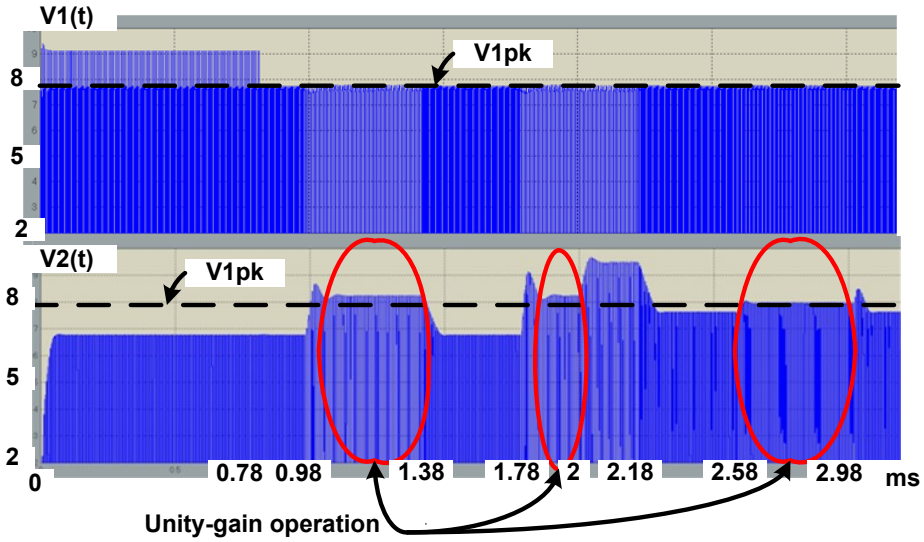

Figure 4.15: Unity-gain frequency tracking performance.

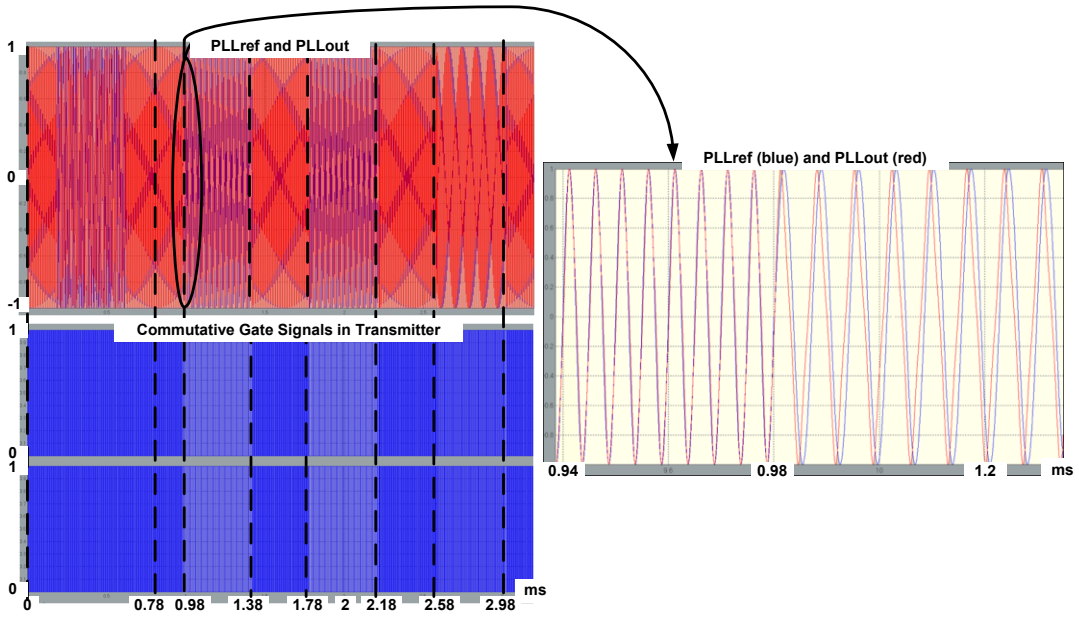

Figure 4.16: PLL operation and commutative gate signals.

4.4.2 Experimental Validation

Figure 4.17 shows the experimental set-up of Figure 4.1 without the switches, Q9 and Q10. The reason for excluding Q9 and Q10 is that they are *not* necessary for experimentally validating the proposed UGFT control model, since the process of unity gain frequency tracking control requires *only* that a known fixed resistive load, $R_e' =$

$\frac{8}{\pi^2}R_X$, be present in the SS resonant tank. Also, it should be mentioned that the transmitter-side switch network can be either a half-bridge or full-bridge configuration. The UGFT control method is *not* affected by either choice of switch network configuration.

The UGFT tracking procedure programmed into the digital controller is as follows. The phase shift Φ_{vid} at frequency f_α is measured by the controller. Equation 35 is used to estimate the voltage gain $\|G_V(j2\pi f_\alpha)\|$ and this value is substituted into Equation 36 to determine the unity gain frequency reference f_O*. The control and data measurements are performed using the Texas Instruments F28335 digital control card whose specifications are summarized in Chapter 2.

Regarding the experimental parameters listed in Table 4.3, it should be noted that the procedure for choosing the parameters focused on accurate measurements of Φ_{vid}. The data for Φ_{vid} is obtained by measuring the pulse width of the output of ultrafast comparators using the ECAP module built in the F28335. Using large values for f_{nom} and R_e', and a very low value for the primary-side current sensing resistor (Rsense) is desirable for maximizing efficiency, but it causes a high value of f_α and significant noise and leakage EMI that affect the Φ_{vid} measurements in the experimental set-up. The choice of actual values was a trade-off between these conflicting requirements.

In Figure 4.18 (a), the voltage gain (top), $\|G_V(j\omega)\|$, and phase shift (bottom), $\Phi_{vid}(j\omega)$, are plotted in simulation using the parameters in Table 4.3 along with experimentally extracted coupler parameters at varied k caused by varied misalignment. Voltage gain curves are quite linear in the range of $f_\alpha \leq f_S \leq 2f_\alpha$. Also, as can be seen from Figure 4.18 (b), the relationship between $\|G_V(j2\pi f_S)\|$ and $\Phi_{vid}(j2\pi f_S)$ for $f_\alpha \leq f_S \leq 2f_\alpha$ and $0.5 \leq k \leq$

0.83 is quite linear as well. The curve in Figure 4.18 (b) is used to determine the curve fitting parameters to be substituted in Equation 35.

Figure 4.19 shows the SS resonant tank input voltage (V1(t)), input current ($i_{Le1}(t)$), and the output of ultra-fast comparator whose pulse width represents the phase shift (Φ_{vid}) between V1(t) and $i_{Le1}(t)$. In this figure, the linear curve-fitting equations programmed in the control card are shown, and the interrupt service routine execution of the equations is visually described.

The accuracy evaluation of the curve-fitting equations (programmed in the F28335 control card) was performed by first collecting actual f_O* data that were being inputted into the PWM module by the controller at different misalignments. After that, frequency-domain simulations were performed using the experimentally-extracted resonant tank parameters without Rsense = 1 Ω. The goal was to see what voltage gains were to be expected at operating frequency f_O*. Also from these simulations, *analytical* values of unity gain frequencies f_O for different misalignments were collected as predicted by the model of Figure 4.2. The data are listed in Table 4.4 and prove that the single set of curve-fitting equations (UGFT control model) can be used to achieve the unity gain operation for fairly large *k* variation.

Figure 4.20 shows the output voltage of the SS resonant converter reaching the voltage level of unity gain operation after the controller applies f_O* as the converter switching frequency at time t ≈ tz. The voltage level of unity gain operation in Figure 4.20, represented by the straight solid green line in both Figure 4.20 (a) and Figure 4.20 (b), is approximately 3.6-3.7 V. This is because the supply voltage (Vg) of the SS resonant converter is 10 V, the primary stage is a half bridge configuration causing a 50 % voltage

reduction and the rectifier in the receiver performs passive diode rectification, causing two additional diode drops.

Figure 4.21 shows various waveforms captured while the SS resonant converter is operating at f_O* determined by the UGFT control model. In this figure, the rectifier in the receiver performs active synchronous rectification. Therefore, the output voltage, Vout, is slightly less than 5V (due to conduction of R_{ds_on}) when Vg = 10V is applied. As can be seen from this figure, the operating frequencies for each of Figure 4.21 (a)-(c) match those listed in Table 4.4.

While the output power is approximately 1.82W with constant load voltage (CV) and constant load current (CC), various quantities including the efficiency are experimentally measured and listed in Table 14. The experimental data show that the converter efficiency is about 15-19% higher *with* the UGFT control compared to the efficiency under fixed frequency operation *without* the UGFT control.

Furthermore, with the UGFT control, the need for an additional converter or regulator is minimized as indicated by the almost constant supply voltage and supply current (Vg and Ig) in Table 4.5 for the UGFT case. This also shows that losses in linear voltage regulators used widely in current wireless charging systems can be significantly reduced. On the other hand, without the UGFT control, Vg needs to be varied for delivering constant voltage and constant current output, indicating the requirement of an additional converter or linear voltage regulator, which decreases the overall system efficiency drastically.

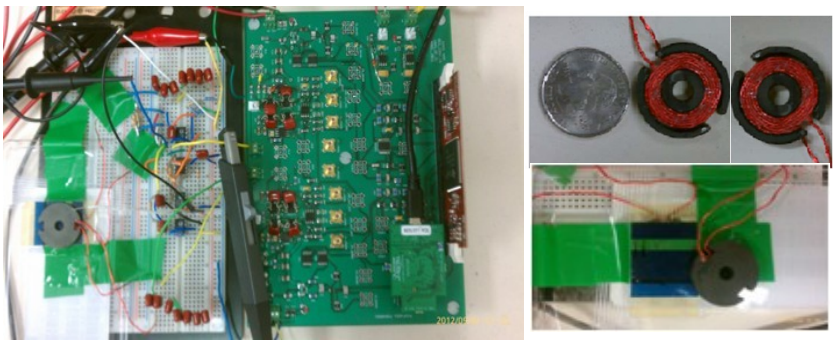

Figure 4.17: Experimental setup for the SS resonant converter.

TABLE 4.3 EXPERIMENTAL SS RESONANT TANK PARAMETERS

Unity Gain Frequency when *k* is the Highest in an Allowed Variation Range, f_{nom} (kHz)	≈ 190
Highest Coupling Coefficient, k_{max}	≈ 0.83
Resonant Capacitors (C: C_1 and C_2) [nF]	≈ 718
Leakage Inductances, (L_e: L_{e1} and L_{e2}) [nH]	≈ 0.974
Magnetizing Inductance, L_m [µH]	≈ 1.623
Current Sensing Resistor, Rsense [Ω]	≈ 1
Effective Load (R_e') in Simulation [Ω]	≈ 8.1
Linear Control Model Extraction Reference Point, f_α [kHz]	≈ 177

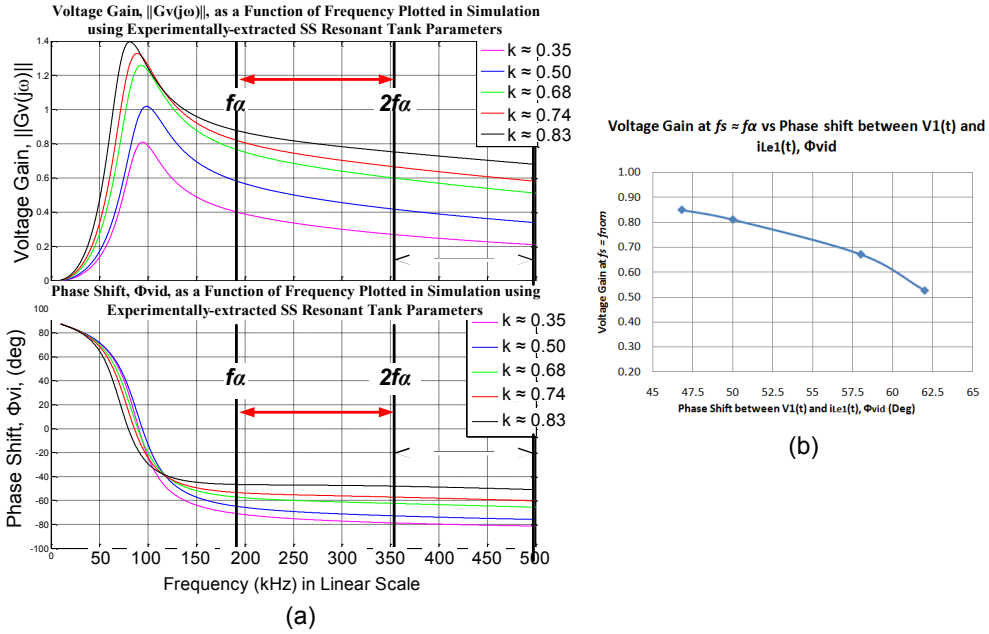

Figure 4.18: Voltage gain [$||G_V(j\omega)||$] and phase shift [$\Phi_{vid}(j\omega)$] (a) plotted in simulation using experimentally-extracted parameters for various *k*, and the linear relationship between them at $f_S \approx f_\alpha$ (b)-Note:Rsense of 1Ω added.

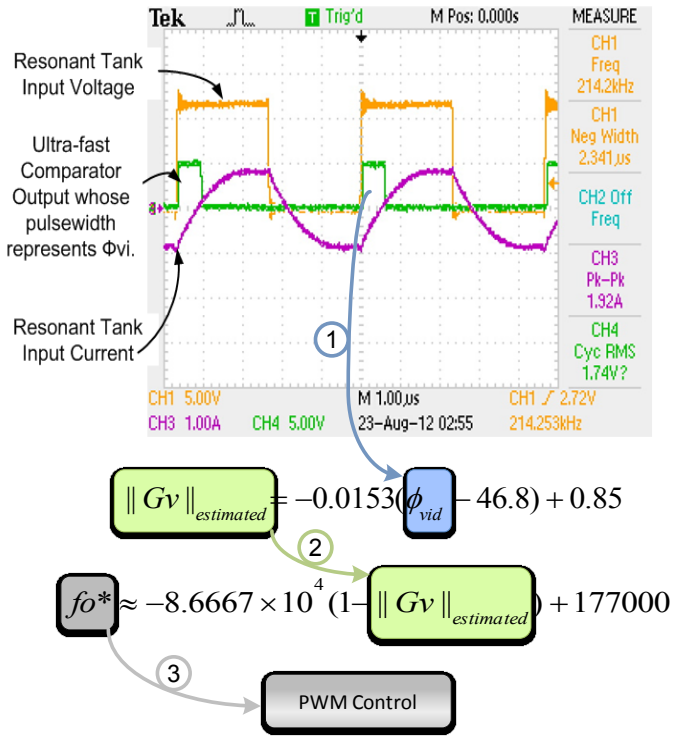

Figure 4.19: SS resonant tank's input voltage, V1(t), input current, $i_{Le1}(t)$, and output of ultra-fast comparator whose pulse width is the phase shift, Φ_{vid}, between V1(t) and $i_{Le1}(t)$.

TABLE 4.4 ACCURACY EVALUATION OF UGFT CONTROL MODEL EQUATION

Misalignment, M (mm)	**Ratio of M to Pot Core Diameter**	***k***	**Actual *fo**** **(kHz)**	**Analytical *fo*** **(kHz)**	**Voltage Gain at *fs* = *fo****
0	0	0.83	164	168.05	1.05
1.5	0.06	0.74	159.8	162.62	1.01
3	0.12	0.68	149.2	152.9	1.02
4.5	0.18	0.5	143.8	131.2	0.87

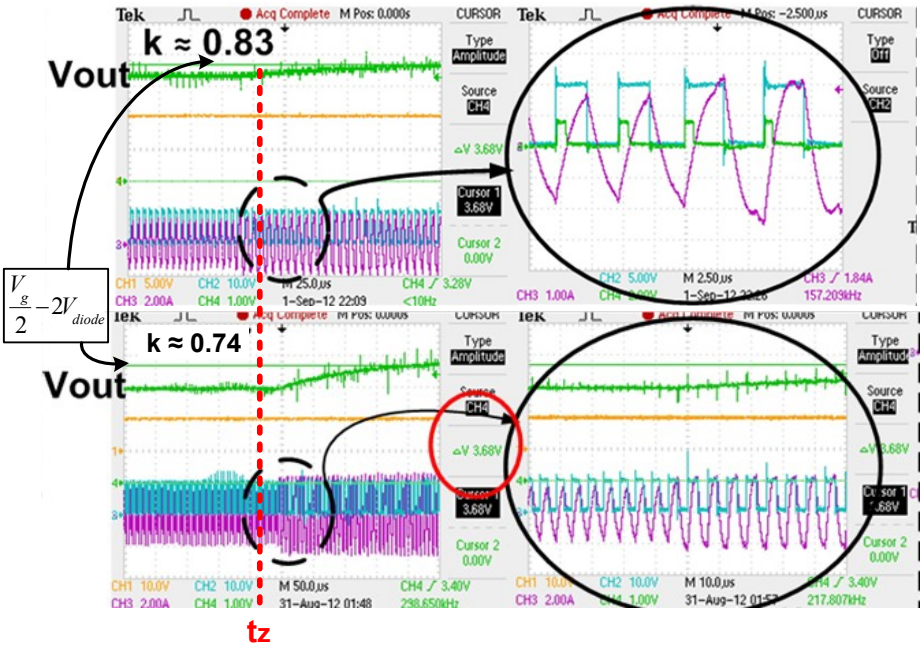

Figure 4.20: Various waveforms captured to show the UGFT control operation at $k \approx 0.83$ (a) and $k \approx 0.74$ (b) while performing passive diode rectification.
Note: At t ≈ tz, f_O* is applied as f_S of the converter.

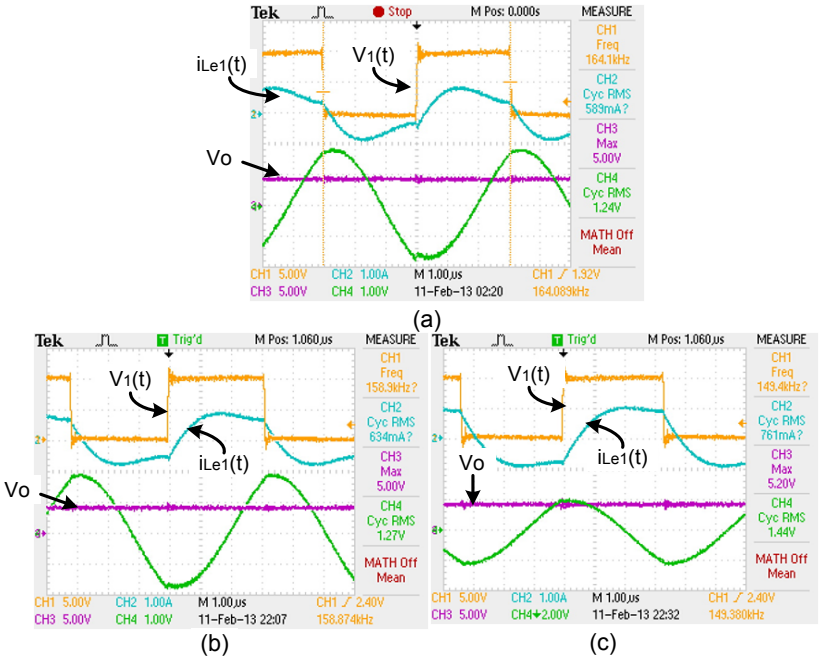

Figure 4.21: Various waveforms captured while operating at f_O* calculated by the UGFT control model for $k \approx 0.83$(a), $k \approx 0.74$(b), and $k \approx 0.68$(c) - Note: The output voltage (Vo) is approximately 5V while the supply voltage (Vg) of 10V is applied, indicating the operation of the SS resonant converter at $f_S \approx f_O$*.

TABLE 4.5 EXPERIMENTAL EFFICIENCY DATA

k	Vg (V)	Ig(A)	Vout (V)	Iout (A)	Efficiency(%)
Under fixed frequency operation (f_S = 200kHz) without UGFT					
0.83	≈ 12.3	≈ 0.30	≈ 4.270	≈ 0.427	≈ 49.4
0.74	≈ 12.68	≈ 0.30	≈ 4.273	≈ 0.427	≈ 48.0
0.68	≈ 14.03	≈ 0.31	≈ 4.271	≈ 0.427	≈ 41.9
Under Unity Gain Frequency Tracking, UGFT ($f_S \approx f_O$*)					
0.83	≈ 10.00	≈ 0.28	≈ 4.268	≈ 0.427	≈ 65.1
0.74	≈ 10.03	≈ 0.28	≈ 4.270	≈ 0.427	≈ 64.8
0.68	≈ 9.91	≈ 0.30	≈ 4.270	≈ 0.427	≈ 61.4

4.5 CHAPTER SUMMARY

In this work, SS resonant converter characteristics under resistive load condition are compared with those under Li-ion battery load condition to demonstrate how to obtain the desirable characteristics with both types of load. It is shown that obtaining the single voltage gain peak condition is required for achieving various desirable features. One of these features is high robustness against f_S tracking error, and variations in Q and k. High robustness can significantly improve overall charging system efficiency by minimizing the need for using an additional voltage regulator stage commonly used in current commercial wireless chargers for portable electronics. Other features include appropriate charging current control via f_S modulation and good accuracy of a linear curve-fitting model for voltage gain control in the extended ZVS region. These features significantly reduce control complexity and further increase the overall efficiency while decreasing the cost of implementation by reducing the component count.

Furthermore, under these conditions the proposed Unity Gain Tracking Control (UGFT) method is applicable, which adjusts the switching frequency for leakage inductance compensation under allowed magnetic coupling variation without communication between a transmitter and a receiver. Compensating the leakage inductances is highly desirable for maximizing the efficiency in a resonant tank, and doing so under allowed k variations is important for increasing the receiver positioning flexibility. It is shown that using only a single UGFT control model, the unity gain frequency operation can be tracked and achieved for a fairly wide range of k variation. This indicates that with *only* a *few* different sets of UGFT control models (each set applicable to a bounded k range), the unity gain frequency operation can be obtained for a wide range of k variation. The proposed UGFT control method is validated in both simulation and experiment. The results show that the method performs well. Furthermore, it is demonstrated experimentally, for the constant output power delivery of 1.8 W, that the converter efficiency is significantly improved (approximately 15-19 % higher) when compared with the fixed frequency operation of conventional wireless charging systems. Also, the voltage gain variation is very small (*less* than 1 %) when the proposed UGFT control is applied. This small variation can reduce the losses in linear voltage regulators that are used widely in current wireless charging systems for portable electronics. Therefore, overall efficiency with the proposed UGFT control method can be even higher than conventional wireless charging systems without the need for communication while reducing both component count and complexity in control.

CHAPTER 5

NOVEL OPTIMAL DESIGN METHODS FOR ASYMMETRICAL SERIES-SERIES (SS) RESONANT TANK AND ASYMMETRICAL SERIES-PARALLEL (SP) RESONANT TANK IN LOOSELY-COUPLED WIRELESS POWER TRANSFER APPLICATIONS

5.1 INTRODUCTION AND LITERATURE REVIEW

In this chapter, optimal design methods for the SS and SP resonant tank topologies in Figure 1.3 are proposed and validated.

As previously mentioned, there are two main types of resonant tank. One is *asymmetrically*-implemented resonant tank (ART) type, and the other is *symmetrically*-implemented resonant tank (SRT) type. In a resonant tank of ART type, primary-side inductance and secondary-side inductance can be largely different, because primary-side coil (Tx) and secondary-side coil (Rx) of a coupler have different physical geometries, whereas in a resonant tank of SRT type, primary-side inductance and secondary-side inductance are equal. Thus, in SRT type, relative self-inductance condition is $L_{S1} = L_{S2}'$, whereas in ART type, it can be $L_{S1} > L_{S2}'$, $L_{S1} = L_{S2}'$, or $L_{S1} < L_{S2}'$.

To minimize leakage flux (in order to maximize coil-to-coil efficiency), one would employ a resonant tank of SRT type. Thus, conventionally, the majority of studies on magnetically loosely-coupled wireless charging systems has considered only resonant tanks utilizing *symmetrical* core geometry for the primary and secondary as in [8]-[9], [24], [31], and [33]-[34]. However, in many wireless charging applications, it is becoming more desirable to minimize the weight and size of Rx. To increase the receiver

positioning flexibility, a larger Tx is employed, as in [37]-[40], to provide a stronger and/or more uniform magnetic field in the region where a Rx is located. Furthermore, in many applications, Rx geometry is limited by the dimensions of the movable battery-powered system, whereas the transmitter coil geometry is *less* limited. Consequently, the need for *asymmetrical* coupler implementation is increasing. It should be noted that ART type, which generates more leakage flux, is used for systems with typically lower (loose) magnetic coupling compared to SRT type.

To derive analytical solutions that are applicable to both ART and SRT types, it is important to analyze *general* resonance characteristics of SS and SP resonant tanks. The existing scientific literature lacks in terms of performing detailed analysis on general resonance characteristics and of providing general analytical equations for determining various notable quantities. For example, although [8]-[9] and [37] provide brief comparisons on these topologies under certain conditions, they do not provide *general* analytical equations for determining various important frequency-domain quantities such as peak voltage gain, load-independent voltage gain, load-independent current gain, multiple resonant frequencies of notable features, desirable boundaries for operating frequency (ω_s) range, voltage gain at ω_s, current gain at ω_s, circulating current gain at ω_s, and how these quantities change depending on magnetic coupling coefficient (k) and load (R_e').

Conventionally, as in [6], [8], and [35], analytical equations for design optimization involve quality factors that describe the relationship between resonant elements and parasitic resistance terms such as winding resistance and capacitor ESRs. Although such equations can allow convenient calculation of expected resonant tank power efficiency,

they do not provide insight into various important frequency-domain quantities. Instead, design implication from these expressions is straightforward: a general goal in optimal design process is to minimize all parasitic resistances.

However, optimal design of resonant tank parameters for a desired nominal load is not straightforward and not easy to intuitively understand. Therefore, quality factors in this chapter are defined by Q_L in Equation 37 to describe the relationship between resonant elements and effective load (*unlike* the conventional expressions for quality factor). As in Figure 1.3, the subscripts $_{SS}$ and $_{SP}$ are added in Equation 37 to distinguish between the expressions for SS and SP resonant tanks. Also, for $||G_V(j\omega)||$, $||G_i(j\omega)||$, and $||G_{iLm}(j\omega)||$ in this chapter, the subscripts $_{SS}$ and $_{SP}$ are added for the same reason. For example, $||G_V(j\omega)||_{SS}$ represents a general expression of voltage gain magnitude transfer function for SS resonant tank, while $||G_V(j\omega)||_{SP}$ represents that for SP resonant tank.

$$Q_L = \begin{cases} Q_{L_{SS}} = R_{eSS}{}' \sqrt{\frac{C_1}{L_{s2}{}'}} \text{ for SS Resonant Tank} \\ Q_{L_{SP}} = R_{eSP}{}' \sqrt{\frac{C_2{}'}{L_{s2}{}'}} \text{ for SP Resonant Tank} \end{cases} \quad \text{..... Equation (37)}$$

To *maximize* robustness in voltage gain and current gain *without* significantly increased circulating current in a magnetic coupler, it is very important to analyze these two quantities for each of the resonant tanks along with circulating current gain. A resonant tank should then be designed to exhibit an optimal Q_L for a desired nominal load, R_e' – Note: In typical battery charging applications, a nominal R_e' is approximately constant on *most* of the state of charge (SoC) curve (in the constant current charging stage) as can be found in [25]-[26]. Therefore, for a battery load, a desired nominal load R_e' can be determined from the nominal voltage rating and typical constant current charge rating of the battery.

It should be noted that minimized circulating current contributes to increased coil-to-coil power transfer efficiency, and robust voltage gain contributes to maintaining desirable power transmission level under k variation. By avoiding accumulation of significant losses in an additional downstream converter or linear voltage regulator, small fluctuations in voltage gain provided by maximized robustness can contribute to increasing the overall efficiency of a wireless charging system.

Furthermore, robust voltage gain can decrease control complexity, analytical complexity, and cost of implementation. For example, development and implementation of robust control systems to avoid bifurcation phenomena [32] can significantly increase the system complexity. In order to minimize the system complexity, it is highly desirable for robust voltage gain to be achieved at a *fixed* desirable operating frequency.

Also, in currently available wireless charging systems, multi-layer coils in array are implemented, as in [12] and [36], to create uniform magnetic field on a charging platform. Although such implementation improves the receiver positioning flexibility by exhibiting almost constant k on the charging platform area, cost of implementation can increase significantly. By obtaining robust voltage gain without significantly-increased circulating current, the number of coils may be reduced *while* desirable charging speed can still be maintained under k variation.

However, there are tradeoffs between voltage gain robustness and coil-to-coil efficiency. For example, depending on Q_L selection, coil-to-coil efficiency can be maximized at the cost of minimized robustness of $\|G_V(j\omega)\|$, and vice versa. More details regarding tradeoffs are discussed later in this chapter.

To achieve good compromise between these tradeoffs via optimal Q_L selection, this chapter presents novel, *general* optimal design methods for loosely-coupled SS and SP resonant tank topologies. It begins with performing *general* frequency-domain analysis for SS resonant tank topology and SP resonant tank topology. This is because in order to derive analytical equations applicable to both ART and SRT types, it is important to understand *general* resonance characteristics.

After the detailed analysis and evaluation on *general* frequency-domain characteristics, various *general* analytical equations in *design-oriented* forms are derived. As will be shown later in this chapter, these equations allow determining various important frequency-domain quantities. Using these equations, design methods for optimally designing loosely-coupled SS resonant tank and loosely-coupled SP resonant tank are presented. For all possible relative inductance conditions: $L_{S1} > L_{S2}'$, $L_{S1} = L_{S2}'$, and $L_{S1} < L_{S2}'$, the design methods allow convenient calculation of SS and SP resonant tank parameters needed for *achieving* desirable frequency-domain characteristics in loosely-coupled systems. Detailed simulation and experimental results are reported to evaluate and to validate the novel optimal design methods.

For convenient analysis and to provide expressions directly meaningful for practical design, it is highly desirable that all analytical equations be derived only in terms of k, Q_L, or quantities that do *not* change significantly under k variation. In *general* under k variation, the *ratio* between L_{S1} and L_{S2}' does *not* change *significantly*, although there can be significant changes in each of L_{S1} and L_{S2}'.

In magnetically *loosely-coupled* systems, it can be assumed that changes in both L_{S1} and L_{S2}' due to k variation are small. This means that with fixed values of resonant

capacitances (C_1 and C_2'), self-resonant frequencies, ω_{LS1} (Equation 38) and ω_{LS2} (Equation 39), do *not* change much when k is low (e.g. $k < 0.35$).

$$\omega_{Ls1} = \frac{1}{\sqrt{C_1 L_{S1}}} \quad \text{..... Equation (38)}$$

$$\omega_{Ls2} = \frac{1}{\sqrt{C_2{}' L_{S2}{}'}} \quad \text{..... Equation (39)}$$

In this chapter, *general* analytical equations for determining various quantities of interest are derived and expressed only in terms of the physically-meaningful quantities that include k (Equation 1), Q_L (Equation 37), ω_{Ls1} (Equation 38), ω_{Ls2} (Equation 39), *ratio* between L_{S1} and L_{S2}', and *ratio* between C_1 and C_2'.

Throughout analysis and discussion, it should be noted that the resonant capacitances, C_1 and C_2', are considered fixed. Also, the resonant tank models in Figure 1.3 and their quantities are used in the analysis It should be noted that this means that with all of the secondary parameters referred to the primary side, voltage gain $\|G_V(j\omega_o)\|_{SS} = \left\|\frac{V_o{}'(j\omega_o)}{V_i(j\omega_o)}\right\|$ of the SS resonant tank topology can be unity while the actual voltage gain (ratio of non-referred output voltage magnitude $\|V_o(j\omega_o)\|$ to input voltage magnitude $\|V_i(j\omega_o)\|$) depends on magnetic coupler turns ratio. Therefore, throughout general analysis and discussion, unity voltage gain of the SS resonant tank topology refers to $\|G_V(j\omega_o)\|_{SS} = \left\|\frac{V_o{}'(j\omega_o)}{V_i(j\omega_o)}\right\| = 1$.

5.2 Derivation Of General Analytical Equations In Frequency Domain For SS Resonant Tank Topology

5.2.1 General Analytical Solutions For SS Resonant Tank

For SS resonant tank topology, general equations for voltage gain $\|G_V(j\omega)\|_{SS}$ and current gain $\|G_i(j\omega)\|_{SS}$ are derived in Equation 40 and Equation 41 respectively. Circulating current gain $\|G_{iLm}(j\omega)\|_{SS}$ is *equal* to $\|1 - G_i(j\omega)_{SS}\|$.

$$\| G_V(j\omega) \|_{SS} = \left| \frac{-j\omega^3 C_1 C_2' Lm \mathrm{Re}_{SS}'}{\omega^4 C_1 C_2' (Le_1(Le_2'+Lm) + Le_2' Lm) - \omega^2 (C_1(Le_1+Lm) + C_2'(Le_2'+Lm)) + 1 - j\omega C_2' \mathrm{Re}_{SS}' (\omega^2 C_1 (Le_1+Lm) - 1)} \right|$$ ..... Equation (40)

$$\|G_i(j\omega)\|_{SS} = \left| \frac{-\omega^2 C_2' L_m}{1-\omega^2 C_2' L_{S2}' + j\omega C_2' R_{eSS}'} \right|$$ ..... Equation (41)

Ideally, coil-to-coil efficiency of a SS resonant tank is maximized when both of the leakage inductances, L_{e1} and L_{e2}', are fully compensated by their series capacitors, C_1 and C_2'. This condition corresponds to when *short-circuited primary leakage* resonant frequency, f_{OVp} (Equation 42) and *short-circuited secondary leakage* resonant frequency, f_{OVs}, (Equation 43) are *equal* to each other. Only under this condition, *load-independent* voltage gain of unity can be obtained.

$$f_{OVp} = \frac{\omega_{OVp}}{2\pi} = \frac{1}{2\pi\sqrt{C_1 L_{e1}}} = \frac{\omega_{Ls1}}{2\pi\sqrt{1-k\sqrt{\frac{L_{S2}'}{L_{S1}}}}}$$ ..... Equation (42)

$$f_{OVs} = \frac{\omega_{OVs}}{2\pi} = \frac{1}{2\pi\sqrt{C_2' L_{e2}'}} = \frac{\omega_{Ls2}}{2\pi\sqrt{1-k\sqrt{\frac{L_{S1}}{L_{S2}'}}}}$$ ..... Equation (43)

In Figure 5.1 (a), voltage gain ($\|G_V(j\omega)\|_{SS}$), current gain ($\|G_i(j\omega)\|_{SS}$), and circulating current gain ($\|G_{iLm}(j\omega)\|_{SS}$) are plotted for $L_{S1} > L_{S2}'$, whereas in Figure 5.1 (b), these quantities are plotted for $L_{S1} < L_{S2}'$. In both figures, Q_{Lss} variation is imposed by changing

R_{eSS}' – See Equation (37). Since both $L_{S1} > L_{S2}$' and $L_{S1} = L_{S2}$' exhibit $f_{OV1} < f_{ip} < f_{VP} < f_{OV2}$, whereas $L_{S1} < L_{S2}$' does *not,* the plots for $L_{S1} = L_{S2}$' need not be shown.

General analysis will be performed for two separate cases of $L_{S1} \geq L_{S2}$' and $L_{S1} < L_{S2}$'. In this section, *general* equations for all of the frequencies indicated in Figure 5.1 are derived.

Figure 5.1 shows that there exist two resonant frequencies (f_{OV1} and f_{OV2}) where load-independent voltage gains occur. *General* expressions for the two resonant frequencies of *load-independent* voltage gains are derived as f_{OV1} (Equation 44) and f_{OV2} (Equation 45).

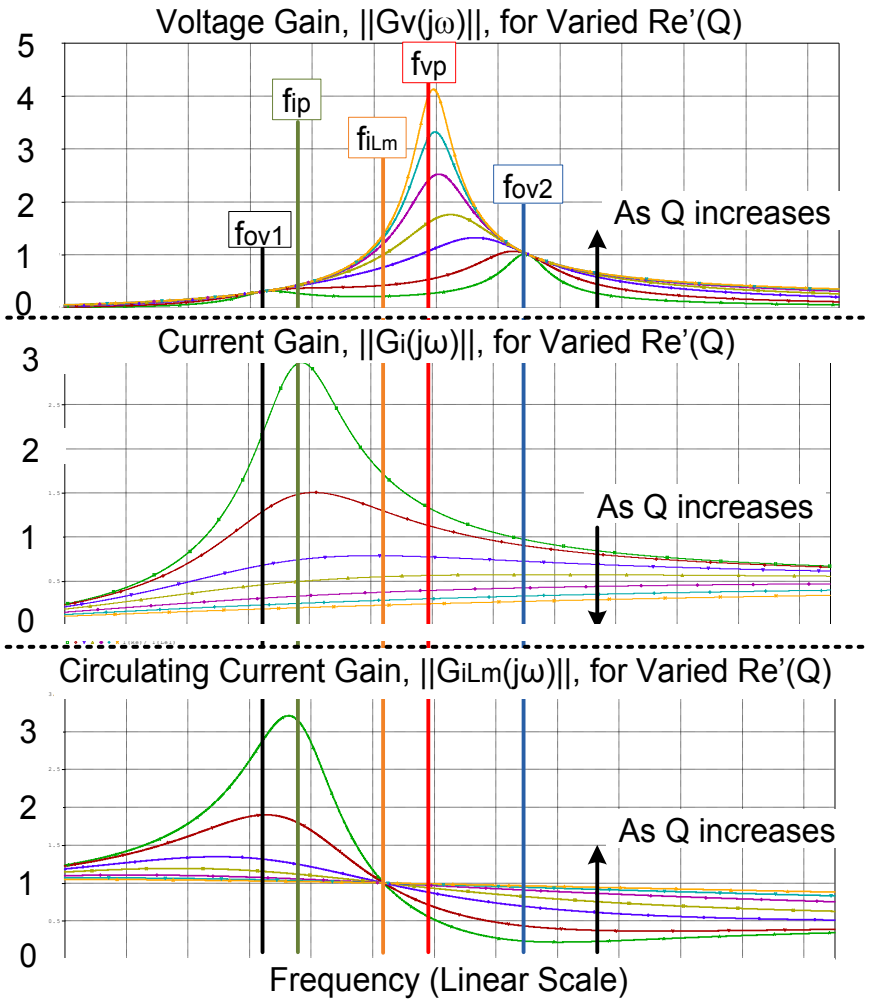

(a)

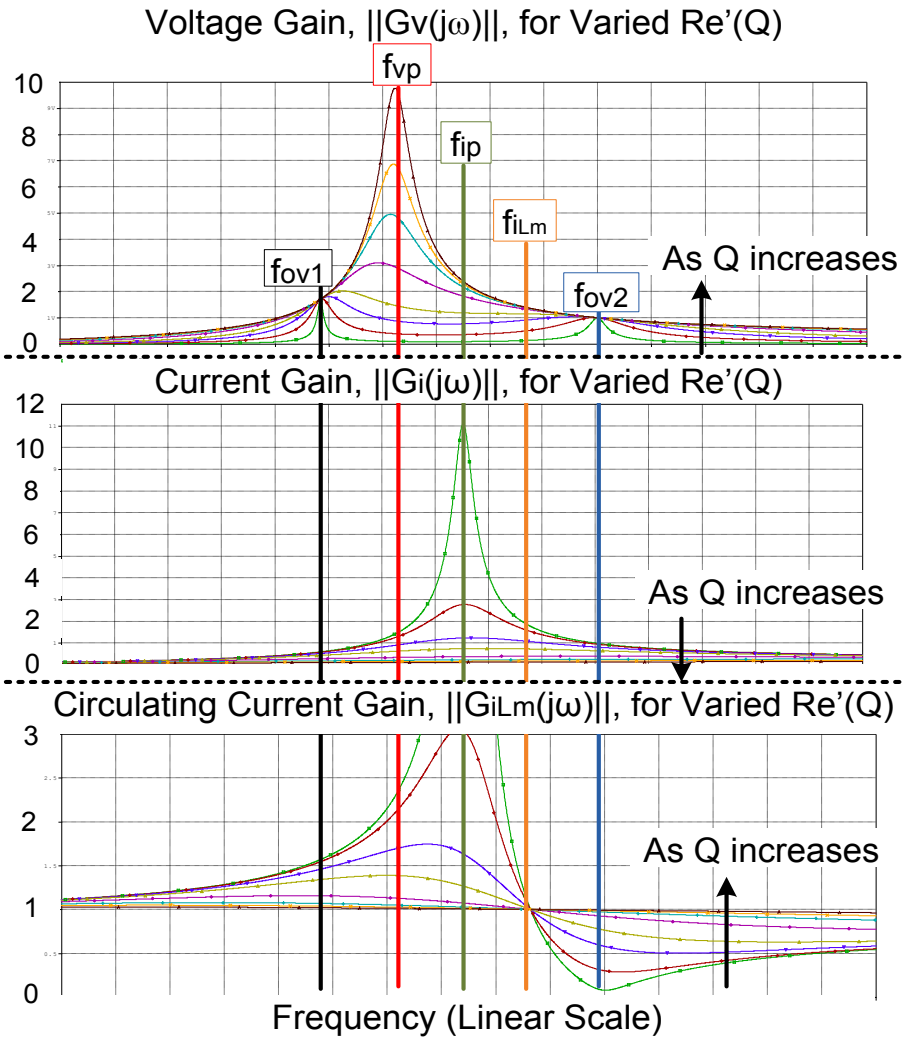

(b)

Figure 5.1: Voltage gain ($\|G_V(j\omega)\|_{SS}$), current gain ($\|G_i(j\omega)\|_{SS}$), and circulating current ($\|G_{iLm}(j\omega)\|_{SS}$) for varied effective resistive load under $L_{S1} > L_{S2}$ (a) and $L_{S1} < L_{S2}$ (b).

$$f_{OV1} = \frac{\omega_{OV1}}{2\pi} = \frac{1}{2\pi}\sqrt{\frac{\omega_{Ls1}{}^2+\omega_{Ls2}{}^2-\sqrt{\omega_{Ls1}{}^4+2(2k^2-1)\omega_{Ls1}{}^2\omega_{Ls2}{}^2+\omega_{Ls2}{}^4}}{2(1-k^2)}} \quad \text{..... Equation (44)}$$

$$f_{OV2} = \frac{\omega_{OV2}}{2\pi} = \frac{1}{2\pi}\sqrt{\frac{\omega_{Ls1}{}^2+\omega_{Ls2}{}^2+\sqrt{\omega_{Ls1}{}^4+2(2k^2-1)\omega_{Ls1}{}^2\omega_{Ls2}{}^2+\omega_{Ls2}{}^4}}{2(1-k^2)}} \quad \text{..... Equation (45)}$$

In both Figure 5.1 (a) and Figure 5.1 (b), it should be noted that $\|G_V(j2\pi f_{OV2})\|_{SS}$ is unity and independent of Q_{Lss}. Therefore, this unity gain condition indicates that $f_{OV2} = f_{OVp} = f_{OVs}$.

As Q_{Lss} increases, $\|G_V(j\omega)\|_{SS}$ exhibits a single resonant peak rather than two load-independent peaks at f_{OV1} and f_{OV2}. The frequency, at which this single voltage gain peak occurs, rapidly approaches *open-circuited load* resonant frequency, f_{Vp}, which is *equal* to $\frac{\omega_{Ls1}}{2\pi}$.

In *general*, a well-defined single peak is obtained when peak voltage gain, $\|G_V\|_{max}$, is approximately equal or greater than $1.5\|G_V(j2\pi f_{ov2})\|_{SS}$ for $L_{S1} \geq L_{S2}'$, *or* when $\|G_V\|_{max}$ is approximately equal or greater than $1.5\|G_V(j2\pi f_{ov1})\|_{SS}$ for $L_{S1} < L_{S2}'$. This can be observed from Figure 5.1 as well. The plots for $\|G_i(j\omega)\|_{SS}$ show that resonant frequency of peak current gain, $\|G_i\|_{max}$, and resonant frequency of peak circulating current gain, $\|G_{iLm}\|_{max}$, rapidly approach *open-circuited input* resonant frequency, f_{ip}, which is *equal* to $\frac{\omega_{Ls2}}{2\pi}$.

As can be seen from $\|G_{iLm}(j\omega)\|$ plots in Figure 5.1, there exists *load-independent* circulating current gain of *unity* at $f_{iLm.}$ A *general* expression for the resonant frequency (f_{iLm}) is derived as Equation 46.

$$f_{iLm} = \frac{\omega_{iLm}}{2\pi} = \frac{\omega_{Ls2}}{2\pi}\sqrt{\frac{2}{2-k\sqrt{\frac{L_{S1}}{L_{S2}'}}}} \quad \text{..... Equation (46)}$$

For applications with $L_{S1} > L_{S2}'$ or $L_{S1} = L_{S2}'$, the operation frequency (f_S) must *not* be below *open-circuited load* resonant frequency f_{Vp} to *avoid* the danger of moving out of ZVS range by falling below the resonant peak. Also, as can be seen from $\|G_{iLm}(j\omega)\|_{SS}$ curves in Figure 5.1 (a), the circulating current gain *increases rapidly* as f_S *decreases* below f_{Vp}. This further emphasizes that operation under $f_S < f_{Vp}$ must be avoided.

As can be seen from $\|G_{iLm}(j\omega)\|_{SS}$ curves in Figure 5.1 (b), the circulating current gain *increases very rapidly* as f_S *decreases* below f_{iLm}. Therefore, for applications with $L_{S1} < L_{S2}'$, the operation frequency (f_S) should *not* be lower than f_{iLm} in order to *avoid* significant circulating current. In fact, regardless of the inductance inequality conditions, it can be concluded that operating under $f_S < f_{OV2}$ is *not* desirable for maximizing coil-to-coil efficiency.

Unless $L_{S1} = L_{S2}'$ and $\frac{\partial L_{e1}}{\partial k} = \frac{\partial L_{e2}'}{\partial k}$, resonant frequencies, f_{OVp}, f_{OVs}, and f_{OV2}, change differently under k variation. Also, peak voltage gain increases as k decreases, and to explain this phenomenon, a general expression for voltage gain at f_{Vp}, $\|G_V(j2\pi f_{Vp})\|_{SS}$, is derived as Equation 47. As can be seen from this equation, decrease in k causes $\|G_V(j2\pi f_{Vp})\|_{SS}$ to increase. When this occurs, Figure 5.1 shows that increase in $\|G_V(j2\pi f_{Vp})\|_{SS}$ corresponds to increase in maximum available voltage gain $\|G_V\|_{max}$ *regardless* of whether voltage gain exhibits a single peak or two peaks.

$$\left\|G_V(j2\pi f_{Vp})\right\|_{SS} = \frac{Q_{LSS}}{k} \quad \text{..... Equation (47)}$$

Since the frequency of minimum circulating current changes depending on $\|G_V\|_{max}$ condition, and since non-linear changes in all of the resonant frequencies are different in both magnitude and direction, tracking and achieving the frequency of maximum efficiency under a wider range of k variation can be impractical. Also, it should be noted that even if load-independent voltage gain, $\|G_V(j2\pi f_{OV2})\|_{SS}$, is tracked to achieve operation at f_{OV2}, $\|G_V(j2\pi f_{OV2})\|_{SS}$ can generate voltage gain well above the desired value and can consequently cause more losses in an additional downstream converter or linear voltage regulator. In order to understand how this load-independent voltage gain changes,

a general expression for $\|G_V(j2\pi f_{OV2})\|_{SS}$ is derived and defined as $|G_V|_{ind}SS$ in Equation 48.

$$|G_V|_{ind}SS = \|G_V(j2\pi f_{OV2})\|_{SS} = k\sqrt{\frac{L_{S2}'}{L_{S1}}}\left[1 + \frac{2(1-k^2)}{\left(\frac{\omega_{Ls2}}{\omega_{Ls1}}\right)^2 + 2k^2 - 1 + \sqrt{\left(\frac{\omega_{Ls2}}{\omega_{Ls1}}\right)^4 + 2\left(\frac{\omega_{Ls2}}{\omega_{Ls1}}\right)^2 (2k^2-1) + 1}}\right]$$

..... Equation (48)

In summary, by using Equation 1 and equations 37 through 48, general frequency-domain characteristics and various important features of SS resonant tank topology can be understood. Furthermore, using these equations in design-oriented form allows rapid calculation of SS resonant tank parameters required for achieving all possible resonance characteristics (thus, for achieving any Q_{Lss} condition for a specified nominal load, R_{eSS}').

Various design equations for determining optimal Q_{Lss} are derived in the next two sections separately for loosely-coupled SS resonant tank with $L_{S1} \geq L_{S2}$' and with $L_{S1} < L_{S2}$'.

5.2.2 Design Equations for Loosely-coupled SS Resonant Tank with $L_{S1} \geq L_{S2}$'

Proposed optimization process begins with determining how resonant frequencies should be selected. For SS resonant tank, it is desirable to achieve the unity gain condition of $2\pi f_S = \omega_{OVp} = \omega_{OVs} = \omega_{OV2}$ when k is at its highest value, k_{max}, in an allowed k variation range. Under this condition, coil-to-coil efficiency can be maximized. Also, since f_{OV2} *decreases* as k *decreases* – See Equation 45, this frequency condition *guarantees* that converter operation is performed *always* above resonance and therefore is within ZVS-capable region under k variation.

General design equations applicable to loosely-coupled SS resonant tank topology are derived under the condition that switching frequency is fixed always at a value that satisfies $2\pi f_S = \omega_{OVp} = \omega_{OVs} = \omega_{OV2}$ for $k = k_{max}$. For example, if leakage inductances are fully compensated at f_S = 500 kHz when $k = k_{max}$, switching frequency f_S remains always at 500 kHz as k decreases. It will be shown that such fixed switching frequency operation can achieve good compromise between various tradeoffs. For now, it should be mentioned that since available peak voltage gain increases as k decreases, voltage gain curve becomes sharp and highly non-linear. Consequently, even a small error in frequency tracking occurring in attempt to track a load-independent voltage gain frequency can cause operation to fall out of ZVS region. Furthermore, frequency tracking error can cause voltage gain to be very high, causing significantly large circulating current (reactive power) and high losses in an additional downstream converter or linear voltage regulator.

From this point on, quantities with the subscript, '$\_k_{max}$', correspond to their values when $k = k_{max}$ (specific condition), and quantities with the subscript, '$\_k$', correspond to their values at $k \leq k_{max}$ (general condition).

In order to derive analytical expressions that can approximate voltage gain, current gain, and circulating current gain under k variation when the switching frequency is fixed at $\omega_S\_SS\_k_{max} = \omega_{OVp}\_k_{max} = \omega_{OVs}\_k_{max} = \omega_{OV2}\_k_{max}$, it is important to determine which of ω_{OVp} (Equation 42), ω_{OVs} (Equation 43), and ω_{OV2} (Equation 45) has the *lowest* sensitivity against k variation.

For loosely-coupled systems with $L_{S1} \geq L_{S2}'$, $\left|\frac{\partial(\omega_{ovp})}{\partial k}\right|$ is *lower* than $\left|\frac{\partial(\omega_{ovs})}{\partial k}\right|$ and $\left|\frac{\partial(\omega_{ov2})}{\partial k}\right|$. Consequently, it is important to derive an expression for $\omega_{OVp\_k_{max}}$ in terms of ω_{OVp_k} for all k in an allowed loosely-coupled k range. Assuming the small variations in L_{S1} and L_{S2}' in a loosely-coupled k range, an expression for approximating $\omega_{OVp\_k_{max}}$ in terms of ω_{OVp_k} is derived as Equation 49.

$$\omega_{OVp\_k_{max}} \approx \omega_{OVp\_k}\sqrt{\frac{1-k\sqrt{\frac{L_{S2}'}{L_{S1}}}}{1-k_{max}\sqrt{\frac{L_{S2}'}{L_{S1}}}}} \quad \text{..... Equation (49)}$$

The following expressions are then derived to approximate $\|G_V(j\omega_{ovp\_k_{max}})\|_{SS}$ (Equation 50), $\|G_i(j\omega_{ovp\_k_{max}})\|_{SS}$ (Equation 51), and $\|G_{iLm}(j\omega_{ovp\_k_{max}})\|_{SS}$ (Equation 52) for $0 < k \leq k_{max}$ in loosely-coupled systems. The resonant capacitances, C_1 and C_2', are selected so that Equation 53 is satisfied - **Note**: Satisfying Equation 53 is equivalent to achieving the desirable frequency condition of $\omega_{OVp\_k_{max}} = \omega_{OVs\_k_{max}} = \omega_{OV2\_k_{max}}$.

$$\left\|G_V\left(j\omega_{ovp\_k_{max}}\right)\right\|_{SS} \approx \left\|G_V\left(j\omega_{ovp\_k}\right)\right\|_{SS} =$$

$$\frac{kQ_{L_{SS}}}{\sqrt{{k_{max}}^2{Q_{L_{SS}}}^2 - \frac{\left[k^2 - k_{max}\sqrt{\frac{L_{S2}'}{L_{S1}}}\left(\frac{(\omega_{LS2})^2}{(\omega_{LS1})^2}k_{max}\sqrt{\frac{L_{S2}'}{L_{S1}}} - \frac{(\omega_{LS2})^2}{(\omega_{LS1})^2} + 1\right)\right]^2}{k_{max}\sqrt{\frac{L_{S2}'}{L_{S1}}} - 1}}} \quad \text{..... Equation (50)}$$

$$\left\|G_i\left(j\omega_{ov_p}\_k_{max}\right)\right\|_{SS} \approx \left\|G_i\left(j\omega_{ov_p}\_k\right)\right\|_{SS} =$$

$$\frac{1}{\frac{C_1}{C_2'}\left(\frac{1}{k}\sqrt{\frac{L_{S1}}{L_{S2}'}} - \frac{k_{max}}{k}\right)\sqrt{\left(\frac{(\omega_{Ls1})^2}{(\omega_{Ls2})^2\left(k_{max}\sqrt{\frac{L_{S2}'}{L_{S1}}} - 1\right)} + 1\right)^2 - \frac{C_2'(\omega_{Ls1})^2 Q_{L_{SS}}{}^2}{C_1(\omega_{Ls2})^2\left(k_{max}\sqrt{\frac{L_{S2}'}{L_{S1}}} - 1\right)}}} \quad \text{..... Equation (51)}$$

$$\left\|G_{iLm}\left(j\omega_{ov_p}\_k_{max}\right)\right\|_{SS} \approx \left\|G_{iLm}(j\omega_{ov_p}\_k)\right\|_{SS} ==$$

$$\frac{\sqrt{\left(\frac{(\omega_{Ls1})^2\left(1-k\sqrt{\frac{L_{S1}}{L_{S2}'}}\right)}{(\omega_{Ls2})^2\left(k_{max}\sqrt{\frac{L_{S2}'}{L_{S1}}} - 1\right)} + 1\right)^2 - \frac{C_2'(\omega_{Ls1})^2 Q_{L_{SS}}{}^2}{C_1(\omega_{Ls2})^2\left(k_{max}\sqrt{\frac{L_{S2}'}{L_{S1}}} - 1\right)}}}{\sqrt{\left(\frac{(\omega_{Ls1})^2}{(\omega_{Ls2})^2\left(k_{max}\sqrt{\frac{L_{S2}'}{L_{S1}}} - 1\right)} + 1\right)^2 - \frac{C_2'(\omega_{Ls1})^2 Q_{L_{SS}}{}^2}{C_1(\omega_{Ls2})^2\left(k_{max}\sqrt{\frac{L_{S2}'}{L_{S1}}} - 1\right)}}} \quad \text{..... Equation (52)}$$

$$\frac{C_2'}{C_1} = \frac{L_{S1}\left(1-k_{max}\sqrt{\frac{L_{S2}'}{L_{S1}}}\right)}{L_{S2}'\left(1-k_{max}\sqrt{\frac{L_{S1}}{L_{S2}'}}\right)} \quad \text{..... Equation (53)}$$

5.2.3 Design Equations for Loosely-coupled SS Resonant Tank with $L_{S1} < L_{S2}'$

For loosely-coupled systems with $L_{S1} < L_{S2}'$, $\left|\frac{\partial(\omega_{ov_s})}{\partial k}\right|$ is *lower* than $\left|\frac{\partial(\omega_{ov_p})}{\partial k}\right|$ and $\left|\frac{\partial(\omega_{ov_2})}{\partial k}\right|$. Consequently, it is important to derive an expression for $\omega_{OVs}\_k_{max}$ in terms of ω_{OVs}_k. Assuming the small variations in L_{S1} and L_{S2}' in loosely-coupled k range, an expression for approximating $\omega_{OVs}\_k_{max}$ in terms of ω_{OVs}_k is derived as Equation 54.

$$\omega_{OVs}\_k_{max} \approx \omega_{OVs}\_k\sqrt{\frac{1-k\sqrt{\frac{L_{S1}}{L_{S2}'}}}{1-k_{max}\sqrt{\frac{L_{S1}}{L_{S2}'}}}} \quad \text{..... Equation (54)}$$

The following expressions are then derived to approximate $\|G_V(j\omega_{ov_s}\_k_{max})\|_{SS}$ (Equation 55), $\|G_i(j\omega_{ov_s}\_k_{max})\|_{SS}$ (Equation 56), and $\|G_{iLm}(j\omega_{ov_s}\_k_{max})\|_{SS}$ (Equation 57) for $0 < k \leq k_{max}$. Again in these equations, the resonant capacitances, C_1 and C_2', are selected so that Equation 53 is satisfied.

$$\left\|G_V\left(j\omega_{ov_s}\_k_{max}\right)\right\|_{SS} \approx \left\|G_V\left(j\omega_{ov_s}\_k\right)\right\|_{SS} =$$

$$\frac{k Q_{L_{SS}} \left(\frac{\omega_{Ls2}}{\omega_{Ls1}}\right)}{\sqrt{\left(\frac{C_2'}{C_1}\right) Q_{L_{SS}}{}^2 \left(1 - k_{max}\sqrt{\frac{L_{s1}}{L_{s2}'}} - \frac{(\omega_{Ls2})^2}{(\omega_{Ls1})^2}\right)^2 + \left(1 - k_{max}\sqrt{\frac{L_{s1}}{L_{s2}'}}\right)^3 \left(\frac{\frac{(\omega_{Ls2})^2}{(\omega_{Ls1})^2} + 1}{k_{max}\sqrt{\frac{L_{s1}}{L_{s2}'}} - 1} + \frac{(\omega_{Ls2})^2}{(\omega_{Ls1})^2} \frac{(1-k^2)}{\left(k_{max}\sqrt{\frac{L_{s1}}{L_{s2}'}} - 1\right)^2} + 1\right)^2}}$$

..... Equation (55)

$$\left\|G_i\left(j\omega_{ov_s}\_k_{max}\right)\right\|_{SS} \approx \left\|G_i\left(j\omega_{ov_s}\_k\right)\right\|_{SS} = \frac{k}{\sqrt{k_{max}{}^2 + \frac{(\omega_{Ls1})^2}{(\omega_{Ls2})^2} Q_{L_{SS}}{}^2 \left(1 - k_{max}\sqrt{\frac{L_{s1}}{L_{s2}'}}\right)}}$$ .... Equation (56)

$$\left\|G_{iLm}\left(j\omega_{ov_s}\_k_{max}\right)\right\|_{SS} \approx \left\|G_{iLm}\left(j\omega_{ov_s}\_k\right)\right\|_{SS} = \sqrt{\frac{\frac{L_{s1}}{L_{s2}'}(k_{max} - k)^2 + \frac{C_2'}{C_1} Q_{L_{SS}}{}^2 \left(1 - k_{max}\sqrt{\frac{L_{s1}}{L_{s2}'}}\right)}{\frac{L_{s1}}{L_{s2}'} k_{max}{}^2 + \frac{C_2'}{C_1} Q_{L_{SS}}{}^2 \left(1 - k_{max}\sqrt{\frac{L_{s1}}{L_{s2}'}}\right)}}$$

..... Equation (57)

In summary, when SS resonant converter operation is performed always at $\omega_S\_SS\_k_{max}$ (equal to $\omega_{OVp}\_k_{max} = \omega_{OVs}\_k_{max} = \omega_{OV2}\_k_{max}$), equations 50 through 53 allow approximation of voltage gain, current gain, and circulating current under k variation for loosely-coupled SS resonant tank with $L_{S1} \geq L_{S2}$' while equations 53 through 57 allow approximation of these quantities with $L_{S1} < L_{S2}$'.

5.3 Derivation Of General Analytical Equations In Frequency Domain For SP Resonant Tank Topology

This section provides various general analytical equations for analyzing various notable quantities of the SP resonant tank topology.

5.3.1 General Analytical Solutions For SP Resonant Tank

For SP resonant tank, general equations for voltage gain $\|G_V(j\omega)\|_{SP}$ and current gain $\|G_i(j\omega)\|_{SP}$ are given in Equation 58 and Equation 59 respectively.

$$\| G_V(j\omega) \|_{SP} = \left| \frac{\omega^2 C_1 L_m R_{eSP}'}{\omega^4 R_{eSP}' C_1 C_2' L_{S1} L_{S2}' (1-k^2) - \omega^2 R_{eSP}' (C_1 L_{S1} + C_2' L_{S2}') + R_{eSP}' - j(\omega^3 C_1 L_{S1} L_{S2}' (1-k^2) - \omega L_{S2}')} \right| \quad \text{..... Equation (58)}$$

$$\|G_i(j\omega)\|_{SP} = \left| \frac{j\omega L_m}{R_{eSP}'(\omega^2 C_2' L_{s2}' - 1) - j\omega L_{s2}'} \right| \quad \text{..... Equation (59)}$$

The resonant frequency, at which the *imaginary* part in the denominator of Equation 58 becomes zero, is determined by the short-circuited load resonant frequency (ω_{ov}) in Equation 60. Also, the resonant frequency at which the *real* part in the denominator of Equation 59 becomes zero is defined as the open-circuited input resonant frequency (ω_{oi}) in Equation 61.

$$\omega_{ov} = \frac{1}{\sqrt{C_1\left(L_{e1} + \frac{L_m L_{e2}'}{L_m + L_{e2}'}\right)}} = \frac{\omega_{Ls1}}{\sqrt{1-k^2}} \quad \text{..... Equation (60)}$$

$$\omega_{oi} = \frac{1}{\sqrt{C_2' L_{s2}'}} = \omega_{Ls2} \quad \text{..... Equation (61)}$$

Substituting Equation 60 into Equation 58, it can be shown that the voltage gain at frequency ω_{ov} is load-independent, and this load-independent voltage gain, $|G_V|_{ind}SP$, is

defined as Equation 62. Similarly, substituting Equation 61 into Equation 59 results in load-independent current gain, $|G_i|_{ind}SP$, defined by Equation 63.

$$|G_V|_{ind}SP = \|G_V(j\omega_{ov})\|_{SP} = \frac{L_{s2}'}{L_m} = \frac{1}{k}\sqrt{\frac{L_{s2}'}{L_{s1}}} \quad \text{..... Equation (62)}$$

$$|G_i|_{ind}SP = \|G_i(j\omega_{oi})\|_{SP} = \frac{L_m}{L_{s2}'} = k\sqrt{\frac{L_{s1}}{L_{s2}'}} \quad \text{..... Equation (63)}$$

This means that ω_{ov} is the frequency at which leakage inductances, L_{e1} and L_{e2}', are shorted out, and ω_{oi} is the frequency in which circulating currents through L_m and C_2' are minimized.

Three different modes having distinct resonant characteristics can be identified based on the relative values of ω_{ov} and ω_{oi}: Mode A for $\omega_{ov} > \omega_{oi}$, Mode B for $\omega_{ov} = \omega_{oi}$, and Mode C for $\omega_{ov} < \omega_{oi}$. Voltage gain, $\|G_V(j\omega)\|_{SP}$, and current gain, $\|G_i(j\omega)\|_{SP}$, of the SP resonant tank topology are plotted in Figure 5.2 for these three different modes.

From equation 60 and 61, it follows that modes A, B, and C also correspond to the conditions: $\frac{\omega_{Ls1}}{\omega_{Ls2}} > \sqrt{1-k^2}$, $\frac{\omega_{Ls1}}{\omega_{Ls2}} = \sqrt{1-k^2}$, and $\frac{\omega_{Ls1}}{\omega_{Ls2}} < \sqrt{1-k^2}$ respectively. Therefore, depending on the choice for a nominal *k* value in the design process, all three modes may be observed throughout the charging process. For example, if $k = 0.2$ is selected as the nominal condition for achieving Mode B in a desired *k* variation range of $0.1 \leq k \leq 0.3$, then Mode A is observed as *k* increases above 0.2, and Mode C is observed as *k* decreases below 0.2.

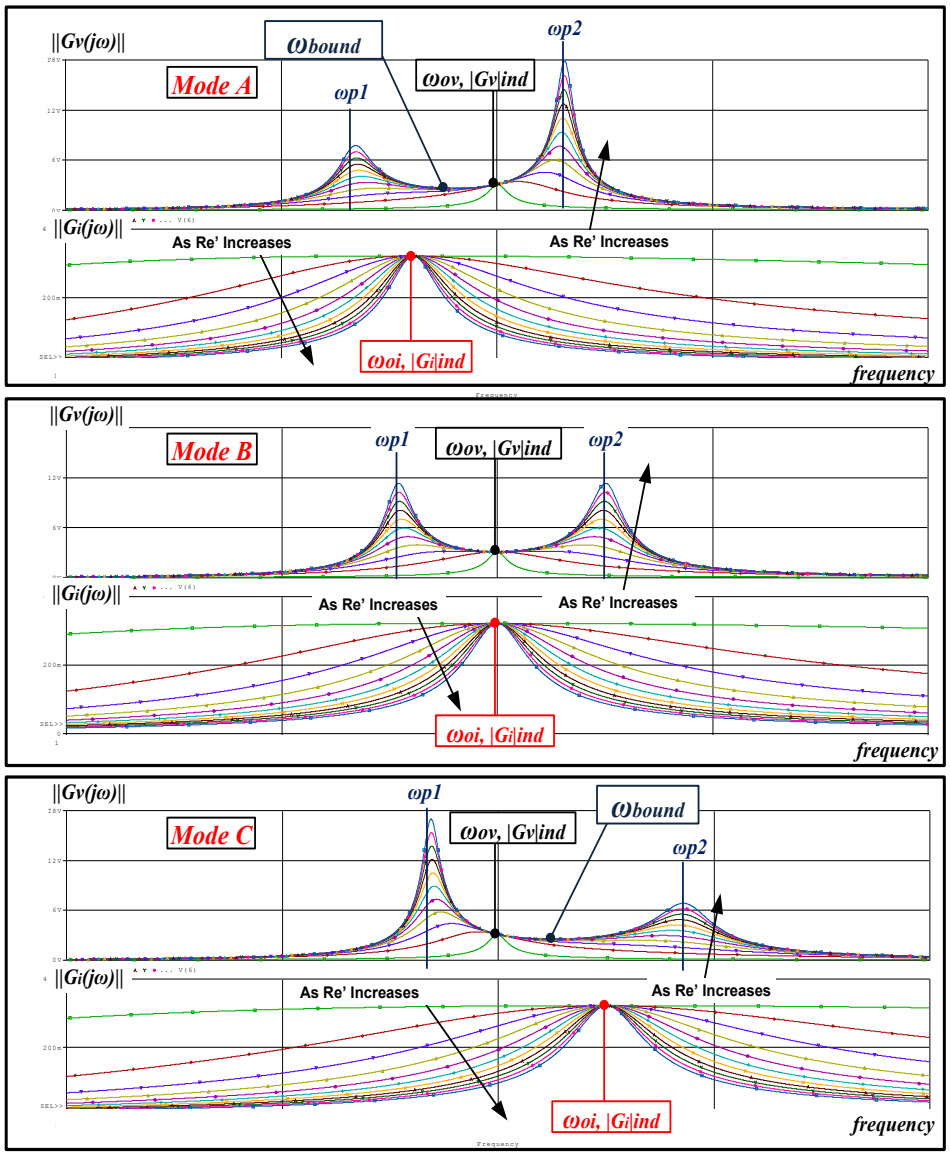

Figure 5.2: Voltage gain, $\|G_V(j\omega)\|_{SP}$, and current gain, $\|G_i(j\omega)\|_{SP}$, of SP resonant tank with fixed k under Re' (Q_{Lsp}) variation.
Note: Mode A: $\omega_{ov} > \omega_{oi}$; Mode B: $\omega_{ov} = \omega_{oi}$; Mode C: $\omega_{ov} < \omega_{oi}$.

Referring to the plots of Figure 5.2, the following general observations can be made. The current gain function $\|G_i(j\omega)\|_{SP}$ has a maximum at resonant frequency ω_{oi} and becomes sharper as Q_{Lsp} (or R_{eSP}') increases. The voltage gain function $\|G_V(j\omega)\|_{SP}$ exhibits a single maximum at resonant frequency ω_{ov} for low Q_{Lsp}. As Q_{Lsp} increases, two maxima with a value larger than $|G_V|_{ind}SP$ appear at resonant frequencies ω_{P1} and ω_{P2}.

Unlike the voltage gain at ω_{ov}, voltage gains at these two resonant frequencies (ω_{P1} and ω_{P2}) are Q_{Lsp}-dependent.

In Mode A, voltage gain peak at ω_{P1} is smaller than voltage gain peak at ω_{P2}, and the opposite occurs in Mode C. In Mode B, the two peaks are equal in magnitude.

General equations for determining resonant frequencies, ω_{P1} and ω_{P2}, are derived as Equation 64 and Equation 65 respectively. The geometric mean of these two resonant frequencies results in the boundary frequency, ω_{bound} (Equation 66). In Mode B, ω_{bound} is equal to $\omega_{ov} = \omega_{oi}$.

$$\omega_{P1} = \omega_{LS1}\omega_{LS2}\sqrt{\frac{2}{\omega_{LS1}^{\ 2} + \omega_{LS2}^{\ 2} + \sqrt{\omega_{LS1}^{\ 4} + \omega_{LS2}^{\ 4} + 4\omega_{LS1}^{\ 2}\omega_{LS2}^{\ 2}\left(k^2 - \frac{1}{2}\right)}}} \quad \text{..... Equation (64)}$$

$$\omega_{P2} = \omega_{LS1}\omega_{LS2}\sqrt{\frac{2}{\omega_{LS1}^{\ 2} + \omega_{LS2}^{\ 2} - \sqrt{\omega_{LS1}^{\ 4} + \omega_{LS2}^{\ 4} + 4\omega_{LS1}^{\ 2}\omega_{LS2}^{\ 2}\left(k^2 - \frac{1}{2}\right)}}} \quad \text{..... Equation (65)}$$

$$\omega_{bound} = \sqrt{\omega_{P1}\omega_{P2}} = \sqrt{\omega_{ov}\omega_{oi}} \quad \text{..... Equation (66)}$$

In terms of efficiency in SP resonant tank, operating in Mode B is optimal. In order to prove this analytically, a simplified transformer model of SP resonant tank can be shown using dependent current source and dependent voltage source as in Figure 5.3. In this figure, the input voltage of SP resonant tank is denoted as V_i, and the input current is denoted as I_i. The output voltage and output current of SP resonant tank are denoted as V_O and I_O respectively.

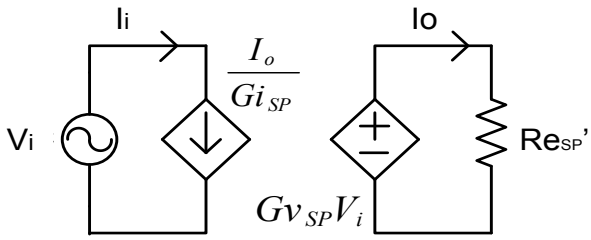

Figure 5.3: Simplified transformer model of SP resonant tank

The input power is a complex power, $S_{in} = V_iI_i^*$, while the output power, P_{out}, delivered to R_{eSP}' can be represented as $P_{out} = V_OI_O = V_OI_O^*$. The complex input power can also be represented as Equation 67 in terms of voltage gain $G_V(j\omega)_{SP}$, current gain $G_i(j\omega)_{SP}$, and P_{out}.

$$S_{\text{in}} = V_i I_i^* = \left(\frac{V_O}{G_V(j\omega)_{SP}}\right)\left(\frac{I_O^*}{G_i(j\omega)_{SP}^*}\right) = \frac{P_{out}}{(G_V(j\omega)_{SP})(G_i(j\omega)_{SP}^*)} \quad \text{..... Equation (67)}$$

If operating frequency achieves $\omega = \omega_{ov} = \omega_{oi}$ in Mode B, then Equation 62 and Equation 63 can be substituted into the denominator of Equation 67. It can be concluded that $S_{in} = P_{out}$ in Mode B at $\omega = \omega_{ov} = \omega_{oi}$. Since the condition, $S_{in} = P_{out}$, is indicative of ideal efficiency of unity with zero input reactive power, it is proven that operating at switching frequency ω_s equal to $\omega_{ov} = \omega_{oi}$ in Mode B is optimal in terms of efficiency.

In order to decide whether it is desirable to obtain Mode B at $k = k_{max}$ or at $k < k_{max}$, it is of interest to examine the input impedance of the SP resonant tank, because it determines soft switching operation of the primary-side switch network. Figure 5.4 shows the graphical representation (not in scale) of input impedance, $\|Z_i(j\omega)\|_{SP}$, characteristics. Figure 5.4 (a) corresponds to the condition of $\|G_V\|_{max} = |G_V|_{ind}SP$ (low Q_{Lsp}), and Figure 5.4 (b) corresponds to the condition of $\|G_V\|_{max} >> |G_V|_{ind}SP$ (high Q_{Lsp}). Thus, Figure 5.4 shows how Q affects the frequency ranges in which SP resonant tank input impedance is

resistive, capacitive, or inductive - Note: Input impedance $Z_i(j\omega)_{SP}$ satisfies the equation

$$Z_i(j\omega)_{SP} = R_{eSP}' \frac{G_i(j\omega)_{SP}}{G_V(j\omega)_{SP}}.$$

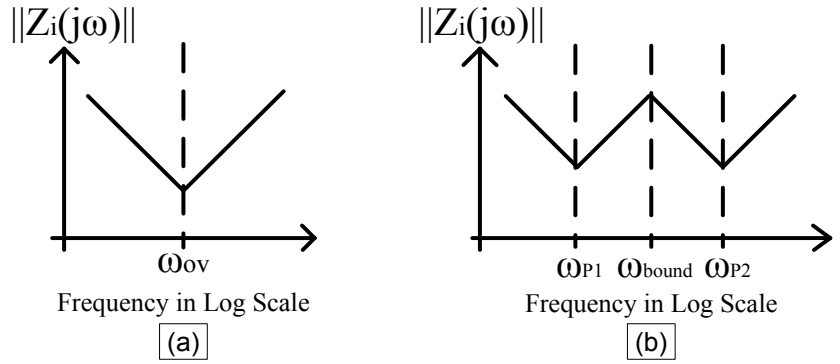

Figure 5.4: Graphical representation of input impedance, $||Z_i(j\omega)||_{SP}$, characteristics for $||G_V||_{max} = |G_V|_{ind}SP$ (a) and for $||G_V||_{max} >> |G_V|_{ind}SP$ (b).

To reduce switching losses, the primary-side switch network should operate either in zero voltage switching (ZVS) or in zero voltage zero current switching (ZVS-ZCS). ZVS-ZCS is achieved only at the resonant frequencies, where the input impedance is *resistive*. ZVS requires that $Z_i(j\omega)_{SP}$ be *inductive*. Therefore, switching frequency (ω_S) must satisfy that $\omega_{ov} \leq \omega_S$ for low Q_{Lsp}, as can be seen in Figure 5.4 (a). For high Q_{Lsp}, ω_S must satisfy either of two conditions: $\omega_{P1} \leq \omega_S \leq \omega_{bound}$ or $\omega_{P2} \leq \omega_S$, as can be seen in Figure 5.4 (b).

Based on this consideration, it turns out that Mode A is *not* desirable, because in Mode A, $||G_V(j\omega_s)||_{SP}$ characteristic for $\omega_{P1} \leq \omega_S \leq \omega_{bound}$ is *highly* load (Q_{Lsp}) dependent and non-linearly changing, and *also* can become *very* sensitive to switching frequency tracking error depending on the Q_{Lsp} value. Furthermore, $Z_i(j\omega_s)_{SP}$ for $\omega_{P1} \leq \omega_S \leq \omega_{bound}$ may become capacitive for a large load (low Q_{Lsp}). This forces the resonant tank to be designed to exhibit a very large Q_{Lsp} to avoid capacitive input impedance. But a very large Q_{Lsp} is undesirable, because it causes very large circulating currents in a coupler

and parallel resonant capacitor. The other alternative is to operate in the other inductive region at $\omega_{P2} \leq \omega_S$: this eliminates the danger of capacitive $\|Z_i(j\omega_S)\|_{SP}$, but it increases the reactive power. Thus, achieving a sufficient voltage gain (comparable to $|G_V|_{ind}SP$) causes large reactive power, and consequently the current gain becomes undesirably small.

Mode A needs to be avoided, and, to do so, the resonant tank needs to be designed to exhibit Mode B for the highest k (k_{max}) in an expected k range. When Mode B is achieved at $k = k_{max}$, Mode C is inevitably entered as k decreases. Mode A will not be considered further.

Again, in order to distinguish between quantities achieved at $k = k_{max}$ (specific condition), and the same quantities exhibited at $k \leq k_{max}$ (general condition), the subscripts, "$\_k_{max}$" and "$\_k$", will be used in this section. For example, $\omega_{ov}\_k_{max}$ is the resonant frequency of load-independent voltage gain of SP resonant tank when $k = k_{max}$, whereas ω_{ov}_k is that when $k \leq k_{max}$.

In order to show various effects of k variation, Figure 5.5 shows $\|G_V(j\omega)\|_{SP}$ and $\|G_i(j\omega)\|_{SP}$ as k decreases from k_{max}. The red curves are obtained in Mode B at $k = k_{max}$. The black curves are obtained at $k < k_{max}$. As k *decreases*, Figure 5.5 shows that ω_{ov} *decreases* (thus, $\omega_{ov}\_k_{max} > \omega_{ov}\_k$), whereas ω_{oi} *increases* (thus, $\omega_{oi}\_k_{max} < \omega_{oi}\_k$). From Figure 5.5, the following observation can also be made: if switching frequency $\omega_S\_SP\_k_{max}$ is fixed at $\omega_{ov}\_k_{max} = \omega_{oi}\_k_{max}$, input impedance $Z_i(j\omega_S\_SP\_k_{max})_{SP}$ changes *from* being *resistive to* being *inductive* as Mode B becomes Mode C. This is indicated in Figure 5.5 by $\omega_S\_SP\_k_{max} = \omega_{ov}\_k_{max} = \omega_{oi}\_k_{max}$ being at the mid-point of two voltage gain peaks and at the peak of current gain in Mode B and being in the frequency range of the *monotonically-decreasing* voltage gain curve in Mode C.

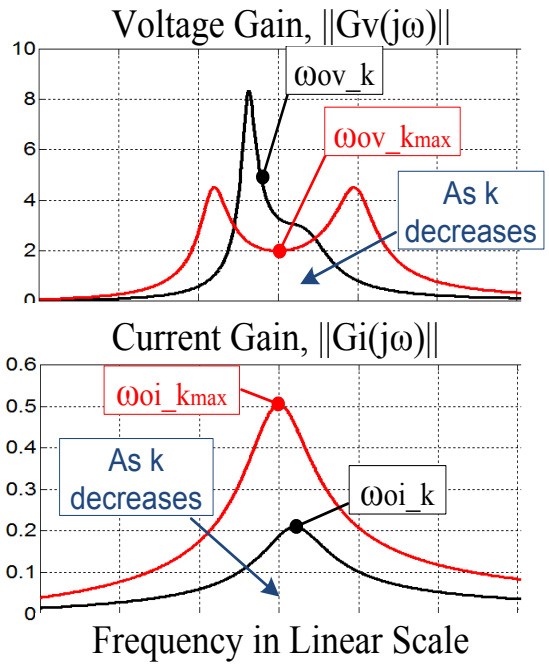

Figure 5.5: Voltage gain $\|G_V(j\omega)\|_{SP}$ (top) and current gain $\|G_i(j\omega)\|_{SP}$ (bottom) under varied k: as Mode B becomes Mode C.

For an optimal performance, it is proposed to perform fixed switching frequency operation of SP resonant tank at switching frequency $\omega_S\_SP\_k_{max}$: as a result, for $k = k_{max}$, the operation is in Mode B under ZVS-ZCS, and for all other $k < k_{max}$ operation occurs in Mode C under ZVS. This fixed switching frequency operation avoids control complexity in tracking and achieving under k variation *either* $\omega_S\_SP\_k = \omega_{ov}\_k$ *or* $\omega_S\_SP\_k = \omega_{oi}\_k$. It should be noted that tracking and achieving *either* $\omega_S\_SP\_k = \omega_{ov}\_k$ *or* $\omega_S\_SP\_k = \omega_{oi}\_k$ may not be desirable because of the following conflicting characteristics:

- Operating at $\omega_S\_SP\_k = \omega_{oi}\_k$ when $k < k_{max}$ provides minimized circulating currents, however can exhibit undesirably low voltage gain because leakage inductances are not compensated.
- Operating at $\omega_S\_SP\_k = \omega_{ov}\_k$ when $k < k_{max}$ provides full compensation of leakage inductances, however can exhibit undesirably high circulating current losses. Also, as can be observed from both Figure 5.2 and Figure 5.5, $|G_V|_{ind}SP\_k$ (equal to

$||G_V(j\omega_{ov}\_k)||_{SP}$) can be much larger than $|G_V|_{ind}SP\_k_{max}$ (equal to $||G_V(j\omega_{ov}\_k_{max})||_{SP}$) when $k < k_{max}$. Therefore, it can cause significantly-increased losses in an additional converter or linear voltage regulator.

Thus, by operating always at $\omega_S\_SP\_k_{max} = \omega_{ov}\_k_{max} = \omega_{oi}\_k_{max}$, a good compromise can be obtained between these conflicting features so that ZVS-ZCS or ZVS without significantly large reactive power can be performed under k variation. Also, depending on Q_{Lsp}, it is possible to make the red and black voltage gain curves in Figure 5.5 intersect at $\omega_{ov}\_k_{max}$. Since $||G_V(j\omega_s\_SP\_k_{max})||_{SP}$ is not decreasing monotonically as k decreases, this means that with optimal Q_{Lsp} selection, voltage gain robustness can be maximized so as to obtain almost constant voltage gain under k variation.

Again, in order to determine analytical expressions for voltage gain, current gain, and circulating current gain at the fixed frequency of $\omega_s\_SP\_k_{max}$ under k variation, it is important to determine first the robust frequency that does *not* vary significantly under k variation. This robust frequency depends on the relative values of L_{S1} and L_{S2}'.

For SP resonant tank, two different sets of approximations can be derived separately for two different cases of $L_{S1} \leq L_{S2}$' and $L_{S1} > L_{S2}$'.

5.3.2 Design Equations for Loosely-coupled SP Resonant Tank with $L_{S1} \leq L_{S2}$'

In loosely-coupled systems, it can be concluded based on Equation 61 that ω_{oi}_k is only slightly higher than $\omega_S\_SP\_k_{max} = \omega_{ov}\_k_{max} = \omega_{oi}\_k_{max}$ when $k < k_{max}$, This is because in loosely-coupled systems $\left|\frac{\partial L_{S2}}{\partial k}\right|$ is very small.

Furthermore, since obtaining Mode B requires $C_1 > C_2$' when $L_{S1} \leq L_{S2}$', it can be concluded based on Equation 60 and Equation 61 that the magnitude of *decrease* in load-

independent voltage gain frequency is *larger* than that of *increase* in load-independent current gain frequency, that is $\left|\frac{\partial \omega_{OV}}{\partial k}\right| > \left|\frac{\partial \omega_{Oi}}{\partial k}\right|$.

Therefore, determining quantities of interest at ω_{oi} (Equation 61) provides approximation for the quantities of interest under the fixed frequency operation at $\omega_S\_SP\_k_{max}$. To approximate $\|G_V(j\omega_S\_SP\_k_{max})\|_{SP}$, a *general* equation for voltage gain at the frequency of load-independent current gain, $\|G_V(j\omega_{oi})\|_{SP}$, is derived as Equation 68. It can be easily verified that Equation 68 becomes Equation 62 *iff* $\omega_{ov} = \omega_{oi}$ (Mode B operation).

$$\left\|G_V(j\omega_S\_SP\_k_{\max})\right\|_{SP} \approx \left\|G_V(j\omega_{oi})\right\|_{SP} = \frac{Q_{LSP}}{\sqrt{k^2 Q_{LSP}{}^2 \frac{L_{S1}}{L_{S2}'} + \left(\frac{1-k^2}{k}\right)^2 \frac{L_{S1}}{L_{S2}'} + \frac{1}{k^2}\left(\frac{C_2'}{C_1}\right)^2 \frac{L_{S2}'}{L_{S1}} - 2\left(\frac{1-k^2}{k^2}\right)\left(\frac{C_2'}{C_1}\right)}}$$

..... Equation (68)

Since C_1 and C_2' are selected to obtain $\omega_{ov}\_k_{max} = \omega_{oi}\_k_{max}$, ratio $\frac{C_2'}{C_1}$ is a fixed value determined by Equation 69, which is obtained by equating Equation 60 and Equation 61.

$$\frac{C_2'}{C_1} = \left(1 - k_{\max}{}^2\right)\frac{L_{S1}}{L_{S2}'} \quad \text{..... Equation (69)}$$

As k decreases below k_{max} (for $\omega_{ov}\_k < \omega_S\_SP\_k_{max} < \omega_{oi}\_k$ occurring due to k decrease), Equation 68 can be used for approximating what $\|G_V(j\omega_S\_SP\_k_{max})\|_{SP}$ is. Thus, maximum robustness in voltage gain is achieved when Equation 68 remains close to $|G_V|_{ind}SP\_k_{max}$ under k variation.

In order to approximate the current gain at the fixed frequency, $\omega_S\_SP\_k_{max}$, under k variation, Equation 63 can be used as long as Q_{Lsp} is not very high: with a *very high* value

of Q_{Lsp}, it *cannot* be assumed that $\|G_i(j\omega_S\_SP\_k_{max})\|_{SP} \approx \|G_i(j\omega_{oi}\_k)\|_{SP}$. Instead, with a very high Q_{Lsp}, it is $\|G_i(j\omega_S\_SP\_k_{max})\|_{SP} << \|G_i(j\omega_{oi}\_k)\|_{SP}$, which is undesirable - Note: $\omega_S\_SP\_k_{max} \approx \omega_{oi}\_k_{max}$.

In order to evaluate the effects of Q_{Lsp} on the circulating current, i_{Lm}, through L_m, a *general* expression for $\|G_{iLm}(j\omega_{oi})\|_{SP}$ is derived as Equation 70. This equation can be used for estimating the circulating current in a coupler under k variation when the converter operation is performed at the fixed switching frequency, $\omega_S\_SP\_k_{max}$.

$$\|G_{iLm}(j\omega_S\_SP\_k_{\max})\| \approx \|G_{iLm}(j\omega_{oi})\| = \sqrt{k^2\left(Q_{LSP}{}^2+1\right)\frac{L_{S1}}{L_{S2}'} - 2k\sqrt{\frac{L_{S1}}{L_{S2}'}} + 1} \quad \text{..... Equation (70)}$$

5.3.3 Design Equations for Loosely-coupled SP Resonant Tank with $L_{S1} > L_{S2}$'

In a loosely-coupled system with $L_{S1} > L_{S2}$', obtaining Mode B requires $C_1 < C_2$', and the magnitude of *decrease* in load-independent voltage gain frequency may be *comparable* to or *smaller* than that of *increase* in load-independent current gain frequency (that is $\left|\frac{\partial\omega_{OV}}{\partial k}\right| \le \left|\frac{\partial\omega_{Oi}}{\partial k}\right|$). In this case, an expression for a better approximation of $\omega_S\_SP\_k_{max}$ can be Equation 71 rather than $\omega_S\_SP\_k_{max} \approx \omega_{oi}\_k$. In derivation of Equation 71, it is assumed that $\left|\frac{\partial L_{S1}}{\partial k}\right|$ and $\left|\frac{\partial L_{S2}}{\partial k}\right|$ are small. With fixed values for the resonant capacitors (C_1 and C_2'), it follows from Equation 60 that the relationship between the resonant frequency of load-independent voltage gain at $k = k_{max}$ and that at $k \le k_{max}$ can be expressed as Equation 71.

$$\omega_S\_SP\_k_{\max} \approx \left(\omega_{OV}\_k\right)\sqrt{\frac{1-k^2}{1-k_{\max}^2}} \quad \text{..... Equation (71)}$$

By substituting Equation 71 into Equation 58, Equation 72 is derived. Equation 72 is equal to Equation 62 *iff* $k = k_{max}$. If larger $\left|\frac{\partial L_{S1}}{\partial k}\right|$ is expected, for example when a higher value is expected for k_{max}, the geometric mean between Equation 60 and Equation 71 can be used to improve the accuracy of approximation for ω_S_SP_k_{max} under k variation. This geometric mean can be applied by replacing all of k_{max} terms in Equation 72 with k_M (weighted k_{max}) defined as Equation 73 – Note: $k_M = k_{max}$ *iff* $k = k_{max}$.

Applying this geometric mean places *approximated* ω_S_SP_k_{max} closer to *actual* ω_S_SP_k_{max}, thus it can be used to more accurately represent $\frac{\partial\left\|G_V(j\omega_S\_SP\_k_{\max})\right\|}{\partial k}$ and $\frac{\partial\left\|G_V(j\omega_s\_SP\_k_{\max})\right\|}{\partial Q_{L_{SS}}}$. In order to approximate current gain, $\|G_i(j\omega_s$_SP_$k_{max})\|_{SP}$, Equation 74 is derived by substituting Equation 71 into Equation 59. Also, circulating current gain, $\|G_{iLm}(j\omega_s$_SP_$k_{max})\|_{SP}$, can be approximated using Equation 75.

$$\left\|G_V(j\omega_S\_SP\_k_{\max})\right\| \approx \sqrt{\frac{1}{\left[\frac{k^2-k_{\max}^2}{k\left(k_{\max}^2-1\right)}\left(\frac{C_2'}{C_1}\right)\sqrt{\frac{L_{S2}'}{L_{S1}}}-\left(\frac{k_{\max}^2}{k}\right)\sqrt{\frac{L_{S1}}{L_{S2}'}}\right]^2-\left(\frac{C_2'}{C_1}\right)\left(\frac{1}{k^2Q_{LSP}{}^2}\right)\left(\frac{\left(k^2-k_{\max}^2\right)^2}{k_{\max}^2-1}\right)}}$$ ..... Equation (72)

$$k_M=\left(\frac{k_{\max}^2-1}{k^2-1}\right)^{\frac{1}{4}}\sqrt{k^2+\sqrt{\frac{1-k^2}{1-k_{\max}^2}}-1}$$ ..... Equation (73)

$$\|G_i(j\omega_s\_SP\_k_{max})\|_{SP} \approx \frac{k}{\sqrt{\frac{C_1}{C_2'}Q_{Lsp}{}^2\left(1-k_{max}{}^2\right)\left(1-\frac{\omega_{Ls1}{}^2}{\omega_{Ls2}{}^2\left(1-k_{max}{}^2\right)}\right)^2+\frac{L_{S2}'}{L_{S1}}}}$$ ..... Equation (74)

$$\|G_{iLm}(j\omega_{s\_}SP\_k_{max})\|_{SP} \approx \sqrt{\frac{Q_{Lsp}{}^2\left(1-\frac{\omega_{Ls1}{}^2\left(1-k\sqrt{\frac{L_{S1}}{L_{S2}'}}\right)}{\omega_{Ls2}{}^2\left(1-k_{max}{}^2\right)}\right)^2+\frac{\omega_{Ls1}{}^2\left(1-k\sqrt{\frac{L_{S1}}{L_{S2}'}}\right)^2}{\omega_{Ls2}{}^2\left(1-k_{max}{}^2\right)}}{Q_{Lsp}{}^2\left(1-\frac{\omega_{Ls1}{}^2}{\omega_{Ls2}{}^2\left(1-k_{max}{}^2\right)}\right)^2+\frac{\omega_{Ls1}{}^2}{\omega_{Ls2}{}^2\left(1-k_{max}{}^2\right)}}} \quad \text{..... Equation (75)}$$

In summary, using equation 58 through 67, general frequency-domain characteristics and various notable features of SP resonant tank topology can be analyzed. By using equation 58 through 75, the SP resonant tank topology of both ART type and SRT type can be analyzed in loosely-coupled systems. Furthermore, using equations 68 thorough 75 allows approximation of loosely-coupled SP resonant tank parameters required for achieving desirable resonance characteristics (desirable Q_{Lsp} condition for a desired nominal load, R_{eSP}').

5.4 Summary Of General Analytical Equations And Design Equations

Sections 5.2 and 5.3 present several novel accomplishments for analyzing and designing SS resonant tank and SP resonant tank of both ART and SRT types. Detailed frequency-domain analysis is performed for the resonant tanks to evaluate resonance characteristics and to derive general analytical equations in design-oriented form. By using these equations, analysis can be performed for SS and SP resonant tanks in both tightly-coupled and loosely-coupled wireless power transfer applications. By making assumptions applicable to magnetically loosely-coupled applications, various analytical design equations are derived for the two resonant tank topologies.

For each of the resonant tank topologies, the corresponding analytical design equations are derived separately depending on relative values of L_{S1} and L_{S2}' and are in terms of physically-meaningful quantities such as coupling coefficient, quality factor,

ratio between C_1 and C_2', and ratio between L_{S1} and L_{S2}'. Consequently, these equations provide high practical usefulness and allow convenient design procedures.

By using various analytical equations, analytical comparative study on SS and SP resonant tank topologies can be performed in order to provide an analytical method for deciding which of the two topologies is desirable for a certain application. Also, optimal design methods for magnetically loosely-coupled SS and SP resonant tanks can be developed, so that Q_{Lss} and Q_{Lsp} can be optimized for a desired nominal load. It will be demonstrated later that optimizing Q_{Lss} and Q_{Lsp} maximizes power delivery robustness against *k* variation without significantly-increased circulating current in a coupler.

Comparative study and optimal design methods are presented in the following sections, which include various results from simulation and experiment for evaluation and validation of proposed optimal design methods that use the presented analytical design equations.

5.5 Analytical Comparative Study on SS and SP Resonant Tank Topologies

In this section, comparative study is performed for three different categories. One of these categories is general comparison. The other two include evaluation of robustness in voltage gain and current gain (power delivery robustness), and evaluation of circulating current (coil-to-coil efficiency). These two evaluations are performed in detail using simulations under $L_{S1} \approx L_{S2}$'.

5.5.1 General Comparison

In general with unity turns ratio in a magnetic coupler, the SS resonant tank topology allows obtaining load-independent *unity* voltage gain *regardless* of relative values of L_{S1} and L_{S2}' - See Equation 48 under the condition of f_{OV2} (Equation 45) = f_{OVp} (Equation 42)

= f_{OVs} (Equation 43). When $L_{S1} = L_{S2}$' under *k* variation, the value of load-independent voltage gain remains at unity while the frequency of this unity voltage gain changes. However, when L_{S1} and L_{S2}' are different under *k* variation, the value of load-independent voltage gain does *not* remain at unity while the frequency of load-independent changes also. This means that, in SS resonant tank design process, it is known prior to the design process that a desirable load-independent voltage gain is unity regardless of coupler geometry. Consequently, since a desirable (or an expected) value of voltage gain is known prior to selection of coupler geometry, optimization of coupler and Q_{Lss} for a desired load condition is more flexible.

On the other hand, for the SP resonant tank topology, its load-independent voltage gain depends *only* on *k* and relative values of L_{S1} and L_{S2}' - See Equation 62. This means that expected voltage gain *cannot* be known *unless* a desired coupler geometry has been evaluated for its *k* and relative values of L_{S1} and L_{S2}'. For example, let us assume that a magnetic coupler is optimized while accounting for achieving optimal Q_{Lsp} for a desired output voltage of 1V. Then, a supply with adjustable voltage must be implemented to satisfy Equation 62, so that 1 V output is produced for the optimized coupler. Therefore, in SP resonant tank design process, design complexity increases significantly if optimization of coupler and Q_{Lsp} need to satisfy *both* fixed supply voltage and fixed load voltage. In conclusion, the SP resonant tank topology is a *less* flexible in terms of design process: either the supply voltage or load voltage should be adjustable.

In terms of minimizing the circulating current in a coupler, SS resonant tank performs better than SP resonant tank. In SS resonant tank, it is *possible* to obtain values of current gain and load-independent voltage gain that are both *close* to (but never equal to) one

under very low Q_{Lss} condition –See equations 50 and 51 for ω_{OVp} (Equation 42) = ω_{OVs} (Equation 43) while $k = k_{max}$ and $L_{S1} = L_{S2}$'. This condition of both current gain and load-independent voltage gain values being close to one represents maximized real power or equivalently minimized reactive power. However, achieving this condition is *impractical* at low k (in loosely-coupled wireless power transfer applications). In SP resonant tank, it is *impossible* to achieve current gain and load-independent voltage gain to be one *unless* k is near one (near perfect coupling) – See equation 62 and 63. These limitations will be explained later in more detail when comparing current gains of loosely-coupled SS and SP resonant tanks.

In a SS resonant converter, its output low-pass filter can be just a shunt capacitor in parallel with a load. However, in a SP resonant converter, its output low-pass filter needs to have a decoupling filter inductor, so as to prevent the output filter capacitor (in parallel with a load) from interacting with the parallel resonant capacitor, C_2'. Thus, conduction loss in the filter inductor in a SP resonant converter can also be a noticeable negative effect on overall system efficiency.

In summary, it can be said that ideally SS resonant tank is better than SP resonant tank in terms of power efficiency and in terms of minimizing power stage component count. However, as further evaluations in sections 5.5.4 through 5.6 will show, SS resonant tank cannot provide several advantages that SP resonant tank can. In order to perform various evaluations, ranges of interest for load-dependent quality factors, Q_{Lss} and Q_{Lsp}, are defined in sections 5.5.2 and 5.5.3 respectively.

5.5.2 Upper Boundary for Q_{Lss}

To determine the Q_{Lss} range of interest, SS resonant tank's voltage gain $||G_V(j\omega)||_{SS}$ can be analyzed. For SS resonant tank, exhibiting a high single voltage gain peak near *open-circuited load* resonant frequency, ω_{Ls1} due to high Q_{Lss} indicates undesirably large circulating current in a coupler. Once SS resonant tank is designed to achieve ω_{OVp} (Equation 42) = ω_{OVs} (Equation 43) = ω_{OV2} (Equation 45), it exhibits a well-defined single voltage gain peak approximately when $||G_V||_{max} \geq 1.5||G_V(j\omega_{ov2})||_{SS}$ for $L_{S1} \geq L_{S2}'$, *or* approximately when $||G_V||_{max} \geq 1.5||G_V(j\omega_{ov1})||_{SS}$ for $L_{S1} < L_{S2}'$. Substituting $||G_V(j\omega_{Vp})||_{SS} = 1.5$ into $||G_V(j\omega_{VP})||_{SS} = \frac{Q_{Lss}}{k}$, an *approximation* for SS resonant tank's quality factor threshold, Q_{THss}, is proposed as Equation 76. This is proposed as the upper boundary for Q_{Lss} range.

$$Q_{THSS} \approx 1.5k \quad \text{..... Equation (76)}$$

5.5.3 Upper Boundary for Q_{LSP}

When SP resonant tank is designed to exhibit two voltage gain peaks, circulating current loss can be significant. Therefore, it is important to determine the upper bound (Q_{THsp}) for Q_{Lsp} selection. As can be seen in Figure 5.2 for Mode B, two resonant peaks appear near ω_{P1} and ω_{P2} in voltage gain for large Q_{Lsp}, whereas for low $Q_{Lsp,}$ only a single resonant peak occurs at ω_{ov} in voltage gain. In this section, a normalized analysis is performed to determine a *general* equation for Q_{THsp}. In this analysis, in order to avoid dealing with *k*-dependent (inductance-dependent) $|G_V|_{ind}SP$ and $|G_i|_{ind}SP$, normalized voltage gain ($||G_V(j\omega)||_{SPn}$ defined as Equation 77) and normalized current gain ($||G_i(j\omega)||_{SPn}$ defined as Equation 78) are used. Without losing general applicability, the

normalization produces a reference scale in which both load-dependent voltage gain and load-independent current gain are unity.

$$\| G_V(j\omega) \|_{SPn} = \frac{\| G_V(j\omega) \|_{SP}}{| G_V |_{ind\ SP}} \quad \text{..... Equation (77)}$$

$$\| G_i(j\omega) \|_{SPn} = \frac{\| G_i(j\omega) \|_{SP}}{| G_i |_{ind\ SP}} \quad \text{..... Equation (78)}$$

Under the condition of $\frac{\omega_{L_{S1}}}{\omega_{L_{S2}}} = \sqrt{1-k^2}$ (or equivalently, Mode B: $\omega_{ov} = \omega_{oi}$), it can be found that $\|G_V(j\omega_{P1})\|_{SPn} = \|G_V(j\omega_{P2})\|_{SPn}$, and a general expression is derived as Equation 79, which can also be represented as $\| G_V(j\omega_{P1}) \|_{SPn} = \| G_V(j\omega_{P2}) \|_{SP\_n} = \frac{Q_{Lsp}(k\sqrt{4-3k^2}-k^2)}{\sqrt{2(k^2-1)(k^2+k\sqrt{4-3k^2}-2)}}$.

Furthermore, it can be found in Mode B that $\|G_i(j\omega_{P1})\|_{SPn} = \|G_i(j\omega_{P2})\|_{SPn}$ as well. A general expression for $\|G_i(j\omega_{P1})\|_{SPn} = \|G_i(j\omega_{P2})\|_{SPn}$ is derived as Equation 80. By using Equation 79 and Equation 80, a general mathematical relationship between $\|G_V(j\omega_{P1})\|_{SPn}$ and $\|G_i(j\omega_{P1})\|_{SPn}$ can be derived as Equation 81.

$$\| G_V(j\omega_{P1}) \|_{SPn} = \| G_V(j\omega_{P2}) \|_{SPn} = \frac{Q_{Lsp}(k\sqrt{4-3k^2}+k^2)}{\sqrt{2(k^2-1)(k^2-k\sqrt{4-3k^2}-2)}} \quad \text{..... Equation (79)}$$

$$\| G_i(j\omega_{P1}) \|_{SPn} = \| G_i(j\omega_{P2}) \|_{SPn} = \sqrt{\frac{1-k^2}{k^2(Q_{Lsp}{}^2-1)+1}} \quad \text{..... Equation (80)}$$

$$\| G_i(j\omega_{P1}) \|_{SPn} = \sqrt{\frac{1}{\| G_V(j\omega_{P1}) \|_{SPn}{}^2+1}} \quad \text{..... Equation (81)}$$

It turns out that upper boundary (Q_{THsp}) for Q_{Lsp} can be found from Equation 81 under the condition of $||G_V(j\omega_{P1})||_{SPn} = ||G_i(j\omega_{P1})||_{SPn}$: $\| G_V(j\omega_{P1}) \|_{SPn} = \| G_i(j\omega_{P1}) \|_{SPn} = \frac{\sqrt{2(\sqrt{5}-1)}}{2} \approx 0.786$. By substituting this condition into Equation 80, a general expression for the upper boundary (Q_{THsp}) for Q_{Lsp} selection can be derived as Equation 82.

$$Q_{THsp} = \frac{1}{k}\sqrt{(1-k^2)\left(\frac{2}{\sqrt{5}-1}-1\right)} \quad \text{..... Equation (82)}$$

To verify this finding, normalized voltage gain $||G_V(j\omega)||_{SPn}$ (red curve) and normalized current gain $||G_i(j\omega)||_{SPn}$ (green curve) are plotted in Figure 5.6 for the condition of $Q_{Lsp} = Q_{THsp}$ in linear frequency scale. As can be seen from this figure, $||G_V(j\omega_{P1})||_{SPn} = ||G_V(j\omega_{P2})||_{SPn} = ||G_i(j\omega_{P1})||_{SPn} = ||G_i(j\omega_{P2})||_{SPn} \approx 0.786$. Also, it can be seen that when $||G_V(j\omega_{P1})||_{SPn}$ and $||G_V(j\omega_{P2})||_{SPn}$ are greater than or equal to 0.786, two voltage gain peaks appear.

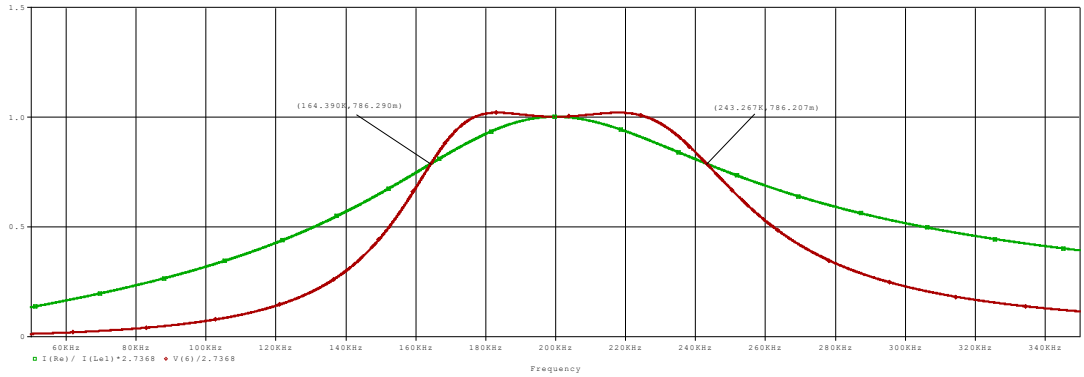

Figure 5.6: Normalized voltage gain $||G_V(j\omega)||_{SPn}$ (red curve) and normalized current gain $||G_i(j\omega)||_{SPn}$ (green curve) plotted for the condition of $Q_{Lsp} = Q_{THsp}$ in linear frequency scale.

In summary, $Q_{Lss} \geq Q_{THss}$ and $Q_{Lsp} \geq Q_{THsp}$ are not of significant interest for optimal design of SS and SP resonant tanks. In fact, the accuracy of approximation by proposed

design equations for loosely-coupled SS resonant tank can decrease significantly for $Q_{Lss} \geq Q_{THss}$ when $k < k_{max}$ because voltage gain curve, current gain curve, and circulating current gain curve can exhibit very sharp slopes, causing even small errors in the frequency approximation (such as Equation 49) to generate large errors in these quantities. Also, the accuracy of approximation by proposed design equations for loosely-coupled SP resonant tank can decrease significantly for $Q_{Lsp} \geq Q_{THsp}$ when $k < k_{max}$ for the same reason of sharp slopes increasing the sensitivity of various quantities at the switching frequency approximations (such Equation 71).

5.5.4 Evaluation using a loosely-coupled asymmetrical coupler with $L_{S1} \approx L_{S2}$'

First in evaluation and design, a range of interest or an expected range for k needs to be determined along with the ratio between C_1 and C_2' and the ratio between L_{S1} and L_{S2}'. It was previously shown that designing magnetic couplers can be aided by performing finite element simulations (FES). It was also shown that from FES, self-inductances and T-equivalent circuit parameters (L_{e1}, L_{e2}', L_m, and k) can be directly determined with good accuracy. Therefore using Ansys Maxwell 3D FES, an asymmetrical coupler employing flat-spiral coil on a ferrite disk plate (Tx) and flat-spiral coil in a ferrite pot-core (Rx) is designed as shown by Figure 5.7. For simplicity, the magnetic coupler has the turns ratio of unity (6:6). The radial depth of Tx was then adjusted to obtain the condition of $L_{S1} \approx L_{S2}' \approx 2.677$ μH. As a result of the FES, an expected k range and ratio $\frac{L_{S1}}{L_{S2}'}$ are determined. Ratio $\frac{C_1}{C_2'}$ can then be determined using Equation 53 for SS resonant tank or using Equation 69 for SP resonant tank. The expected parameters in Table 5.1 are used for analytical comparative study.

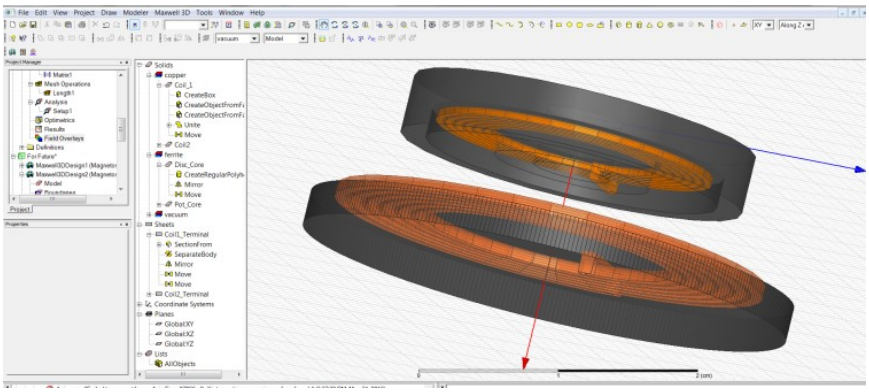

Figure 5.7: Screenshot of Ansys Maxwell 3D FES used for aiding experimental design of asymmetrical coupler (Tx in circular flat-planar core and Rx in circular pot core).

TABLE 5.1 EXPECTED PARAMETERS USED FOR EVALUATING Q_L EFFECTS FOR $L_{S1} = L_{S2}$'

Ratio $\frac{L_{S1}}{L_{S2}'}$	$\frac{L_{S1}}{L_{S2}'} \approx 1$
Highest k in an expected coupling range, k_{max}	$k_{max} \approx 0.37$
Lowest k in an expected coupling range, k_{min}	$k_{min} \approx 0.06$
For SS Resonant Tank	
Using Equation 53 for full-leakage inductance compensation at k_{max}, $\frac{C_2'}{C_1}$	$\frac{C_2'}{C_1} = 1$
Using Equation 48, $\lvert G_V \rvert_{ind}SS\_k_{max}$	At k_{max}, $\lvert G_V \rvert_{ind}SS = 1$
For SP Resonant Tank	
Using Equation 69 to obtain $\omega_{ov} = \omega_{oi}$ at k_{max}, $\frac{C_2'}{C_1}$	$\frac{C_2'}{C_1} \approx 0.863$
Using Equation 62, $\lvert G_V \rvert_{ind}SP\_k_{max}$	At k_{max}, $\lvert G_V \rvert_{ind}SP \approx 2.703$

The quantities in Table 5.1 for SS resonant tank are substituted into equations 50 through 52, and then in Figure 5.8, Matlab 3D plots are plotted for $k_{min} \leq k \leq k_{max}$ and $0.01 \leq Q_{Lss} \leq 1.5k_{max}$ - Note: $Q_{THss} = 1.5k$. In all of the plots in Figure 5.8, Q_{Lss} and k are

the x-axis and y-axis quantities respectively. In Figure 5.8 (a), voltage gain $||G_V(j\omega_S\_SS\_k_{max})||_{SS}$ (Equation 50) is plotted as the z-axis quantity. In Figure 5.8 (b), current gain $||G_i(j\omega_S\_SS\_k_{max})||_{SS}$ (Equation 51) is plotted as the z-axis quantity. In Figure 5.8 (c), circulating current gain $||G_{iLm}(j\omega_S\_SS\_k_{max})||_{SS}$ (Equation 52) is plotted as the z-axis quantity. In each of these plots, the color spectrum indicates the magnitude of z-axis quantity. The color spectrum is set up so that a color changes when the magnitude of its corresponding z-axis quantity changes approximately by 0.1 with one exception: the voltage gain plot in Figure 5.8 (a) contains the dark red region which represents $|G_V|_{ind}SS\_k_{max} - 0.2|G_V|_{ind}SS\_k_{max} \leq ||G_V(j\omega_S\_SS\_k_{max})||_{SS} \leq |G_V|_{ind}SS\_k_{max}$. In this case, since $|G_V|_{ind}SS\_k_{max} = 1.0$, the dark red region represents voltage gain magnitude between 0.8 and 1.0, thus representing 20 % variation in voltage gain at the fixed frequency.

The quantities in Table 5.1 for SP resonant tank are substituted into Equation 68 and Equation 70, and then Matlab 3D plots are plotted in Figure 5.9 for $k_{min} \leq k \leq k_{max}$ and $0.01 \leq Q_{Lsp} \leq 1.974$ - Note: $Q_{THsp} \approx 1.974$ when $k = k_{max} = 0.37$. In this figure, Q_{Lsp} and k are the x-axis and y-axis quantities respectively. In Figure 5.9 (a), voltage gain $||G_V(j\omega_S\_SP\_k_{max})||_{SP}$ (Equation 68) is plotted as the z-axis quantity. In Figure 5.9 (b), circulating current gain $||G_{iLm}(j\omega_S\_SP\_k_{max})||_{SS}$ (Equation 70) is plotted as the z-axis quantity. The current gain is not plotted, because $||G_i(j\omega_S\_SP\_k_{max})||_{SP}$ is approximately $|G_i|_{ind}SP$ (Equation 63) as long as Q_{Lsp} is not undesirably high ($Q_{Lsp} < Q_{THsp}$). Again, in each of these plots, the color spectrum indicates the magnitude of z-axis quantity. The voltage gain plot in Figure 5.9 (a) is set up so that it contains the black region that represents $|G_V|_{ind}SP\_k_{max} - 0.1|G_V|_{ind}SP\_k_{max} \leq ||G_V(j\omega_S\_SP\_k_{max})||_{SP} \leq |G_V|_{ind}SP\_k_{max} + 0.1|G_V|_{ind}SP\_k_{max}$. In this case, since $|G_V|_{ind}SP\_k_{max} \approx 2.703$, the black region represents

voltage gain magnitude between 2.433 and 2.973. The red region in Figure 5.9 (a), which is defined as region "X", is set up to represent $\|G_V(j\omega_S\_SP\_k_{max})\|_{SP} > |G_V|_{ind}SP\_k_{max} + 0.1|G_V|_{ind}SP\_k_{max}$. So in this case, it represents voltage gain increase by 10 % or greater: in this case, $\|G_V(j\omega_S\_SP\_k_{max})\|_{SP} > 2.973$.

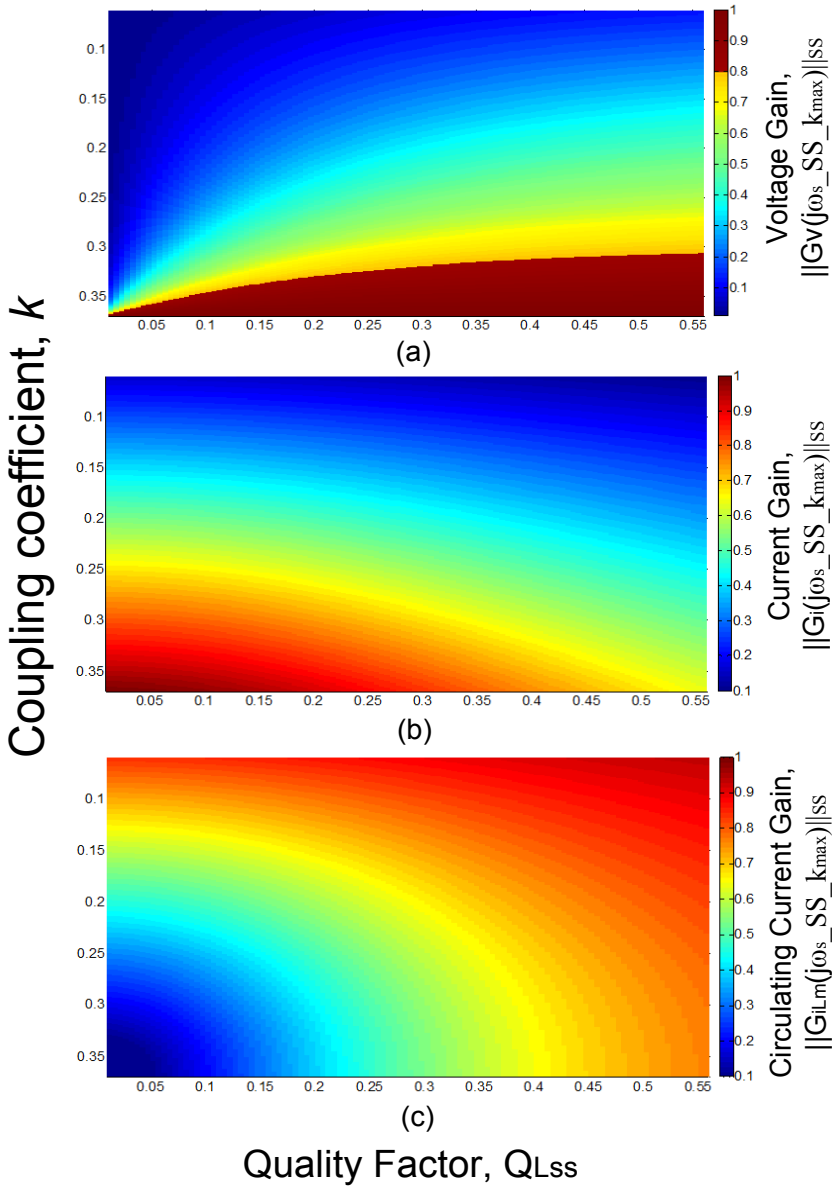

Figure 5.8: SS resonant tank's voltage gain (a), current gain (b), and circulating current gain (c) with $\omega_S\_SS\_k_{max}$ fixed at $\omega_{OVp}\_k_{max} = \omega_{OVs}\_k_{max} = \omega_{OV2}\_k_{max}$ for $L_{S1} \approx L_{S2}$'.

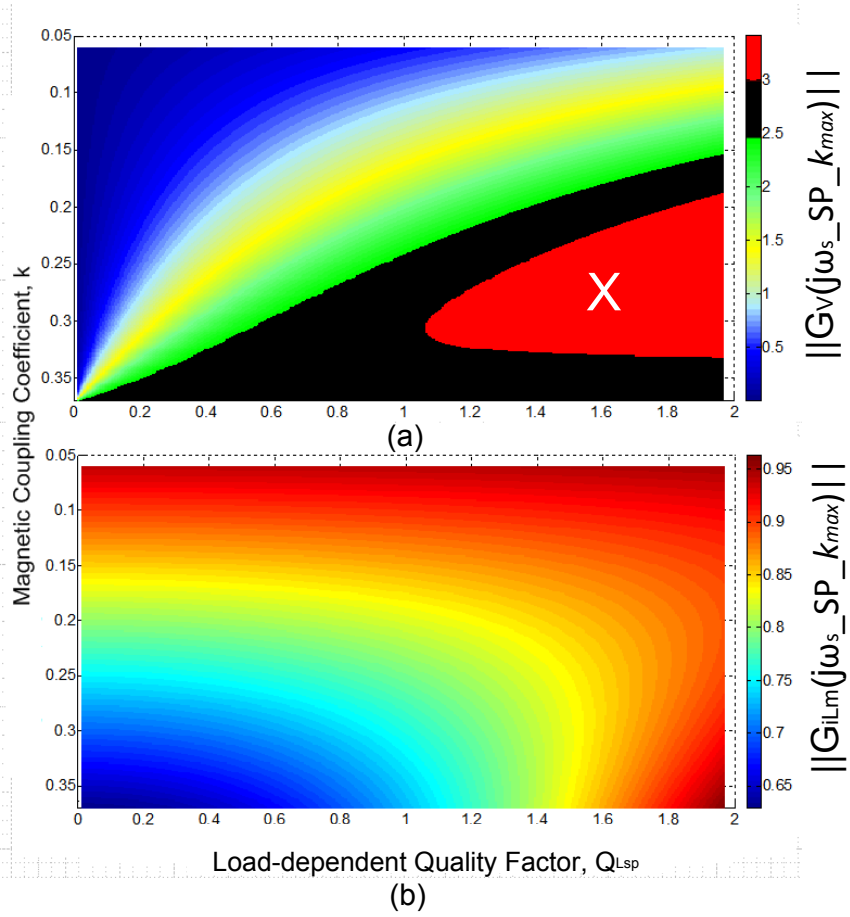

Figure 5.9: SP resonant tank's voltage gain (a) and circulating current gain (b) with $\omega_S\_SP\_k_{max}$ fixed at $\omega_{OV}\_k_{max} = \omega_{Oi}\_k_{max}$ for $L_{S1} = L_{S2}'$.

5.5.5 Comparative Study on Voltage Gain

From Figure 5.8 (a), it can be seen that $||G_V(j\omega_S\_SS\_k_{max})||_{SS}$ decreases *monotonically* as k decreases. By increasing Q_{Lss}, it is possible to increase the robustness in $||G_V(j\omega_S\_SS\_k_{max})||_{SS}$ so that voltage gain variation within 20 % is maintained for a wider range of k. However since increasing Q_{Lss} does not increase the red region in Figure 5.8 (a) by much, it does not have significant benefit of creating robust voltage gain for a wide range of k.

From Figure 5.9 (a), it can be seen that $||G_V(j\omega_S\_SP\_k_{max})||_{SP}$ does *not* necessarily decrease *monotonically* as k decreases. This is indicated by region X in which voltage

gain is increased for a certain range of k. Therefore, being in region X due to undesirably high Q_{Lsp} has diminishing return in obtaining robust voltage gain against k variation. Thus from Figure 5.9 (a), it is decided that selecting $Q_{Lsp} \geq 1.2$ when $k = k_{max}$ is not desirable, and the threshold for such quality factor of diminishing return is denoted as Q_H: in this example $Q_H = 1.2$. In general, it can be verified that Q_H is always below Q_{THsp}.

From observing Figure 5.9 (a) for $Q_{Lsp} < 1.2$, it can be concluded that by increasing Q_{Lsp}, it is possible to increase the robustness in $||G_V(j\omega_S\_SP\_k_{max})||_{SP}$ so that voltage gain at the fixed frequency does not vary by more than 10 % for a wider range of k. Also, since the rate of increase in the black region of Figure 5.9 (a) due to increase in Q_{Lsp} is much higher than the rate of increase in the red region of Figure 5.8 (a) due to increase in Q_{Lss}, it can be said that SP resonant tank can exhibit more robust voltage gain for a wider range of k compared to SS resonant tank. In this example, with $Q_{Lsp} \approx 1.1$ achieved at $k = k_{max}$, SP resonant tank's voltage gain at fixed frequency exhibits the percentage of variation within $\pm$ 10 % approximately for $0.23 < k \leq 0.37$ (about 38 % variation in k). On the other hand, for SS resonant tank, it is impractical for the voltage gain at fixed frequency to exhibit less than 20 % variation for more than about 19 % variation in k.

5.5.6 Comparative Study on Current Gain

By comparing Figure 5.8 (b) with $|G_i|_{ind}SP$ (Equation 63), it can be said that achievable current gain in SS resonant tank is higher than that in SP resonant tank. This is because $||G_i(j\omega_S\_SS\_k_{max})||_{SS}$ is not as significantly limited by k as $||G_i(j\omega_S\_SP\_k_{max})||_{SP} \approx |G_i|_{ind}SP$ is. Also since SP resonant tank has one additional circulating current path (parallel resonant capacitor C_2' branch) compared to SS resonant tank, lower current gain in SP resonant tank is expected. The additional circulating current path in SP resonant

tank can be an issue under very small load (large R_{eSP}') condition. To understand this, it should be noted that increase in R_{eSP}' causes SP resonant tank's voltage gain curve to exhibit two resonant peaks that are higher than load-independent voltage gain, $|G_V|_{ind}$SP. On the other hand, current gain curve of SP resonant tank exhibits a single resonant peak of load-independent current gain regardless of R_{eSP}' but becomes very sharp as R_{eSP}' increases. This means that circulating current through the parallel resonant capacitor, C_2', can be very significant under small load condition. This is an issue that may be resolved by implementing a power supply that has a desirably limited power delivery rating to avoid significant losses.

From observing Figure 5.8 (a) and Figure 5.8 (b), it can be seen as previously mentioned that achieving both $||G_V(j\omega_S\_SS\_k_{max})||_{SS}$ and $||G_i(j\omega_S\_SS\_k_{max})||_{SS}$ to be close to 1.0 is possible. For example, for $Q_{Lss} \leq 0.2$, both $||G_V(j\omega_S\_SS\_k_{max})||_{SS}$ and $||G_i(j\omega_S\_SS\_k_{max})||_{SS}$ can be above 0.9 although only for a very limited *k* range. However, it should be noted that it is *impractical* to optimize overall wireless charging system for achieving $||G_i(j\omega_S\_SS\_k_{max})||_{SS}$ above 0.9 at low *k* by achieving a very low value of Q_{Lss}. This is because such low Q_{Lss} requires that C_1 is very *low* and/or L_{S2}' is very *large* for a *given* R_{eSS}' – See Equation 37 for Q_{Lss}. Increasing L_{S2}' can be done by increasing the inductance of Tx and/or by increasing Tx to Rx turns ratio – See Figure 1.3. In either case, winding copper loss increases due to increase in parasitic winding resistance, which increases the sensitivity of voltage gain (power delivery) against *k* variation. Decreasing C_2' can be done by decreasing the value of secondary-side resonant capacitance (C_2) and/or by increasing Tx to Rx turns ratio. Decreasing C_2 requires operating frequency to

increase. This causes natural reduction of coupler inductances and therefore is a conflicting requirement.

Since achieving *both* $\|G_V(j\omega_S\_SS\_k_{max})\|_{SS}$ and $\|G_i(j\omega_S\_SS\_k_{max})\|_{SS}$ to be close to or above 0.9 at low k is impractical, a practical solution for optimal design is to achieve $\|G_V(j\omega_S\_SS\_k_{max})\|_{SS}$ and $\|G_i(j\omega_S\_SS\_k_{max})\|_{SS}$ to be almost equal to each other for as wide k range as possible.

In order to analyze equality condition of these two quantities, Figure 5.10 shows 3D plots the *ratio* (G_{Ratio}) of $\|G_V(j\omega_S\_SS\_k_{max})\|_{SS}$ *to* $\|G_i(j\omega_S\_SS\_k_{max})\|_{SS}$ for the same ranges as before for Q_{Lss} and k but with the different range of z-axis: $0.8 \leq G_{Ratio} = \frac{\|G_V(j\omega_S\_SS\_k_{max})\|_{SS}}{\|G_i(j\omega_S\_SS\_k_{max})\|_{SS}} \leq 1.1$. In Figure 5.10, the black line represents $G_{Ratio} \approx 1.0$. The red region represents $0.9 \leq G_{Ratio} \leq 1.1$, thus it represents $\pm$ 10 % variation in G_{Ratio}. As can be seen, achieving $G_{Ratio} = 1$ at $k = k_{max}$ is impractical as expected – Note: Impractically low Q_{Lss} is required. However, it can be practical to achieve $G_{Ratio} = 1$ at $k < k_{max}$. Furthermore, it is possible to achieve $\|G_V(j\omega_S\_SS\_k_{max})\|_{SS}$ and $\|G_i(j\omega_S\_SS\_k_{max})\|_{SS}$ to be almost equal for a fairly wide range of k as shown in Figure 5.10. For example, by achieving $Q_{Lss} \approx 0.415$, it is possible to maximize the k range in which $0.9 \leq G_{Ratio} \leq 1.1$. With $Q_{Lss} \approx 0.415$, it is expected that $\|G_V(j\omega_S\_SS\_k_{max})\|_{SS} \approx \|G_i(j\omega_S\_SS\_k_{max})\|_{SS}$ for $0.06 \leq k \leq 0.23$. It is also expected that $\|G_V(j\omega_S\_SS\_k_{max})\|_{SS} > 1.1\|G_i(j\omega_S\_SS\_k_{max})\|_{SS}$ for $0.23 < k \leq 0.37$.

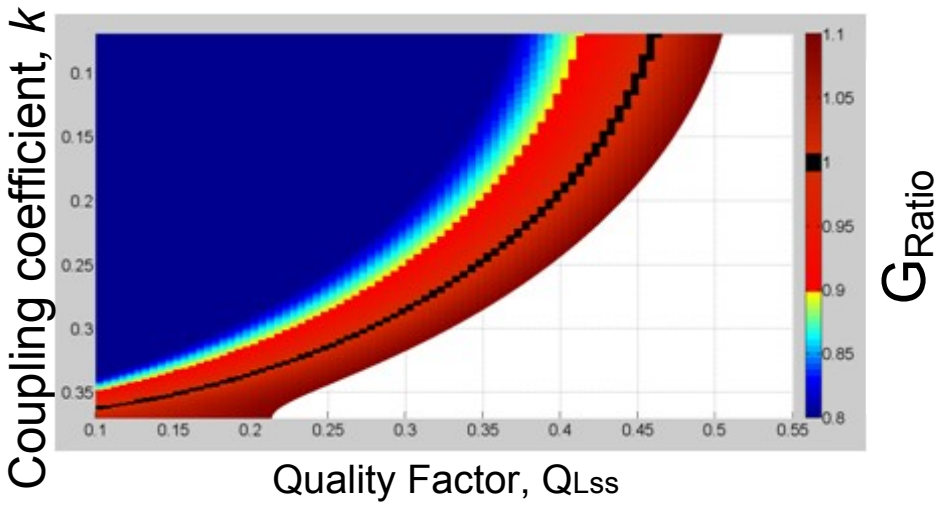

Figure 5.10: Matlab 3D plot for ratio, G_{Ratio}, of $||G_V(j\omega_S\_SS\_k_{max})||_{SS}$ to $||G_i(j\omega_S\_SS\_k_{max})||_{SS}$.

Achieving this equality condition is very desirable. To understand this, it should be noted that unity ratio of $||G_V(j\omega_S\_SS\_k_{max})||_{SS}$ to $||G_i(j\omega_S\_SS\_k_{max})||_{SS}$, $G_{Ratio} = \frac{||G_V(j\omega_S\_SS\_k_{max})||_{SS}}{||G_i(j\omega_S\_SS\_k_{max})||_{SS}} = 1$, means that the magnitude of input impedance of SS resonant tank is equal to the magnitude of load impedance of SS resonant tank. That is $||Z_i(j\omega_S\_SS\_k_{max})||_{SS} = ||Z_L(j\omega_S\_SS\_k_{max})||_{SS} = R_{eSS}'$. If this condition is achieved for a wide range of k, then the frequency of minimum circulating current gain becomes very robust against k variation and remains at $\omega_S\_SS\_k_{max}$ for a wide range of k. Consequently, under this condition, optimal compromise between voltage gain and current gain is achieved at fixed frequency while providing minimized circulating current gain. These phenomena are demonstrated in Figure 5.11, which plots voltage gain ($||G_V(j\omega)||_{SS}$), current gain ($||G_i(j\omega)||_{SS}$), and circulating current gain ($||G_{iLm}(j\omega)||_{SS}$) under k variation. The left figure inside the red box is obtained with optimal Q_{Lss}, whereas the right figure inside the black box is obtained with 0.463*optimal Q_{Lss}. The axes are in the same scale for all of the plots, and the desirable fixed frequency, $\omega_S\_SS\_k_{max}$, is 200 kHz in Figure

5.11. Under the k variation, optimal Q_{Lss} maintains $||G_V(j\omega_S\_SS\_k_{max})||_{SS} \approx ||G_i(j\omega_S\_SS\_k_{max})||_{SS}$ while $||G_{iLm}(j\omega_S\_SS\_k_{max})||_{SS}$ is at the minimum. However, the lower Q_{Lss} provides $||G_V(j\omega_S\_SS\_k_{max})||_{SS} << ||G_i(j\omega_S\_SS\_k_{max})||_{SS}$ without significantly reducing $||G_{iLm}(j\omega_S\_SS\_k_{max})||_{SS}$ compared to that under optimal Q_{Lss} condition. Therefore, it can be concluded that optimal Q_{Lss} achieves an optimal compromise between voltage gain and current gain at the desirably-fixed frequency while circulating current gain is minimized.

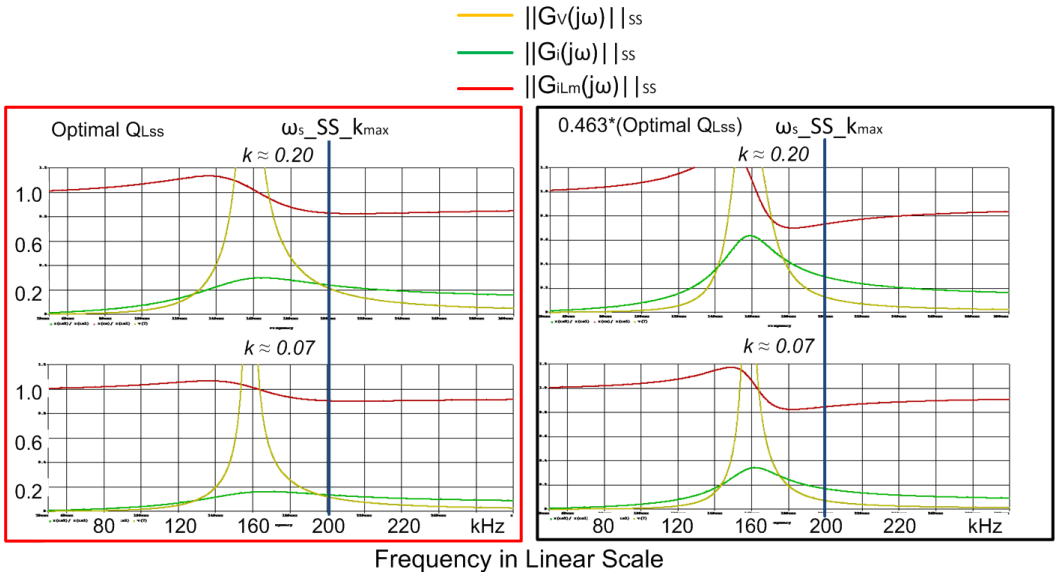

Figure 5.11: Voltage gain ($||G_V(j\omega)||_{SS}$), current gain ($||G_i(j\omega)||_{SS}$), and circulating current gain ($||G_{iLm}(j\omega)||_{SS}$) under k variation for optimal Q_{Lss} (left figure inside the red box) and for 0.463*optimal Q_{Lss} (right figure inside the black box - Note: $\omega_S\_SS\_k_{max}$ = 200 kHz.

5.5.7 Comparative Study on Circulating Current Gain

By comparing Figure 5.8 (c) and Figure 5.9 (b), it can be seen that circulating current in a magnetic coupler is significantly lower for SS resonant tank as expected.

To further evaluate circulating current gain, coil-to-coil current gain characteristics (magnitude of frequency-domain ratio of secondary-side coil current, i_{Le2} in Figure 1.3, to primary-side coil current, i_{Le1} in Figure 1.3) can be considered. It can be assumed that variations in Q_{Lss} and Q_{Lsp} are imposed by R_{eSS}' and R_{eSP}'. By looking at the i_{Le2} branch

in each of SS and SP resonant tanks in Figure 1.3, it can be concluded that in SS resonant tank, the real component of impedance introduced to i_{Le2} is R_{eSS}', whereas in SP resonant tank, the real component of impedance, $R_e\{Z_{load}\_SP(j\omega)\}$, introduced to i_{Le2} is Equation 83. As this equation shows, $R_e\{Z_{load}\_SP(j\omega)\}$ decreases as R_{eSP}' increases. Consequently, coil-to-coil current gain increases significantly with increasing R_{eSP}'. As [37] briefly explains, this real component compression causes power loss in Rx to increase significantly. Again, this issue can be resolved by implementing a power supply that has a desirably limited power delivery rating to avoid significant losses.

$$\mathrm{Re}\{Z_{Load}\_SP(j\omega)\} = \frac{R_{eSP}'}{1+(\omega C_2' R_{eSP}')^2} \quad \text{..... Equation (83)}$$

5.5.8 Comparative Study on Maintaining ZVS of Primary-side Switch Network

In order to understand the ZVS conditions under *k* variation, it is of interest to analyze for each of the resonant tank topologies the input impedance, $||Z_i(j\omega)||_{SS}$, and phase shift, $\Phi_{vi}(j\omega)$, between resonant tank input voltage and input current.

Under the fixed operating frequency condition, input impedance $||Z_i(j\omega_s\_SS\_k_{max})||_{SS}$ of SS resonant tank is either resistive or inductive. It is resistive at $k = k_{max}$ for $||G_V||_{max} = 1$ and inductive at $k = k_{max}$ for $||G_V||_{max} > 1$ (large Q_{Lss}). As *k* decreases, $||G_V||_{max}$ increases, and the resonant frequency of load-independent voltage gain decreases. Consequently, $||Z_i(j\omega_s\_SS\_k_{max})||_{SS}$ becomes more and more inductive with decreasing *k*. As a result, $||\Phi_{vid}(j\omega_s\_SS\_k_{max})||_{SS}$ gets closer to 90 degrees ($i_{Le1}(t)$ lagging $V_i(t)$ by almost 90 degrees) with decreasing *k*. With almost fully-charged battery (large Q_{Lss}), $||\Phi_{vid}(j\omega_s\_SS\_k_{max})||_{SS}$ is even closer to 90 degrees due to significantly-increased peak voltage gain (large

$||G_V||_{max}$). It should be noted that large values of $||\Phi_{vid}(j\omega_s\_SS\_k_{max})||_{SS}$ are undesirable for obtaining and maintaining ZVS transitions.

For SP resonant tank, $||Z_i(j\omega_s\_SP\_k_{max})||_{SP}$ at $k = k_{max}$ is resistive *regardless* of $||G_V||_{max}$ (Q_{Lsp}). However, like $||Z_i(j\omega_s\_SS\_k_{max})||_{SS}$, it also becomes more and more inductive with decreasing k. Therefore, a main difference is that $||\Phi_{vid}(j\omega_s\_SP\_k_{max})||_{SP}$ is zero and Q_{Lsp}-independent at $k = k_{max}$, whereas $||\Phi_{vid}(j\omega_s\_SS\_k_{max})||_{SS}$ depends on Q_{Lss} for all k conditions.

For both SS and SP resonant tanks, maintaining ZVS for a wide range of k is desirable, therefore evaluating only $||\Phi_{vid}(j\omega_s\_SS\_k_{max})||_{SS}$ and $||\Phi_{vid}(j\omega_s\_SP\_k_{max})||_{SP}$ is not desirable. Instead, more desirable figures of merit are $\frac{\partial||\Phi_{vid}(j\omega_s\_SS\_k_{max})||_{SS}}{\partial k}\Big|_{Q_{Lss}=optimal\ value\ achieved\ at\ k=k_{max}}$ and $\frac{\partial||\Phi_{vid}(j\omega_s\_SP\_k_{max})||_{SP}}{\partial k}\Big|_{Q_{Lsp}=optimal\ value\ achieved\ at\ k=k_{max}}$, because comparing these quantities can show complexity in development of control for maintaining ZVS under k variation.

The next section shows examples of optimal designs of SS and SP resonant tanks in *simulation* to evaluate $\Phi_{vid}(j\omega_s\_SS\_k_{max})_{SS}$ and $\Phi_{vid}(j\omega_s\_SP\_k_{max})_{SP}$ under k variation with optimal Q_{Lss} and Q_{Lsp} achieved at $k_{max} = 0.37$. In these optimal design examples, the parameters in TABLE 5.1 are used. For *simplicity*, R_{eSS}' and R_{eSP}' are adjusted to obtain optimal quality factor.

5.5.9 SIMULATION EVALUATION OF $\Phi_{VID}(J\Omega_S\_SS\_K_{MAX})_{SS}$ AND $\Phi_{VID}(J\Omega_S\_SP\_K_{MAX})_{SP}$

Using the expected inductance values from FES performed for Figure 5.7 and assuming that leakage inductance compensation is achieved at 300 kHz, SS resonant tank

parameters are $L_{e1} = L_{e2}' \approx 1.687$ μH, $L_m \approx 0.99$ μH, and $C_1 = C_2' \approx 166.83$ nF. In order to achieve $Q_{Lss} \approx 0.415$, it must be that $R_{eSS}' \approx 1.66\ \Omega$ - See Equation 37 for Q_{Lss}. Plotting $\Phi_{vid}(j\omega)_{SS}$, $\|G_V(j\omega)\|_{SS}$, and $\|G_i(j\omega)\|_{SS}$ using these parameters, Figure 5.12 is obtained at $k = k_{max} \approx 0.37$. In this figure, the blue trace at the top figure is $\Phi_{vid}(j\omega)_{SS}$, and the bottom figure contains two traces representing $\|G_V(j\omega)\|_{SS}$ with the green trace and $\|G_i(j\omega)\|_{SS}$ with the red trace.

By performing FES further, the T-equivalent model parameters at $k < k_{max}$ are also extracted. Using these T-equivalent model parameters, plots such as those in Figure 5.12 are simulated, and then simulation data for $\Phi_{vid}(j\omega_S\_SS\_k_{max})_{SS}$ are extracted and listed in Table 5.2 – Note: $\omega_S\_SS\_k_{max} = 2\pi(300\text{kHz})$.

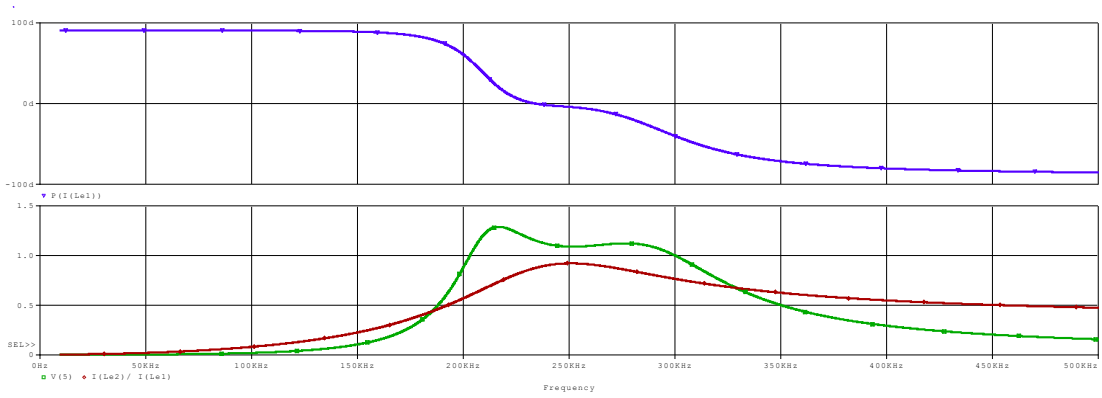

Figure 5.12: Simulation plots for $\Phi_{vid}(j\omega)_{SS}$, $\|G_V(j\omega)\|_{SS}$, and $\|G_i(j\omega)\|_{SS}$ obtained using the T-equivalent model parameters extracted from FES – Note: $\omega_S\_SS\_k_{max}=2\pi(300\text{kHz})$.

TABLE 5.2 PARAMETRIC SIMULATION DATA FOR EVALUATING $\Phi_{vid}(j\omega_S\_SS\_k_{max})_{SS}$ UNDER k VARIATION WITH AN OPTIMAL Q_{Lss} ACHIEVED AT $k = k_{max}$

k	$\Phi_{vid}(j\omega_S\_SS\_k_{max})_{SS}$ (degrees)
0.37	-40.41
0.33	-54
0.198	-79.43
0.066	-88.99

Under the same compensating frequency condition, SP resonant tank parameters are $L_{e1} = L_{e2}' \approx 1.687$ μH, $L_m \approx 0.99$ μH, $C_1 \approx 121.79$ nF, and $C_2' \approx 105.14$ nF. In order to achieve $Q_{Lsp} \approx 1.1$, it must be that $R_{eSP}' \approx 5.55\ \Omega$ - See Equation 37 for Q_{Lsp}. Plotting $\Phi_{vid}(j\omega)_{SP}$, $\|G_V(j\omega)\|_{SP}$, and $\|G_i(j\omega)\|_{SP}$ using these parameters, Figure 5.13 is obtained. In this figure, the blue trace at the top figure is $\Phi_{vid}(j\omega)_{SP}$, and the bottom figure consists of two traces representing $\|G_V(j\omega)\|_{SP}$ with the green trace and $\|G_i(j\omega)\|_{SP}$ with the red trace. Again, using the same inductance values at $k \leq k_{max} = 0.37$ obtained from FES, simulation data for $\Phi_{vid}(j\omega_s\_SP\_k_{max})_{SP}$ are obtained and listed in Table 5.3 – Note: $\omega_s\_SP\_k_{max} = 2\pi(300\text{kHz})$.

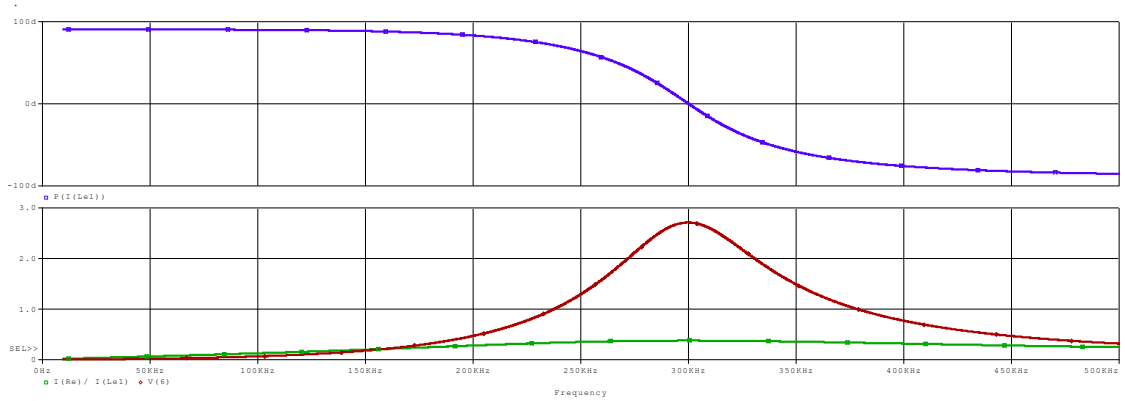

Figure 5.13: Simulation plots for $\Phi_{vid}(j\omega)_{SP}$, $\|G_V(j\omega)\|_{SP}$, and $\|G_i(j\omega)\|_{SP}$ obtained using the T-equivalent model parameters extracted from FES – Note: $\omega_S\_SP\_k_{max}=2\pi(300\text{kHz})$.

TABLE 5.3 PARAMETRIC SIMULATION DATA FOR EVALUATING $\Phi_{vid}(j\omega_s\_SP\_k_{max})_{SP}$ UNDER k VARIATION WITH AN OPTIMAL Q_{LSS} ACHIEVED AT $k = k_{max}$

k	$\Phi_{vid}(j\omega_s\_SP\_k_{max})_{SP}$ (degrees)
0.37	0.00
0.33	-11.07
0.198	-64.26
0.066	-87.61

Comparing the simulation data in Table 5.2 and Table 5.3, it can be concluded that in SS resonant tank, the magnitude of its input current lag with respect to its input voltage is larger at each k compared to that in SP resonant tank. That is $||\Phi_{vid}(j\omega_s\_SS\_k_{max})||_{SS}(k) > ||\Phi_{vid}(j\omega_s\_SP\_k_{max})||_{SP}(k)$ for all k. Therefore, for a narrower k variation range, SP resonant tank can maintain ZVS in the primary-side switch network better than SS resonant tank. Also, SP resonant tank allows obtaining both ZVS and ZCS in the primary-side switch network for a single value of k in a range.

However, the phase lag in SS resonant tank changes *monotonically* in a more *linear* manner under k variation as expected from the results of UGFT control model previously shown in Chapter 4. The phase lag in SP resonant tank changes in a *non-linear* manner. That is $\left|\frac{\partial||\Phi_{vid}(j\omega_s\_SS\_k_{max})||_{SS}}{\partial k}\right|\Big|_{Q_{Lss}=optimal\ value\ achieved\ at\ k=k_{max}}$ is more constant than $\left|\frac{\partial||\Phi_{vid}(j\omega_s\_SP\_k_{max})||_{SP}}{\partial k}\right|\Big|_{Q_{Lsp}=optimal\ value\ achieved\ at\ k=k_{max}}$. This means that in SS resonant tank, development of control such as dead-time control for maintaining ZVS is less complex.

5.6 How to Design Resonant Tank to Exhibit Optimal Q_L

Based on Figure 5.10, for optimally designing loosely-coupled SS resonant tank, it is decided that the design goal is to obtain Q_{Lss} as close as possible to 0.415 at $k = k_{max}$ for a desired nominal value for R_{eSS}'.

Based on Figure 5.9, for optimally designing SP resonant tank, the design goal is to maximize voltage gain robustness by maximizing Q_{Lsp} at $k = k_{max}$ without exceeding the limit (Q_H). Based on Figure 5.9, achieving $Q_{Lsp} = 1.1$ at $k = k_{max}$ for a desired nominal

value for R_{eSP}' provides good compromise between maximization of voltage gain robustness and minimization of circulating current.

It should be noted that optimal values of Q_L depend on applications: it is important to determine how much one could gain by maintaining a desired level of power delivery under *k* variation at the cost of reduced coil-to-coil efficiency.

Typically in a resonant tank design process, inductance value for one side of a magnetic coupler is known since it is desirable for one Tx to be capable of transmitting power to various types of Rx. So in proposed design methods for loosely-coupled SS and SP resonant tanks, switching frequency and the ratio between L_{S1} and L_{S2}' are tunable parameters while a desired nominal value of R_e' is specified.

However, if it is required to use both sides of a coupler that had been already constructed, choices for C_1 and C_2' (thus switching frequency) can be adjusted to obtain a Q_L value *as close as possible* to an optimal value for a specified nominal value of R_e'.

The next section shows examples of optimal designs of SS and SP resonant tanks to *experimentally* validate the proposed design methods for optimizing Q_{Lss} and Q_{Lsp}.

5.7 Experimental Results of Optimal Designs

The asymmetrical coupler in Figure 5.7 is experimentally constructed as shown in Figure 5.14. The Tx-to-Rx distance is set up to be approximately 5mm. Also, as can be seen, an evaluation board is experimentally constructed. This board can employ either a SS resonant tank or a SP resonant tank and is implemented for low power applications with maximum power ≤ 20W at maximum voltage ≤ 15V and maximum current ≤ 3A. For experimental evaluation, the target switching frequency is between 200 – 350 kHz,

and a desired load is selected as $R_{eSS}' \approx 2.43\ \Omega$ and $R_{eSP}' \approx 3.70\ \Omega$, assuming that it is desired to obtain output power of 12 W at output voltage of 6 V.

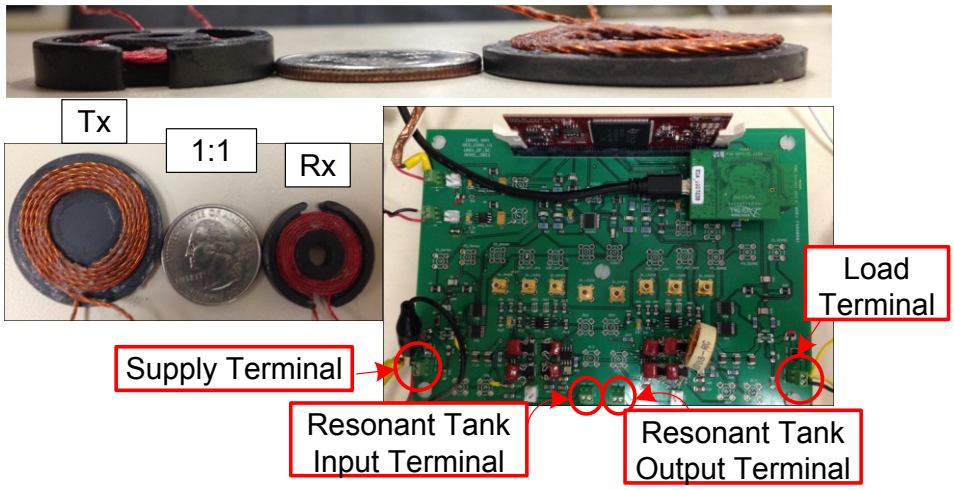

Figure 5.14: Experimental setup of resonant converter evaluation board containing experimental construction of the asymmetrical coupler shown in Figure 5.7

5.7.1 Experimental Results of Optimal Design of SS Resonant Tank

Based on Equation 37, Equation 42, and Equation 43, it can be concluded that selecting the highest operating frequency possible is desirable for minimizing Q_{Lss} for a specified R_{eSS}' and approximately unity ratio between L_{S1} and L_{S2}'. In this case, $R_{eSS}' \approx 2.43\ \Omega$.

At Tx-to-Rx distance of approximately 5mm and misalignment of approximately 0mm, the coupler is experimentally characterized, and the extracted coupler parameters are listed in Table 5.4. As listed in this table, $L_{S1} = 2.58\ \mu H$ and $L_{S2}' = 2.60\ \mu H$. These are slightly different from the target condition of $L_{S1} \approx L_{S2}' \approx 2.677\ \mu H$ from the FES. So, the resonant capacitor values are adjusted based on the extracted coupler parameters to more precisely obtain $\omega_{OVp}\_k_{max} = \omega_{OVs}\_k_{max} = \omega_{OV2}\_k_{max}$. By selecting the operating frequency of 350 kHz for Q_{Lss} tuning, the *nominal* resonant capacitor values parameters in Table 5.4 are obtained and experimentally implemented. Thus, $Q_{Lss} \approx 0.54$ is expected with the parameters in Table 5.4 for $R_{eSS}' \approx 2.43\ \Omega$.

Table 5.4 Nominal Parameters of Experimentally-implemented SS Resonant Tank

$L_{e1}(\mu H)$	$L_m(\mu H)$	$L_{e2}'(\mu H)$	k_{max}	$C_1(nF)$	$C_2'(nF)$
1.63	0.95	1.65	0.367	127.2	126.2

In Figure 5.15, experimental curve for voltage gain magnitude ($||G_V(j\omega)||_{SS}$ in Figure 5.15 (a)) and current gain magnitude ($||G_i(j\omega)||_{SS}$ in Figure 5.15 (b)) of the SS resonant tank are plotted at $Q_{Lss} \approx 0.53$ for $R_{eSS}' \approx 2.4\ \Omega$. As can be seen from this figure, it is precisely achieved that $\omega_{OVp}\_k_{max} = \omega_{OVs}\_k_{max} = \omega_{OV2}\_k_{max} \approx 2\pi(357.99)(10^3)$ rad/s. Since the previously proposed boundary Q_{THss} (Equation 76) concludes that values of Q_{Lsp}

approximately equal or greater than 0.555 cause a well-defined single resonant peak in voltage gain, a single resonant peak in voltage gain is exhibited experimentally.

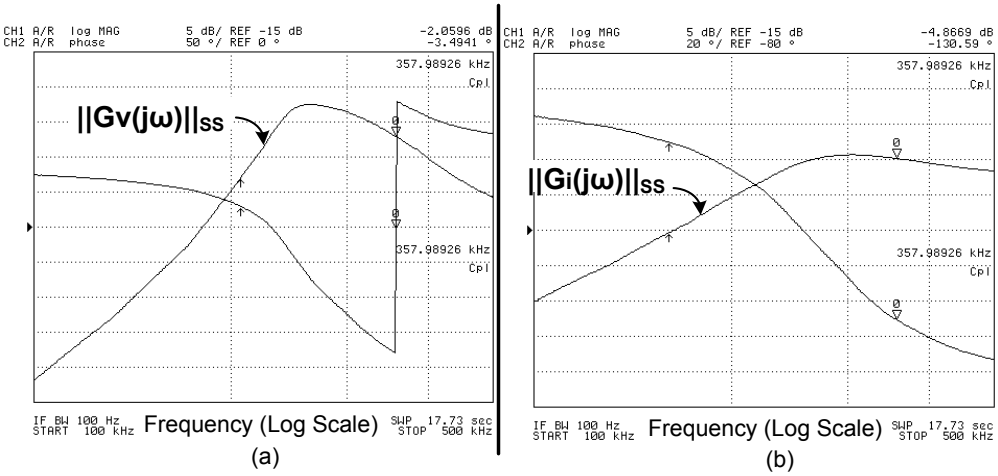

Figure 5.15: Experimental plots for voltage gain magnitude, $||G_V(j\omega)||_{SS}$, (a) and current gain magnitude, $||G_i(j\omega)||_{SS}$, (b) of SS resonant tank.

Experimental data for $||G_V(j\omega_S\_SS\_k_{max})||_{SS}$ and $||G_i(j\omega_S\_SS\_k_{max})||_{SS}$ at three different values of Q_{Lss} are collected at varied k and listed in Table 5.5. The three different values of Q_{Lss} are denoted as LQ for $Q_{Lss} \approx 0.27$, Opt Q for $Q_{Lss} \approx 0.43$, and HQ for $Q_{Lss} \approx 0.53$. For simplicity, the variation of Q_{Lss} is imposed by varying Re_{SS}'. Also, $||G_V(j\omega_S\_SS\_k_{max})||_{SS}$ is denoted as λ, and $||G_i(j\omega_S\_SS\_k_{max})||_{SS}$ is denoted as ξ. Using Table 5.5, experimental data for G_{Ratio} (the ratio of λ to ξ) are plotted in Figure 5.16 at LQ, Opt Q, and HQ.

TABLE 5.5 EXPERIMENTAL DATA FOR $||G_V(j\omega_S\_SS\_k_{max})||_{SS}$ (λ) AND $||G_i(j\omega_S\_SS\_k_{max})||_{SS}$ (ξ) AT THREE DIFFERENT VALUES OF Q_{LSS} UNDER k VARIATION

	LQ $Q_{Lss} \approx 0.27$		**Opt Q** $Q_{Lss} \approx 0.43$		**HQ** $Q_{Lss} \approx 0.53$	
k	**λ**	**ξ**	**λ**	**ξ**	**λ**	**ξ**
0.37	0.682	0.747	0.750	0.638	0.785	0.571
0.35	0.677	0.733	0.701	0.611	0.773	0.556
0.33	0.525	0.644	0.588	0.543	0.636	0.490
0.25	0.386	0.539	0.461	0.452	0.499	0.406
0.19	0.282	0.431	0.340	0.356	0.385	0.325
0.07	0.169	0.282	0.217	0.236	0.241	0.212

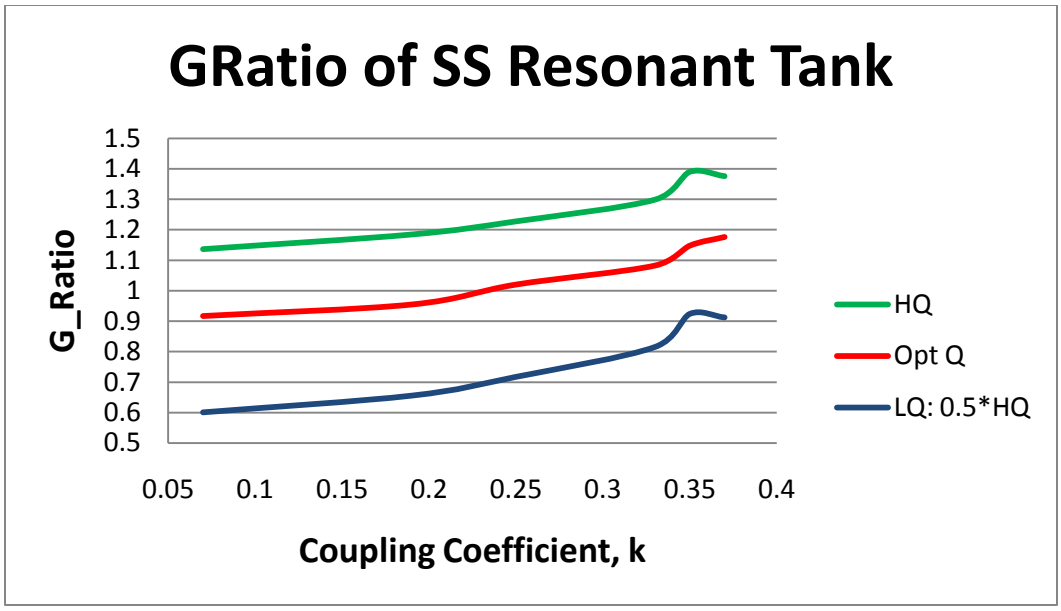

Figure 5.16: Experimental data for G_{Ratio} (the ratio of experimental voltage gain, λ, to experimental current gain, ξ) at LQ, Opt Q, and HQ.

From Table 5.5 and Figure 5.16, the following conclusions can be made. Due to the presence of parasitic resistances (coupler winding resistances and resonant capacitor ESRs), the experimental voltage gain, λ, is less than 1.

According to the expectations from Figure 5.10, $Q_{Lss} \approx 0.415$ maximizes the k range in which $0.9 \leq G_{Ratio} \leq 1.1$, and it is expected that $G_{Ratio} > 1.1$ with $Q_{Lss} \approx 0.415$ for $0.23 < k \leq 0.37$. With experimentally implemented Opt Q ($Q_{Lss} \approx 0.43$), Figure 5.16 shows that $0.9 \leq G_{Ratio} \leq 1.1$ for the wide range of $0.07 \leq k \leq 0.33$, which is *desirably* wider than the expected k range and is almost the entire range of k.

The major reason why the condition of $G_{Ratio} > 1.1$ is *not* exhibited with Opt Q for the wide range of k is as follows: voltage gain $\|G_V(j\omega)\|_{SS}$ is affected by *both* primary-side and secondary-side parasitic resistances, whereas current gain $\|G_i(j\omega)\|_{SS}$ is affected by secondary-side parasitic resistances.

In summary, experimental G_{Ratio} data in Figure 5.16 are in good agreement with the expectations from the Matlab 3D color spectrum plot of G_{Ratio} in Figure 5.10. Furthermore, from Figure 5.10, it can be expected that HQ ($Q_{Lss} \approx 0.53$) would cause $G_{Ratio} > 1.1$ for $0.07 \leq k \leq 0.37$. This expectation is also met as can be seen in Figure 5.16. For optimal design of SS resonant tank, the proposed design method can be used to determine an optimal Q_{Lss} so that G_{Ratio} remains close to unity under k variation.

5.7.2 Experimental Results of Optimal Design of SP Resonant Tank

For SP resonant tank, $R_{eSP}' \approx 3.7\ \Omega$ is selected as previously mentioned. The target operating frequency of 200 kHz is chosen. Substituting this frequency into Q_{Lsp} (Equation 37) and into ω_{oi} (Equation 61), the values $L_{S2}' \approx 2.677\mu H$ and $C_2' \approx 236.6nF$ are calculated. Consequently, $L_{S1} \approx 2.677\mu H$ for the given target condition of unity ratio between L_{S1} and L_{S2}'. Substituting this L_{S1} and the switching frequency into Equation 60, $C_1 \approx 274.1nF$ is then calculated.

Since $L_{S1} = 2.58\mu H$ and $L_{S2}' = 2.60\mu H$ are slightly different from the target condition of $L_{S1} \approx L_{S2}' \approx 2.677\mu H$, the resonant capacitor values are adjusted based on the extracted coupler parameters to more precisely obtain $\omega_{oi}\_k_{max} = \omega_{ov}\_k_{max}$ at $Q_{Lsp} \approx 1.1$. The experimentally-implemented SP resonant tank parameters are listed in Table 5.6.

In Figure 5.17, experimental curve for voltage gain magnitude ($||G_V(j\omega)||_{SP}$ in Figure 5.17 (a)) and current gain magnitude ($||G_i(j\omega)||_{SP}$ in Figure 5.17 (b)) of the SP resonant tank are plotted at $Q_{Lsp} \approx 1.1$ for $R_{eSP}' \approx 3.7\ \Omega$. As can be seen from this figure, $\omega_{ov}\_k_{max} \approx \omega_{oi}\_k_{max} \approx 2\pi(213.73)(10^3)$ rad/s.

TABLE 5.6 EXPERIMENTALLY-IMPLEMENTED SP RESONANT TANK PARAMETERS

L_{e1}(μH)	L_m(μH)	L_{e2}'(μH)	k_{max}	C_1(nF)	C_2'(nF)
1.63	0.95	1.65	0.367	248.5	213.3

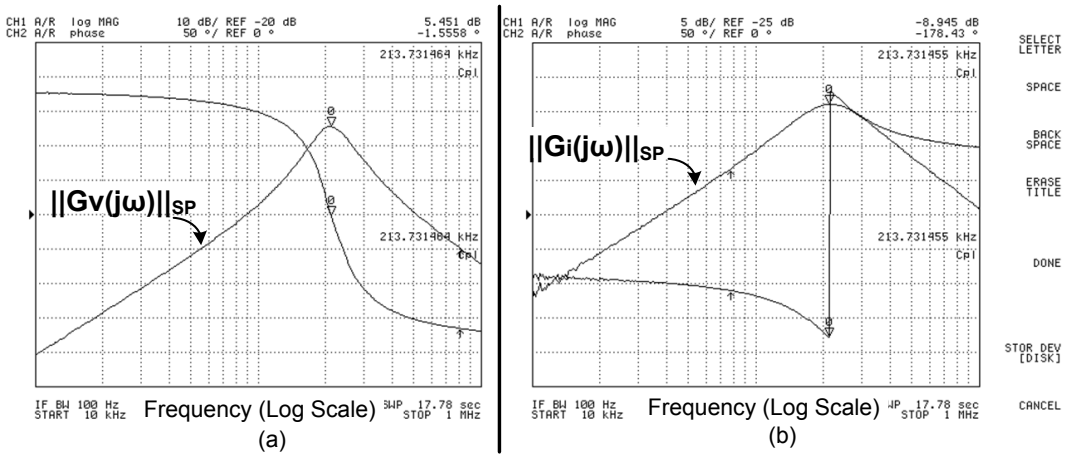

Figure 5.17: Experimental plots for voltage gain magnitude, $||G_V(j\omega)||_{SP}$, (a) and current gain magnitude, $||G_i(j\omega)||_{SP}$, (b) of SP resonant tank.

At fixed $\omega_S_SP_k_{max} \approx 2\pi(213.73)(10^3)$rad/s, experimental data for $||G_V(j\omega_S\_SP\_k_{max})||_{SP}$ and $||G_i(j\omega_S\_SP\_k_{max})||_{SP}$ are collected at three different Q_{Lsp} conditions (LQ: $Q_{Lsp} \approx 0.36$; Opt Q: $Q_{Lsp} \approx 1.1$; HQ: $Q_{Lsp} \approx 3.2$) while k is varied from $k_{max} \approx 0.367$ to $k_{min} \approx 0.07$. In the experiment, variation in Q_{Lsp} is imposed by changing R_{eSP}'. Table 5.7 lists the data. In this table, voltage gain $||G_V(j\omega_S\_SP\_k_{max})||_{SP}$ and current gain $||G_i(j\omega_S\_SP\_k_{max})||_{SP}$ are denoted as α and β respectively. As can be seen, at $k_{max} \approx 0.37$, $||G_V(j\omega_S\_SP\_k_{max})||_{SP}$ is not the load-independent (Q-independent) value of $|G_V|_{ind}SP$ is not 2.703 at k_{max}. This is due to inevitable loss effects caused by parasitic resistance terms such as primary-side capacitor's ESR and winding resistances. Although the effects of parasitic resistance terms can be especially significant at voltage gain resonant peaks, the proposed optimal Q_{Lsp} design method is expected to perform well. This is because $\omega_S\_SP\_k_{max}$ in general is located well above ω_{P1}, thus $||G_V(j\omega_S\_SP\_k_{max})||_{SP}$ is more

robust against parasitic resistance terms. This expectation is met as supported by the experimental data that follow.

TABLE 5.7 EXPERIMENTAL DATA FOR $\|G_V(j\omega_S\_SP\_k_{max})\|_{SP}$ (α) AND $\|G_i(j\omega_S\_SP\_k_{max})\|_{SP}$ (β)

	LQ ($Q_{Lsp} \approx 0.36$)		**Opt Q ($Q_{Lsp} \approx 1.1$)**		**HQ ($Q_{Lsp} \approx 3.2$)**	
k	**α**	**β**	**α**	**β**	**α**	**β**
0.37	1.198	0.368	1.873	0.357	2.296	0.316
0.35	1.165	0.352	1.899	0.341	2.347	0.312
0.33	1.046	0.309	1.901	0.296	2.512	0.263
0.25	0.802	0.263	1.740	0.245	2.649	0.209
0.19	0.523	0.200	1.354	0.193	2.618	0.176
0.07	0.157	0.062	0.442	0.060	1.078	0.051

By plotting the data of Table 5.7 in Figure 5.18, it can be clearly seen in Figure 5.18 (a) that, with Opt Q, voltage gain $\|G_V(j\omega_S\_SP\_k_{max})\|_{SP}$ is well maintained for a fairly large k variation range of $0.25 < k \leq 0.37$ approximately. Also, it can be seen in Figure 5.18 (b) that current gain $\|G_V(j\omega_S\_SP\_k_{max})\|_{SP}$ at Opt Q remains very close to that at LQ. Although LQ generates the maximum current gain as expected, the voltage gain at LQ becomes undesirably small for even a small decrease in k. The robustness in voltage gain characteristics at Opt Q can outweigh the small increase in current gain achieved at LQ. It should be noted that the HQ value above $Q_H \approx 1.2$ is undesirable as expected. At HQ > Q_H, the voltage gain significantly increases as k decreases to $k \approx 0.21$ while the current gain is much lower compared to the current gains at LQ and Opt Q.

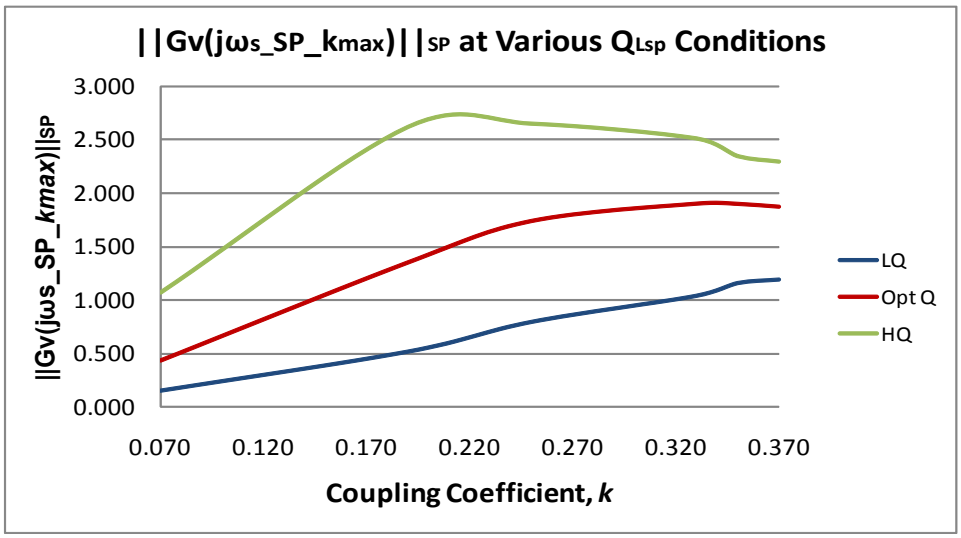

(a)

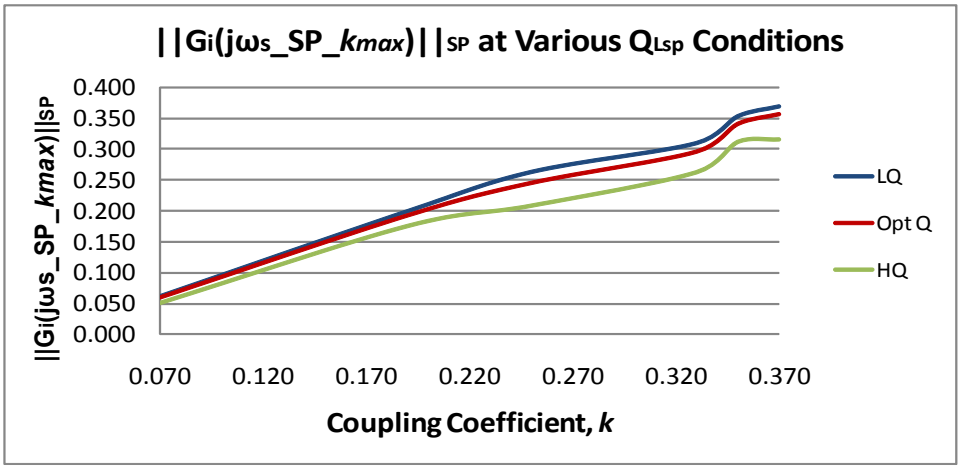

(b)

Figure 5.18: Voltage gain $\|G_V(j\omega_S\_SP\_k_{max})\|_{SP}$ (a) and current gain $\|G_i(j\omega_S\_SP\_k_{max})\|_{SP}$ (b) for experimental data in Table 5.7.

For more detailed analysis, circulating currents are evaluated by operating the SP resonant converter with the switching frequency and supply voltage fixed at 214 kHz and 3 V respectively while *k* is varied. In Figure 5.19 (a), resonant tank input voltage ($V_1(t)$ in *yellow*), primary-side coil current ($i_{Le1}(t)$ in *purple*), secondary-side coil current ($i_{Le2}(t)$ in *green*), and circulating current in the coupler ($i_{Le1}(t)$- $i_{Le2}(t)$ in *red*) are plotted for LQ.

The same quantities are plotted in Figure 5.19 (b) for Opt Q and in Figure 5.19 (c) for HQ.

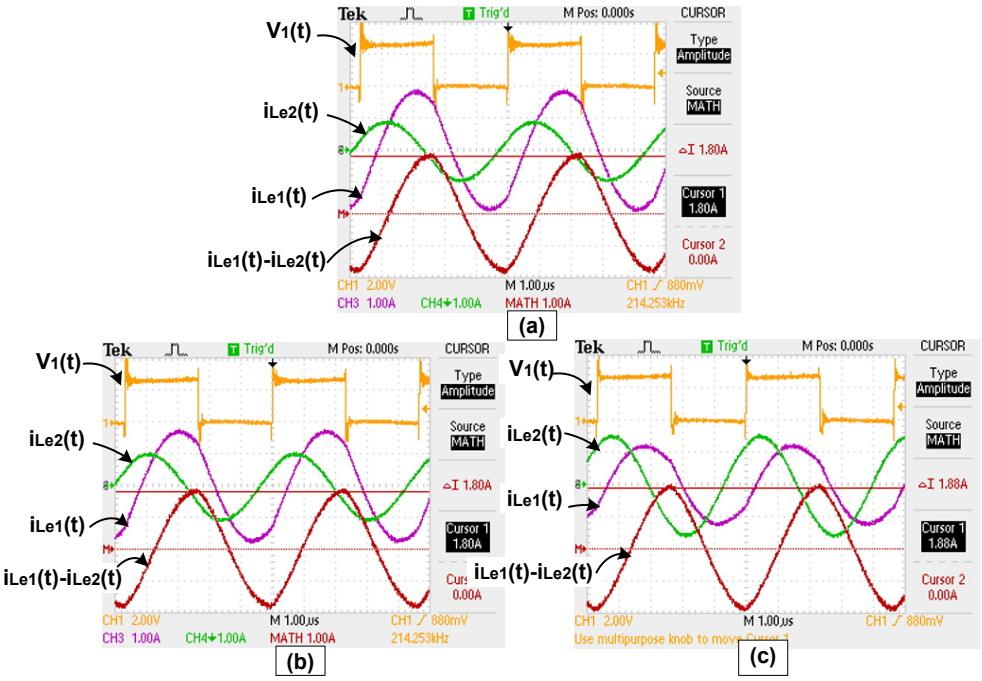

Figure 5.19: Experimental waveforms of resonant tank input voltage ($V_1(t)$ in yellow), primary-side coil current ($i_{Le1}(t)$ in purple), secondary-side coil current ($i_{Le2}(t)$ in green), and circulating current in the coupler ($i_{Le1}(t)$- $i_{Le2}(t)$ in red) for LQ: $Q_{Lsp} \approx 0.36$ (a), Opt Q: $Q_{Lsp} \approx 1.1$ (b), and HQ: $Q_{Lsp} \approx 3.2$ (c).

As can be seen in Figure 5.19, all of the current waveforms at the different Q_{Lsp} values are sinusoidal with the same phase conditions *and* with very small distortions. Thus, it is possible to calculate the circulating currents for different Q_{Lsp} values by measuring peak values of circulating currents (red waveforms) and dividing them by corresponding supply currents (I_{in}) (purple waveforms) in each Q_{Lsp} condition.

Table 5.8 lists the experimental data for evaluating the circulating currents in the coupler. This table shows the figure of merit highlighted in red. As can be seen, Opt Q does *not* cause circulating currents much larger than those at the LQ, whereas the HQ > Q_H causes much larger circulating currents in the coupler. Therefore, the presented design

equations and optimal Q_{Lsp} criteria allow maximization of robustness in power delivery. This maximization does *not* come at the cost of *significantly* increased circulating current in a coupler.

TABLE 5.8 EXPERIMENTAL DATA FOR EVALUATING THE CIRCULATING CURRENT IN THE COUPLER

$k \approx 0.37$			
	LQ ($Q_{Lsp} \approx 0.36$)	**Opt Q ($Q_{Lsp} \approx 1.1$)**	**HQ ($Q_{Lsp} \approx 3.2$)**
I_{in}	0.513	0.442	0.241
$i_{Le1}(t) - i_{Le2}(t)$	1.60	1.56	1.56
$(i_{Le1}(t) - i_{Le2}(t)) / I_{in}$	3.119	3.529	6.473
$k \approx 0.2$			
I_{in}	0.433	0.426	0.357
$i_{Le1}(t) - i_{Le2}(t)$	1.80	1.80	1.88
$(i_{Le1}(t) - i_{Le2}(t)) / I_{in}$	4.157	4.225	5.266
$k \approx 0.07$			
I_{in}	0.302	0.301	0.306
$i_{Le1}(t) - i_{Le2}(t)$	2.20	2.20	2.24
$(i_{Le1}(t) - i_{Le2}(t)) / I_{in}$	7.285	7.309	7.320

5.8 SUPPLEMENTARY SIMULATION RESULTS FROM OPTIMAL DESIGNS WITH $L_{S1} > L_{S2}$'

This section shows optimal design methods applied for $L_{S1} > L_{S2}$', unlike the experimental validation which was for $L_{S1} \approx L_{S2}$'. Therefore, various simulation results in this section are collected for further validation of the design equations.

In simulation, experimentally-extracted T-equivalent model parameters of asymmetrical magnetic coupler in Figure 5.20 are used. The T-equivalent model parameters are listed in Table 5.9. Further information regarding this coupler can be found in [40].

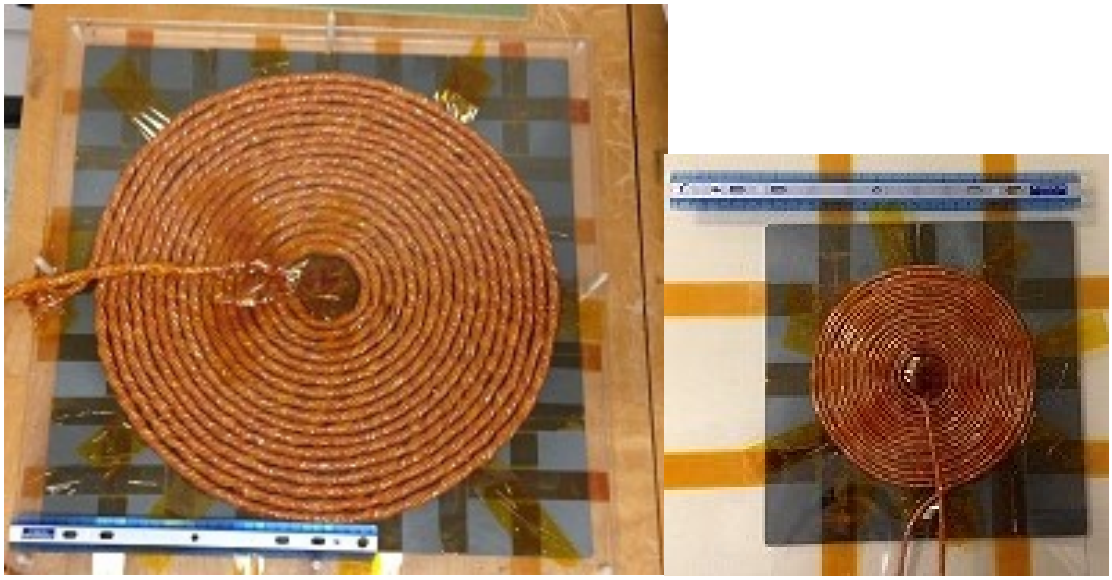

Figure 5.20: Asymmetrical Coupler for 3kW Wireless Charging of EV showing larger Tx(left) and smaller Rx(right).

TABLE 5.9 EXPERIMENTALLY-EXTRACTED T-EQUIVALENT MODEL PARAMETERS OF ASYMMETRICAL COUPLER IN FIGURE 5.20

k	L_{e1} (µH)	L_m (µH)	L_{e2}' (µH)
0.347	85.6	26.8	26.4
0.302	90.4	23.3	29
0.256	90.1	18.9	31.3
0.23	92.1	16.9	33.3
0.18	93	13.1	36.7
0.16	94.7	11.4	37.6
0.14	99.38	10.31	38.82

5.8.1 SIMULATION FOR OPTIMAL Q_{LSS} EVALUATION IN SS RESONANT TANK WITH $L_{S1} > L_{S2}$'

To check the performance of proposed design equations in the presence of stray parameters due to tolerance (in particular, assuming that there are errors in estimating expected values for L_{S1}/L_{S2}' and k_{max}), Matlab 3D plot for G_{Ratio} are plotted in Figure 5.21 for with $\frac{L_{S1}}{L_{S2}'} = 3$ and k_{max} = 0.3, instead of the actual values of $\frac{L_{S1}}{L_{S2}'} \approx 2.1$ and $k_{max} \approx$ 0.347. The black region in this figure represents G_{Ratio} = 1 ($\pm$ 10 %). Therefore,

according to this figure, $Q_{Lss} \approx 0.3$ is optimal for obtaining almost constant $G_{Ratio} = 1$ when $\frac{L_{S1}}{L_{S2}'} = 3$ and $k_{max} = 0.3$.

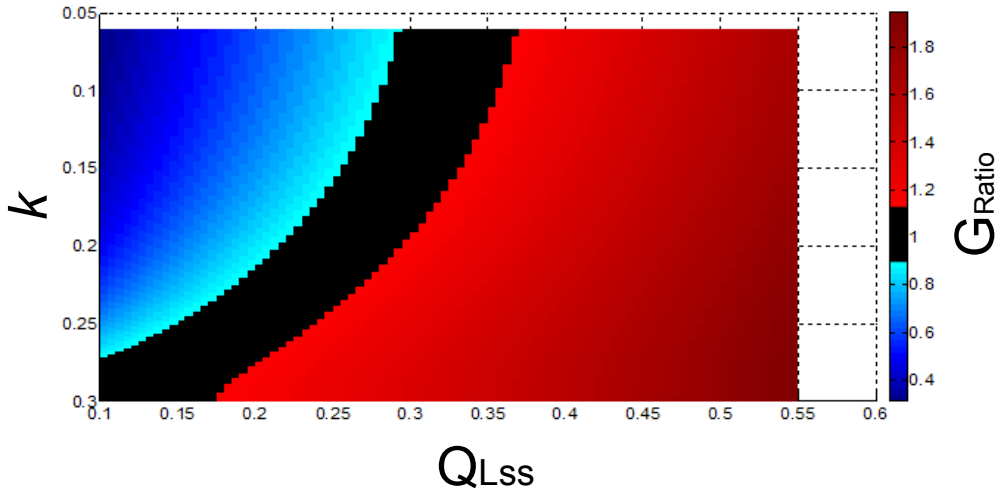

Figure 5.21: Matlab 3D plot for G_{Ratio} are plotted in Figure 5.21 for with $\frac{L_{S1}}{L_{S2}'} = 3$ and $k_{max} = 0.3$, instead of the actual values of $\frac{\mathbf{L_{S1}}}{\mathbf{L_{S2}'}} \approx 2.1$ and $k_{max} \approx 0.347$.

The next step is to check if $Q_{Lss} \approx 0.27$ is a desirable condition for the actual $\frac{L_{S1}}{L_{S2}'} \approx 2.1$ and $k_{max} \approx 0.347$. In order to obtain this quality factor at the actual $k_{max} \approx 0.347$ with the parameters in Table 5.9, R_{eSS}' needs to be approximately 2.862 Ω for ω_s_SS_$k_{max} = 2\pi$(25 kHz). In Figure 5.22, simulation data for G_{Ratio} are collected for LQ, Opt Q, and HQ conditions. Condition LQ represents $Q_{Lss} \approx 0.15$. Condition Opt Q represents $Q_{Lss} \approx 0.286$. Condition HQ represents $Q_{Lss} \approx 0.6$. As can be seen from Figure 5.22, Opt Q ($Q_{Lss} \approx 0.286$) exhibits the least sensitivity of G_{Ratio} against k variation. Furthermore, G_{Ratio} remains close to 1.1 for a wide range of k variation. It should be noted that parasitic resistances are *not* included in collecting the simulation data in Figure 5.22.

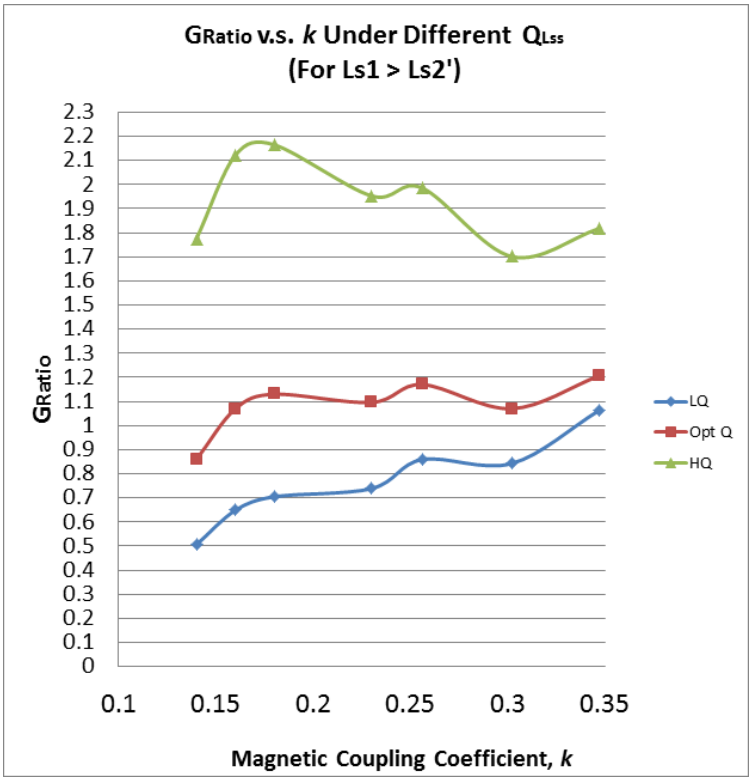

Figure 5.22: Simulation data for evaluation on G_{Ratio} under k variation for different load-dependent quality factors.

5.8.2 Simulation for Optimal Q_{LSP} Evaluation In SP Resonant Tank with $L_{S1} > L_{S2}$'

Again, to check the design equation performance under parameter estimation error due to tolerance (in particular, assuming that there are errors in expected values for L_{S1}/L_{S2}' and k_{max}), Matlab 3D plot for $\|G_V(j\omega_s\_SP\_k_{max})\|_{SP}$ are plotted in Figure 5.23 using equations 69, 72 and 73 with $\frac{L_{S1}}{L_{S2}'} = 3$ and k_{max} = 0.3, instead of the actual values of $\frac{L_{S1}}{L_{S2}'} \approx 2.1$ and $k_{max} \approx 0.347$.

This results in $|G_V|_{ind}SP \approx 1.92$ for $\frac{L_{S1}}{L_{S2}'} = 3$ and k_{max} = 0.3 instead of $|G_V|_{ind}SP \approx 1.99$ for $\frac{L_{S1}}{L_{S2}'} = 2.1$ and k_{max} = 0.347. The black region in Figure 5.23 indicates the condition of

1.92 - 10 % ≤ $||G_V(j\omega_s\_SP\_k_{max})||_{SP}$ ≤ 1.92 + 10 %. The red region indicates an undesirable condition of $||G_V(j\omega_s\_SP\_k_{max})||_{SP}$ > 1.92 + 10 %.

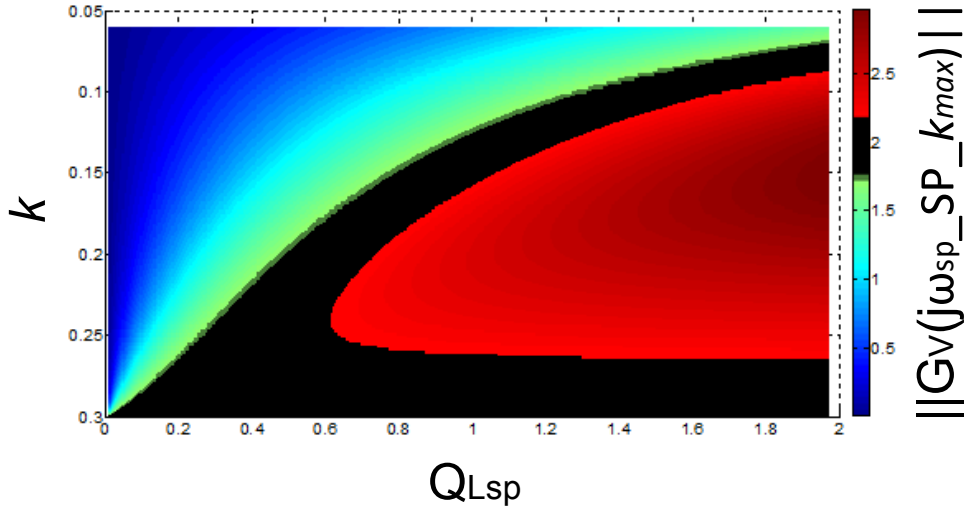

Figure 5.23: Matlab 3D plot for $||G_V(j\omega_s\_SP\_k_{max})||_{SP}$

According Figure 5.23, Q ≈ 0.6 is optimal in terms of obtaining almost constant voltage gain under *k* variation. In order to obtain this quality factor at the actual k_{max} ≈ 0.347 with the parameters in Table 5.9, R_{eSP}' needs to be approximately 5 Ω for $\omega_s\_SP\_k_{max} = 2\pi$(25 kHz).

Using the parameters in Table 5.9 and R_{eSP}' ≈ {2.5; 5; 10} Ω (corresponds to Q_{Lsp} ≈ {0.3; 0.6; 1.2}) in Pspice, simulation data for voltage gain, $||G_V(j\omega_s\_SP\_k_{max})||_{SP}$, are collected. Table 5.10 lists the simulation data. Plotting the data results in Figure 5.24 shows clearly that achieving Q_{Lsp} ≈ 0.6 provides almost constant voltage gain under wide range of *k* variation.

TABLE 5.10 SIMULATION DATA FOR $||G_V(j\omega_s\_SP\_k_{max})||_{SP}$ FOR DIFFERENT Q_{LSP} CONDITIONS

k	LQ ($Q_{Lsp} \approx 0.3$)	Opt Q ($Q_{Lsp} \approx 0.6$)	HQ ($Q_{Lsp} \approx 1.2$)
0.347	1.99	1.99	1.99
0.302	1.31	1.83	2.11
0.256	1.60	2.18	2.47
0.23	1.12	1.85	2.46
0.18	1.07	1.90	2.79
0.16	0.80	1.50	2.48
0.14	0.39	0.76	1.43

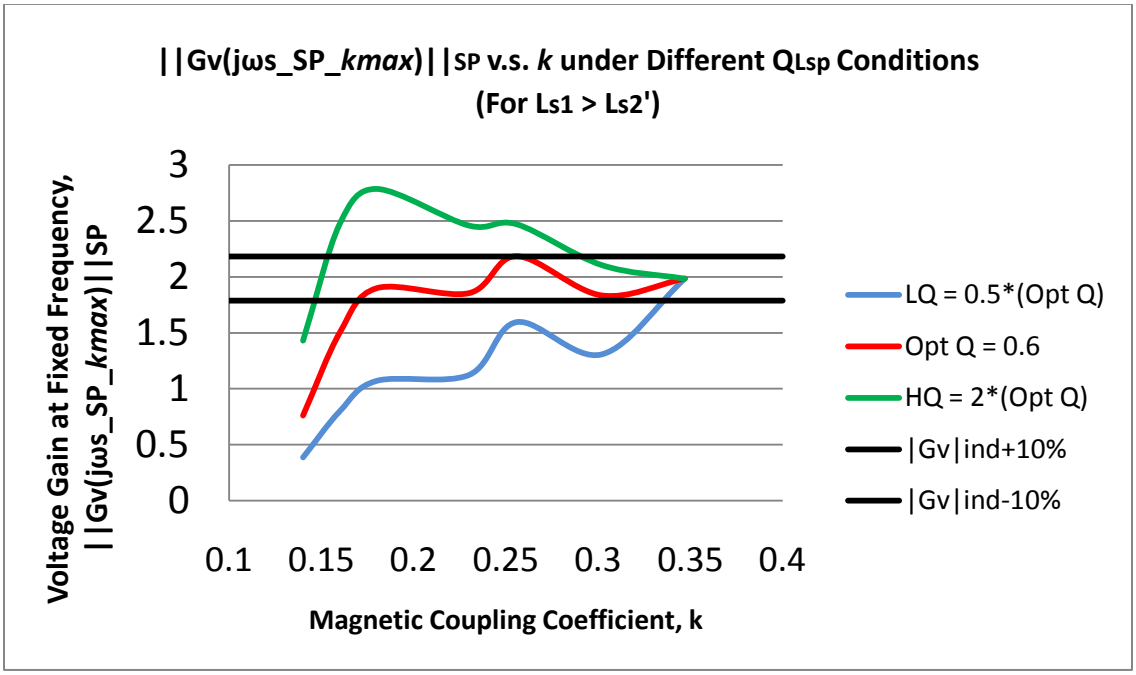

Figure 5.24: Simulation data for voltage gain $||G_V(j\omega_s\_SP\_k_{max})||_{SP}$ under different Q_{Lsp} conditions.

In summary, the proposed design equations for loosely-coupled SS resonant tank and loosely-coupled SP resonant tank successfully allow determining optimal load-dependent quality factors even with possible estimation errors in expected values for $\frac{L_{S1}}{L_{S2}}$, and k_{max}. This further demonstrates practical usefulness of the proposed design methods since

tolerances in $\frac{L_{S1}}{L_{S2}}$, and k_{max} are commonly expected between FES simulation and experimental implementation of a coupler.

5.9 CHAPTER SUMMARY

In this chapter, detailed analysis and comparative study on frequency-domain characteristics of the SS and SP resonant tank topologies are performed. Using various analytical equations derived in design-oriented form, novel optimal design methods for loosely-coupled SS and SP resonant tank topologies are presented.

It is shown that by using the novel design methods, desirable parameters of SS and SP resonant tanks can be conveniently determined to achieve optimal load-dependent quality factors for a desired value of nominal effective resistive load.

For the SP resonant tank with optimal load-dependent quality factor condition achieved at $k = k_{max}$, the simulations and experimental results show that maximizing the robustness in voltage gain and current gain can be achieved at a desirably fixed operating frequency without significantly increased circulating current in a coupler.

Also, for the SS resonant tank with optimal load-dependent quality factor condition achieved at $k = k_{max}$, the simulations and experimental results show that a good compromise can be achieved between voltage gain and current gain, so that approximately equal values of voltage gain and current gain can be maintained for almost entire range of k at a desirably fixed operating frequency while minimizing the circulating current gain.

The experimental results show that the proposed optimal design methods perform well even in the presence of parasitic resistance terms. The supplementary simulation results show that the proposed design equations perform well even with the estimation error in

expected values for L_{S1}/L_{S2}' and k_{max}. Therefore, the proposed design equations are proven to exhibit high practical usefulness.

Based on all of the results in this chapter, it can be concluded that SS resonant tank cannot provide almost constant voltage gain for a wide *k* range without frequency modulation and without significantly large circulating current (significant increase in reactive energy). On the other hand, SP resonant tank can provide almost constant voltage gain for a wide *k* range without high control complexity at a fixed operating frequency. However, SS resonant tank performs better in terms of efficiency. Therefore, in wireless power transfer applications with more limited *k* variation, SS resonant tank is desirable. Such applications may include wireless charging of stationary loads like EVs, TVs, and household appliances. In wireless charging of portable electronics, maintaining good charging speed under *wider k* variation (increased receiver positioning flexibility) is desirable. Therefore, SP resonant tank topology is more suitable. However, it should be noted that a large effective load resistance (e.g. almost fully-charged battery) in SP resonant tank can cause significant power loss in receiver coil. Furthermore, it can also cause large circulating current through the parallel resonant capacitor. These issues may be resolved with a power supply that is desirably limited in power delivery.

In conclusion, the superiority of one resonant tank over the other depends on specific conditions of an application. Using the presented novel optimal design methods, analysis, comparative study, evaluation, and optimal designs can be performed conveniently. Therefore, the design methods allow more detailed comparison to be performed for desired applications rapidly, so that the cost of design optimization process can be minimized.

CHAPTER 6

CONCLUSION, PUBLICATIONS, AND FUTURE WORK

6.1 CONCLUSION

Chapter 1 discusses inductive wireless charging mechanism and background theories of resonant converters: sinusoidal approximation analysis, equivalent circuit modeling, soft switching mechanisms (ZVS and ZCS), and load current control methods. It also describes voltage gain characteristics of commonly-used resonant tanks. Also, various shortcomings of currently-available wireless power transfer technology are described. Motivation and research significance are discussed to explain various significant contributions that three distinctive novel accomplishments in this research make.

Chapter 2 contains a brief summary of the experimental evaluation board set-up, which is used for experimental validation of the novel accomplishments in this research. The performance of this experimental evaluation board is demonstrated by implementing the symmetrical series-series resonant converter. The experimental results for converter waveforms, power transmission efficiency, and soft-switching mechanisms are shown to demonstrate that the experimental evaluation board is working as desired.

In Chapter 3, the first of the novel accomplishments, optimal design method for symmetrical series-series resonant tank topology, is explained. This optimal design method allows rapid and convenient calculation of the resonant tank parameters required

for achieving a desired peak voltage gain condition. Without time-consuming efforts and complexity that the conventional design methods require, this novel optimal design method provides a cost-effective design solution. When different geometries of magnetic coupler are being considered for a wireless charging system, using the design method also allows determining which of the coupler geometry is desirable for a specified nominal resistive load condition. By using the design method, evaluation can be performed rapidly, and it can be easily found that a coupler with higher magnetic coupling can sometimes be less desirable than a coupler with lower magnetic coupling. This is because for a given nominal resistive load condition, achieving desirable voltage gain characteristics can cause larger circulating current loss in a coupler with higher magnetic coupling. With the novel optimal design method, optimization of symmetrical SS resonant tank can be done with low cost in design process.

In Chapter 4, the second of novel accomplishments, unity gain frequency tracking (UGFT) control method, is explained. Without the need for communication between transmitter and receiver, this UGFT control method allows tracking and achieving the unity voltage gain frequency of symmetrical SS resonant tank under receiver positioning variation with respect to transmitter position (under magnetic coupling coefficient, k, variation). This unity voltage gain frequency is the resonant frequency at which leakage inductances are compensated by their series resonant capacitors. At this frequency, maximum power transmission efficiency can be achieved while providing desired voltage gain and current gain. By achieving the unity gain frequency operation without communication, the need for additional downstream linear voltage regulator is eliminated. Also, communication module ICs are not required. Simulation results and

experimental results are shown to demonstrate that the novel UGFT control method performs well in tracking and achieving unity gain frequency under k variation. Experimental comparison results of voltage gain and power efficiency for fixed frequency operation and UGFT control operation show that the UGFT operation allows voltage gain to be maintained well under k variation and also significantly improves power efficiency. With the fixed frequency operation under k variation, significant voltage gain variation occurs while exhibiting much lower power efficiency. This means that in order to maintain constant current constant voltage (CC-CV) charging profile, fixed frequency operation requires an additional converter or linear voltage regulator. Consequently, cost of implementation would increase while undesirably reducing power density and further reducing power efficiency. Therefore, this chapter shows that a symmetrical SS resonant converter implementing the novel UGFT control method provides several desirable features including improved power efficiency, increased power density, lower cost of implementation, and improved receiver positioning flexibility.

Chapter 5 explains the final novel accomplishments, optimal design methods for loosely-coupled asymmetrical series-series (SS) resonant tank and loosely-coupled asymmetrical series-parallel (SP) resonant tank. In this chapter, detailed general analysis on frequency-domain characteristics of the SS and SP resonant tank topologies is performed to derive general analytical equations in design-oriented form consisting of physically meaningful quantities (load-dependent quality factor and expected values for L_{S1}/L_{S2}' and k). For both symmetrical implementation and asymmetrical implementation, these general analytical equations allow determining and evaluating various notable quantities. Using some of the general analytical equations and assuming loosely-coupled

condition, optimal design methods for loosely-coupled SS and SP resonant tank topologies are presented. It is shown that by using these optimal design methods, desirable parameters of SS and SP resonant tanks can be conveniently determined to achieve *optimal* load-dependent quality factors for a desired value of nominal effective resistive load. For the SP resonant tank with optimal load-dependent quality factor condition achieved at $k = k_{max}$, the simulations and experimental results show that maximizing the robustness in voltage gain and current gain can be achieved at a desirably fixed operating frequency without significantly increased circulating current in a magnetic coupler. For the SS resonant tank with optimal load-dependent quality factor condition achieved at $k = k_{max}$, the simulations and experimental results show that a good compromise can be achieved between voltage gain and current gain, so that approximately equal values of voltage gain and current gain can be maintained for almost entire range of k at a desirably fixed operating frequency. It is analytically shown that the circulating current gain is approximately at its absolute minimum at the fixed operating frequency. Various experimental results show that the proposed optimal design methods perform well even under the presence of parasitic resistance terms. The supplementary simulation results are included to prove that the proposed design equations perform well even with the estimation error in expected values for L_{S1}/L_{S2}' and k_{max}. Therefore, the proposed design equations are proven to exhibit high practical usefulness. Comparative study on SS and SP resonant tank topologies is performed to explain advantages and disadvantages of each topology. Based on the comparative study, it can be concluded that for a wireless power transfer application with a narrower range of k variation, SS resonant tank topology is desirable for obtaining higher power efficiency and for

reducing power stage component count. For a wider range of *k* variation, SP resonant tank topology is desirable because smaller variations in voltage gain and current gain can be achieved. Also, for a fairly wide range of *k* variation, phase shift between input voltage and input current of SP resonant tank remains smaller than that of SS resonant tank, meaning that smaller reactive energy would be generated in SP resonant tank.

In conclusion, the novel accomplishments in this research significantly improve efficiency and receiver positioning flexibility, and reduce complexity in design optimization, complexity in control, and cost of implementation.

6.2 PUBLICATIONS

6.2.1 AS THE MAIN (FIRST)AUTHOR

1) Isaac Nam, Roger Dougal, and Enrico Santi, "General Optimal Design Method for Loosely-coupled Series-Series Resonant Tank in Wireless Power Transfer Applications," *Applied Power Electronics Conference and Exposition (APEC), 2014 IEEE* (Accepted for lecture presentation and will be published after the conference).
2) Isaac Nam, Roger Dougal, and Enrico Santi, "Optimal Design Method to Achieve Both Good Robustness and Efficiency in Loosely-coupled Wireless Charging System Employing Series-parallel Resonant Tank with Asymmetrical Magnetic Coupler," *Energy Conversion Congress and Exposition (ECCE), 2013 IEEE,* vol., no., pp.3266-3276, 15-19 Sept. 2013.
3) Isaac Nam, Roger Dougal, and Enrico Santi, "Novel Unity Gain Frequency Tracking Control of Series-series Resonant Converter to Improve Efficiency and Receiver Positioning Flexibility in Wireless Charging of Portable Electronics," *Industrial Applications, IEEE Transaction on* (Edited following IEEE transactions reviewers' comments for final submission).
4) Isaac Nam, Roger Dougal, and Enrico Santi, "Optimal design method for series LCLC resonant converter based on analytical solutions for voltage gain resonant peaks," *Applied Power Electronics Conference and Exposition (APEC), 2013 Twenty-Eighth Annual IEEE* , vol., no., pp.1429-1437, 17-21 March 2013.
5) Isaac Nam, Roger Dougal, and Enrico Santi, "Novel control approach to achieving efficient wireless battery charging for portable electronic

devices," *Energy Conversion Congress and Exposition (ECCE), 2012 IEEE* , vol., no., pp.2482-2491, 15-20 Sept. 2012.

6.2.2 As a Supporting (Second) Author

1) Raffael Haldi, Isaac Nam, Kurt Schenk, and Enrico Santi, "Finite-Element-Simulation-Assisted Optimized Design of an Asymmetrical High-Power Inductive Coupler with a Large Air-Gap for EV Charging" *Energy Conversion Congress and Exposition (ECCE), 2013 IEEE,* 15-19 Sept. 2013
2) Daniel Martin, Isaac Nam, Jonathan Siegers, and Enrico Santi, "Wide bandwidth three-phase impedance identification using existing power electronics inverter," *Applied Power Electronics Conference and Exposition (APEC), 2013 Twenty-Eighth Annual IEEE* , vol., no., pp.334,341, 17-21 March 2013.

6.2.3 Planned Publications

1) The ECCE 2013 paper (2 in Section 6.2.1) is currently being updated for submission to IEEE Transactions by the graduation in December, 2013.
2) The APEC 2014 paper (1 in Section 6.2.1) will be submitted for IEEE Transactions after the conference in March, 2014.

6.3 Future Work

As a future work, two tasks can be considered. One of them is coupler geometry optimization, and the other is ultra-high frequency operation of a resonant converter. This section briefly discusses these two tasks.

6.3.1 Coupler Geometry Optimization

To improve receiver positioning flexibility and maximize robustness in power transmission and efficiency, it is highly desirable to provide uniform magnetic field across a wide surface area of a charging platform. This minimizes magnetic coupling variation with respect to lateral misalignment between transmitter coil and receiver coil. In order to do so, a transmitter coil must be optimally designed. For example, it can be easily determined that an array of flat spiral transmitter coils in multiple layers can be used to create a more uniform magnetic field profile across a charging platform.

However, it is of high interest to determine various optimal transmitter coil geometries that can provide uniform magnetic field without a large part count.

A non-trivial geometry can be used for receiver coil as well in order to obtain improved degrees of freedom in the receiver coil movement with respect to the transmitter coil. For example, besides the variations in lateral misalignment and coil-to-coil distance, angular misalignment can occur. With an orthogonal configuration in magnetic field generation direction and pick-up direction, magnetic coupling is at its worst. With more sophisticated receiver coil design, such as a multi-pickup in which three circular coils are implemented orthogonally in x, y, and z directions, magnetic coupling can become more robust against angular misalignments.

6.3.2 Ultra-high Frequency Operation

With increased demand in power density, it is desirable to increase the operation frequency to MHz range. In doing so, either using small resonant capacitors or using parasitic stray capacitances of air-core coupler coils can be used. Although using parasitic capacitances of air-core coils leads to higher design complexity compared to using small resonant capacitors for magnetic core coupler, it can be desirable to eliminate the core losses. Transmitter coil and receiver coil must be carefully designed to achieve desirable parasitic resistance-dependent quality factor as well as desirable load-dependent quality factor while minimizing skin effect and proximity losses.

Although ZVS and ZCS are used for switching loss minimization, it is difficult to maintain them for wide variation ranges of k and load. Therefore, in ultra-high frequency operation, SiC or GaN switches can be used to minimize switching losses under hard-switching.

Various issues to be resolved include EMI and undesirable signal oscillations occurring in switching loops. Therefore, it is necessary to implement shielding and proper circuit layout along with snubbers, common-mode filters, differential-mode filters, and so on.

REFERENCES

[1] Gyu Bum Joung and Bo H. Cho, "An Energy Transmission System for an Artificial Heart Using Leakage Inductance Compensation of Transcutaneous Transformer", *IEEE Transactions on Power Electronics, vol. 13, no. 6, pp.1013-1022, Nov. 1998.*

[2] A. Ghahary and B. H. Cho, "Design of a Transcutaneous Energy Transmission System using a Series Resonant Converter," *IEEE Power Electronics Specialists Conf. Rec., 1990, pp. 1–8.*

[3] M. Takahashi, K. Watanabe, F. Sato, H. Matsuki, "Signal transmission system for high frequency magnetic telemetry for an artificial heart", *IEEE Transactions on Magnetics, vol. 41, no. 10, pp. 4173-4175, Oct. 2005.*

[4] Ping Si, Aiguo Patrick Hu, David Budgett, Simon Malpas, Joseph Yang and Jinfeng Gao, "Stabilizing the Operating Frequency of a Resonant Converter for Wireless Power Transfer to Implantable Biomedical Sensors", *1st International Conference on Sensing Technology (ICST), pp 477-482, Nov, 2005.*

[5] Rongxiang Wu; Raju, S.; Mansun Chan; Sin, J.K.O.; Yue, C.P., "Silicon-Embedded Receiving Coil for High-Efficiency Wireless Power Transfer to Implantable Biomedical ICs," *Electron Device Letters, IEEE* , vol.34, no.1, pp.9,11, Jan. 2013

[6] J.L. Villa, Jesús Sallán, Andrés Llombart, and José Fco Sanz, "Design of a high frequency Inductively Coupled Power Transfer System for electric vehicle battery charger", *Elsevier Applied Energy, pp.355-363, 2008.*

[7] M. Prabhakar, "Selection Criteria and Analysis of LCC Resonant DC-DC Converters for Automotive Applications", *Modern Applied Science, vol. 3, no. 7, pp 21-31, July, 2009.*

[8] Takanashi, Hiroya; Sato, Yukiya; Kaneko, Yasuyoshi; Abe, Shigeru; Yasuda, Tomio, "A large air gap 3 kW wireless power transfer system for electric vehicles," *Energy Conversion Congress and Exposition (ECCE), 2012 IEEE* , vol., no., pp.269-274, 15-20 Sept. 2012.

[9] Chwei-Sen Wang; Stielau, O.H.; Covic, G.A, "Design considerations for a contactless electric vehicle battery charger," *IEEE Transactions on Industrial Electronics,* vol.52, no.5, pp. 1308- 1314, Oct. 2005.

[10] Huy Hoang; Seunggyu Lee; Youngsu Kim; Yunho Choi; Bien, F., "An adaptive technique to improve wireless power transfer for consumer electronics," *Consumer Electronics, IEEE Transactions on* , vol.58, no.2, pp.327,332, May 2012

[11] Ahn, D.; Hong, S., "Effect of Coupling Between Multiple Transmitters or Multiple Receivers on Wireless Power Transfer," *Industrial Electronics, IEEE Transactions on* , vol.60, no.7, pp.2602,2613, July 2013.

[12] Wireless Power Consortium (Qi), "Wireless Power Specifications Part 1: System Description: Wireless Power Transfer" (ver. 1.0.2 vol. 1) [Online] Available:http://www.wirelesspowerconsortium.com/downloads/wireless-power-specification-part-1.html.

[13] Kamil A. Grajski, Ryan Tseng and Chuck Wheatley, "Loosely-coupled Wireless Power Transfer: Physics, Circuits, Standards", Microwave Workshop Series on Innovative Wireless Power Transmission: Techonologies, Systems and Applications (IMWS), IEEE MTT-S International, 2012.

[14] Y. Jang and M.M. Jovanovic, "A contactless electricity energy transmission system for portable-telephone battery charger", *IEEE Transactions on Industrial Electronics, vol. 50, no. 3, pp. 520-527, June. 2003.*

[15] Yungtaek Jang and Milan M. Jovanovic, "A Contactless Electrical Energy Transmission System for Portable-Telephone Battery Chargers", *IEEE Transactions on Industrial Electronics, Vol. 50, No. 3, pp 520-527, June, 2003.*

[16] C.-G. Kim, D.-H. Seo, J.-S. You, J.-H. Park, and B. H. Cho, "Design of a contactless battery charger for cellular phone," *IEEE Trans. Ind. Electron.*, vol. 48, no. 6, pp. 1238–1247, Dec. 2001

[17] J. A. Taylor, Z. N. Low, J. Casanova, and J. Lin, "A wireless power station for laptop computers," in *Proc. IEEE Radio Wireless Symp.*, 2010, pp. 625–628.

[18] Koichi Hatanaka, F. Sato, H. Matsuki, S. Kikuchi, J. Murakami, M. Kawase, and T. Satoh, "Power transmission of a desk with a cord-free power supply," *IEEE Trans. Magnetics*, vol. 38, no. 5, pp. 3329–3331, Sep. 2002.

[19] Isaac Nam, "Analysis and Optimal Design Method of LCLC Resonant Tank for Bidirectional DC-DC Resonant Converter and LCLC Resonant Converter's Efficiency Performance in Wireless Low Power Transfer Applications", *M.S. Thesis, Electrical Engineering Dept., University of South Carolina,* July, 2009.

[20] Bing Lu, Wenduo Liu, Yan Lian, Fred C. Lee, and Jacobus D. van Wyk, "Optimal Design Methodology for LLC Resonant Converter", *Applied Power Electronics Conference and Exposition 2006 (APEC '06), pp 533-538, Mar, 2006.*

[21] STMicroelectronics (www.st.com), "LLC Resonant Half-bridge Converter Design Guideline", *Application Note, AN2450, Rev. 5, pp 1-32, Oct, 2007*.

[22] Sung-Soo Hong, Sang-Ho cho, chung-Wook Roh, and Sang-Kyoo Han, "Precise Analytical Solution for the Peak Gain of LLC Resonant Converters", *Journal of Power Electronics, Vol. 10, No. 6, pp 680-685, Nov, 2010.*

[23] Junji Hirai, Tae-Woong Kim,and Atsuo Kawamura, " Study on Intelligent Battery Charging Using Inductive Transmission of Power and Information", *IEEE Transactions on Power Electronics, vol. 15, no. 2, pp.335-345, Mar. 2000.*

[24] T. Imura and Y. Hori, “Maximizing Air Gap and Efficiency of Magnetic Resonant Coupling for Wireless Power Transfer Using Equivalent Circuit and Neumann Formula,” *IEEE Trans. Ind. Electron.*, vol. 58, no. 10, pp. 4746–4752, Oct. 2011.

[25] Battery University by CADEX Electronics Inc, "Charging Lithium-ion Batteries"[Online]Available:http://batteryuniversity.com/learn/article/charging_lithium_ion_batteries

[26] Maxim Integrated, "Understanding Li+ Battery Operation Lessens Charging Safety Concerns", *Application Note 4169*, Mar, 2008. [Online]Available:http://www.maximintegrated.com/app-notes/index.mvp/id/4169

[27] Stephan Buller, Marc Thele, Rik W. A. A. De Doncker, and Eckhard Karden, "Impedance-Based Simulation Models of Supercapacitors and Li-Ion Batteries for Power Electronic Applications", *IEEE Transactions on Industry Applications, Vol. 41, No. 3, May/June 2005.*

[28] Hua Bai and Chris Mi, "Eliminate Reactive Power and Increase System Efficiency of Isolated Bidirectional Dual-Active-Bridge DC-DC Converters Using Novel Dual-Phase-Shift Control", *IEEE Transactions on Power Electronics, vol. 23, no.6, pp 2905-2914, Nov. 2008.*

[29] German G. Oggier, Guillermo O. Garcia and Alejandro R. Oliva, "Switching Control Strategy to Minimize Dual Active Bridge Converter Losses", *IEEE Transactions on Power Electronics. vol. 24 no. 7, pp 1826-1838, July, 2009.*

[30] Dehong Xu, Chuanhong Zhao and Haifeng Fan, "A PWM Plus Phase-Shift Control Bidirectional DC-DC Converter", *IEEE Transactions on Power Electronics, vol. 19, no. 3, pp 666-675.*

[31] Chih-Jung Chen; Tah-Hsiung Chu; Chih-Lung Lin; Zeui-Chown Jou, "A Study of Loosely Coupled Coils for Wireless Power Transfer," *Circuits and Systems II: Express Briefs, IEEE Transactions on* , vol.57, no.7, pp.536-540, July 2010.

[32] Chwei-Sen Wang; Covic, G.A.; Stielau, O.H., "Power transfer capability and bifurcation phenomena of loosely coupled inductive power transfer systems," *IEEE Transactions on Industrial Electronics*, vol.51, no.1, pp. 148- 157, Feb. 2004.

[33] Kurschner, D.; Rathge, C.; Jumar, U., "Design Methodology for High Efficient Inductive Power Transfer Systems With High Coil Positioning Flexibility", *IEEE Transactions on Industrial Electronics*, vol.60, no.1, pp.372-381, Jan. 2013.

[34] John Miller; Oak Ridge National Laboratory, “Wireless Plug-in Electric Vehicle (PEV) Charging” Presentation, May, 2012 [Online]Available: http://www1.eere.energy.gov/vehiclesandfuels/pdfs/merit_review_2012/veh_sys_sim/vss061_miller_2012_o.pdf

[35] Tseng, Ryan; von Novak, Bill; Shevde, Sumukh; Grajski, Kamil A., "Introduction to the alliance for wireless power loosely-coupled wireless power transfer system specification version 1.0," *Wireless Power Transfer (WPT), 2013 IEEE* , vol., no., pp.79,83, 15-16 May 2013

[36] Hui, S.Y.R.; Ho, W.W.C., "A new generation of universal contactless Battery Charging platform for portable Consumer Electronic equipment," *Power Electronics, IEEE Transactions on* , vol.20, no.3, pp.620,627, May 2005

[37] Zhen Ning Low; Chinga, R.A.; Ryan Tseng; Jenshan Lin, "Design and Test of a High-Power High-Efficiency Loosely Coupled Planar Wireless Power Transfer System," *Industrial Electronics, IEEE Transactions on* , vol.56, no.5, pp.1801,1812, May 2009

[38] Chih-Jung Chen; Tah-Hsiung Chu; Chih-Lung Lin; Zeui-Chown Jou, "A Study of Loosely Coupled Coils for Wireless Power Transfer," *Circuits and Systems II: Express Briefs, IEEE Transactions on* , vol.57, no.7, pp.536-540, July 2010.

[39] X. Liu and S. Y. R. Hui, "Optimal design of a hybrid winding structure for planar contactless battery charging platform," *IEEE Trans. Power Electronics*, vol. 23, no. 1, pp. 455–463, Jan. 2008.

[40] Raffael Haldi, Isaac Nam, Kurt Schenk, and Enrico Santi, "Finite-Element-Simulation-Assisted Optimized Design of an Asymmetrical High-Power Inductive Coupler with a Large Air-Gap for EV Charging" *Energy Conversion Congress and Exposition (ECCE), 2013 IEEE,* vol., no., pp.3635-3642, 15-19 Sept, 2013